CHARACTERIZATION AND NETWORK CONSEQUENCES OF LOW SPREADING LOSS IN UNDERWATER ACOUSTIC NETWORKS

A Dissertation Presented

by

JAMES W. PARTAN

Submitted to the Graduate School of the
University of Massachusetts Amherst in partial fulfillment
of the requirements for the degree of

DOCTOR OF PHILOSOPHY

September 2013

School of Computer Science

CHARACTERIZATION AND NETWORK CONSEQUENCES OF LOW SPREADING LOSS IN UNDERWATER ACOUSTIC NETWORKS

A Dissertation Presented

by

JAMES W. PARTAN

Approved as to style and content by:

Brian Levine, Chair

James Kurose, Member

James Preisig, Member

Dennis Goeckel, Member

Michael Zink, Member

Lori Clarke, Department Chair
School of Computer Science

ACKNOWLEDGMENTS

First, I would like to thank my committee and advisors, in particular Jim Preisig and Brian Levine, for their incredible support, encouragement, and help. Brian really kept me going through the hard parts of this work. His advice focusing me on the next step towards completion really allowed me to see that finishing this work was achievable. His energy and enthusiasm in each meeting was infectious, and gave me a boost every time. Jim Preisig has been mentoring me for fifteen years at this point, and his steadfast support has been incredible, keeping me going. I could not have finished this work without the support of both Brian and Jim — thank you both. Jim Kurose also provided help, and has amazing insights into what are the interesting parts of problems.

My professional home for the past fifteen years, and to continue after graduate school, has been the Acoustic Communications group at the Woods Hole Oceanographic Institution. Lee Freitag is a great mentor and group leader. His practical engineering wisdom and experience are nearly unmatched, his tireless work ethic is inspiring, our projects are interesting (and, thanks to Lee, our funding has been reliable!), and he creates a fun work environment, leading by example in every way. Sandipa Singh has been my closest day-to-day colleague since 2000, and she is a great engineer and friend to work with. Eric Gallimore has been our FPGA and circuit guru, and is the best young engineer I've ever had the pleasure of working with. Keenan Ball designs an amazing amount of electro-mechanical hardware, interfacing our systems to every underwater vehicle around. Peter Koski is always the one who gets to go on icebreakers and to Arctic ice camps! At least we get to share the experiences vicariously at the Captain Kidd when he returns. Each July, we all look forward to the arrival of Milica Stojanovic, our annual summer visitor — she makes the summers much more fun, and is without question our intellectual heavyweight.

Also at WHOI, I'm looking forward to continued collaboration with Tom Hurst, Mark Baumgartner, and Aran Mooney on passive acoustic detection and classification of marine mammals;

Mike Jakuba and James Kinsey on deep sea untended robotic exploration; and Greg Packard on autonomous deep sea search and survey operations. Mark Johnson was one of my original and most influential engineering mentors — his minimalist and elegant design principles guide me nearly daily.

Professors Bill and Diana Spears provided a great lab-away-from-home for me at the University of Wyoming during our time in Laramie. I loved having a workplace to go to, and talking with technical colleagues in their swarm robotics group. I have fond memories of the crisp, clear air of Wyoming, Laramie's pleasant walkable downtown, and the millions of acres of National Forest fifteen minutes out of town.

My friends Jon Woodruff, Boris Margolin, Dirk Koopmans, Mike Jakuba, Chris Roman, Nick Lowell, Oscar Pizarro, and others have been great. Thanks to Morgaine Beck as well for her advice and guidance through many of the hard parts of this thesis.

And my family has been the most important support for me. My parents and brother have always supported me and been those closest to me. I have loved living nearby, and being able to see my Mom frequently. My Dad died just before I started at UMass, and we miss him. My extended family in all directions — Johnsons, Heidorns, Partans, Paiges — is one of my great sources of joy, love, and support, and I love spending time with all of you.

My wife, Elsa, has provided more love and support than I ever imagined anyone could. She has always believed in me, and she has always been an inspiration to me. Thank you, Elsa! I love you! And our daughter Kate is such a joy — we love you so much, Kate!

ABSTRACT

CHARACTERIZATION AND NETWORK CONSEQUENCES OF LOW SPREADING LOSS IN UNDERWATER ACOUSTIC NETWORKS

SEPTEMBER 2013

JAMES W. PARTAN

B.A., WILLIAMS COLLEGE

B.A., UNIVERSITY OF CAMBRIDGE

M.S., MASSACHUSETTS INSTITUTE OF TECHNOLOGY

Ph.D., UNIVERSITY OF MASSACHUSETTS AMHERST

Directed by: Professor Brian Levine

This thesis presents several related pieces of work on underwater acoustic networks (UANs). Underwater wireless networks generally use acoustics, as radio is heavily attenuated and light is strongly scattered underwater.

UANs are becoming more widely deployed for scientific, environmental, industrial, and military applications. The network nodes can be stationary sensor nodes, underwater vehicles, surface buoys or vehicles providing a gateway to radio networks, or bottom nodes providing a gateway to cabled undersea networks.

Packet detection in interference in UANs, and its critical role in the effectiveness of collision-avoidance medium-access control (MAC) protocols, is a primary focus of this thesis. Spreading loss measures the decrease in received energy as a function of range, and determines the level of long-range interference.

We present a new spreading model, the mixed-exponent spreading model, for UAN nodes using a matched-filter detector as a low-power wakeup detector. Under this model, there are distinct spreading-loss exponents for packet detection and interference, due to the matched-filter detector's signal processing. We validate this spreading model numerically, and with direct measurements of the spreading exponents from shallow-water experimental data. The widely used, but poorly grounded, "practical spreading" model is inconsistent with our experimental measurements. Our results suggest caution for its continued use to model performance of UANs.

Building on our spreading analysis, we analyze the effectiveness of collision-avoidance MAC protocols in UANs, namely what fraction of collisions are avoided when using the protocol, independent of propagation delay. The low spreading loss in UANs, in particular with the mixed-exponent spreading model, can lead to low collision-avoidance effectiveness compared with radio networks.

In addition, we argue that many UANs will be relatively mobile and sparse relative to terrestrial sensor networks, reducing the importance of network energy consumption and throughput of medium-access control protocols as metrics. This survey challenges some of the assumptions made in past UAN research, with a goal of aiding researchers entering the area of UANs from terrestrial sensor networks.

Finally, we document the design decisions for a new underwater acoustic modem, as a contribution to researchers entering the field from terrestrial sensor networks.

TABLE OF CONTENTS

LIST OF TABLES

Table **Page**

LIST OF FIGURES

Figure **Page**

INTRODUCTION

This thesis presents several related pieces of work on underwater acoustic networks (UANs). Underwater wireless networks generally use acoustics, as radio is heavily attenuated and light is strongly scattered underwater.

UANs are becoming more widely deployed for scientific, environmental, industrial, and military applications. The network nodes can be stationary sensor nodes, underwater vehicles, surface buoys or vehicles providing a gateway to radio networks, or bottom nodes providing a gateway to cabled undersea networks.

Packet detection in interference in UANs, and its critical role in the effectiveness of collision-avoidance medium-access control (MAC) protocols, is a primary focus of this thesis. Spreading loss measures the decrease in received energy as a function of range, and determines the level of long-range interference.

In Chapter 2, we present a new spreading model, the mixed-exponent spreading model, for UAN nodes using a matched-filter detector as a low-power wakeup detector. Under this model, there are distinct spreading-loss exponents for packet detection and interference, due to the matched-filter detectors signal processing. We validate this spreading model numerically, and with direct measurements of the spreading exponents from shallow-water experimental data. The "practical spreading" model, which is widely used to model UANs, but which is poorly grounded in experiment and theory, is inconsistent with our experimental measurements. Our results suggest caution for its continued use to model performance of UANs.

Building on our spreading analysis, in Chapter 3, we analyze the effectiveness of collision-avoidance MAC protocols in UANs, namely what fraction of collisions are avoided when using the protocol, independent of propagation delay. The low spreading loss in UANs, in particular with the

mixed-exponent spreading model, can lead to low collision-avoidance effectiveness compared with radio networks.

In addition, in Chapter 1, we argue that many UANs will be relatively mobile and sparse relative to terrestrial sensor networks, reducing the importance of network energy consumption and throughput of medium-access control protocols as metrics. This survey challenges some of the assumptions made in past UAN research, with a goal of aiding researchers entering the area of UANs from terrestrial sensor networks.

Finally, in Chapter 4, we document the design decisions for a new underwater acoustic modem, as a contribution to researchers entering the field from terrestrial sensor networks.

The following sections of this chapter provide an additional introduction to each of the topics mentioned above.

Practical Issues in Underwater Acoustic Networks

Chapter 1 presents a practical introduction to UANs which we completed and published in 2006 and 2007 [84, 85]. The goal of this chapter is to aid researchers entering the field of UANs from the terrestrial wireless sensor network community. Our survey followed several other surveys of UANs that drew primarily from terrestrial sensor networks, and that focused primarily on the challenges of medium access control (MAC) protocols with long acoustic propagation delays, and that assumed that network nodes were severely energy-constrained and relatively dense.

We based our survey on extensive experience with actual deployments of underwater vehicles and sensor networks. We highlighted other critical underlying physical and economic differences between UANs and terrestrial radio-based sensor networks, and questioned the focus of the earlier surveys on energy efficiency and MAC throughput as the primary metrics for performance of UANs. We argue that, although there is no single UAN design, due to enduring economic and physical constraints, UANs in general will remain sparser and more mobile than terrestrial radio-based sensor networks for otherwise similar applications.

In mobile networks, propulsion energy will generally dominate communication, and so network energy constraints are not universal in UANs. The cost of underwater instrumentation and the size

of the regions to be instrumented also leads towards sparse and mobile networks. In sparse regions of the network, the MAC protocol does not necessarily determine throughput.

Our survey brought together the communities and literature of ocean engineering and terrestrial wireless sensor networks, providing a more practically-grounded survey than its predecessors. It has been widely cited.

The contributions of Chapter 1 are:

- *We bring practical experience from deployments as well as literature from the ocean engineering literature into the sensor network community.* Previous UAN surveys were drawing largely from terrestrial sensor networking literature, and did not adequately emphasize the importance of mobility in UANs, nor the sparseness of many UANs.

- *We identify and diagram UAN operating regimes* versus geographic area and node population. We identify the network challenges in regimes ranging from dense, small networks to sparse, geographically large networks. There is no single regime for UANs, but in general they are likely to be *sparser and more mobile* than terrestrial sensor networks with similar applications.

- *In mobile networks, the energy efficiency of the network is not necessarily a constraint*, since the network energy consumption is usually dominated by vehicle propulsion energy. This is in contrast to the assumptions of many sensor networks, as well as the assumptions of previous UAN surveys.

- *In sparse networks, channel access is not necessarily a constraint.* Many papers in UANs focus on energy-efficient medium access control protocols, which are not necessarily important for in sparse regions of mobile UANs.

- *We highlighted the issue of channel access for periodic acoustic navigation signals, which for physical reasons share the communications band in mobile UANs, unlike in terrestrial radio-based networks.*

- We also raised the issue of *long-term fairness in disconnected mobile UANs*, where mobile nodes returning briefly to a connected region of the network need increased access to the channel relative to nodes remaining in the connected region.

Speading Models: Understanding Interference in UANs

Interference is an inherent property of wireless networks, including UANs. The physical-layer details of received energy as a function of range from the transmitter, as well as the signal processing details of packet detection, determine the impacts of interference on medium access control (MAC) network protocols. The goal of Chapter 2 is to understand packet detection in UANs in the presence of interference. In turn, understanding packet detection in interference allows us to determine the effectiveness of collision-avoidance MAC protocols in UANs, which is the topic of Chapter 3.

Chapter 2 presents the results of basic research into the physical-layer underwater acoustic spreading model. Spreading models describe how the acoustic energy at a point receiver decreases when moving away from the transmitter; there are other energy loss components, namely absorption loss and scattering and reflection losses at boundaries, but within the operating regime of links in a UAN, spreading loss is generally the most significant pathloss component.

For example, in free space far from boundaries, received energy generally decreases with "spherical spreading", scaling as $1/r^2$ at range r from the transmitter. Simple models of spreading loss generally are described by a *spreading exponent*, k, modeling the energy as decreasing as $1/r^k$.

Spreading loss is a primary component in determining the level of interference from distant nodes in a UAN. Due to waveguide effects in underwater acoustic channels, spreading losses in UANs have been assumed to be significantly lower than corresponding pathloss in terrestrial radio-based networks, which would lead to larger long-range interference relative to radio-based networks.

The widely-used "practical spreading" model in UANs, with a spreading exponent of $k = 1.5$ has minimal theoretical or experimental grounding. In designing acoustic communications methods for single-user, point-to-point links, the details of the spreading loss are relatively unimportant compared with correcting for the time-varying channel. The existing spreading models therefore have been adequate for the acoustic communications community, but are not adequate for modeling

and designing UANs. As more and larger underwater acoustic networks are deployed, the details of the spreading model will become important for modeling and designing larger networks. In addition, the details of the packet detection method are critical, because the most vulnerable period for network interference is at the moment of packet detection.

The contributions of Chapter 2 include:

- *We derive an alternate spreading model, which call the mixed-exponent model*, using physical reasoning. The mixed-exponent model applies to energy-constrained acoustic modems that use matched-filter detectors as a low-power wakeup detector. A distinction is drawn between the spreading exponents for the matched-filter detector's response to the wakeup signal versus distant interference. The model retains most of the simplicity of the "practical spreading" model, aiding in intuitive physical understanding of network performance.

- *We validate the mixed-exponent model* in uniform soundspeed profiles using two distinct numerical acoustic propagation packages, on based on raytracing and one based on solving the forward-propagating wave equation.

- *We analyze data from the Kauai Acomms MURI 2011 (KAM11) shallow-water field experiment, directly measuring energy-loss exponents.* With scattering losses from the boundaries, we are measuring energy-loss exponents rather than spreading-loss exponents. For modeling shallow-water underwater acoustic networks, we recommend generalizing the spreading loss model to an energy-loss model that includes scattering losses. We identify periods in time where simple exponent models appear to hold, and other periods where they do not.

- *We provide physical explanations for propagation differences explaining the differences between periods when simple spreading-loss exponent models appear to hold, and when they do not.*

- *The "practical spreading" model is inconsistent with the measured energy-loss exponent values* for this particular experiment. The measured energy-loss exponents, k, were significantly larger than 2, compared with $k = 1.5$ for the practical spreading model. Caution should be used if "practical spreading" is used to model network performance.

- *We partially validate the mixed-exponent model from the field experiment data analysis.* In most cases, even when simple exponent models do not hold, there is a difference between the exponents for packet detection and interference. Usually *the energy-loss exponent for packet detection is larger than that for interference, implying that long-range interference will be a problem for MAC protocols in UANs.* Due to experimental limitations, we were not able to validate or invalidate the waterdepth-dependence and bandwidth-dependence of the transition ranges in the mixed-exponent spreading model.

- Using results developed in Chapter 3, on the effects of spreading on the effectiveness of RTS/CTS MAC protocols, *we evaluate RTS/CTS effectiveness for a potential network deployed at the field experiment site*, using the energy-loss exponent measurements from the KAM11 field experiment.

- The extreme variability acoustic propagation at the KAM11 experiment site suggests that *robustness* of network protocols would be critical in such an environment, likely in a tradeoff with energy consumption.

Collision-Avoidance Effectiveness in UANs

The *effectiveness* of a collision-avoidance medium access control (MAC) protocol is a measure of how well the protocol prevents packet collisions. Effectiveness depends upon the level of interference from distant nodes which cannot detect the MAC control packets, and hence cannot follow the protocol. The level of interference and ability to detect packets are in turn affected by the spreading loss. Effectiveness is different from throughput, and effectiveness does *not* depend upon propagation delay.

Despite well-known throughput issues due to propagation delay, collision-avoidance MAC protocols are used due to their simplicity in building ad hoc wireless networks. The goal of Chapter 3 is to understand what physical-layer effects govern collision-avoidance effectiveness in UANs, and what the level of collision-avoidance effectiveness will be in different UAN scenarios.

In Chapter 3, we present analytic and simulation results analyzing the effects of spreading loss on the effectiveness of MACAW-based (RTS/CTS) MAC protocols. We have published an earlier and shorter version of this chapter [83]. We significantly extend earlier work [135] analyzing network implications of a simple pathloss model for radio-based 802.11 MAC efficiency to a more involved model of the underwater channel. We incorporate models for spreading loss, absorption loss, and ambient noise specific to the underwater acoustic channel. We present results for both the "practical spreading" model as well as the mixed-exponent spreading model. We show the detailed effects of spreading loss, ambient noise, and detection threshold on RTS/CTS effectiveness in UANs. Under the "practical spreading" model, the decreased spreading loss relative to radio-based networks leads to significantly increased long-range interference, in particular at lower carrier frequencies. Furthermore, the mixed-exponent spreading model detailed in Chapter 2 leads to even more pronounced long-range interference, further emphasizing the importance of spreading loss in understanding UAN performance. As a potential solution, we propose modifying the standard RTS/CTS protocol with a long-range CTS signal to reduce collisions. Transmit power control and frequency agility are alternate methods of improving spatial reuse, but are not always possible due to limitations of underwater acoustic modems and transducers.

The contributions of Chapter 3 include:

- *We identify collision-avoidance effectiveness as an additional area of performance loss for RTS/CTS MAC protocols in UANs, independent of propagation delay and throughput.*

- *We first extend previous radio-based work [135] in order to analyze RTS/CTS effectiveness for the "practical spreading" model for UANs.* With this simple spreading-only channel model, neglecting absorption and ambient noise, the results initially suggest that RTS/CTS effectiveness is significantly lower in UANs than in radio networks, with RTS/CTS handshakes beginning to lose effectiveness for node separations of only 22% of the maximum range, versus about 56% for radio networks, for typical parameters.

- *We next derive analytic expressions explaining how various physical-layer communication parameters affect RTS/CTS effectiveness in UANs*, with a more realistic underwater acoustic

channel model, incorporating absorption and ambient noise, and again using the "practical spreading" model with a spreading exponent of $k = 1.5$. These communication parameters include detection threshold, node separation, transmit power, and center frequency (determining absorption coefficients and ambient noise power). We find that the strong effects from absorption improve spatial reuse for most intermediate node separations to approximately the level of collision-avoidance performance in radio networks.

- *We analyze how the mixed-exponent spreading model studied in Chapter 2 affects RTS/CTS effectiveness.* With this model, RTS/CTS effectiveness drops significantly compared with the widely used "practical spreading" model, especially at lower frequencies. For example, at 3 kHz center frequency, on average the RTS/CTS handshake would suppress under 10% of potential interferers for all but the smallest node separations.

- *We validate the results from our analytical model with network simulations* incorporating the channel model and physical layer.

Micromodem-2: An Acoustic Modem Enabling Next-Generation UANs

Chapter 4 details and documents the design decisions for a new underwater acoustic modem, the Micromodem-2, to enable the next generation of underwater acoustic networks. We have published the design analysis as a conference paper [48], describing the design decisions, motivations, considerations, and tradeoffs. The goal of this chapter is to aid other groups designing underwater acoustic modems, in particular those coming from the terrestrial wireless sensor network community.

The modem's design goals were drawn in large part from the experience and analysis underlying the survey in Chapter 1, as well as the spatial reuse results of Chapters 2 and 3. We designed the modem to be highly scalable, to support both energy-constrained multi-year deployments as well as computationally-contrained, short-term, mobile deployments. The modem design is frequency-agile to deal with, and to take advantage of, the highly frequency-dependent absorption component of the channel's pathloss. As a result, we support carriers from below 1 kHz for 100 km network links under the ice in the Arctic, up to carriers well over 100 kHz to support high data rate communication

between vehicles passing at close range, for instance data mules in a sparse mobile network. The modem goes well beyond typical communication functionality to support the precision transmit and receive timing required for underwater acoustic vehicle navigation, as discussed in Chapter 1. In addition, it has a shared medium access transmit queue to allow both communication and navigation signals to operate in a shared channel. The modem is designed to support transmit power control and frequency agility to improve spatial reuse by reducing the long-range interference described in Chapters 2 and 3.

The contributions of Chapter 4 include:

- *We document design decisions and tradeoffs* for the electronics hardware design of an underwater acoustic modem, to aid other researchers in their own designs.

- *Design decisions were drawn from extensive deployment experience,* as well as the practical considerations described in Chapter 1.

- *Frequency agility* is designed in from the start, allowing operation from below 1 kHz to over 100 kHz, and supporting new wideband transducers. Long-range, low-frequency, low-datarate links are supported, for example for 100 km links under the Arctic ice at 1 kHz and 10 bps [40]. In addition, short-range, high-frequency, higher-datarate links will be supported with carrier frequencies over 100 kHz, improving data rate, covertness, and spatial reuse as well as RTS/CTS effectiveness as described in Chapter 3.

- *Precision timing* is supported and tightly integrated, with precision and power consumption ranging from an onboard 2 ppm temperature-compensated crystal consuming 3 μW, up to chip-scale atomic clocks with drifts on the order of milliseconds per year consuming about 120 mW. As described in Chapter 1, precision timing is critical for vehicle navigation methods that use travel-time measurements. Critically for scientific surveys, vehicle navigation allows sensor measurements to be geo-referenced. On small underwater vehicles, a single acoustic transducer is generally shared between acoustic communication and navigation, so navigation functions must be integrated with the acoustic modem.

- *We describe interface requirements for robust integrations* in vehicles and subsea systems, again drawing from deployment experience. These include practical details on voltage ranges and power supply protection, input and output protection, and data interfaces.

Summary

In this thesis, we present several related areas of work in underwater acoustic networks (UANs).

In Chapter 1, we document practical considerations, UAN deployment experience, and ocean engineering literature to aid researchers entering the field from the terrestrial wireless sensor network community. We question the widely-used assumptions of energy-constrained nodes and MAC throughput as the primary metrics of UAN performance, and we argue that counterexamples will be common with mobile and sparse UANs.

Chapter 2 examines packet detection in interference in UANs from first principles, with the goal of providing the background for the analysis in Chapter 3 on the effectiveness of collision-avoidance medium-access control (MAC) protocols in UANs.

The effects of interference on collision-avoidance medium-access control (MAC) protocols in UANs are governed in large part by spreading loss and packet detection. The widely used "practical spreading" model with a spreading-loss exponent of $k = 1.5$ is poorly grounded in theory and experiment. To allow us to understand and properly model the performance of collision-avoidance MAC protocols in UANs in Chapter 3, we studied spreading loss and packet detection in interference in UANs in Chapter 2.

In Chapter 2, we derive the mixed-exponent spreading model from first principles of packet detection. We validate the mixed-exponent spreading model with numerical acoustic propagation packages. In a shallow-water experiment, we directly measured the spreading-loss exponent, generalized to an energy-loss exponent when incorporating scattering losses from the surface and bottom. The measured energy-loss exponents, k, were larger than 2, and therefore were *inconsistent with the "practical spreading"* model, which is widely used to model UANs. We partially validated the mixed-exponent model from the experimental field data, in that there were different exponents for packet detection and interference. Furthermore, the measured energy-loss exponent for packet

detection was generally smaller than the measured energy-loss exponent for interference, implying that the effectiveness of MAC protocols will be reduced, as studied in Chapter 3.

In Chapter 3, we analyze the effects of spreading loss models on RTS/CTS-based MAC protocols, with both the "practical spreading" model as well as the mixed-exponent spreading model studied in Chapter 2. Despite well-known throughput issues due to propagation delay, these protocols are used due to their simplicity in building ad hoc wireless networks. Our contribution is to identify and analyze another signficant type of performance loss, namely low collision-avoidance effectiveness and decreased spatial reuse due to low spreading loss.

Finally, in Chapter 4, drawing on our survey analysis in Chapter 1 and our spreading loss analysis in Chapters 2 and 3, we document the design decisions for an improved underwater acoustic modem to enable the next generation of UANs. We have published the design motivations, tradeoffs, decisions as a contribution to other acoustic modem developers, in particular those coming from the terrestrial wireless sensor network community.

CHAPTER 1

A SURVEY OF PRACTICAL ISSUES IN UNDERWATER NETWORKS

1.1 Introduction

Underwater sensor networks are attracting increasing interest from researchers in terrestrial radio-based sensor networks. There are important physical, technological, and economic differences between terrestrial and underwater sensor networks. Previous surveys have provided thorough background material in underwater communications, and an introduction to underwater networks. This past work has included detail on the physical characteristics of the channel [17, 91], on underwater acoustic communications [42, 64, 113], and surveys of underwater acoustic networks [4, 20, 55, 112]. In this survey, we highlight a number of important practical issues that are not emphasized in the recent surveys of underwater networks, with references from the ocean engineering literature, and an intended audience of researchers who are moving from radio-based terrestrial networks into underwater networks.

We believe that many, though not all, underwater networks will remain characterized by more expensive equipment, higher mobility, sparser deployments, and different energy regimes when compared with terrestrial sensor networks. We discuss the role of these factors in the different set of challenges that face underwater networks. We identify several of these points in the outline below, and we expand upon them in later sections.

In Section 1.2, we provide a classification scheme for underwater networks. Link-layer range, node density, and geographic coverage of nodes are key factors in determining the type of network deployed.

---

[1]This chapter is published as: J.Partan, J.Kurose, and B.N. Levine. A Survey of Practical Issues in Underwater Networks. *ACM SIGMOBILE MC2R*, 11(4), 2007. [85]

The key differentiating factor for underwater networks is the use of an acoustic channel. In Section 1.3, we review the basics of such channels. We also mention results from underwater optical and radio communication systems, explain the half-duplex nature of the channel, and discuss the impact of the physical layer on network topology.

Medium access control (MAC) protocols for underwater acoustic sensor networks are still an open problem. In Section 1.4, we briefly review recent work and mention some directions for future work, including a brief overview of the difficulties with CDMA underwater. For stationary sensor networks, the combination of high propagation delays with energy constraints introduces a new MAC operating regime.

We make an economic argument in Section 1.5 that many (though not all) underwater sensor networks will remain *more mobile and more sparse* than terrestrial sensor networks, even as node cost falls. Though sampling is highly non-uniform, the world-wide ocean is vast, and for decades to come, there will be more places to explore than can be covered by dense sensor networks. In mobile underwater networks, there is often contention between communication and navigation signals sharing the same physical channel, leading to new MAC issues. In addition, the combination of mobility and sparsity introduces *long-term fairness* as a MAC issue, perhaps leading to prioritized access for nodes that are rarely in contact.

The energy costs in underwater acoustic networks are different from those in terrestrial radio-based networks, as we discuss in Section 1.6. In acoustic networks *transmit power dominates* compared with receive power. Protocols that optimize energy usage need to be evaluated with this in mind. In addition, in mobile underwater networks with high propulsion energy costs, minimizing network communication energy is not always an important concern. Thus, protocol designers may want to consider alternate metrics, such as reliability, fairness, quality-of-service, or covertness.

1.2 Underwater Network Operating Regimes

Underwater networks can be characterized by their *spatial coverage* and by the *density of nodes*. These factors have significant implications for the MAC- and network-layer issues that must be

addressed at design time. In this section, we create a taxonomy of underwater network operating regimes with the goal of providing context for the discussion later in this chapter.

Our taxonomy is illustrated in Figure 1.1. We characterize the spatial extent of a network by comparing it to the acoustic range of the nodes. If all nodes are in direct contact, we have a single-hop network, with either centralized or distributed control. In networks covering larger areas, communications will require multiple hops to reach destinations. When the geographic coverage is greater than the unpartitioned link-layer coverage of all nodes, routing requires techniques from disruption-tolerant networking (DTN). When even the mobility of nodes does not overlap, no techniques exist to form a network.

There are several additional differences of note between terrestrial radio-based networks and underwater acoustic sensor networks. One is that large populations of nodes in small areas can cause conflicts between throughput and navigation, as we discuss below in Section 1.5.2. A second point is that densely populating even a moderately large geographic area can be prohibitively expensive, as we discuss in Section 1.5.1. This latter point makes DTNs an attractive solution, as we discuss in Section 1.5.3.

In practice, all of the network types shown in Figure 1.1 are relevant and can exist within an extended network. In other words, clusters of single- or multi-hop networks can be deployed that use DTN routing to exchange information infrequently.

In the following sections, we discuss the physical layer and medium access protocols, with particular attention to the differences between underwater networks and terrestrial radio-based networks.

1.3 Physical Layer

The physical characteristics of the underwater acoustic channel are well-described in Catipovic [17] and Preisig [91], and they are summarized here. In addition, we review recent work in long-wave radio and optical underwater networks, and explain some technological limitations for space-constrained nodes, influencing network topology and leading to a half-duplex channel.

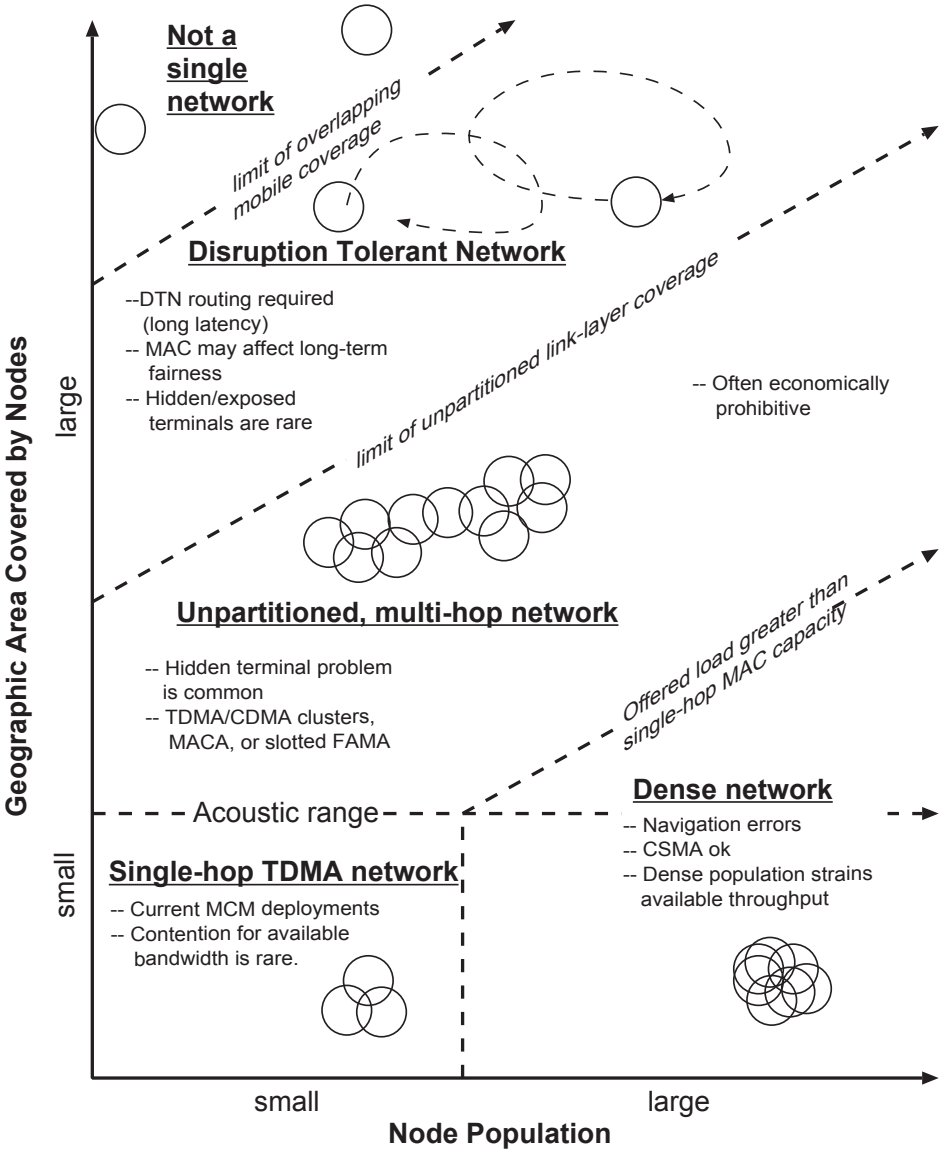

Figure 1.1. A taxonomy of underwater networking regimes.

1.3.1 Physical Channel

Almost all underwater communication uses *acoustics*. Radio waves are extremely strongly attenuated in salt water [101]. Long-wave radio, however, can be used for short distances; for example, about 1kbit/sec at carriers of 1–100kHz for ranges up to 6–20m [32, 101]. Light is strongly

scattered and absorbed underwater, though blue-green wavelengths may be used for short-range, high-bandwidth connections in *extremely clear* (often very deep) water. In very clear water, optical modems are expected to achieve data rates up to several Mbits/sec at ranges up to 100m [30]. Underwater optical communication is also being considered for very low-cost, short-range connections of order 1–2m at standard IrDA rates such as 57.6kbits/sec [101, 128].

For longer ranges and more typical water clarity, acoustic communication is the only practical method. A rough performance limit for current acoustic communications is the limit of 40 km·kbps for the range-rate product, though this mostly applies to vertical channels in deep water, and it dramatically overestimates the performance in difficult shallow-water, horizontal channels [64].

The speed of sound underwater is approximately 1500 m/s, 2e5 times lower than the speed of light. This leads to *large propagation delays* and relatively large motion-induced Doppler effects. Phase and amplitude fluctuations lead to a *high bit-error probability* relative to most radio channels, requiring forward error correction (also called error correction coding). In addition, the acoustic channel has strong attenuation with increasing frequency [117], leading to very *limited bandwidth*.

Multipath interference is common in underwater acoustic networks, causing frequency-selectivity of the channel. This frequency-dependent interference is generally *time-varying* due to surface waves or vehicle motion, causing *fading*. To achieve high bandwidth efficiency, computationally intensive adaptive equalizers are generally required [113], though OFDM-based systems may provide a lower-complexity alternative [115]. While multipath interference is mostly a source of difficulty, recent work using arrays for both transmit and receive (multiple-input, multiple-output, or *MIMO*) takes advantage of the independent channels created by different multipath paths to increase throughput [42].

Over longer paths, ray bending can lead to *shadow zones*, or spatial regions where almost no acoustic signal exists [17]. Also, strong attenuation (on the order of 20dB/m or even higher, persisting for tens of seconds) can occur in near-surface regions with bubble clouds, which are entrained into the water by breaking waves [28]. Both of these effects cause network connectivity dropouts. Relatively small movements can sometimes lead to significantly better channel conditions, and mobile nodes may be able to take advantage of this.

Although the underwater acoustic channel is time-varying, *propagation delays can certainly be estimated*, and are stable enough to use in setting parameters for network protocols.

1.3.2 Technological Limitations

Standard acoustic transducers cannot simultaneously transmit and receive. On space-constrained autonomous underwater vehicles (AUVs) and compact stationary nodes, transducers in different frequency bands generally cannot be spatially separated far enough to provide full-duplex connections, since the transmitted signals will saturate the receivers even when the bands are fairly widely separated. Underwater network communications are therefore almost always *half-duplex*. Furthermore, transducer sizes are proportional to wavelength, and due to space constraints, small AUVs are often restricted to using higher center frequencies, generally above 10kHz.

Another issue is that it is easy for small AUVs to transmit at high data rates but often harder for them to receive at high rates. (A high data rate in shallow water would be 5kbits/sec at a range of 2km, for example; a low rate at this range might be as low as 80bits/sec.) The two main reasons for this asymmetry are propulsion noise and some difficulties in mounting receiver arrays on small AUVs [34, 37].

Higher data rates typically use phase-shift keying (PSK) [94], which can be transmitted with a single transducer. Due to the multipath interference, however, equalizing PSK works much better with the spatial diversity provided by an array of receivers [113]. A vertical array is best for equalizing the multipath structure of a typical shallow-water horizontal channel, while a horizontal array can work well for multi-user CDMA systems (see Section 1.4.2), because users are generally separated azimuthally [34]. Either conformal horizontal arrays or small vertical arrays can be used on AUVs, but performance is somewhat degraded due to propulsion noise and space constraints. On the other hand, frequency-hopped frequency-shift-keying (FH-FSK) [94] provides a lower data rate, which is more robust to AUV propulsion noise and can be received with a single transducer.

The asymmetry in send and receive rates is technological rather than fundamental, but is a current reality, and is one reason that star topologies with base stations are common in existing mobile underwater networks [38]. In these networks, AUVs receive small commands using a low

data rate, and transmit larger sensor data packets at a high data rate back to the base station, generally a gateway buoy with a vertical array to receive PSK, and a radio antenna above the water [72]. *Issues at the physical layer can drive topology, affecting routing, medium access, and even applications.*

1.4 MAC Protocols

Medium access control (MAC) is an unresolved problem in underwater acoustic networks [4, 20, 55, 112], but has been studied for decades in traditional radio networks [94, 98], and has received significant attention in radio-based sensor networks as well, recently reviewed by Ali et al. [5].

We briefly review recent work in underwater MAC protocols in Section 1.4.1, discuss some challenges with CDMA in Section 1.4.2, and outline possible future directions in Section 1.4.3.

1.4.1 Recent Work in Underwater MAC

A range of MAC protocols have been explored in underwater networks.

The Seaweb experiments have been the most extensive and longest-running series of underwater acoustic networking deployments. Seaweb '98 and '99 used FDMA due to modem limitations. With the limited bandwidth and frequency-selectivity of the underwater channel, this was not ideal [96]. More recent Seaweb experiments have used hybrid TDMA-CDMA clusters (see below) with MACA-style [62] RTS/CTS/DATA handshakes. Seaweb includes selective retransmit and provision for channel-adaptive protocol parameters. Seaweb goes well beyond the MAC-layer, and also uses neighbor discovery to determine network routing tables, though using a centralized server architecture [95]. Deployment and configuration takes more than a day, and operate for many days, covering regions of over 100 km^2 [96].

Freitag et al. [38] describe a single-hop, star-topology AUV network for Mine Countermeasures (MCM) operations. These networks can be rapidly deployed (about 1 hour), and operate for many hours over regions of order 5 km^2, with many deployments to date. A central gateway buoy provides remote operator control of the AUVs using TDMA with low-rate (e.g., 80bits/sec) commands sent

to the AUVs and high-rate (e.g., 5kbits/sec) data returned to the operator via the gateway buoy. The AUV navigation pings (see Section 1.5.2) are also coordinated by the network.

Açar and Adams [1] describe ACMENet, which uses a centralized TDMA protocol, with adaptive data rates and power control. They report results from sea trials, and provide background discussion on multiple access and MAC protocols for underwater networks.

Smith et al. [110] describe an ad hoc network protocol based on CSMA/CA, with prioritized messages and improved access for multi-packet transfers. They report results from a small demonstration. Lapierre et al. [66] propose using CSMA/CD, although it is unclear how the collision detection will work in a half-duplex channel. In general, CSMA-based protocols are vulnerable to both hidden and exposed terminal problems [94].

In multi-hop underwater networks, hidden terminals will be common. MACA [62] uses RTS, CTS, and DATA packets to reduce the hidden terminal problem, and MACAW [11] adds ACK at the link-layer, which can be helpful in the unreliable underwater channel [112]. FAMA [46] extends the duration of the RTS and CTS packets to prevent collisions with data packets. The efficiency of these protocols are impacted heavily by propagation delays, due to their multi-way handshakes.

A number of adaptations have been proposed to adopt MACA, MACAW, and FAMA for underwater networks. Molins and Stojanovic [76] recently proposed Slotted FAMA, adding timeslots to FAMA to limit the impact of propagation delays, with simulation results. Another approach to limit the impact of long RTS/CTS handshake packets is proposed by Peleato and Stojanovic [86], where handshake timing is proportional to the separation of the communicating nodes, and the receivers can tolerate some interference from more distant nodes. As a small part of their review article, Sözer et al. [112] described a simulation using MACA with an added WAIT command to reduce collisions and to improve power efficiency. Kebkal et al. [63] propose a means to reduce the impact of propagation delay on FAMA- and MACAW-based protocols, with ACK and DATA packets simultaneously in flight. They also suggest an extension to FAMA, using CDMA for the RTS packets, to develop a collision-free FAMA protocol. Related ideas are proposed in more detail in Foo et al. [31], with CDMA extensions to MACA and references to the radio-based MAC literature.

Foo et al. also simulate a MACAW-based underwater network, and also adapt the AODV reactive ad-hoc routing protocol for a sparse underwater network with low mobility.

Another potential approach is using combined TDMA-CDMA clusters, used in current Seaweb implementations, and described in more detail by Salvá-Garau and Stojanovic [99]. This allows shortening the TDMA slot lengths, but increases overhead (cluster assignment) and the potential for interference from a neighboring cluster (using a different code). Doukkali and Nuaymi compare several approaches to underwater MAC, and adopt TDMA-CDMA clusters as well [23].

Energy efficiency is also important in underwater networks (see Section 1.6). In terrestrial sensor networks, energy constraints have led to coordinated-sleeping MAC protocols such as S-MAC [137]. Park and Rodoplu [81] extend these ideas and others, proposing UWAN-MAC, an energy-efficient MAC protocol for delay-tolerant underwater sensor networks; the combination of energy constraints and high propagation delays is a new operating regime for MAC protocols. They also provide references to MAC protocols in underwater networks and terrestrial sensor networks.

1.4.2 CDMA

Code-division multiple access (CDMA) [94] is a conflict-free multiple access method which is promising for future underwater networks. Implementing a CDMA-based underwater network is very challenging, however, as we discuss briefly below.

Multi-user spread-spectrum methods include frequency-hopped spread spectrum (FHSS, using FSK modulation, and lower data rates) and direct-sequence spread spectrum (DSSS, using PSK modulation, and higher data rates); the term CDMA usually refers to multi-user DSSS [43,94]. Each user is assigned a different spreading code with which to transmit. While this reduces each user's throughput compared with the single-user case, users can transmit packets without considering what other users are doing. This would effectively solve many of the MAC problems related to high propagation delay. Furthermore, CDMA has no hard limit on the number of users, and DSSS-based CDMA can perform especially well in multipath environments [41].

Stojanovic and Freitag [118] report very promising CDMA results for four users. An important caveat for this work, however, is that the received power for each of the users was equal. If the

received power for all users are not roughly similar, signals from distant users cannot be received successfully [94]. This is the *near-far* problem. This requires that the transmit power of each user be controlled, as each user's channel varies. This is certainly possible, but *CDMA is more tractable in radio channels than in underwater acoustic channels.* In CDMA-based cell phone networks, closed-loop power control updates are sent 800 times per second, with the feedback propagated at the speed of light. Open-loop power control is also used, where nodes set their transmit power based on the received signal strength from the base station (see Rappaport, Section 10.4, *CDMA Digital Cellular Standard (IS-95)* [94]). Underwater networks have a time-varying, half-duplex channel with a low propagation speed, and so closed-loop transmitter power control is a difficult and open problem. The range of received powers, however, can be moderately wide — up to about 10dB — easing the power control problem somewhat, but with high computational complexity [120].

As an additional note, the power control required with CDMA usually implies a star topology with a single base-station receiver, rather than an arbitrary ad hoc topology. Morns et al. [77], however, describe a decentralized configuration using CDMA. Each node in a cluster has its own receive timeslot, during which other nodes can transmit to it using CDMA.

1.4.3 Future Directions

Cross-layer optimization and adaptive parameter setting is important given the limited bandwidth and high propagation delays of underwater channels. The control packets in many MAC protocols can provide a means to sample the channel and set network parameters, for example measuring propagation delays to set timeouts, received signal strength to set transmit power, or signal-to-noise ratio to set coding rates. Networks such as Seaweb [95,96] and ACMENet [1] include provisions for adaptation, but is an important feature to emphasize.

The frequency-dependent attenuation of the underwater channel is different from the radio channel, and it might be used in several different ways. While logistically difficult, a dual-frequency (but still half-duplex) modem [35, 37] could use a lower-frequency transducer for a longer-range, lower-bandwidth link, and a high-frequency transducer for a short-range, high-bandwidth link. This would increase throughput on individual short-range links, and also improve spatial reuse,

increasing the network's overall throughput. Such a system might also split control and data; long-range control signals would help alleviate hidden-terminal problems.

Some new approaches also try to preserve the broadcast nature of the channel, for *omnicast* within swarms of AUVs, as suggested by Schill et al. [102], using TDMA to share control and data for collective behavior of AUVs in an underwater long-wave radio network.

Finally, propagation delays have been dealt with in satellite and fiber optic networks for many years. In satellite radio networks, several approaches include demand-assignment multiple access (DAMA) [88] and interleaved collision-resolution protocols [70]. Fiber optic networks have used slotted Aloha and coding to deal with propagation delays on the order of 1000 slots, much higher than in satellite channels [97]. These approaches may provide new ideas for MAC in underwater acoustic networks.

1.5 Mobility and Sparsity

Terrestrial sensor networks generally assume fairly dense, continuously connected coverage of an area using inexpensive, stationary nodes. In contrast, economics push many underwater networks towards sparse and mobile deployments.

As we discuss in Section 1.5.1, underwater sensor nodes are expensive, and areas of interest in ocean environments are often large, which implies sparse network deployments. Ship-based surveys and sensor deployments are also expensive, and a sparse sensor network with stationary nodes is limited. This has led to the widespread use of mobile AUVs.

In a mobile sensor network, nodes require periodic navigation information. For physical reasons, in underwater networks, navigation and communication signals often share frequency bands. The combined demands on the channel for both navigation and communication places further limits on the density of mobile nodes in a network. We survey network-based approaches to navigation in Section 1.5.2.

The sparsity and mobility of many underwater networks means that disruption-tolerant networks (DTNs) will arise, and mobility patterns strongly influence performance in DTNs. We briefly

introduce results from terrestrial DTNs in Sections 1.5.3 and 1.5.4, with applicability to underwater networks.

Finally, the sparsity and mobility implies a new operating regime for MAC protocols. As we discuss in Section 1.5.5, in some networks, MAC protocols may prioritize access for AUVs that are within communication range only briefly, to maintain long-term fair access to the channel.

1.5.1 Economics of Oceanographic Operations

We believe that many, though not all, underwater networks will be sparsely deployed for a long time to come, largely because of the economic costs of individual nodes, but also because of the potentially huge areas to be surveyed. There are several components to the costs of these networks, including fabrication, deployment, and recovery.

Fabrication. An acoustic modem with a rugged pressure housing currently costs[1] roughly $3k. This does not include any underwater sensors, which are often more expensive than the modem itself. Supporting hardware can also drive up costs; e.g., a simple underwater cable connector is often over $100. The high costs are due in part to the rugged construction required to survive storms at sea and deployment at depth[2], but largely due to a small market of demanding users (military, industrial, scientific), and no consumer market to speak of.

Significantly less expensive sensors, vehicles, and modems (500m-range acoustic and very short-range optical and radio) are being designed and built [55,58,101,105,128]. These efforts may change the economics for dense underwater sensor networks, as we discuss further below.

Deployment. Oceanographic research ships typically cost from about $5k/day for a coastal boat to $25k/day for a large ocean-going ship [125] (and more when submersibles are used), and their operations are limited in rough weather. Once deployed, stationary or mobile sensor nodes can

[1] All our estimates are in US dollars.

[2] The pressure increases by an additional atmosphere for every 10m of depth, so even a "shallow"-water (generally 100m) instrument must be able to withstand 10 atmospheres, while "deep"-water instruments (typically 4km) must be rated to at least 400 atmospheres.

operate autonomously in almost any weather, a significant advantage. Nodes, however, must be robust and well-engineered, since any repairs will be very expensive.

Recovery. Until nodes are inexpensive (i.e., disposable) and underwater networks have enough bandwidth to enable nodes to fully offload all interesting archived sensor data, recovery will remain a costly operation. Mobile nodes can make the recovery process somewhat easier by moving themselves to a rendezvous point.

Economics and flexibility have led to the use of AUVs as a key element in most underwater network architectures. They operate autonomously once deployed and they have relatively easy deployment and recovery (e.g., about \$2k/day for coastal deployment and recovery from a small boat). While AUVs are inexpensive relative to ship time, they are not cheap, starting at over \$50k and usually over \$250k per vehicle to fabricate and equip. Given the huge size of the ocean, there is a spatial coverage for which deploying an unpartitioned sensor network of AUVs becomes cost-prohibitive, for any given application.

Currently, economics drive underwater sensor networks to be sparse and mobile, as pointed out by several others [20, 55], as well as by us. There are some applications for which a dense, stationary network makes economic sense, for example the oilfield monitoring application described by Heidemann et al. [55]. The low-cost modems being developed within that project could enable dense underwater sensor networks for other applications, but we believe that sparse and mobile sensor networks will still certainly remain in operation. The ocean covers 70% of the Earth's surface, with an average depth of 4km. This is an immense volume of ocean to survey, even when considering that coverage is generally highly focused and non-uniform. No matter how cheap nodes become, sparse and mobile will remain an important type of underwater sensor network. Ideally, the network protocols will adapt to let mobile nodes move easily between sparse and dense regions of an extended sensor network.

1.5.2 Contention between Navigation and Data Signals

Autonomous mobile vehicles require navigation information. Underwater, this cannot be supplied by GPS, so, for AUVs, it is often supplied by acoustic transponders, generally in a *long-baseline* (LBL) configuration [39]. In typical high-speed REMUS surveys, each vehicle pings navigation transponders roughly three times per minute to minimize navigation errors. Due to the frequency- and range-dependent attenuation of the channel, high-resolution navigation systems and high-throughput communications systems covering a region of a given size will generally use similar center frequencies, hence often have interfering signals. In fact, because of this, navigation and communication systems often even share the same transducer [38].

MAC protocols in mobile underwater networks therefore need to be able to share the channel between network communications and navigation signals, with a given navigation quality-of-service. When many vehicles are in an area, each vehicle must reduce the rate at which it pings LBL transponders, which leads to navigation errors.

Several network-based navigation methods have been presented. Freitag et al. [39] describe results from a passive navigation system, where a large number of vehicles can passively share navigation signals, analogous to terrestrial GPS, without each vehicle actively pinging a transponder. When vehicles need a more accurate location fix, they can request a slot for an active LBL ping. Elsewhere, Freitag et al. [35], have outlined a system for collaborative AUV searches, where high-quality inertial navigation information from a master vehicle is transmitted to companion vehicles, using synchronized hardware clocks and one-way travel-time measurements. Stojanovic et al. [119] propose a protocol for collaborative mapping with AUVs. AUVs share their individual maps over the broadcast network, in the process making travel-time measurements and creating a unified map, which can in turn be used for routing. Ouimet et al. [80] describe experiments with Seaweb using a broadcast ping packet for AUV localization. Another protocol, ICoN [61], prioritizes navigation and communication packets to ensure that AUVs receive adequate navigation information, yet are still responsive to command packets.

1.5.3 Disruption-Tolerant Networks

In a sparse and mobile network, DTNs will arise as the link-layer coverage becomes partitioned. When the mobility of nodes overlap, they have transfer opportunities from the time they discover one another until they are out of acoustic range. Even in radio networks, the amount of data that can be transferred during each opportunity is the most constrained resource; the bandwidths of acoustic modems exacerbate this constraint. (By comparison, the limits on storage at each node are less problematic: storage is generally inexpensive, compact, and energy efficient.) A series of non-contemporaneous meetings between nodes can form a path to a destination. If meetings are frequent and common, then the total throughput that can be delivered by the network can be reasonable for data that remains valuable after long delays. DTNs can also be used to connect geographically remote clusters of nodes.

DTNs have primarily been researched under the assumptions of radio-based terrestrial networks, yet many of the techniques are directly applicable to underwater networking. Most approaches replicate packets *epidemically* during intermittent opportunities for transfer. At the same time, the protocols attempt to limit replication to only the nodes that appear to have some path to the destination. Many approaches to discovering non-contemporaneous paths to destinations use historic information about which nodes meet regularly [13, 14, 22, 67, 69, 138]. Several other techniques are complementary. For example, old packets representing delivered data can be removed from the network using broadcast acknowledgments [13], and network coding [132, 139] can be used to efficiently take advantage of multiple paths.

1.5.4 Network-Motion Interactions

While the motion of vehicles is primarily determined by their survey patterns, networks can influence the motion in several ways. The most typical is through adaptive and collaborative sampling, where sensor data influences survey patterns [68].

In addition, there is a growing body of work that seeks to improve DTN performance by making use of vehicles with controllable movements. Dunbabin et al. [25] have deployed a system on an AUV in a test pool that plans a route to visit stationary underwater nodes in known locations.

Zhao et al. [140–142] have several works that investigate DTN routing based on ferries that operate on planned mobility paths; the paths are designed to optimize network performance and known to all other nodes. Burns et al. [14–16] have proposed a method for robotic agents to dynamically adjust movements according to perceived network conditions and according to multiple network objectives, such as maximizing delivery rate and minimizing delivery latency.

Finally, in terms of MAC protocols, AUVs might alter their survey tracklines to alleviate hidden- or exposed-terminal problems and to increase spatial reuse, in a MAC incorporating actual physical "backoffs".

1.5.5 MAC Fairness in Mobile Networks

With the large propagation delays of the underwater acoustic channel, it is advantageous to transmit packet trains rather than individual packets [114]. Long packet trains can capture the channel, however, and in a mobile DTN, AUVs may move out of range before they are allowed sufficient access to the channel.

This is especially true with AUVs such as the next generation of REMUS vehicles, doubling their speed to 5m/s, and likely reducing their acoustic transmission range to maintain covert communications. With current REMUS vehicles (2.5m/s speed, 2km communication range), a back-of-the-envelope characteristic time to stay within contact is 2km/(2.5m/s)=13 minutes, or about 130 slots for 4-second, 20-kbit data packets with 2-second propagation delays. For the next generation, with a speed of 5m/s and a covert communication range of perhaps 500m, the characteristic time within contact drops to about 2 minutes, or about 20 slots.

In such a network, *long-term average fairness* in accessing the channel becomes an issue. When a previously disconnected AUV re-enters contact briefly, it must be given prioritized access to the channel. One possible mechanism to achieve this is a MAC protocol that adapts its prioritization or backoff probability distribution to account for mobility and disconnectedness, perhaps along with utility-based metrics. We are considering this problem, among others.

1.6 Energy Efficiency

Energy is limited in both terrestrial and underwater sensor networks. Energy efficiency has been a top priority in MAC protocols for terrestrial sensor networks, with coordinated-sleeping protocols such as S-MAC [137], extended into underwater networks with UWAN-MAC [81]. In addition, a range of approaches to energy-efficient and latency-tolerant underwater network protocols are discussed by Heidemann et al. [55].

Despite the constraints on overall system energy, in some mobile underwater acoustic networks, communication energy is not a critical metric for which to optimize. Along similar lines, some terrestrial sensor networks are starting to optimize MAC protocols for a wider range of metrics, such as reliability and quality-of-service [5].

While energy efficiency is likely to improve for both modems and vehicles, current numbers are included below, for comparison purposes.

1.6.1 Communication Energy Costs

In most terrestrial radio networks, the power required for transmitting and receiving are approximately the same, with the respective energies being determined by the time spent in the transmit or receive states. In underwater acoustic networks, *transmit power dominates*, and is typically about 100 times more than receive power. A standard acoustic modem currently uses about 0.2W while listening for incoming packets, between 0.2W and 2W for equalizing and decoding packets (depending on the packet's data rate), and typically 50W for transmitting. These figures are representative of sending packets over a range of 2-3km at a 25kHz center frequency, ranging from FH-FSK at 80bits/sec (for poor channel conditions; 0.2W to detect and decode) to PSK at 5kbits/sec (for good channel conditions; 0.2W to detect, 2W during equalization and decoding) [36]. For good channel conditions and shorter ranges, however, the transmit power can be lower, potentially as low as 1W for good conditions and short (500m) ranges [33]. As processors become more energy-efficient, the receive power will continue to drop, while the transmit power will remain roughly constant, as it is determined by channel physics and detector algorithms.

1.6.2 AUV Energy Costs

As we discussed in Section 1.5, underwater sensor networks are likely to be more mobile than terrestrial sensor networks, with AUVs as a key element of networks. For many AUVs, the *propulsion power dominates* network-communication power. Although energy on AUVs is clearly limited, there will be important underwater networks for which network communication energy efficiency is not a primary concern.

As examples, REMUS-class AUVs have missions which are high-speed (1.0m/s-2.9m/s) and short-duration (generally 5-20 hours). Missions can be extended by recharging at sub-sea docking stations. Their "hotel" power load (non-propulsion power: sensors, communication, control computers) is typically about 30W, with a propulsion power consumption ranging from 15W at the optimum speed of 1.5m/s, to 110W at 2.9m/s [121]. In contrast, gliders are low-speed, long-duration vehicles [131]. A glider with electric propulsion has a total power consumption (hotel and propulsion) of about 2W at speeds of 0.2m/s-0.4m/s, for a mission of up to about one month. Thermally-powered gliders use variable buoyancy to extract propulsion energy from ocean thermoclines, have extremely long missions (many months or years), and have an extremely low hotel power budget [130]. For high-speed AUV missions, network communication energy can be neglected, whereas it is critical for long-duration glider missions.

1.6.3 Future Energy Directions

Finally, transmit power may be limited for reasons other than battery capacity. One standard networking reason would be to promote spatial reuse. In addition, a concern is the acoustic *impact on marine mammals*, and for military networks, maintaining covert communications is also an important goal.

1.7 Conclusions

We have summarized a number of practical issues differentiating underwater acoustic networks from terrestrial radio-based sensor networks. There is no single operating regime for underwater networks, and a wide range will exist. Nevertheless, we believe that many important underwater

networks will be more mobile and more sparse than terrestrial sensor networks, with different energy and economic considerations. Underwater network protocols will have to adapt to moving between sparse and dense regions, with different optimization metrics for each regime.

CHAPTER 2

MIXED-EXPONENT SPREADING MODEL: THEORETICAL, NUMERICAL, AND EXPERIMENTAL INVESTIGATION

2.1 Introduction

Interference is fundamental to wireless networks. Physical-layer spreading loss is a major determining factor in the level of interference experienced by nodes in a network. In particular, interference affects the effectiveness of medium access control (MAC) protocols.

Research in underwater acoustic networks (UANs) has brought together several different communities, including computer scientists, underwater acoustic communication engineers, and ocean acousticians. The spreading models and approaches that were adequate for these communities — underwater acoustic communications, deep-water ocean acoustics, and terrestrial radio-based wireless networks — are not necessarily adequate for analyzing underwater acoustic networks. In particular, despite the significant role spreading loss plays in determining underwater network performance, it has been largely neglected in the underwater acoustic networking literature.

Many underwater acoustic networks are modeled using the "practical spreading" model with a spreading exponent of $k = 1.5$ [112], which has little grounding in theory or experiment [18]. In comparison with terrestrial radio networks, often modeled with spreading exponents of $2 \leq k \leq 6$ [94], spreading exponents in UANs are generally assumed to be much smaller, which would lead to increased long-range interference relative to radio networks.

In this chapter, we attempt to question and to test the validity of the spreading models that are assumed to be valid by many researchers in underwater acoustic networks.

There are several contributions in this chapter:

- In Section 2.3, using physical reasoning *we derive an alternate spreading model, which we call the mixed-exponent model.* The moment of packet detection is the most vulnerable period for

network interference [135], and so the detection model is critically important in determining interference. The mixed-exponent model applies to energy-constrained acoustic modems that use matched filter detectors as a low-power wakeup detector. A distinction is drawn in the spreading exponents for the matched filter's response to the wakeup signal versus distant interference.

- In Section 2.4, *we validate the mixed-exponent model* using the raytracing acoustic propagation package Bellhop.

- In Section 2.5, *we provide additional validation of the mixed-exponent model* using RAM, an underwater acoustic propagation modeling package which solves the forward-propagating wave equation. Both the theoretical derivation mixed-exponent model as well as the raytracing results are based on high-frequency ray approximations with lossless boundary reflections. The RAM results provide a more independent validation, with no ray approximation, and with lossy bottom reflections. With both Bellhop and RAM, we use uniform soundspeed profiles.

- In Section 2.6, *we analyze data from a shallow-water field experiment, directly measuring energy-loss exponents*. With scattering losses from the boundaries, we are measuring energy-loss exponents rather than spreading-loss exponents. We identify periods in time where simple exponent models appear to hold, and other periods where they do not. For this particular experiment, even when simple exponent models do hold, the energy-loss exponent values are significantly larger than 2, and are therefore *not consistent with the "practical spreading" model*. For modeling shallow-water underwater acoustic networks, we recommend generalizing the spreading loss model to an energy-loss model that includes scattering losses. Furthermore, caution should be used if "practical spreading" is used to model network performance.

  In addition, *we partially validate the mixed-exponent model from the field experiment data analysis*. In most cases, even when simple exponent models do not hold, there is a difference between the exponents for packet detection and interference. Usually *the energy-loss exponent for packet detection is larger than that for interference, implying that long-range interference will be a problem for MAC protocols in UANs*.

- In Section 2.7, we use results developed in the next chapter, Chapter 3, on the effects of spreading on the effectiveness of RTS/CTS MAC protocols, along with the energy-loss exponent measurements of Section 2.6 to *evaluate RTS/CTS effectiveness for a potential network at our field experiment site.*

In the first section of this chapter, we start by summarizing previous work that has led to the presently accepted spreading model.

2.2 Previous Work and Present Model

The physical channel models used in reseach on underwater acoustic networks (UANs) have primarily come from the underwater acoustic communications community. The spreading model in particular was introduced by Sözer et al. [112] and Stojanovic [117], who in turn refer to Coates [18], who summarizes the model's basis simply as:

> A "practical" law, intermediate between the spherical and cylindrical laws, is thus often invoked for "first-cut" calculations in sonar system design.

Sözer and Stojanovic are certainly aware of the limitations of the practical spreading model, and use it just for convenience in calculations and system-level design. Nevertheless, it has become standardized as the default spreading model used to model UANs.

The "practical spreading" model is adequate for high-level system design of many acoustic communications links, in large part because the details of the spreading loss model are not significant in acoustic communications research; the communications challenges are in estimating and tracking the time-varying multipath channel [17, 42, 64, 113], and spreading losses change slowly for a point-to-point link. As a result, the practical spreading model, with minimal theoretical or experimental grounding, has become the standard spreading model for underwater acoustic network research without significant questioning. In contrast to the situation with point-to-point communication links, interference is a fundamental aspect of wireless networks, and the details of the spreading model are important.

The ocean acoustics community has performed much of the fundamental reseach that in turn underlies and informs the underwater acoustic communications community. Ocean acoustics re-

searchers primarily analyze signal propagation in the frequency domain rather than the time domain [44], and again deal with point-to-point propagation without interferers. Detection of incoming packets, however, is performed in the time domain, and potentially in the presence of interfering packets in a multipath waveguide formed by the watercolumn and its boundaries.

Finally, spreading has not been explored by the new underwater acoustic networking community, largely in favor of studying the effects of greatly increased propagation delay relative to radio channels [3, 20, 55]. Terrestrial radio-based wireless networks typically experience higher pathloss exponents (hence less long-range interference) than in underwater acoustic networks, perhaps also leading researchers coming from radio-based networks to ignore spreading loss (see Chapter 3). An additional reason that the networking community specifically might have neglected spreading is that of the two pathloss terms, spreading loss and absorption loss, spreading loss is polynomial in distance and absorption loss is exponential in distance. Perhaps counterintuitively, spreading is generally the more important of the pathloss terms precisely because it is polynomial rather than exponential: the exponential pathloss term (absorption) ultimately limits a link's maximum range and maximum bandwidth, but within the operating range of a communications link, the polynomial pathloss term (spreading) is more usually important in determining network performance, as shown in Figure 2.1.

Recently, several groups [7, 52, 87] have have integrated the ocean acoustics modeling package Bellhop [79, 90] as a physical propagation layer in the network simulator ns2 [74]. This approach is promising and interesting. It will provide more realistic pathlosses compared with the practical spreading model, but it has the disadvantage that the black box of Bellhop may obscure the intuitive physical understanding promoted by simpler models.

Furthermore, these approaches have not incorporated our hypothesized distinction between incoherent processing of interference and coherent, single-arrival processing of packet detection, which we present in the next section.

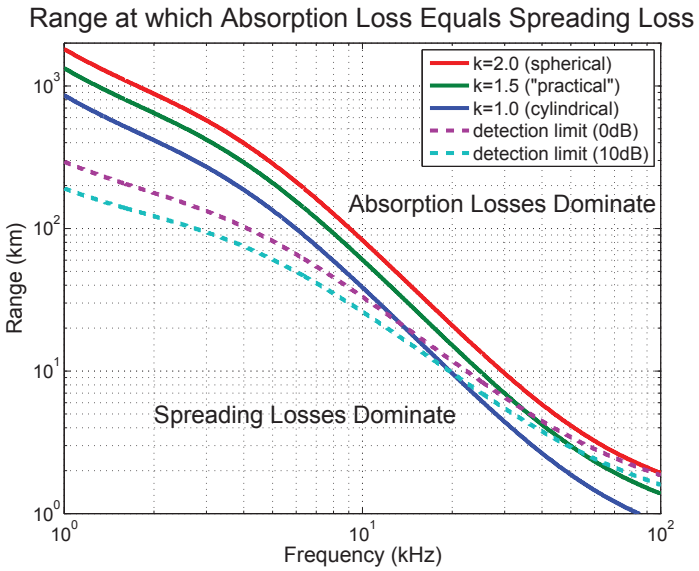

Figure 2.1. The solid lines show the range, for a given frequency, where the absorption loss equals the spreading loss for several spreading exponents k. The absorption loss is modeled with Thorp's expression [117,126]. The dashed lines show maximum detection ranges for SNR detection thresholds of 0 dB and 10 dB. The figure shows that within the typical operating regimes of most underwater acoustic communication links, spreading losses are more significant than absorption losses. The figure also shows that, at lower frequencies, spreading losses dominate absorption losses out to ranges well beyond the detection limit, leading to higher levels of unsuppressed interference at lower frequencies (see Chapter 3). (Note: The SNR is calculated with a transmitter power of 185 dB re:1μPa^2@1m, Thorp absorption, a spreading exponent of $k = 1.5$, a transducer bandwidth of 1/3 the center frequency (i.e., quality factor $Q = 3$), and ambient noise modeled with parameterized power spectral density expressions from [18,117] with a wind speed of 3 m/s and a "shipping factor" of 0.5.)

2.3 Theoretical Basis for Mixed-Exponent Spreading Model

In this section, we use physical reasoning from first principles to provide the theoretical basis for a hypothesized mixed-exponent spreading model. We are not trying to provide detailed propagation modeling such as that done by the ocean acoustics community, but rather to extend the simple and intuitive "practical spreading" model for point-to-point communication links, to a slightly more complicated model which can model the instant of packet detection in the prescence of interference.

The receiver model for our mixed-exponent spreading model is an energy-constrained underwater acoustic modem, running a low-complexity, low-power-consumption matched-filter detector to save

energy while waiting for an incoming packet. Upon detecting an incoming packet, the modem wakes up the primary communications receiver. When the communications receiver finishes processing the packet, the modem returns to the low-power detection state. This is the way that the WHOI Micromodem [36] operates, and the Micromodem in its packet-detection mode specifically is our receiver model.

The model of our communications packet structure is a wakeup signal to trigger the matched-filter detector, followed by a short delay to allow the primary communications receiver to become active, followed by the data packet. In this model, we take the data packet to be a PSK packet, which has a spectrum within the communications band similar to noise.

A matched-filter detector correlates its input against the known wakeup signal, preserving the phase differences among the samples. It has no estimate of the channel's multipath structure. Until the multipath arrivals become unresolvable and start to combine coherently, the matched-filter detector does not combine energy from multiple arrivals. It detects on the energy from a single arrival.

Mathematically, a detection will occur when the peak output energy of the matched-filter detector exceeds a threshold. Denoting the matched-filter coefficients by h_{mf}, the channel's impulse response by h_{channel}, the transmitted wakeup signal by d, and the ambient noise at the receiver by n, the expected value of the detector's peak output energy is

$$\mathbb{E}\left[\text{output}|\text{wakeup signal}\right] = \mathbb{E}\left[\max\left|h_{\text{mf}} * (h_{\text{channel}} * d + n)\right|^2\right] \sim \mathbb{E}\left[\max\left|h_{\text{channel}}[k]\right|^2\right],$$

where $*$ is the convolution operator. In the expression above, we have used the facts that convolution is commutative, and that the matched filter convolved with the desired wakeup signal approximates a delta function (i.e., $(h_{\text{mf}} * d) \approx \delta[k]$), and the processing gain is generally large enough that the noise can be neglected.

For the rest of this chapter, we therefore model the coherent detection energy by the expected value of the peak energy of the channel's impulse response.

An interfering data packet from a distant node that is below the detection threshold will not be detected itself, but its energy will add to the noise floor of the matched filter detector. Energy from all of the multipath arrivals will combine incoherently into the detector's noise floor — the energies of all the multipath arrival sum.

Mathematically, with an undetected interfering packet payload as the detector input, the expected value of the matched-filter detector output will be

$$\mathbb{E}\left[\text{output}|\text{interference}\right] = \mathbb{E}\left[\left|h_{\text{mf}} * \left(h_{\text{channel}} * s + n\right)\right|^2\right],$$

where s is an interfering packet payload, below the detection threshold but still larger than the ambient noise n. In our model, the packet payloads use PSK modulation, which is similar to uncorrelated noise in the frequency band of interest. Let $s' = (h_{\text{mf}} * s)$. If the samples of s' are still uncorrelated, then the detector output due to an interfering packet is

$$\mathbb{E}\left[\text{output}|\text{interference}\right] \approx \mathbb{E}\left[\left|h_{\text{channel}} * s'\right|^2\right] \approx \sigma_{s'}^2 \sum_{k=0}^{N-1} \left|h_{\text{channel}}[k]\right|^2,$$

or proportional to the incoherent sum of the energy in the channel's impulse response.

In a coherent energy sum, the sum of the complex amplitudes is taken first, and the magnitude-squared of the sum is the energy. In an incoherent energy sum, the sum of the squared magnitudes of the individual amplitudes is taken.

For the rest of this chapter, we therefore model the interference energy by the incoherent sum of energy in the channel's impulse response.

The acoustic energy transmitted from a point source (without absorption losses) spreads spherically as it propagates away from the source, i.e., decays as r^{-k} with spreading exponent $k = 2$. As the energy from the point source reflects from the sea surface and the seafloor in shallow water (or refracts from sound speed gradients in deep water), the energy in different multipath paths recombines in the far-field.

The energy in both the interference and the wakeup signal will spread spherically close to their source, until the range at which another multipath arrival combines with them in the appropriate

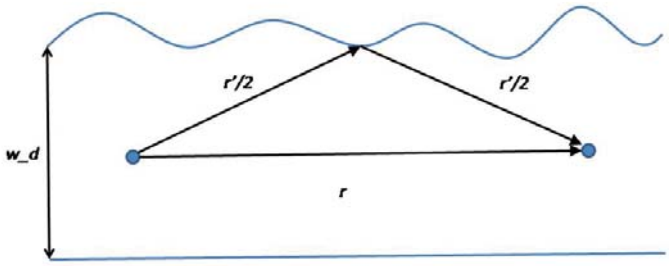

Figure 2.2. Geometry for transition range analysis. The source and receiver are separated by the direct path of length r, with a surface-bounce path of length r'. The water depth is w_d, and the source and receiver are located at depth $w_d/2$.

way. We have called this range the *transition range*. The transition range for interfering packets is the range at which the first additional multipath arrival combines incoherently. The transition range for the wakeup signal, as coherently processed by the matched-filter detector, is the range at which the first additional multipath arrival becomes unresolvable in time.

2.3.1 Transition Range for Coherent Processing (Packet Detection)

We want to derive an order-of-magnitude estimate of the range where the transition away from spherical spreading occurs, for coherent packet detection.

Let r be the separation between the transmitter and receiver. Let w_d be the water depth in the shallow-water case (or a measure of the vertical extent of the sound channel in the deep-water case). Let the signal have bandwidth B.

For an order-of-magnitude approximation, consider a source and receiver that are each at a depth of $w_d/2$, halfway down the water column. Consider just one arrival from the direct path and one arrival from the path with a single surface-bounce, shown in Figure 2.2.

In this geometry, the direct path has length r, and the surface-bounce path has length

$$r' = 2\sqrt{\left(\frac{r}{2}\right)^2 + \left(\frac{w_d}{2}\right)^2} \tag{2.1}$$

The pathlength difference between the two paths is

$$\Delta r = r' - r = \left(2\sqrt{\left(\frac{r}{2}\right)^2 + \left(\frac{w_d}{2}\right)^2}\right) - r = r\left(\sqrt{1 + \left(\frac{w_d}{r}\right)^2} - 1\right) \approx \frac{1}{2}\frac{w_d^2}{r},$$

where the approximation is for large separations relative to the water depth, $r \gg w_d$. The pathlength difference leads to a difference in arrival times,

$$\Delta t = \frac{\Delta r}{c} \approx \frac{w_d^2}{2rc}.$$

With a signal bandwidth B, the time resolution is of order $1/B$. For the direct-path and surface-bounce path, if $\Delta t < 1/B$, then the arrivals are not resolvable, and energy from other arrivals combines coherently into the peak of the matched-filter detector. This gives an approximate transition range of order

$$r_{T,\mathrm{coh}} \approx \frac{w_d^2 B}{2c}.$$

If $r \gg r_{T,\mathrm{coh}}$, then the arrivals are not resolvable.

Next we will derive the coherent spreading exponent beyond the transition range. The key question here is: How many arrivals are non-resolvable from the direct-path arrival as a function of range?

First, we conceptually extend Figure 2.2 to a find the pathlength for a ray with N bounces. The pathlength is

$$r_N = 2N\sqrt{\left(\frac{r}{2N}\right)^2 + \left(\frac{w_d}{2}\right)^2}.$$

For $r \gg w_d$, the N-bounce pathlength becomes

$$r_N \approx r + \frac{N^2 w_d^2}{2r}.$$

The direct pathlength, with zero bounces, r_0, is just the horizontal range r.

For the arrival with N bounces, as well as all arrivals with fewer bounces, to become non-resolvable from the direct-path arrival, we need

$$\frac{\Delta r}{c} \leq \frac{1}{B},$$

where $\Delta r = r_N - r = N^2 d^2 / 2r$. Therefore, at equality, we have the maximum number of bounces a ray can have and still be non-resolvable from the direct-path arrival:

$$N_{\text{b,n.r.}}(r) = \sqrt{\frac{2cr}{Bw_d^2}}.$$

At range r, all rays with $N_{\text{b,n.r.}}(r)$ or fewer bounces will be non-resolvable from the direct-path arrival. Rays with more than $N_{\text{b,n.r.}}(r)$ bounces will be resolvable in time from the direct-path arrival. There are $(2N+1)$ rays with N or fewer bounces (one direct path, plus one ray initially propagating down, and one ray initially propagating up for each combination of N bounces).

Again, in a coherent energy sum, the sum of the complex amplitudes is taken first, and the magnitude-squared of the sum is the energy. In an incoherent energy sum, the sum of the squared magnitudes of the individual amplitudes is taken.

The expected value of the coherent energy is then the expected value of the energy in the coherent sum of the arrivals that are non-resolvable from the direct-path arrivals, i.e., the arrivals from paths with $N_{\text{b,n.r.}}(r)$ or fewer bounces:

$$\mathbb{E}\left[\text{coherent energy}\right] \approx \mathbb{E}\left[\left|\sum_{i=0}^{2N_{\text{b,n.r.}}(r)} a_i(r)\right|^2\right],$$

where $a_i(r)$ is the complex amplitude of the i^{th} arrival as a function of range r. Due to random fluctuations ("micro-multipath") in phase along each path [17], the complex amplitudes of the different arrivals, $a_i(r)$ are uncorrelated, so

$$\mathbb{E}\left[\text{coherent energy}\right] \approx \sum_{i=0}^{2N_{\text{b,n.r.}}(r)} \mathbb{E}\left[\,|a_i(r)|^2\right] \sim 2N_{\text{b,n.r.}}(r)\left(\frac{|a_o|}{r}\right)^2 \sim 2\left(\sqrt{\frac{2cr}{Bw_d^2}}\right)\left(\frac{|a_o|}{r}\right)^2 \sim r^{-1.5} \tag{2.2}$$

Here we have assumed that each of the arrivals individually experiences spherical spreading, and that all the rays have similar energy when transmitted, i.e., the transmitter is omnidirectional. Therefore the expected value of the energy in a single arrival as a function of range is

$$\mathbb{E}\left[|a_i(r)|^2\right] = \left(\frac{|a_o|}{r}\right)^2,$$

where $|a_o|^2$ is proportional to the total transmitted energy.

Equation 2.2 shows that the expected value of the overall coherent energy sum therefore scales as $k = 1.5$ for ranges beyond the coherent transition range.

2.3.2 Spreading Model for Incoherent Energy (Interference)

For interference, the situation is different. Energy combines incoherently for the entire length of the *delay spread*, the delay from the first multipath arrival until the last arrival of appreciable energy.

With perfectly reflecting boundaries, there would be no incoherent energy lost in the depth-range plane, but the energy would still spread azimuthally, i.e., cylindrical spreading with $k = 1$.

The key question here is: How long do we have to sum energy in delay in order to capture the entire delay spread of the channel?

The idealization of perfectly reflecting lossless boundaries is not realistic, and would lead to an infinite delay spread. There is an angle dependence to the reflection coefficients, due to roughness at the surface and due to both bottom roughness as well as the impedance mismatch of acoustic propagation in the water column versus acoustic propagation in the bottom [75].

We approximate the surface and bottom reflection coefficient magnitudes as unity up to a grazing angle of $\theta_{\max}$, and zero for larger grazing angles. (The grazing angle is the angle between the horizontal and the propagation path, the complement of the angle of incidence.)

We again consider a ray with N bounces, discussed in the previous section on the coherent energy transition range. The launch angle of this ray from the source is the same as its grazing angle with the boundaries. So for reflection coefficients with a given maximum grazing angle $\theta_{\max}$, there is a maximum launch angle which is propagated from the source. Therefore there is a ray

with a maximum number of bounces, because any ray with more bounces would have a steeper launch angle, and would not be reflected.

Expressing the maximum launch angle in terms of the number of bounces for the steepest reflected ray,

$$\tan(\theta_{\max}) = \left(\frac{w_d/2}{r/2N_{\text{steepest}}} \right)$$

Using the Taylor series of $\arctan(x) = x - x^3/3 + \cdots$ to first order,

$$\theta_{\max} \approx \frac{N_{\text{steepest}} w_d}{r},$$

or

$$N_{\text{steepest}}(r) = \frac{r\theta_{\max}}{w_d}.$$

The pathlength difference between the steepest reflected ray and the direct path is

$$\Delta r = r_N - r = \frac{w_d^2 N_{\text{steepest}}^2}{2r},$$

using the result on pathlength difference from the previous section on the coherent transition range. The maximum delay spread is the maximum pathlength difference divided by the speed of sound, or

$$\delta_{\max}(r) = \frac{\Delta r_N}{c} = \frac{w_d^2 N_{\text{steepest}}^2}{2rc} = \frac{r\theta_{\max}^2}{2c}. \tag{2.3}$$

If we integrate incoherent across the entire delay spread for a given maximum launch angle, we will have captured all of the incoherent energy, and the incoherent will spread cylindrically, i.e., $k = 1$.

The transition range to go from spherical to cylindrical spreading for incoherent energy depends upon the maximum launch angle. In terms of range, the first ray to return to a receiver in the middle of the water column will be the steepest reflected ray. The range at which it will return to a receiver in the middle of the water column will be $r/N_{\text{steepest}} = w_d/\theta_{\max}$. The incoherent energy transition range is therefore proportional to the water depth, increasing for decreasing maximum launch angles.

It should be noted that in general, the steepest reflected ray will be resolved in time from the direct-path arrival, and so the maximum number of bounces for an arrival which is not resolved from the direct-path arrival will be less than the number of bounces in the steepest reflected ray, i.e., $N_{\text{b,n.r.}}(r) \leq N_{\text{steepest}}$. Equality would only be achieved if the range r were large enough that no arrivals at all are resolved from the direct-path arrival.

2.3.3 Summary of Mixed-Exponent Spreading Model

Summarizing the derivations above, the coherent transition range is

$$r_{T,\text{coh}} \approx \frac{w_d^2 B}{2c}.$$

Before the transition range, coherent energy spreads spherically with exponent $k = 2$. Afterwards, it spreads with exponent $k = 1.5$.

The incoherent transition range is

$$r_{T,\text{inc}} \approx w_d/\theta_{\max},$$

where $\theta_{\max}$ is the maximum propagating launch angle, which will usually be determined by the angular dependence of the reflection coefficients. Before the transition range, incoherent energy will spread spherically with exponent $k = 2$, and cylindrically after the transition range, with exponent $k = 1$.

2.3.4 Implications of the Mixed-Exponent Spreading Model

Even with the practical spreading model, long-range interference is already a larger problem for underwater acoustic networks than it is in radio-based terrestrial wireless networks. With the hypothesized mixed-exponent spreading model, there will be a significant regime where interfering packets will experience smaller pathlosses than detection of desired packets. Therefore, under the hypothesized mixed-exponent spreading model, long-range interference will be a larger problem for

underwater acoustic networks than would be predicted by the practical spreading model. Chapter 3 describes the effects of the various spreading models on network medium access (MAC) protocols.

The next three sections of this chapter are dedicated to measuring spreading exponents and transition ranges. The next section, Section 2.4, validates the mixed-exponent spreading model using Bellhop, a raytracing propagation package. Since our model was derived using ray approximations, we also want to validate it using a different propagation modeling package. In Section 2.5, we also validate the existence of different transition ranges for coherent and incoherent processing, using RAM, which does not make ray approximations.

Finally, in Section 2.6, we measure spreading exponents from field data. From the field data, we are able to partially validate the mixed-exponent spreading model: There were measured differences between the coherent and incoherent spreading-loss exponents, with the coherent exponent usually larger, implying unsuppressed long-range interference will be present. The hypothesized transition ranges were not observed in the experimental data, though the only data were from ranges larger than the incoherent transition range and smaller than the coherent transition range.

2.4 Raytracing Modeling and Validation of Mixed-Exponent Spreading Model

The contribution of this section is validation of the mixed-exponent model in an idealized environment. All the predictions that were made in Section 2.3.3 are validated, namely the location of the coherent and incoherent transition regions as a function of depth and bandwidth, as well as the values of the coherent and incoherent exponents before and after the transition regions.

Our hypothesized mixed-exponent model of spreading exponents and transition ranges was derived using physical reasoning on rays in an idealized channel with uniform soundspeed and lossless reflection coefficients (reflection coefficients of magnitude 1.0 for all angles for surface and bottom). The results in this section are using a raytracing model with uniform soundspeed and perfect reflection coefficients. So while the agreement between theory and modeling results is

excellent, the underlying assumptions in both cases are nearly identical. Therefore this section is considered to be only one step in the validation of the theory.

2.4.1 Introduction to Bellhop

Bellhop [90] is a widely-used ocean acoustics raytracing program[1]. Raytracing is a high-frequency approximation, approximating the acoustic propagation as geometric rays refracting in the soundspeed profile and reflecting from the boundaries. Raytracing methods are generally considered acceptable approximations so long as the wavelength is small with respect to any physical feature in the environment [59]. At 5.5 kHz, the wavelength is about 27 cm with a nominal soundspeed of 1500 m/s. Our smallest depth is 50 m, or nearly 200 times the wavelength, so using the ray approximation is reasonable.

The ray paths and multipath arrival times are frequency-independent, so raytracing is inherently broadband and very fast computationally. We used Bellhop in its "arrivals" mode where it calculates the arrival times and magnitudes of the multipath rays connecting the source and receiver (the eigenrays of the system). Bellhop outputs the arrivals as an idealized train of infinitely narrow impulses in time, which can then be convolved with a broadening pulse to generate an impulse response of the desired (finite) bandwidth.

One of the strengths of using Bellhop for this work is that we can manipulate the phase of each arrival individually. A fundamental feature of the underwater acoustic channel is the existence of random phase fluctuations on each of the multipath arrivals [17]. Bellhop allows randomizing the phases of arrivals very easily, to investigate coherent and incoherent energy combining.

The primary drawback of validating the model with Bellhop and the idealized environment is that both make similar high-frequency ray approximations and underlying assumptions. Validating the model with an acoustic propagation package that explicitly solves the wave equation would be a stronger result.

---

[1]We are using Bellhop as distributed with the Acoustics Toolbox updated on 1 Sept 2010, downloaded from `http://oalib.hlsresearch.com/` on 13 Jan 2012.

2.4.2 Method and Environment

The environment modeled in Bellhop is a range-independent uniform soundspeed of 1500 m/s. For the results in this section, the surface and bottom are perfectly reflecting, i.e., the surface and bottom reflections are lossless.

The source and receiver are at the same depth, but offset slightly from the center of the water column, to break the symmetry between arrivals with an odd number of reflections. With a uniform soundspeed waveguide, arrivals with an even number of reflections will still be coincident in time. The source and receiver depths are both set to 55% of the overall water depth.

To focus our measurements on spreading loss, no absorption loss is included in the model.

We use model parameters similar to those for the KAM11 experiment described in Section 2.6 of this chapter, namely water depths on the order of 100 m (model runs were performed at water depths of 50 m to 200 m), and signal bandwidths divided down in powers of 2 from the KAM11 bandwidth of 4 kHz, with model runs down to 31 Hz bandwidth.

2.4.3 Construction of Impulse Responses and Phase Randomization

Bellhop outputs the delays and amplitudes of the multipath arrivals for a receiver at a specified range. We discard arrivals whose amplitudes are below -100 dB relative to the largest arrival, and arrivals that are more than a specified delay after the first arrival.

By manipulating the phase of each individual arrival, we generate realizations of a complex-valued impulse train. The delays and magnitudes are set deterministically by Bellhop, and phases randomized uniformly and independently between 0 and 2π.

We convolve each of 1000 realizations of the phase-randomized impulse train with a Gaussian broadening pulse to generate realizations of the impulse response with the desired bandwidth. The Gaussian broadening pulse has its frequency-domain full-width-half-max (FWHM) equal to the desired bandwidth. The convolution is summed with complex amplitudes rather than real magnitudes, so the individual arrivals are coherently combined (i.e., random phases preserved) during the convolution.

Each of the individual impulse response realizations has its incoherent energy estimated as the sum of the magnitude-squared of the impulse response across delay. The reported incoherent energy estimate for a given range is the mean value of incoherent energy for each of the 1000 realizations.

The coherent energy estimate for each individual realization is the magnitude-squared of the *first* peak of that impulse response, for two reasons. First, using the first peak more directly models a practical low-complexity, low-power-consumption matched-filter detector implementation, which will detect on the first peak above the threshold. Second, with a uniform soundspeed and constant-depth waveguide, arrivals with an even number of reflections (e.g., surface-bottom or bottom-surface) will be coincident in time, and some realizations will have large energies. If we selected the global maximum energy of the impulse response rather than the first local maximum, the energy estimate would be skewed by not always averaging from the same peak.

The reported coherent energy estimate for a given range point is the mean value of the coherent energies for the 1000 realizations.

We have also verified that the direct arrival itself (without allowing any multipath combining) experiences spherical spreading loss with range, as expected. Bellhop is not assuming or enforcing any particular spreading model internally.

2.4.3.1 Launch Angles

For these results, the maximum arrival delay we allow is 1500 ms. Using Equation 2.3 for the maximum delay spread, we set the maximum launch angle to $\pm 11^\circ$, for which the estimated delay spread is 1300 ms at 100 km range. While maximum ranges of 100 km are not realistic for shallow water, propagating to large ranges allows us to investigate the coherent transition range over the full set of depths and bandwidths.

Limiting the launch angles does not change the energy exponent estimate. But by limiting the launch angles, Bellhop runs much faster, and the delay spreads are shorter, so the energy calculations on the impulse responses are also much faster. Furthermore, a launch angle limit of $\pm 11^\circ$ is reasonable physically, especially for longer ranges. For example, Figure 2.31 shows modeled surface and bottom reflection coefficients dropping after grazing angles of 10°-20°.

2.4.4 Variation of Impulse Responses with Bandwidth, Range, and Depth

Figures 2.3-2.5 show the variation of impulse responses varying with bandwidth, range, and depth. The figures help to visualize and develop intuition about how impulse responses would differ in different situations. As bandwidth increases, more arrivals are resolved. As range increases, the pathlength differences decrease, and the arrivals get closer together, eventually becoming unresolvable. As depth increases, the pathlength differences increase and arrivals move apart in delay. The number of arrivals as a function of range is plotted in Figure 2.6. The number of arrivals as a function of range increases roughly as the square root of range.

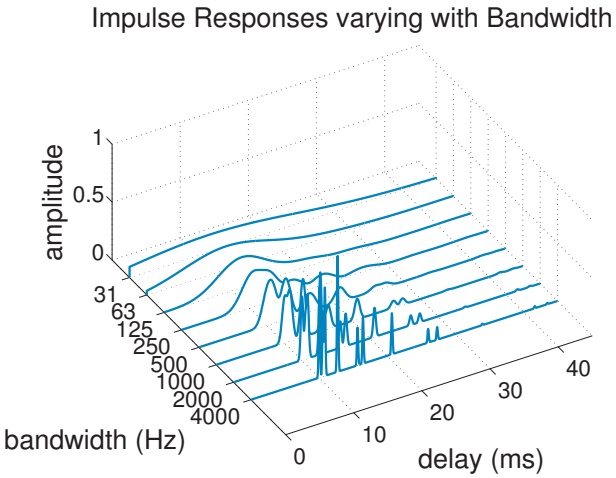

Figure 2.3. Variation of impulse responses with bandwidth. As bandwidth increases, more arrivals are resolved. As range increases, the pathlength differences decrease and arrival resolution decreases. As depth increases, the pathlength differences increase and arrival resolution increases.

2.4.5 Estimation of transition ranges and spreading exponents

The energy estimates are then plotted versus range on a log-log plot. The transition range is manually selected. (The transition ranges are selected manually to help in less-idealized environments, where the energy-versus-range plots can be much more variable.) The spreading exponents, k, are estimated by fitting the model

$$\log_{10}(\text{energy}) = -k \log_{10}(\text{range}) + b$$

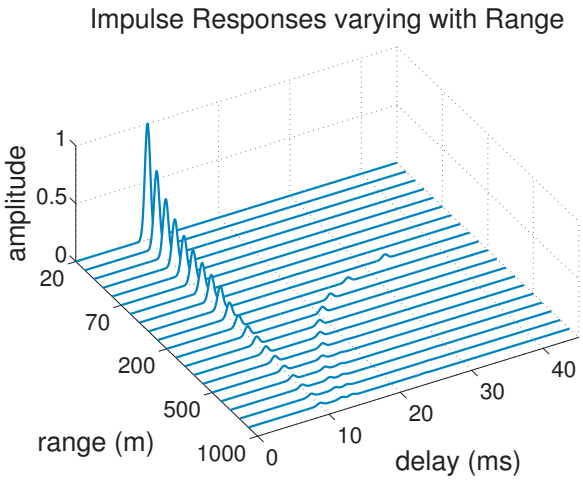

Figure 2.4. Variation of impulse responses with range. As range increases, the pathlength differences decrease and arrival resolution decreases.

using unweighted linear least squares estimates (LLSE) over the selected range. The margins of error are calculated using a 95% confidence interval. The fitting region for the spherical spreading regime extends from the closest modeled range out to the transition range. The region for estimating the exponent beyond the transition range is manually selected such that the slope of the line has stabilized.

2.4.6 Results

Figure 2.7 shows an example of coherent and incoherent energy varying as a function of range, for a fixed bandwidth of 4k Hz and a depth of 100 m. Similar plots are shown in Appendix A, for a fixed bandwidth of 4 kHz and varying depths of 50 m, 75 m, 100 m, 150 m, and 200 m, as well as at a fixed depth of 100 m and varying bandwidths of 4 kHz to 31 Hz. Similar runs were made for every combination of depth and bandwidth.

As described in Section 2.4.3, each energy estimate at each range shown in the energy-versus-range plots such as Figure 2.7 and the plots in Appendix A is the average of 1000 realizations of impulse responses with independent randomized phases.

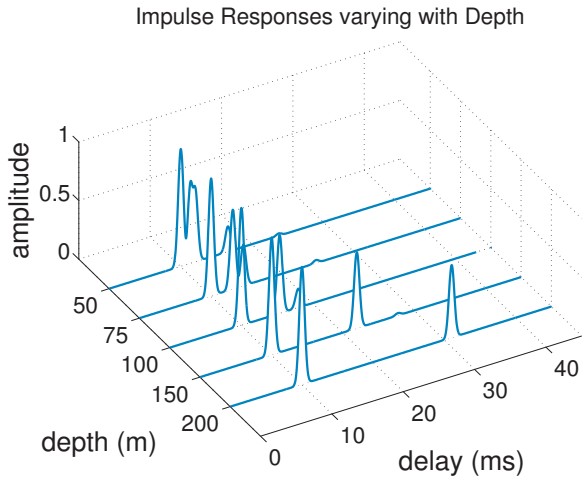

Figure 2.5. Variation of impulse responses with depth. As depth increases, the pathlength differences increase and arrival resolution increases.

The energy in the transition region is more variable since the combining of just a single additional arrival can have a relatively large impact. The estimation error on the value of the transition range is taken to be the spacing of the data points in range, since selection of one range over the neighboring range is sometimes arbitrary. (For points spaced logarithmically in range, the more distant one is always the one at the next higher range value.)

For all the plots in Figure 2.7 and Appendix A, the coherent and incoherent spreading exponent before the transition region is 2.0, and after the transition region, the incoherent spreading exponents are very close to 1.0, while the coherent spreading exponents go to approximately 1.5.

The Bellhop runs were run to a maximum range of 100 km, with logarithmic spacing of the points in range. While this maximum range in unrealistic in these water depths, the goal was to validate the depth- and bandwidth-dependence of the coherent transition range. With the widest bandwidth of 4 kHz and the deepest water depths, 200 m and 150 m, the coherent transition ranges are predicted to be 53 km and 30 km, respectively. There are only a few (range,energy) data points to estimate the coherent spreading exponent beyond these large transition ranges, and so the quality of the exponent estimate is lower and the margins of error are higher. The estimated coherent spreading exponent for a depth of 200 m, bandwidth of 4 kHz is estimated as 1.1 ± 0.5 with

a 95% confidence interval. For depth 150 m, bandwidth 4 kHz, the estimated coherent spreading exponent is 1.3 ± 0.1, again with a 95% confidence interval. The other exponent estimates are extremely close to the hypothesized values.

Figure 2.8 summarizes the coherent transition range versus depth and bandwidth, respectively, as well as the spreading exponents before and after the transition range. Figure 2.9 does the same for the incoherent transition range. The results agree with the hypothesized theory very well.

The model for coherent transition range is

$$r_{T,\text{coh}} = a_c \left(\frac{W d^2}{2c} \right),$$

where W is the signal bandwidth, d is the waterdepth, c is the speed of sound, and a_c is a dimensionless scale factor. The model for the incoherent transition range is $r_{T,\text{inc}} = a_i d$, where again d is the waterdepth and a_i is a dimensionless scale factor. Models derived using dimensional analysis and simple physical reasoning, such as our models of transition ranges, typically have dimensionless scale factors of order unity [6]. The scale factor is essentially related to when a transition is declared to have truly occurred.

The fits in Figures 2.8 and 2.9 use weighted linear least-squares estimates to estimate the single unknown parameter in the models, the scale factors a_c and a_i. To estimate the errors in the estimates of the scale factors, we used weighted LLSE to fit each of the individual curves plotted, and found the maximum deviation in the individual fits from the fit with all of the data.

2.4.7 Conclusions

The results from Bellhop have excellent agreement with the mixed-exponent spreading model. The coherent and incoherent transition ranges and values of the exponents are validated.

It is only a preliminary validation, however, because the derivation of the mixed-exponent model also made the high-frequency ray approximation in a uniform soundspeed channel with perfectly reflecting boundaries.

The next section validates the mixed-exponent spreading model with a RAM, an acoustic propagation modeling package which does not make the ray approximation.

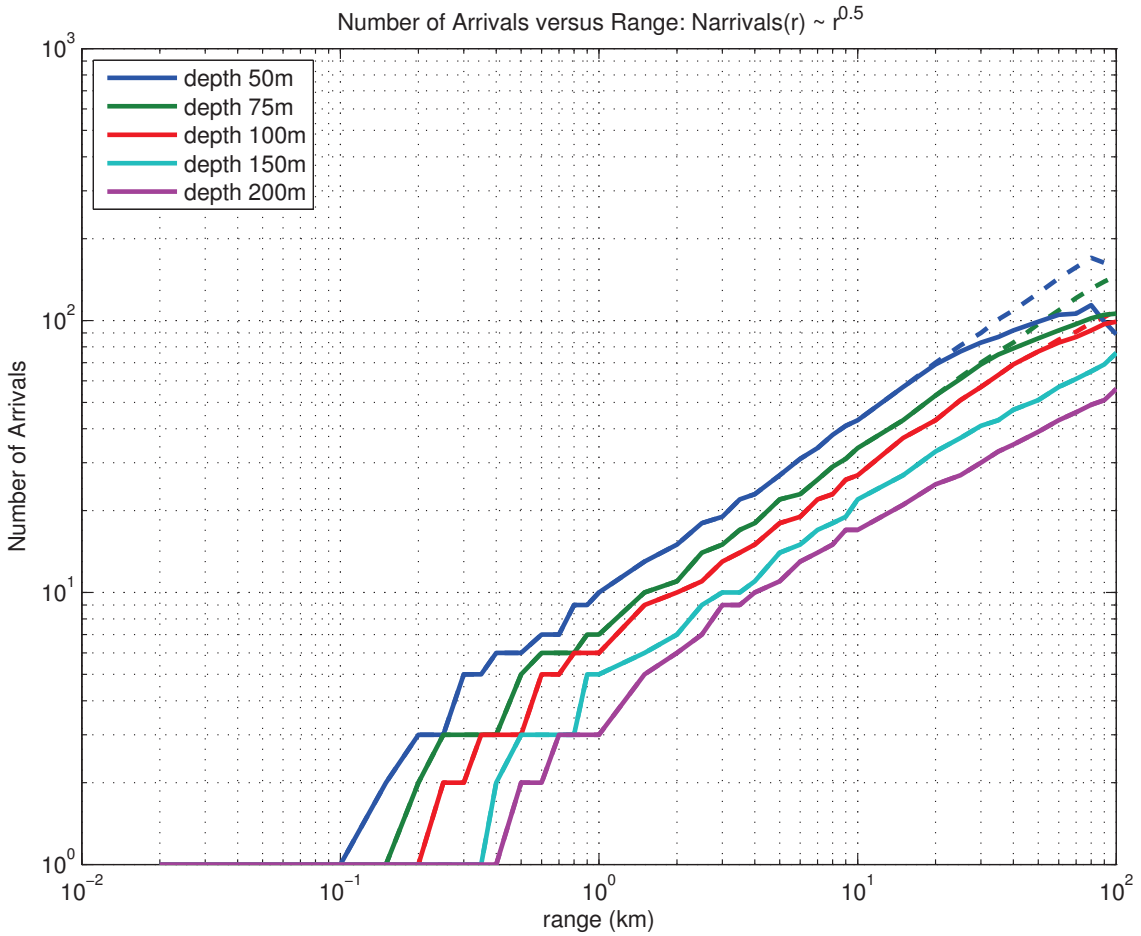

Figure 2.6. The number of arrivals as a function of range increases roughly as the square root of range. Again, in real channels, boundary losses will result in far fewer arrivals being significant; this plot is to aid intuition with an idealized lossless channel. (The number of arrivals for 50 m depth dips slightly at very long ranges because of the large number of boundary interactions. As the boundary interactions increase, even with perfect reflection, the pathlength increases, and along-path spreading continues to reduce the energy. Changing the energy cutoff for arrivals from a minimum of -100 dB to a completely unrealistic minimum of -1000 dB generates the dashed blue line for number of arrivals at 50 m depth, with no dip in the trend line.)

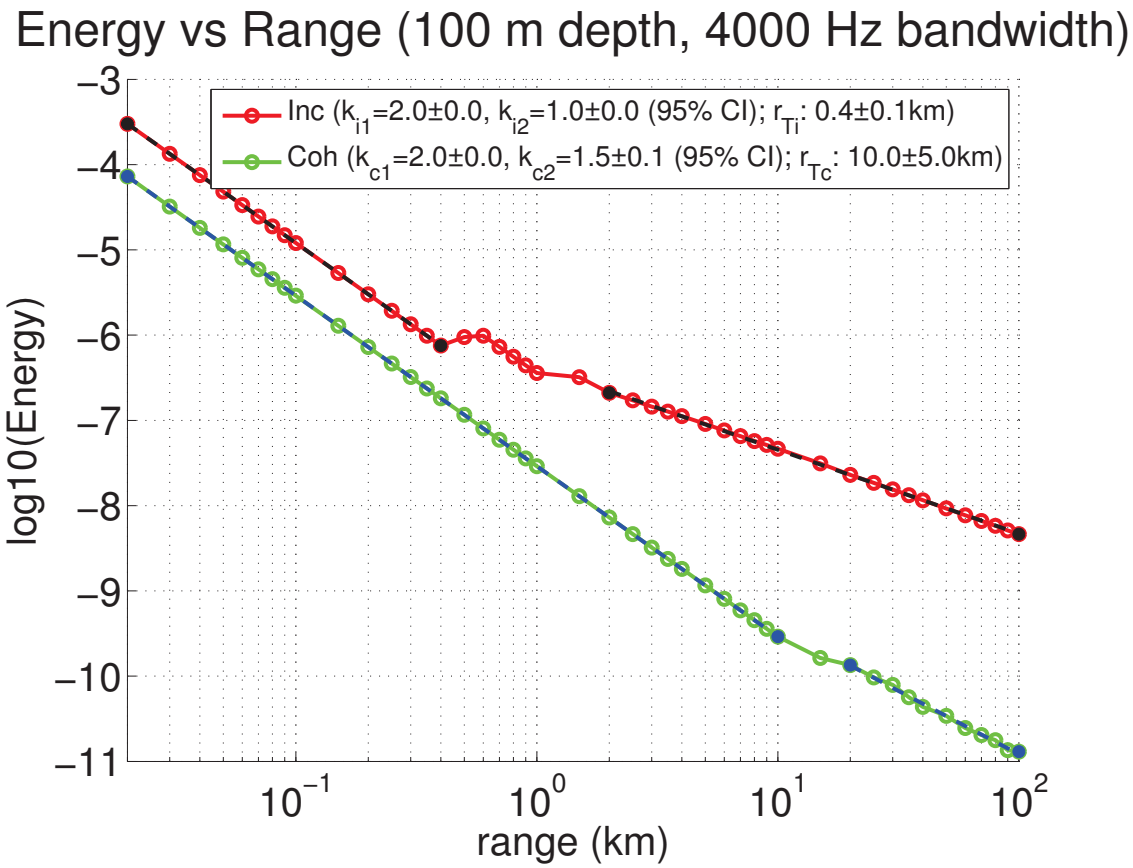

Figure 2.7. Coherent and incoherent energy at a depth of 100 m and a bandwidth of 4 kHz. Incoherent transition range is unaffected by bandwidth, whereas coherent transition range scales linearly with bandwidth. Similar energy-versus-range plots are in Appendix A for a fixed bandwidth of 4 kHz and varying depths of 50 m, 75 m, 100 m, 150 m, and 200 m, as well as at a fixed depth of 100 m and varying bandwidths of 4 kHz to 31 Hz. Each energy estimate at each range is the average of 1000 realizations of impulse responses with independent randomized phases, as described in Section 2.4.3.

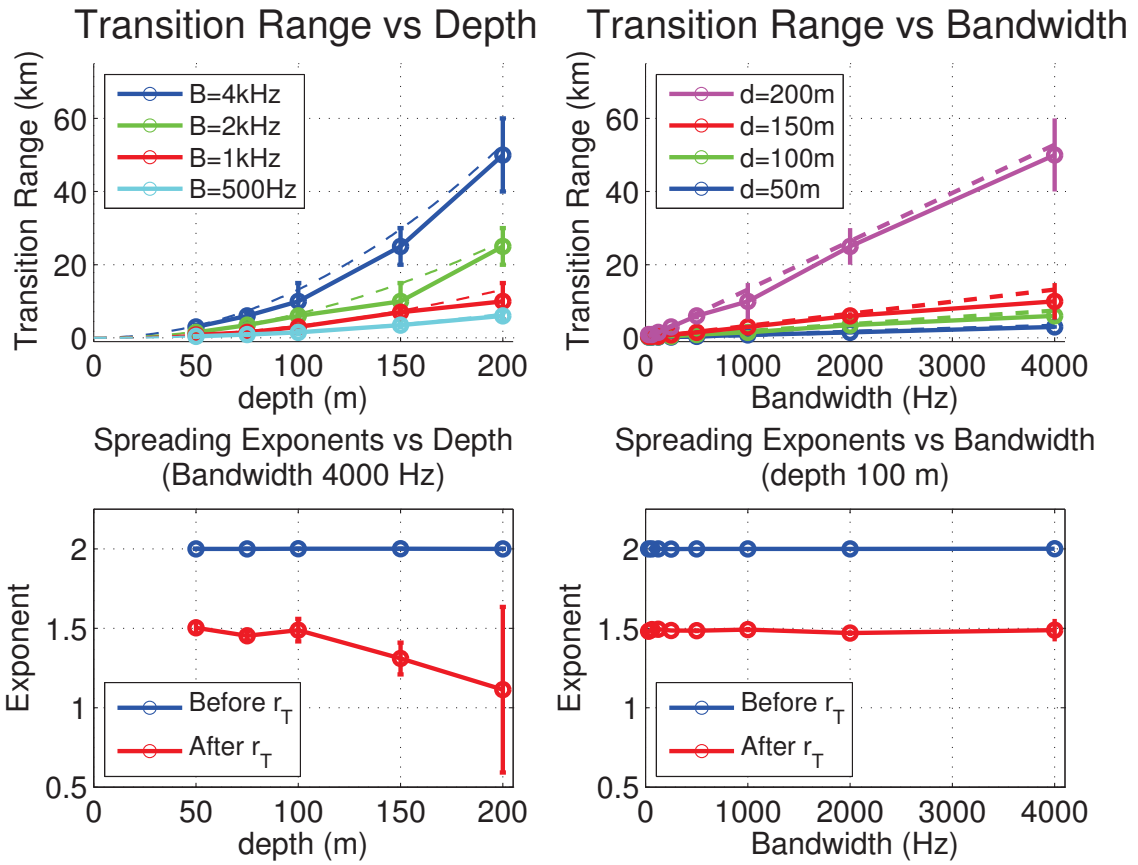

Figure 2.8. In the upper pair of plots, coherent transition range, for several bandwidths and varying depths, as well as several depths and varying bandwidths. In the lower pair of plots, coherent spreading exponents before (blue) and after (red) the transition range, again varying with bandwidth and depth. In the upper pair of plots, the errorbars in transition range show the uncertainty in transition range due to the resolution of the log-spaced data points in range. The uncertainty in the scale factor a_c is estimated by estimating the scale factor for each of the transition-range curves individually, compared against estimating the scale factor from all the curves simultaneously. The reported uncertainties are the largest deviations of the individual estimates below and above the combined estimate. The coherent spreading exponent transitions from spherical spreading ($k_1 = 2$) to $k_2 = 1.5$. As discussed in the text, for 4 kHz bandwidth and the deepest water depths (150 m and 200 m), the coherent transition range is large (30 km and 53 km, respectively), and there are only a few points in range used in the LLS exponent estimate, leading to larger uncertainty in those estimates.

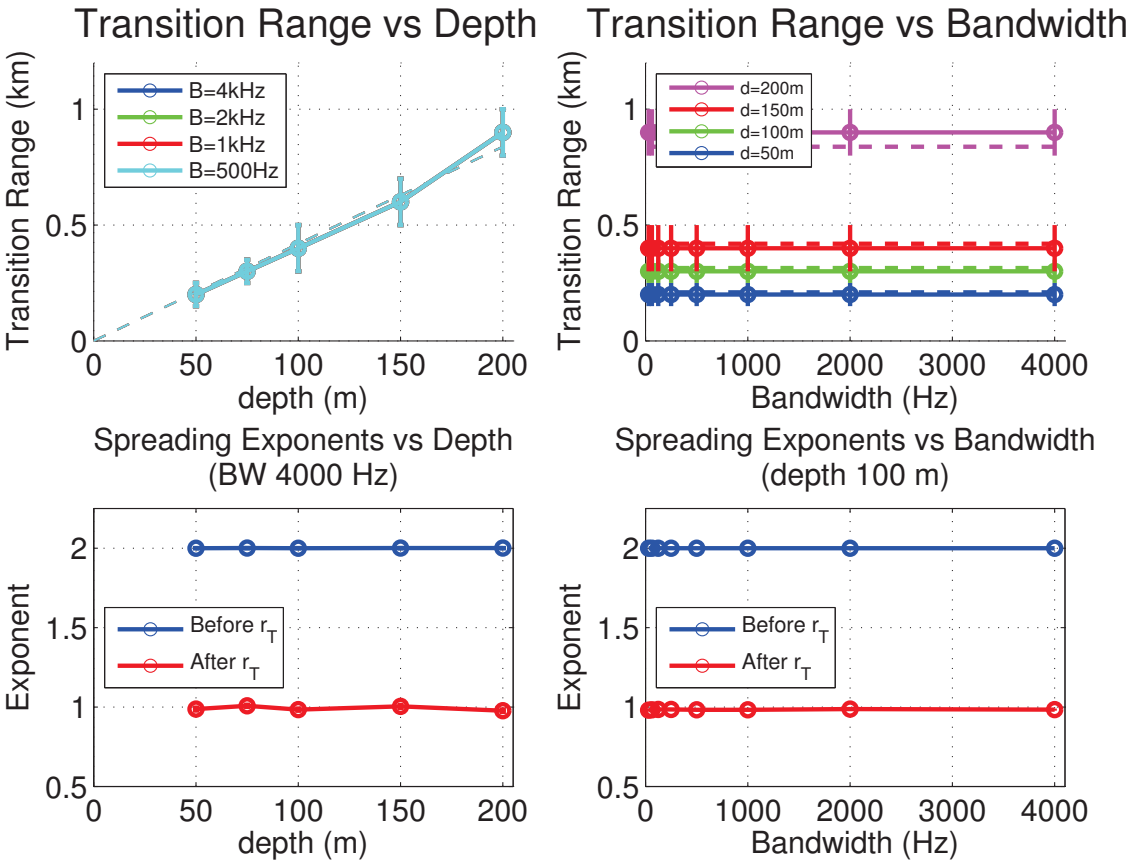

Figure 2.9. Incoherent transition range versus depth and bandwidth. The depth dependence is linear and there is no bandwidth dependence. The scale factor a_i is controlled by the maximum launch angle used in the model runs. Here the maximum launch angle is $\pm 11^\circ$, from which we would expect the first non-direct arrival to combine incoherently at about $a_i \sim 5$ waterdepths; the estimate gives $a_i = 4.2 + \{-0.2, +0.3\}$, with uncertainties calculated as they are for the coherent case. Around the transition range, the incoherent spreading exponent transitions from spherical spreading ($k_1 = 2$) to cylindrical spreading ($k_2 = 1$).

2.5 Wave-Equation Modeling and Validation of Mixed-Exponent Spreading Model

The contribution of this section is further validation of the mixed-exponent spreading model. The results in this section are generated using the RAM [19] acoustic propagation modeling program. RAM solves a "parabolic" approximation to the wave equation, valid for a forward-propagating acoustic wave [59]. It does not make a high-frequency ray approximation as Bellhop does. The hypothesized mixed-exponent spreading model was derived using a ray approximation. While the results from Bellhop had excellent agreement with the hypothesized model, the model and Bellhop both use the high-frequency ray approximation. Therefore validation by RAM of some of the model's key predictions is a stronger result than validation by Bellhop. In particular, the RAM results show two regimes for the spreading exponents, with transitions in the exponents at ranges that have a depth and bandwidth dependence similar to what the model predicts.

The Bellhop results in the previous section were generated using idealized perfect (lossless) reflection coefficients. The RAM results in this section include bottom reflection losses, and effectively some surface reflection loss as well, due to the maximum propagation angle in parabolic equation methods, which can be viewed as a reflection coefficient of zero beyond the maximum propagation angle.

The RAM environment used is therefore less idealized than the Bellhop environment from the previous section, providing an additional measure of validation to the model. RAM is still an idealized modeling program, so it is not definitive validation of the mixed-exponent model, but the model is validated by two distinct propagation modeling methods.

In Section 2.5.1, we describe RAM, and in Section 2.5.2, the modeled environment. In Section 2.5.3, we describe the method for generating impulse responses using RAM. In Section 2.5.4, we describe how the energy estimates are made, including the mechanism used to allow averaging of phase-randomized realizations. We present the energy-versus range and spreading exponent estimates in Section 2.5.4. In Section 2.5.5, we compare the transition ranges and exponent estimates with the mixed-exponent model. We conclude the section on RAM modeling results in Section 2.5.6.

2.5.1 RAM

As mentioned above, RAM implements a parabolic equation method to solve a one-way forward-propagating approximation to the wave equation. A single frequency at a time is propagated through the environment from source to receiver. The output is the complex pressure field at the receiver for that particular frequency. The complex pressure field values can be used as the Fourier synthesis coefficients to construct the time-domain impulse response at the receiver.

An important difference from Bellhop is that the phases of the individual arrivals cannot be manipulated, since arrivals are not explicitly generated. RAM propagates the phase information precisely and deterministically. In some sense, RAM's propagation model is too precise, since it does not provide a straightforward way to include the random micro-multipath phase fluctuations that are present in the real underwater channel [17]. Synthesis of the impulse responses and the method used for randomizing phases of arrivals are described in Section 2.5.3.

The RAM code we are using is Version 1.1, dated 30 April 1998 by M.D. Collins, but it has been modified by J. Preisig and T. Duda to output complex pressure amplitude rather than the magnitude of pressure. In order to build impulse responses, we need the complex pressure amplitude. The source code listing, including the modifications, is in Appendix B.

2.5.2 Modeled Environment

As with Bellhop, the environmental model used with RAM is a range-independent uniform soundspeed of 1500 m/s and a water density of 1.0 g/cm^3. The water depths are again taken to be the same order of magnitude as the 100 m water depth in the KAM11 experiment, discussed in Section 2.6. Water depths of 50 m, 75 m, 100 m, 150 m, and 200 m are modeled to investigate the depth dependence of the mixed-exponent spreading model. The impulse responses, described in the next section, had bandwidths starting at the KAM11 bandwidth of 4 kHz, dividing down to 500 Hz bandwidth in powers of two.

As with Bellhop, the source and receiver are both at 55% of the water depth, offset slightly from the center of the water column, to break the symmetry between arrivals with an odd number of reflections.

The RAM results do not include absorption loss, which again focuses our results primarily on spreading loss.

These results do however include reflection losses from the bottom and surface. By including reflection losses [75], we can validate the spreading model even without perfect reflection coefficients. The seafloor models a typical sediment seafloor, with a sound speed of 1600 m/s and a density of 1.6 g/cm^3. The reflection coefficients are shown in Figure 2.10. An characteristic of parabolic equation methods (including RAM) is that only the wave equation solution is only for forward-propagating waves. As a result, there is a maximum propagation angle, which is about 45° for RAM. One way of viewing this effect is in terms of effective reflection coefficients, which go to zero beyond the maximum propagation angle, as illustrated in Figure 2.10.

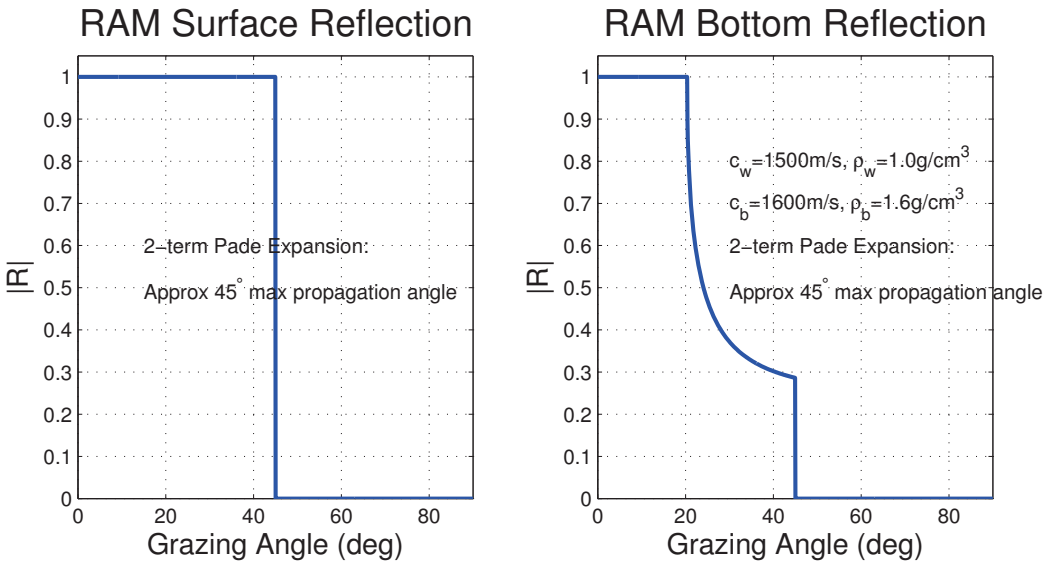

Figure 2.10. Surface and bottom reflection coefficients used for the RAM results. The bottom is modeled as a sediment seafloor. The reflection coefficients effectively go to zero beyond RAM's maximum propagation angle of about 45°. The plotted reflection coefficients are in terms of amplitude; their magnitude-squared values give reflection coefficients for intensity.

2.5.3 Synthesis of Impulse Responses and Method for Phase Randomization

The impulse responses can be constructed using Fourier synthesis [59]. For each frequency run, at passband frequency f_k, RAM outputs the complex pressure field, H_k, at the receiver, including the phase from propagating from the source to the receiver. The complex pressure field values at a given frequency are the Fourier coefficients for the corresponding Fourier synthesis component. The synthesized baseband impulse response, $h[n]$, is

$$h[n] = \sum_{k=-N/2}^{N/2-1} H_k \, \exp\left(-\frac{j\omega_k n}{f_s}\right).$$

We ran RAM at $N = 2048$ frequency components, spanning the KAM11 experiment's band of $B = 4$ kHz bandwidth centered at $f_c = 5.5$ kHz. The passband frequencies where RAM was run were $f_k = f_c + Bk/N$, with $N/2 \leq k \leq (N/2) - 1$. For the baseband synthesis, the baseband sampling rate was $f_s = 10240$ Hz, and the synthesized impulse response was 2048 samples in time, or 200 ms long. The baseband frequencies were $\omega_k = 2\pi Bk/N$, again with $N/2 \leq k \leq (N/2) - 1$. The negative sign in the complex exponential is conventional in acoustics modeling, and is the opposite sign convention from that used in some other research communities.

Narrower bandwidths were generated by filtering the baseband impulse response with Gaussian low-pass filters to avoid introduction of time-domain sidelobes. The frequency-domain full-width-half-max of the low-pass filters was set to be the desired bandwidth. The bandwidths used were 4 kHz, 2 kHz, 1 kHz, and 500 Hz. When filtering the impulse responses to below 500 Hz bandwidth, the energy estimates became very noisy.

2.5.3.1 Phase Randomization of Arrivals

An important part of the coherent energy estimate is phase randomization of the arrivals at the receiver. We are trying to estimate the expected value of the coherent energy. With any given realization of the arrival phases, that particular coherent energy measurement might not be very close to the expected value. With the Bellhop, the phases of the arrivals were immediately available. In RAM, they are not, and the phase at the receiver is deterministically calculated.

The approach we used to randomize the phase of arrivals in RAM was to perturb the receiver location slightly. Visualizing multipath rays converging on the receiver, each ray's pathlength will then change, and the arrival phases will be perturbed as well. We used a 3×3 receiver grid centered on the nominal receiver location. The grid spacing was 10 m, over 30 wavelengths at the center frequency, so the arrival phases are will be randomized in this process. The reported energy estimates are the mean of the energies from the nine receivers. Since the grid spacing was constant with range, at the very smallest ranges the grid size was comparable with the total range, and the variation from receiver to receiver was high.

As future work, it may be possible to investigate randomizing the arrival phases *after* Fourier synthesis. The likely problem with that approach, however, is that the place where phase randomization is critical is in coherent sum of the arrivals which are non-resolvable from the first arrival. It is unclear how the phases of the non-resolvable arrivals could be independently randomized after Fourier synthesis.

2.5.4 Estimation of transition ranges and spreading exponents

Estimating transition ranges and spreading exponents was almost identical to the method used for Bellhop: transition ranges were selected manually, and we used unweighted linear least squares estimates (LLSE) for the exponents. The unweighted LLSE fits appear to fit fairly well despite the relatively large standard deviations on the energy measurements. We did not do a residual analysis for the RAM fits, as we did for the KAM11 fits in Section 2.6.

An example energy-versus-range plot for the RAM results with a water depth of 100 m and a signal bandwidth of 4 kHz is shown in Figure 2.11. Similar energy-versus-range plots are shown in Appendix C for water depths of 50 m, 75 m, 100 m, 150 m, and 200 m at a signal bandwidth of 4 kHz, as well as bandwidths of 4 kHz, 2 kHz, 1 kHz, and 500 Hz at a water depth of 100 m.

One difference between the methods for RAM and Bellhop was in calculating the margins of error. The uncertainty of the energy estimate was negligible with Bellhop's 1000 realizations per point, and we used an explicit closed-form formula for the margin of error for the exponent estimate. For RAM, we bootstrapped [26] 400 trials for each of the LLSE fits, and used the standard deviation

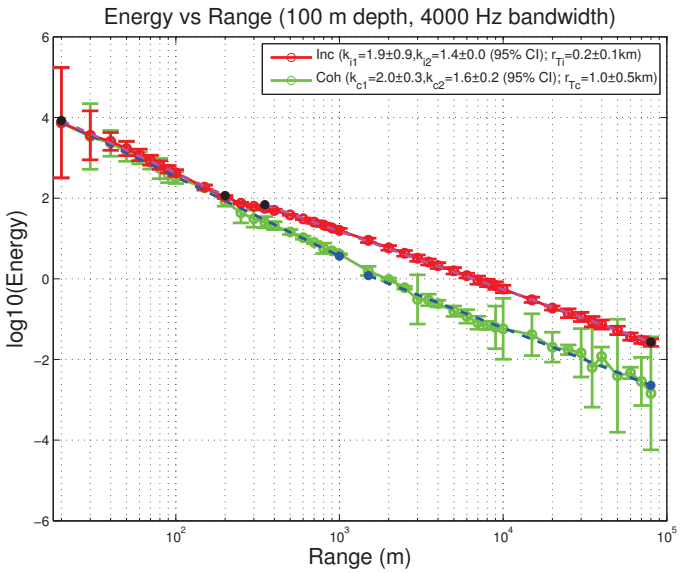

Figure 2.11. Coherent and incoherent energy for a bandwidth of 4 kHz and a depths of 100 m.

of the exponent estimates as the standard error. From the standard error, we calculated margins of error for a 95% confidence interval from a t-distribution with $(N-2)$ degrees of freedom, since the slope and intercept were both estimated.

2.5.5 Results and Discussion

While the results from RAM are significantly noisier than the Bellhop results, there are spreading exponent transitions visible in the plots and in the estimates. The goal of the modeling with RAM was to further validate or invalidate the mixed-exponent spreading model. The results do provide further validation that there are differences between the coherent and incoherent spreading exponents in terms of their transition ranges and dependences upon depth and bandwidth.

In the Bellhop raytracing results from Section 2.4, the incoherent energy exponent beyond the transition range was very close to 1.0, whereas for the RAM results, it is on the order of 1.5. Although this is unconfirmed and is left for future work, it is likely that the incoherent energy-loss exponent is larger for the RAM results than it was for the Bellhop results is due to the reflection coefficients. For the Bellhop raytracing, the boundaries were lossless, while for the RAM modeling,

the boundaries introduce some losses, which would cause additional energy loss. In order to capture the full delay spread for the incoherent energy estimate, rays with more bounces (and hence higher loss) are required than for the coherent energy estimate (i.e., from Section 2.3, the maximum number of bounces for rays which are non-resolvable from direct path is less than the number of bounces of the last ray with the last arrival in the delay spread, the steepest ray: $N_{\text{b,n.r.}} < N_{\text{steepest}}$).

Figures 2.12 and 2.13 show the coherent and incoherent transition ranges versus depth and bandwidth. They also show the estimates of the scale factors a_i and a_c. The estimates of the incoherent scale factor, a_i, are roughly consistent between Bellhop and RAM, considering their maximum angles of $\pm 11^\circ$ and about $\pm 45^\circ$, respectively. The incoherent scale factor estimate from the RAM results is $\hat{a_i} = 2.3 + \{-0.3, +0.1\}$.

There is a significant difference for the coherent scale factor, however. With Bellhop, it was estimated at $\hat{a_c} = 1.0 + (-0.1, +1.5)$. With the RAM results, the estimate is about three times smaller, $\hat{a_c} = 0.3 + (-0.1, +0.2)$.

The first thing which would need to be determined is whether or not this effect is real. Potential issues with selection of transition ranges from noisy curves, the spatial perturbation for phase randomization, or other processing steps would have to be double-checked. But if this result is indeed real, then it would suggest that there is a propagation effect in one of the models that is not being properly captured, potentially indicating an issue with the ray approximation.

The incoherent energy estimates in the spherical spreading region have particularly high margins of error. Three potential improvements would be: (1) scale the receiver perturbation grid, at least at short ranges, to try to reduce the largest error; (2) add more receivers in the perturbed grid; and (3) try weighted LLSE to de-emphasize the noisiest points.

2.5.6 Conclusions

The RAM results further validate the behavior of the mixed-exponent spreading model. RAM does not use a high-frequency ray approximation, and so it is a stronger validation of the mixed-exponent spreading model than Bellhop's validation was, even though Bellhop's results are much clearer. In addition, the RAM environment has reflection losses at the boundaries, validating the

mixed-exponent model in a less-idealized environment than the raytraced Bellhop results, which had lossless boundaries.

The RAM results are noisy, making it difficult to estimate transition ranges and spreading exponents. The method of averaging energy could be extended to average further and reduce noise. With reduced noise, some of the questions about the potential difference in coherent transition range between Bellhop and RAM could be further addressed.

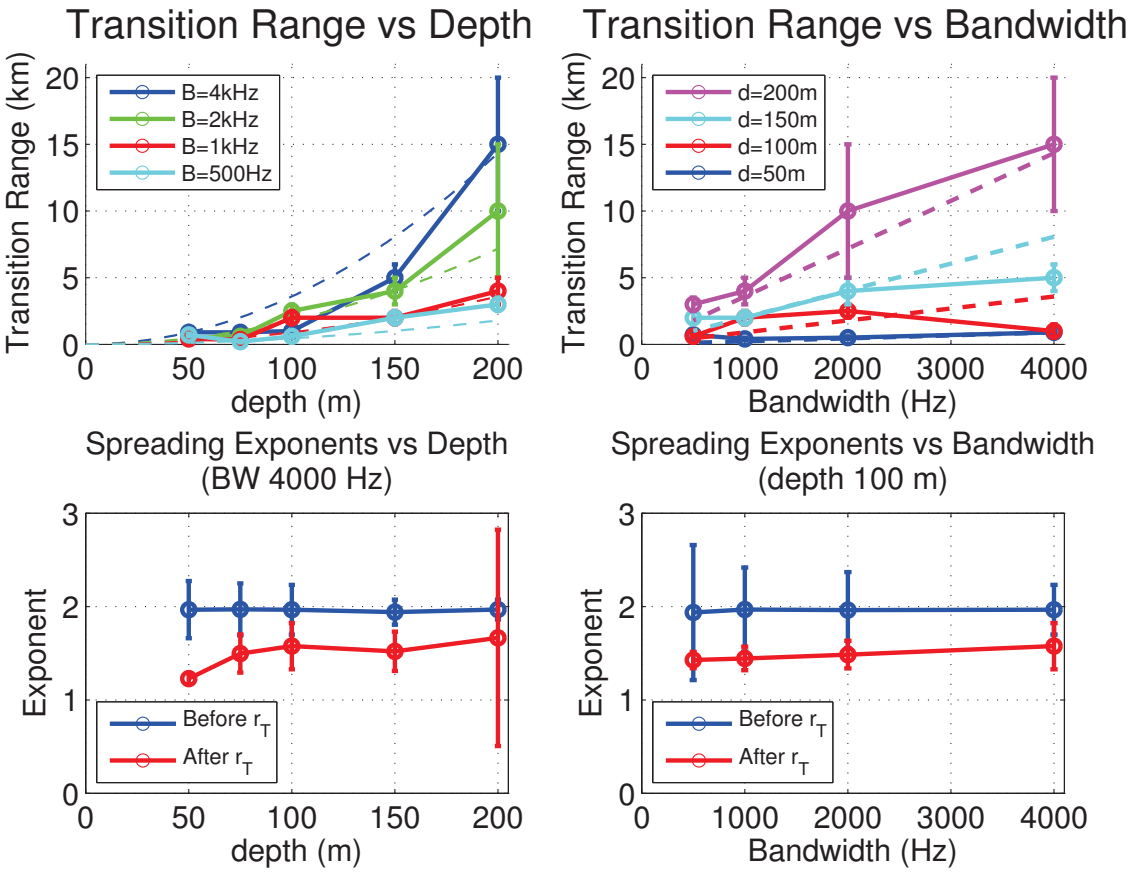

Figure 2.12. Coherent transition range versus depth and bandwidth. The estimate of the coherent scale factor from the RAM results is $\hat{a_c} = 0.3 + \{-0.1, +0.2\}$, or about a factor of three smaller than the scale factor estimate is for the Bellhop results.

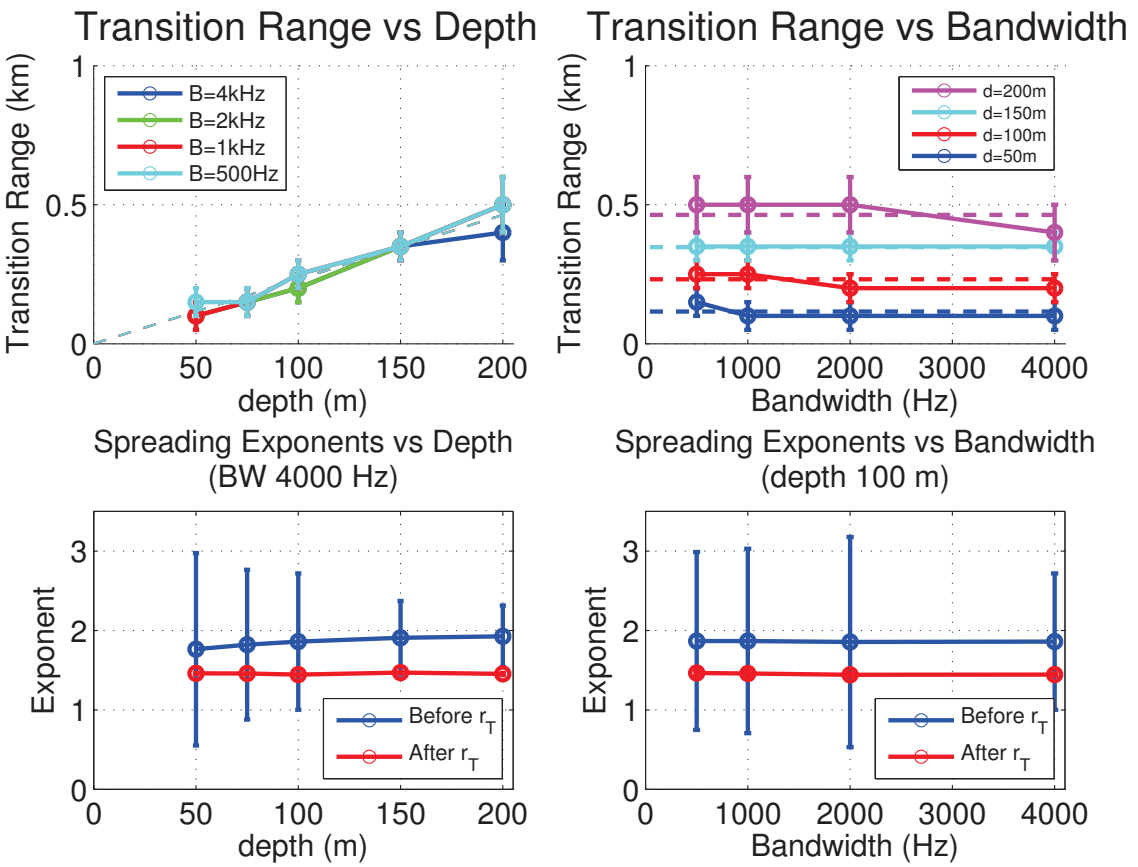

Figure 2.13. Incoherent transition range versus depth and bandwidth. The scale factor ai is controlled by the maximum launch angle used in the model runs. For RAM's parabolic equation method, the maximum launch angle is about $\pm 45°$, which from which we would expect the first non-direct arrival to combine incoherently at roughly $a_i \sim 1$ waterdepth; the estimate gives $\hat{a_i} = 2.3 + \{-0.3, +0.1\}$, with uncertainties calculated as they are for the coherent case.

2.6 Measurement of Spreading Exponents from the KAM11 Field Experiment

The contribution of this section is a measurement of the coherent and incoherent energy-loss exponents from experimental field data. The energy-loss exponents include spreading loss and other losses, such as scattering loss from surface and bottom reflections. One goal of this work was to attempt to validate the mixed-exponent spreading model with field data. A second goal was to determine from field data how often simple spreading loss models are applicable, and, when they are applicable, what the spreading exponents are. The recurring goal of this thesis in general is to evaluate the assumptions underlying research in underwater acoustic networks (UANs).

It has been standard to model UANs using the "practical spreading" model [18, 112], although it is becoming more common to use propagation modeling tools such as Bellhop within simulations of UANs [87]. The advantage of simple spreading models is that they give the researcher physical intuition, while a modeling package such as Bellhop can be a black box without promoting physical insight. On the other hand, it needs to be determined how often the simple spreading models are valid, and if they are valid at times, what the values of the energy loss exponents are.

In the experimental data presented in this chapter, we found significant periods of time in which simple spreading loss models did not hold. In the periods when simple energy-loss exponent models did appear to hold, our estimates of the energy loss exponents were well over 2.0. These results suggest that caution should be exercised when using the "practical spreading" model with a spreading loss exponent of 1.5.

Our experimental field data is from the Kauai Acomms MURI 2011 (KAM11) Experiment [57]. The location was chosen in part due to its highly variable environmental conditions, to test the performance of acoustic communications methods. The location and experiment were *not* chosen or designed to measure spreading exponents.

As one component of the overall KAM11 experiment, a ship towed a transmitter and recordings were made on fixed-location receivers. Among the transmitted signals were channel-characterization signals, from which the received impulse responses as a function of range can be estimated. From

the impulse response estimates, the coherent and incoherent energies can be estimated as function of range, similar to the approach in the first sections of this chapter.

We first describe the source tows and the environment, then the processing methods, the results, and finally potential physical explanations of the results along with suggestions for potential future work. The addition energy loss beyond what is generally expected from spreading loss is currently unexplained, though scattering losses from surface and bottom reflections may be a potential explanation.

2.6.1 Description of Source Tows and Environment

Of the source tow datasets collected during KAM11, three of them had roughly linear ship's tracks at a constant depth (approximately 100 m), and transmitted channel-characterization signals. (Other source tows had circular tracks, had varying water depths, or transmitted acoustic communications test packets rather than channel-characterization signals.)

Those three source tow datasets were conducted on Julian Days JD180, JD189, and JD190 (June 29, July 8, and July 9, 2011, respectively). There were two sets of two receive arrays each, deployed by the Woods Hole Oceanographic Institution (WHOI) and the Scripps Institution of Oceanography. Our results in this chapter are from the two WHOI receive arrays, called "SYS3" and "SYS4". The SYS3 and SYS4 arrays were separated by about 4 km, roughly along the direction of the source tow tracks. The results from the JD180 dataset are not presented, because the receive arrays were deployed high in the watercolumn (15 m depth) and had low signal-to-noise ratios (SNR). The receivers were re-deployed at 45 m depth for datasets JD189 and JD190, resulting in higher SNR. The tows lasted approximately 1.5 to 2 hours each, and the ranges from source to receivers spanned approximately 500 m to 12 km.The nominal source depth was 50 m. The source tow tracks are shown in Figure 2.14, and follow the 100 m constant-depth bathymetry contour. The waterdepth increases rapidly to the west of the track, and decreases to about 50 m depth within 1 km-2 km east of the track. At the longer ranges, the shallow bottom to the east may be partially shadowing receptions at SYS4.

The receive array element spacing were 5 cm and 20 cm for SYS3 and SYS4 respectively, and so the total array lengths were 1.2 m and 4.8 m. Our data analysis uses one channel at the center of each of the receive arrays (channel 12 of 24). If receive energies are statistically independent among the different channels, using multiple channels would improve our energy estimate statistics. The main uncertainty in the exponent estimates, however, is not due to energy variations at a particular range, but rather what appear to be large-scale environmental variations in time and/or range. Therefore, it is unlikely that analyzing multiple channels would improve the estimates of the spreading exponents.

During each source tow, transmissions were made in multiple frequency bands, a low-frequency band centered at 5.5 kHz with approximately 4 kHz of bandwidth, and a mid-frequency band centered at approximately 16.5 kHz with nominally 8 kHz of bandwidth. Absorption loss (and scattering loss) increases with frequency, so to focus on measuring spreading loss rather than absorption loss, we analyzed data from the low-frequency band. Some of transmitted waveforms in the mid-frequency band had spectra which extended into the low-frequency band, requiring filtering to prevent contamination of the estimates of noise energy and incoherent energy.

Figure 2.15 shows example soundspeed profiles during the experiment [57]. The soundspeed profiles vary in both time and space, changing the acoustic propagation characteristics. Typical features of the soundspeed profiles are a surface mixed layer of roughly uniform soundspeed down to depths of roughly 20 m to 40 m, with soundspeed decreasing in the cooler bottom water. Rays propagating in this environment will refract downwards towards the soundspeed minimum, resulting in increased scattering losses from reflections from the seafloor at longer ranges.

The RMS surface wave height[2] was roughly 70 cm-100 cm during the source tows. The wave periods were about 5-7 seconds, which is relatively short, leading to relatively steep waves [57]. The acoustic wavelength at 5.5 kHz center frequency, with a measured soundspeed at the surface of roughly 1537 m/s, is about 28 cm. The RMS surface wave heights are significantly larger than

[2] "Significant" wave height is the standard oceanographic measure, and is what is provided in the trip report. RMS wave height is approximately 1.4 times less than significant wave height.

the acoustic wavelength, and so the surface is acoustically rough at these frequencies [75]. Surface reflections will on average experience relatively large scattering losses.

It is important to note that the experiment location, with its challenging environmental conditions, was selected to provide a proving ground for acoustic communications methods. It was not selected for the purpose of studying spreading exponents. Spreading exponents are an average measure in both time and space, and the single set of realizations from each source tow, and only two source tows complicated the estimation of spreading exponents in this variable environment.

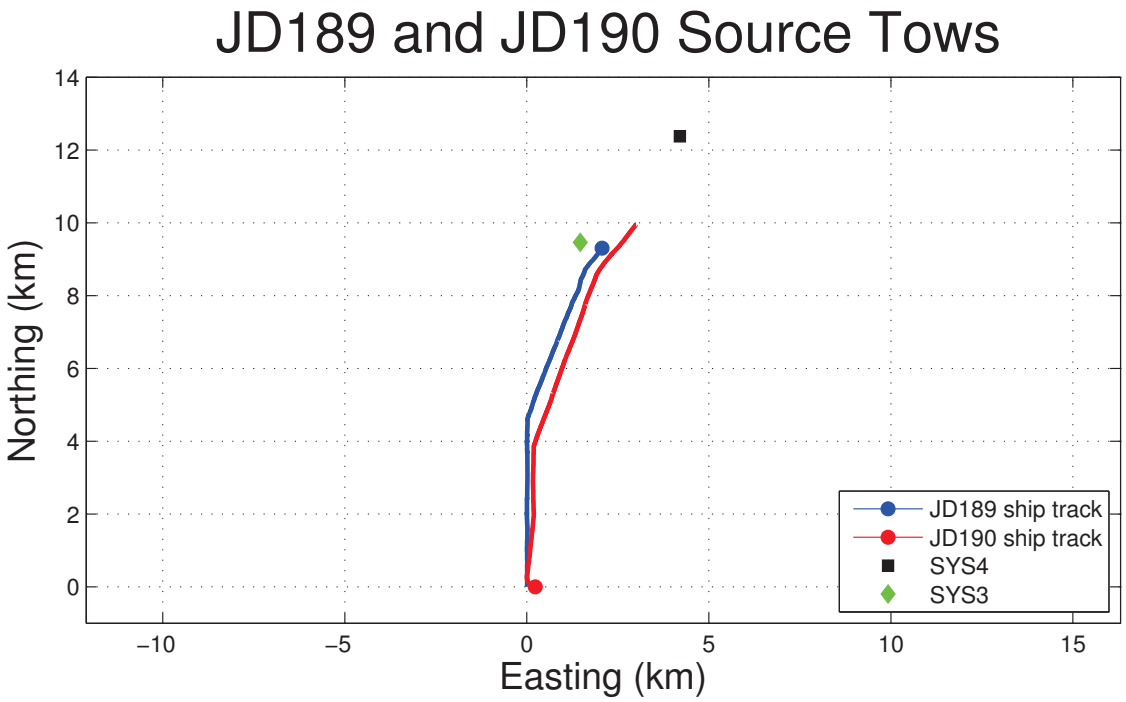

Figure 2.14. Source tow tracks for JD189 and JD190, showing receivers SYS3 and SYS4. The start of each track is shown with a dot. The tracks were about 10 km long, with ranges to SYS3 of about 500 m to 9 km, and ranges to SYS4 of about 4 km to 13 km. The tracks follow the 100 m bathymetry (depth) contour. The nominal source depth was 50 m. The water depth drops to 50 m about 1 km-2 km east of the tracks.

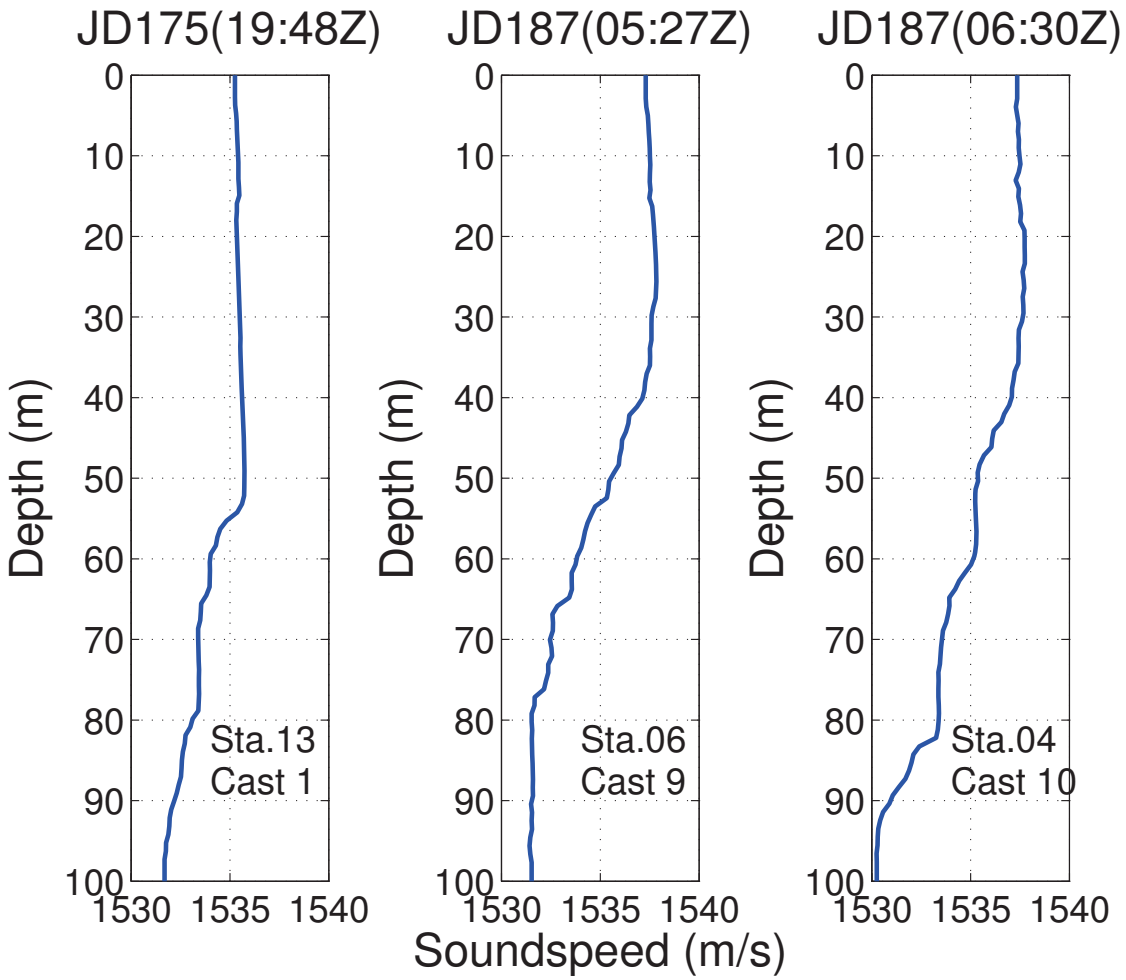

Figure 2.15. Soundspeed profiles from KAM11, showing spatial and temporal variation. There is a mixed surface layer of approximately uniform soundspeed down to about 20 m-50 m depth, with decreasing soundspeed in the deeper colder water. Rays refract toward lower soundspeeds, so this is a downward-refracting environment, refracting rays towards the bottom. The soundspeed profile cast numbers and geo-spatial station location are noted on the plots. The center and right-hand plots are taken about an hour apart, at Stations 4 and 6, which are separated by just over 1 km [57].

2.6.2 Processing Methods

Estimating spreading exponents requires three steps: (1) estimating the range; (2) estimating the received coherent, incoherent, and noise energies; and (3) fitting the spreading model to estimate the spreading exponent. Steps 1 and 2 are detailed in this section, and Step 3 in Section 3.5.4, on Results.

2.6.2.1 Estimating Range

Estimating the range is straightforward. The ship's GPS location during the source tows was recorded, and the GPS locations of the receive arrays were also. The range estimates were taken to be the distance between the ship and each receiver, averaged from the distance at the start and end of each minute-long recording. The ship moved at typical speeds of about 1.6 m/s to 1.8 m/s, or on the order of 100 m during each minute. The range estimate was not corrected for the length of the cable towing the source, which will either slightly increase or decrease the range estimate based on whether the ship was moving towards or away from the receivers.

2.6.2.2 Estimating Received Energy: Coherent, Incoherent, and Noise

In each minute of the experiment, a signal was transmitted from the towed source, and the received signal was recorded on the fixed receivers, segmented into one-minute files. Each transmitted signal was active for approximately 53 seconds out of the minute, followed by approximately six seconds of silence, allowing a propagation delay corresponding to about 9 km of range.

For estimating the received energy, two types of channel-characterization signals were used. One type was linear frequency-modulated (LFM) sweeps, and the other type was maximal-length pseudorandom sequences (MLS) [100]. The center frequency for both signal types was 5.5 kHz. The individual LFM sweeps were 48 ms long, with 4 kHz bandwidth around the center frequency. The sweep repetition period was 144 ms, resulting in a transmit duty cycle of 1/3. The MLS signals had a sequence length of 4095 chips[3] and a chip rate of 2.778 kHz. Each ML sequence had a length

[3]At baseband prior to modulation, ML sequences are composed of pulses with amplitude +1 or -1. A chip is a single pulse of the sequence after modulation.

of 1.4742 seconds, and the sequences were transmitted continuously back-to-back, resulting in a transmit duty cycle of 1.

The original sampling rate was 39.063 kHz=10 MHz/256, derived from the 10 MHz output of an atomic clock, to eliminate clock drift. The MLS signals were transmitted with 36 samples per chip at 100 kHz sampling rate. To end up with an integer number of samples per chip, the recorded signals were resampled to $f_s = 25$ kHz. To keep the processing consistent between LFM and MLS, the LFM signals were also resampled to 25 kHz, although this is not strictly required.

On Julian Day JD189, only MLS signals were transmitted, whereas on JD190 (and JD180), the transmissions alternated between six minutes of LFM signals and six minutes of MLS signals.

The processing steps are summarized here, and detailed below. Summarizing the steps, the signals are Doppler-corrected, demodulated to baseband (zero frequency), and low-pass filtered. The coherent energy estimates are made from the peak energy (magnitude-squared) of the matched-filter output. For the MLS signals, with a duty cycle of 1, incoherent energy and noise estimates are made from the mean energy of the low-pass filtered baseband signals in the signal and noise regions of the recording, respectively. For the LFM signals, with a duty-cycle of 1/3, the incoherent energy estimates are made from the mean of the matched-filter output energy over the manually selected delay spread. The LFM noise energy estimate is also made from the mean of the matched-filter output energy. The MLS and LFM matched filters are normalized to have unity gain, to allow merging of results from the MLS and LFM datasets, as well as directly comparing the coherent, incoherent, and noise energy estimates.

Since the signal and noise are uncorrelated, the incoherent energy estimate is corrected for noise by subtracting the noise energy estimate. Similarly, the coherent energy estimate is also corrected for noise by subtracting the noise energy, but the matched-filter processing gain means that the noise correction is less significant for the coherent energy estimates. The noise energy estimate is not made at the same instant in time as the initial incoherent and coherent energy estimates, but the estimates are made within the same minute-long recording, so the noise energy is likely relatively constant during that time. Obvious impulsive noise spikes were avoided in the manual selection process of the regions for estimating noise and incoherent energy.

The noise-corrected coherent and incoherent energy are then corrected for absorption loss at the center frequency, $f_c = 5.5$ kHz, using Thorp's expression [12]. At 5.5 kHz, Thorp's expression predicts an absorption loss of 0.44 dB/km. (The high end of the band, at 7.5 kHz, has a predicted absorption loss of 0.72 dB/km, while the low end of the band, at 3.5 kHz, has a predicted absorption loss of 0.24 dB/km.)

2.6.3 Detailed Processing Steps

The coherent energy estimates are intended to model the energy received in a matched-filter detector when detecting a packet. A matched-filter detector is a correlator of the expected "replica" signal and the received signal plus noise. For the KAM11 experiment, the expected signal is either an LFM sweep or a subsequence of the ML sequence. The coherent energy estimate is taken to be the peak energy (magnitude-squared) of the matched-filter output. To relate the KAM11 energy estimates and the Bellhop and RAM energy estimates from earlier in this chapter, it is useful to note that the output of a matched filter is an estimate of the channel's impulse response, so the peak of the matched filter output is a measure of the peak of the impulse response.

The matched filter's maximum processing gain for the LFM sweeps is the time-bandwidth product, or nominally about 46 dB. For the ML sequences, the matched filter's maximum processing gain would be equal to the sequence length if the full sequence were used as the replica, or about 72 dB. The matched filter output of an ML sequence is very sensitive to uncorrected Doppler shifts, however, as described by ambiguity function analysis [127]. The Doppler sensitivity increases with sequence length. The MLS signals therefore need to be corrected for their Doppler shifts prior to applying the matched-filter. (In contrast, ambiguity function analysis shows that the matched filter output of an LFM signal is very tolerant of uncorrected Doppler shifts, though the LFM signals were Doppler-corrected anyway to both keep the MLS and LFM processing steps similar, but also to make manual selection of the box bounding the first arrivals on the time-delay plot easier. On a Doppler-corrected signal, the bounding box is a rectangle on the time-delay plot, rather than a general parallelogram.)

The Doppler correction is done iteratively, starting with an initial estimate of the range rate, $\beta = v/c$, either from the previous recording's final Doppler estimate, if one exists, or from the ship's GPS track. Typical tow speeds were on the order of $v = 1.5$ m/s with a soundspeed of roughly 1500 m/s, for a range-rate of order $\beta = 1e-3$. The iteration stopped when the arrival delays on the time-delay plot were approximately constant in time.

With the final estimate of the relative Doppler shift, $(1+\beta)$, the original passband files were resampled with a relative resampling rate of $(1+\beta)$, and demodulated to bring the Doppler-shifted center frequency $f_c(1+\beta)$ to baseband (zero frequency) at the new sampling rate of $f_s(1+\beta)$. A low-pass filter was then applied at baseband with a total bandwidth of 4 kHz, prior to matched filtering and energy estimation. Initially, we used a Gaussian low-pass filter to avoid introducing time-domain sidelobes into the signal. There was contamination from the mid-frequency band, however, with an example shown in Figure 2.16. We therefore sharpened the low-pass filter's frequency cutoff using a 512-tap filter generated using Matlab's `fir1()` function, with a cutoff frequency of 2 kHz, which had a peak-to-sidelobe ratio of 18 dB. For a given low-pass filter, the peak-to-sidelobe ratio will be fixed, and the coherent energy spreading exponent estimate will not be affected.

After Doppler correction, we had typical residual uncorrected Doppler range-rates of about $\beta_{\text{residual}} = 1\text{e}-4$, due to slight variations in transmitter tow speed from instant to instant. The residual range-rate limits the MLS matched filter length. We used an MLS matched-filter length of 600 chips, determined empirically by finding the filter length beyond which processing gain did not significantly improve for many recordings. Some, but not all, recordings benefitted from longer filter lengths. The autocorrelation properties of ML sequences are changed dramatically when using a partial subsequence, and so the matched filter had a peak-to-sidelobe ratio, or effective processing gain, of only about 20 dB.

Despite the limited MLS processing gain, for JD189, MLS files were successfully processed at all the source tow ranges for which files were recorded, out to nearly 13 km. For JD190 SYS4, the low MLS processing gain appeared to have been a limiting factor beyond about 7 km in range, since no receptions were identified beyond that range. With the LFM signal's tolerance for uncorrected

Doppler errors and higher effective processing gain, a few LFM signals were identified and processed beyond 7 km for JD190 SYS4 (two successful measurements at about 9 km and one at about 11 km). Even for the LFM signals, most of the potential receptions beyond 7 km range were not detected or processed.

Alternate MLS processing approaches, such as estimating the impulse response with a recursive-least-squares filter, or tracking and correcting Doppler throughout each recording, could be employed, but aside from the missed MLS signals on JD190, SYS4 at long ranges, the MLS processing gain was not a limiting factor in estimating coherent energy. Fewer missed signals at long ranges would lead to improved spreading exponent estimates.

After the matched filter was applied, the first (and strongest) arrivals were selected manually with a rectangle on a time-delay plot, as shown in Figures 2.17 and 2.18. At each time index in the time-delay plot, there is an impulse response estimate along the delay axis. The maximum energy along the delay axis, within the selected rectangle, was taken to be the coherent energy estimate for the impulse response estimate at that particular time. The rectangle on the time-delay plot constrains the coherent energy estimate to be made at a delay close to the main arrival, which is especially helpful at low SNRs to reduce the likelihood that the maximum energy value is from a noise spike rather than the actual signal. For the LFM signals, there were about 360 impulse response estimates in the 53-second signal, and for the MLS signals, there were about 36 impulse response estimates in the signal. Each of the 360 or 36 coherent energy estimates is saved to allow full statistical characterization.

The LFM signals have their incoherent and noise energies also estimated from the matched-filtered output on a time-delay plot, shown in Figures 2.17 and 2.18. The delay spread (the delay extent from the first arrival to the last arrival considered) is manually selected as a rectangle in time-delay. Depending upon the range, the typical delay spreads go from order 100 ms at close ranges to order 10 ms at long ranges and low SNRs. The incoherent energy estimate is taken to be the mean energy over the delay spread for each impulse response estimate, again generating about 360 or about 36 estimates of incoherent energy for LFM and MLS signals, respectively. Again, all of these estimates are saved for statistical characterization. The noise region is manually selected

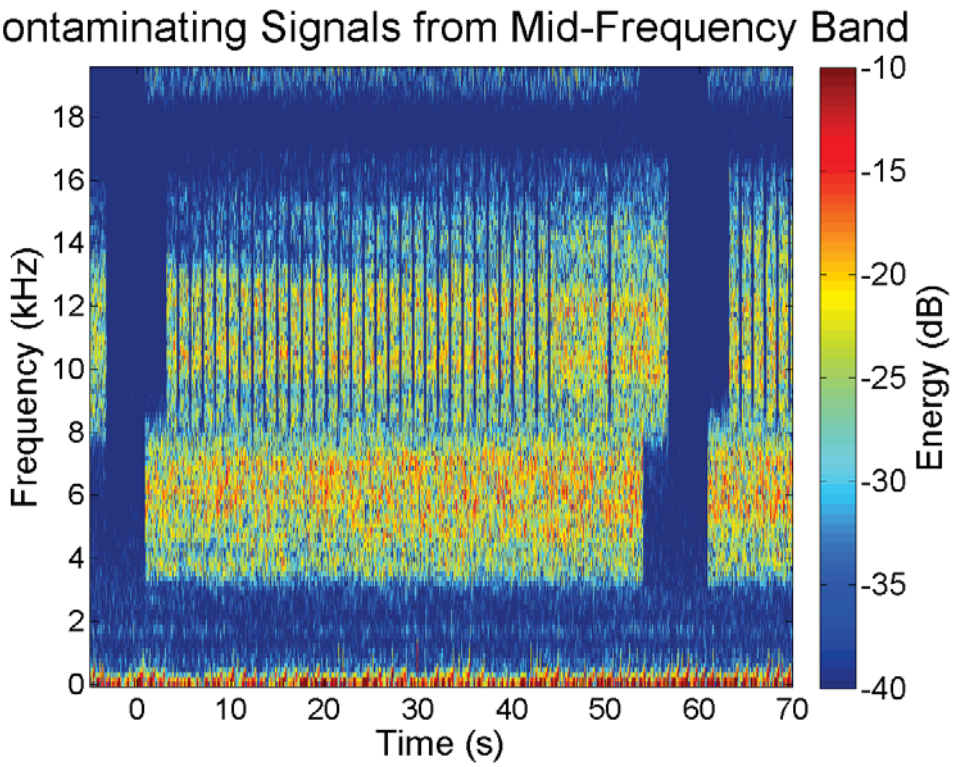

Figure 2.16. Spectrogram showing interference from the mid-frequency band with the low-frequency band of interest. The mid-frequency energy will corrupt the incoherent and noise energy estimates. The two signals have different propagation delays because they are transmitted from different sources. The longer propagation delay pushes the interfering signal into the noise energy estimate region. This spectrogram is made at the original sampling rate of 39 kHz, prior to re-sampling. The low-frequency signal is an MLS signal. The energy scale is in dB relative to the maximum. The recording file plotted is 1890152F0064_C0_S3, channel 12.

from the periods before and/or after the transmitted signal. The noise energy estimate is the mean energy over all the individual samples within the noise region, which can be on the order of 105 samples. All of the individual noise energies (in this case, samples) are saved for statistical characterization.

For the MLS signals, the incoherent and noise energy were estimated directly from the low-pass-filtered baseband signal prior to matched-filtering. The start and end of the received signal, as well as noise regions before and after the packet, were selected manually using a one-dimensional time series plot of the matched filtered output, shown in Figure 2.19. The processing gain of the matched

filter allowed more reliable selection of the signal and noise regions than working from the baseband signal directly. Both the matched-filter and low-pass filter operations were corrected for the filter's group delay, so the signal and noise time indices selected on the matched filter output could be applied directly to the low-pass-filtered baseband signal, which is where the MLS incoherent energy and noise energy estimates were actually made. The MLS incoherent and noise energy estimates are the mean energy (magnitude-squared) of the low-pass-filtered baseband signal during the signal region and noise region, respectively. All of the individual incoherent energies and noise energies (again individual samples) are saved for statistical characterization. Since the MLS incoherent energy estimates are made from on the order of a million samples, and the LFM incoherent energy estimates are made from on the order of 36 to 360 samples (which each are already averages of hundreds to thousands of individual samples), the statistical dispersion of the MLS estimates is much higher than that of the LFM estimates. We discuss this issue further below.

2.6.4 Results

In this section, we first characterize the statistical distributions and statistical dispersion of the energy estimates. Next, we present the estimates of the spreading exponents. Finally, we discuss possible physical explanations for the observations.

Briefly summarizing the results, there is relatively high statistical dispersion in the dataset, particularly in the estimates of incoherent energy and noise energy. The fundamental issue, however, is not the variance of the underlying energy estimates or the robustness of the fits, but that during significant portions of the experiment, the acoustic propagation was more complex than a simple model governed by an energy-loss exponent. The non-uniform and downward-refracting sound-speed profile, combined with scattering losses from the boundaries and a dynamic time-varying environment, lead to a complex propagation environment non well-suited to a simple energy-loss model.

During the periods of the experiment in which a simple energy-loss exponent model was approximated, the exponent estimates are large, over 2.0, and inconsistent with the "practical spreading"

model of $k = 1.5$. The overall energy-loss exponent is a measure of the combination of spreading loss as well as scattering losses.

2.6.4.1 Statistical Characterization of Energy Estimates

Figures 2.21-2.23 show the statistics of the energy estimates for the six low-level datasets: JD190, receivers SYS3 and SYS4 (both LFM and MLS), and JD189, receivers SYS3 and SYS4 (MLS only). The coherent, incoherent, and noise energy estimates are plotted as green, red, and black boxplots, respectively. Even with this first look at the energy estimates, it is clear that there are particular regions and/or times in each low-level dataset where the energy estimates do not decrease with range, and so the propagation for that time and location does not conform to a simple spreading model.

Boxplots succinctly show the median, the central fifty percentiles, "whiskers" showing the extreme values of the distribution, and outliers beyond the whiskers. The central box of the boxplot points shows the middle two quartiles, with the median plotted as a circle. The definition of whiskers is not standardized; in the boxplots shown here, the lower and upper whiskers extend to the 1st percentile value and the 99th percentile value. Outliers beyond the whiskers are plotted with dots. The boxplots are shown without exponent fits, noise correction, or absorption correction, to show the distribution and dispersion of the underlying energy estimates more clearly.

The coherent and incoherent energy estimates from JD189, SYS3 and SYS4 vary weakly with range. For example, for JD189,SYS3, the coherent energy estimate at 600 m is less than the coherent energy estimate at about 2.5 km. For JD189,SYS4, the coherent energy estimate at about 4.5 km is about the same as it is at about 9 km, and the coherent energy estimate increases with range from about 8.5 km to 9 km, rather than decreasing with range as one would expect from a simple spreading exponent model. There is a gap in the JD189,SYS3 files from about 4 km to 5 km due to 12 minutes of ambient noise recordings once every two hours, with no transmissions occurring. There is a large gap in the JD189,SYS4 files from about 4.5 km to about 8.5 km due to recordings missing from the original dataset. Similarly, the JD189,SYS3 files beyond about 5 km (out to about 9 km) are missing from the original dataset.

The JD190 results are closer to following a simple spreading model. (In the plots, note that for JD190, the transmitted signal alternates between MLS and LFM every six minutes.) The energy estimates are generally decreasing with increasing range, though there are places where the energy estimates increase with increasing range, for example from about 2.5 km to 3.5 km on SYS3, and at multiples ranges on SYS4, in particular around 5 km. The JD190,SYS3,LFM plot also shows the transmitter passing close to SYS3, closing from about 1 km, passing within about 700 m of SYS3, and moving away; this is shown in overhead plan view in Figure 2.14, the plot of the source tow track. The two energy estimates at roughly the same ranges (but different bearings) are fairly similar, matching to within about 3 dB (for example, the energy estimates below about 1.5 km on SYS3,LFM, at about 1.5 km on SYS3,MLS). The JD190,SYS4,MLS data only extends to about 7 km because the more distant MLS arrivals on that day could not be identified, due to the limited MLS processing gain combined with propagation conditions.

In the boxplots in Figures 2.21-2.23, the quartiles and whiskers are calculated differently for the different types of energy estimates. The coherent energy and the LFM incoherent energy estimates are calculated as the maximum and mean energy in the impulse responses over the observed delay spread, resulting in about 360 estimates for LFM or about 36 estimates for MLS. The boxplot median, quartiles, whiskers, and outliers are calculated directly from all of these estimates from a given one-minute recording. The MLS noise energy and MLS incoherent energy estimates, however, are calculated as mean energies in the low-pass-filtered baseband signal, and the LFM noise energy is calculated as the mean energy in the matched-filter output. With this approach, there are tens of thousands, to over a million, energy samples underlying each of the mean energy estimates. The energy among all the individual samples in these signals can vary by multiple orders of magnitude, leading to very high statistical dispersion and an overly busy boxplot which is difficult to visualize.

To make the boxplots easier to visualize and to let patterns be revealed from the data, we smooth the noise energy for both MLS and LFM, as well as the incoherent estimates for MLS. We selected smoothing time constants of 20 samples at 25 kHz. This time constant was selected in part to model the frequency response of the matched filters. The baseband matched filters have

approximately a low-pass frequency response, with -3 dB points of about 1200 Hz for LFM and approximately 1300 Hz for MLS, or about 20 samples at 25 kHz in either case.

In the boxplots shown in Figures 2.21-2.23, the noise energy and the MLS incoherent energy are segmented into non-overlapping chunks of the characteristic smoothing times, and the boxplot shows the statistics for the means of the segments rather than the statistics of the individual samples. The overall energy means are unchanged, but the variance and number of outliers are significantly reduced, while physically approximating the response of the matched filter to noise.

The vertical axis plots energy on a log scale rather than the more commonly used decibels, i.e., $10 \log_{10}(\text{energy})$. The spreading exponents are estimated directly from the slope of a log-log plot of energy versus range. For more straightforward comparison with the log-log plots in the next section, the boxplots use a simple log scale on the vertical axis rather than decibels.

For all but the shortest ranges in the source tows, there is significant overlap between the propagation paths from the transmitter to receivers SYS3 and SYS4. In general, the energy measurements made at SYS3 and SYS4 at a given time will likely have some correlation due to the overlapping propagation paths. Because of the 4 km displacement between SYS3 and SYS4, an energy measurement made at a given range on SYS3 will be measured at the same time as a SYS4 measurement at a range which is about 4 km larger.

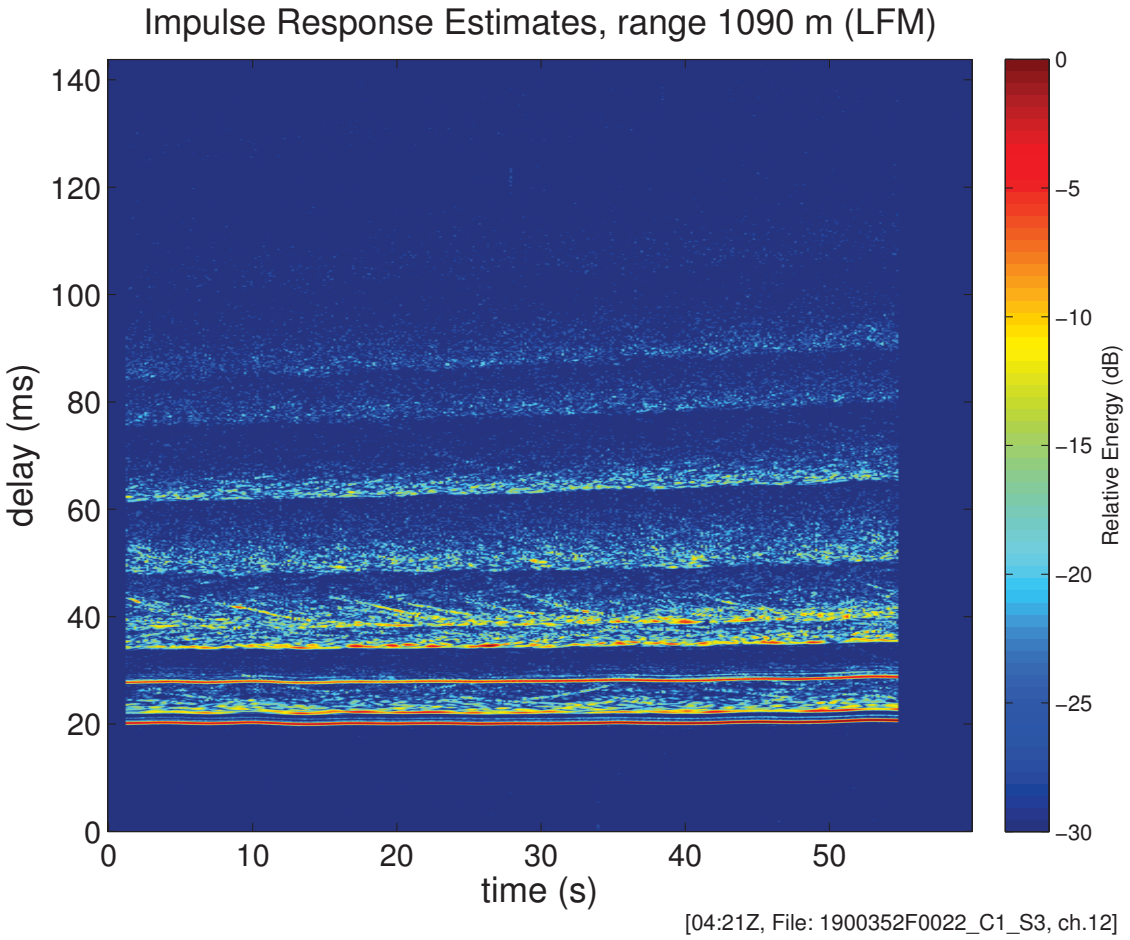

Figure 2.17. A time-delay plot of LFM impulse responses, in a close-range, high-SNR situation. The impulse responses have been Doppler-corrected, so the arrivals are at nearly fixed delays. Figure 2.18 on the next page plots the same data, and is overlaid with the manually-selected energy estimation regions for the coherent, incoherent, and noise estimates. Both plots are relatively large so that the overlaid regions are more readily visible.

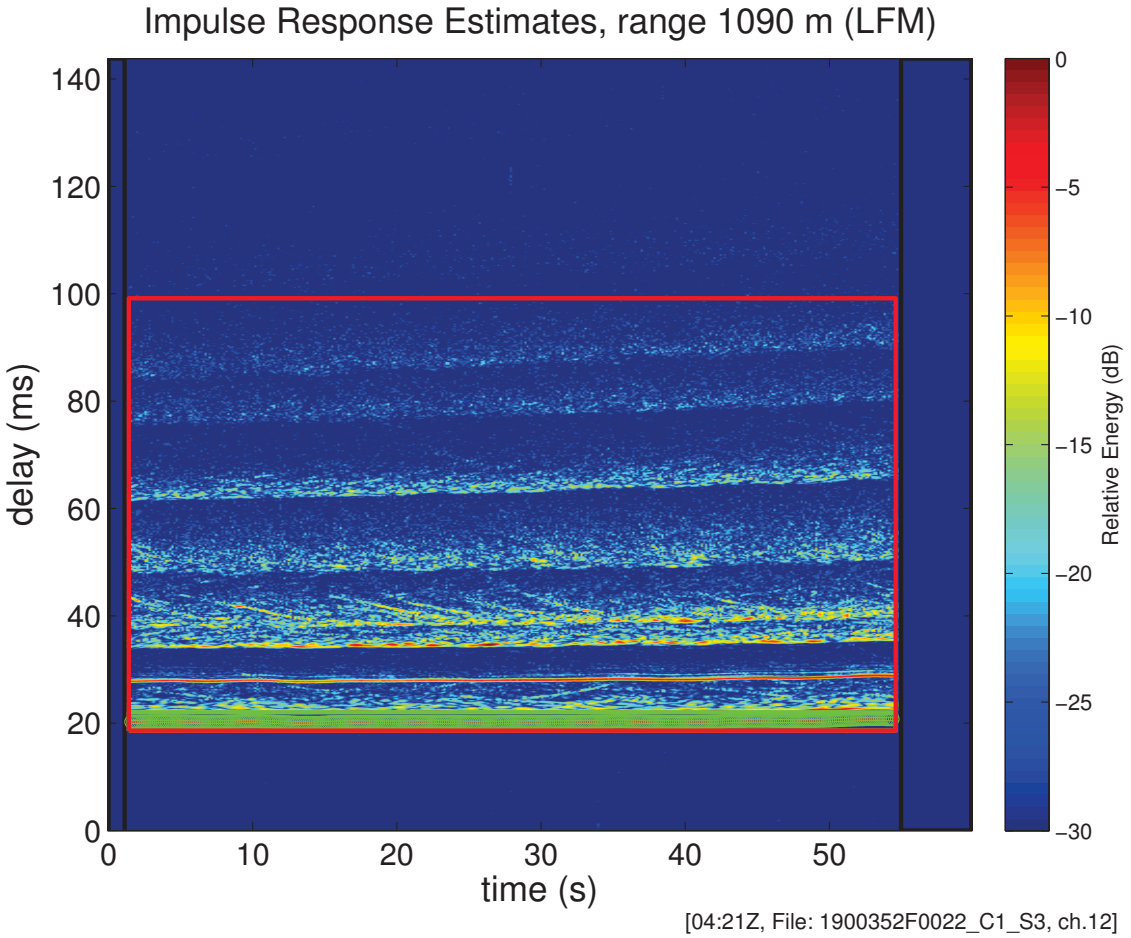

Figure 2.18. A time-delay plot overlaid with the manually-selected energy estimation regions. Figure 2.17 on the previous page displays the same data without the overlays, for comparison. The red rectangle selects the delay spread over which the incoherent LFM energy is estimated, with one estimate for each impulse response (each vertical slice). The small green rectangle at the first arrivals (delay of around 20 ms) is the region over which coherent energy is estimated; the green circles show the locations of maximum energy in the green rectangle, which are the coherent energy estimates. The black rectangles on the left and right, just before and after the transmitted signals, are the regions where the mean noise energy is calculated.

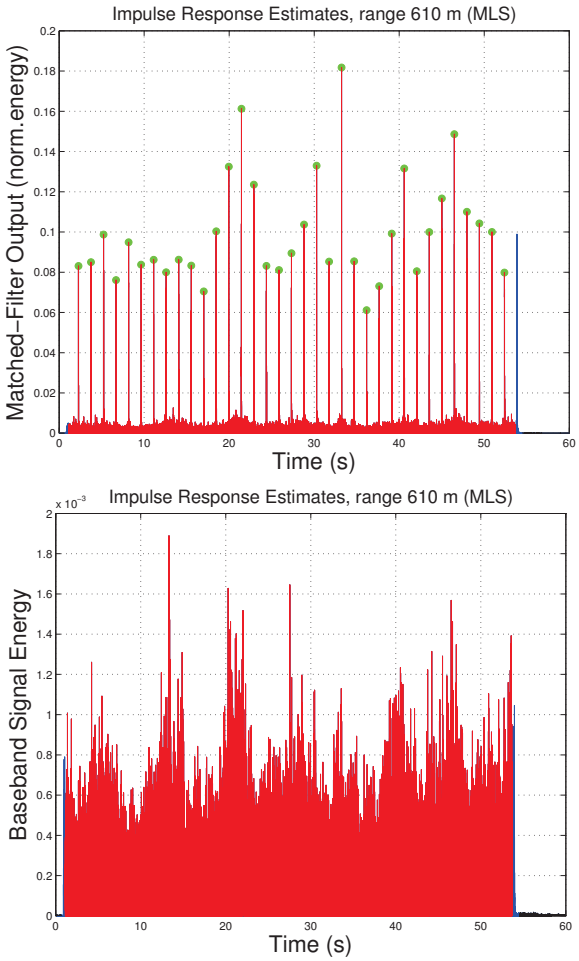

Figure 2.19. For the MLS signals, the regions for the incoherent energy estimate and the noise energy estimate were selected manually from a one-dimensional timeseries of the matched-filter output, shown in the upper plot. The green circles show the coherent energy estimates, which were calculated from the time-delay plot, but here have had their time indices converted to display as a timeseries. The start and end of the signal are manually selected for the incoherent energy estimate region (shown in red), and the noise energy region, shown in black is selected before and/or after the received signal. The blue buffer regions are not included in either estimate, and allow for more conservative selection of what region is signal and what is noise, especially in low-SNR situations where the distinction between signal and noise regions is less obvious. The lower plot shows the baseband signal energy with the incoherent energy region (red), the noise region (black), and the buffer regions (blue). The matched filter output is corrected for the filter's group delay so that the same time indices can be used for the baseband signal. The corresponding time-delay plot is shown in Figure 2.20.

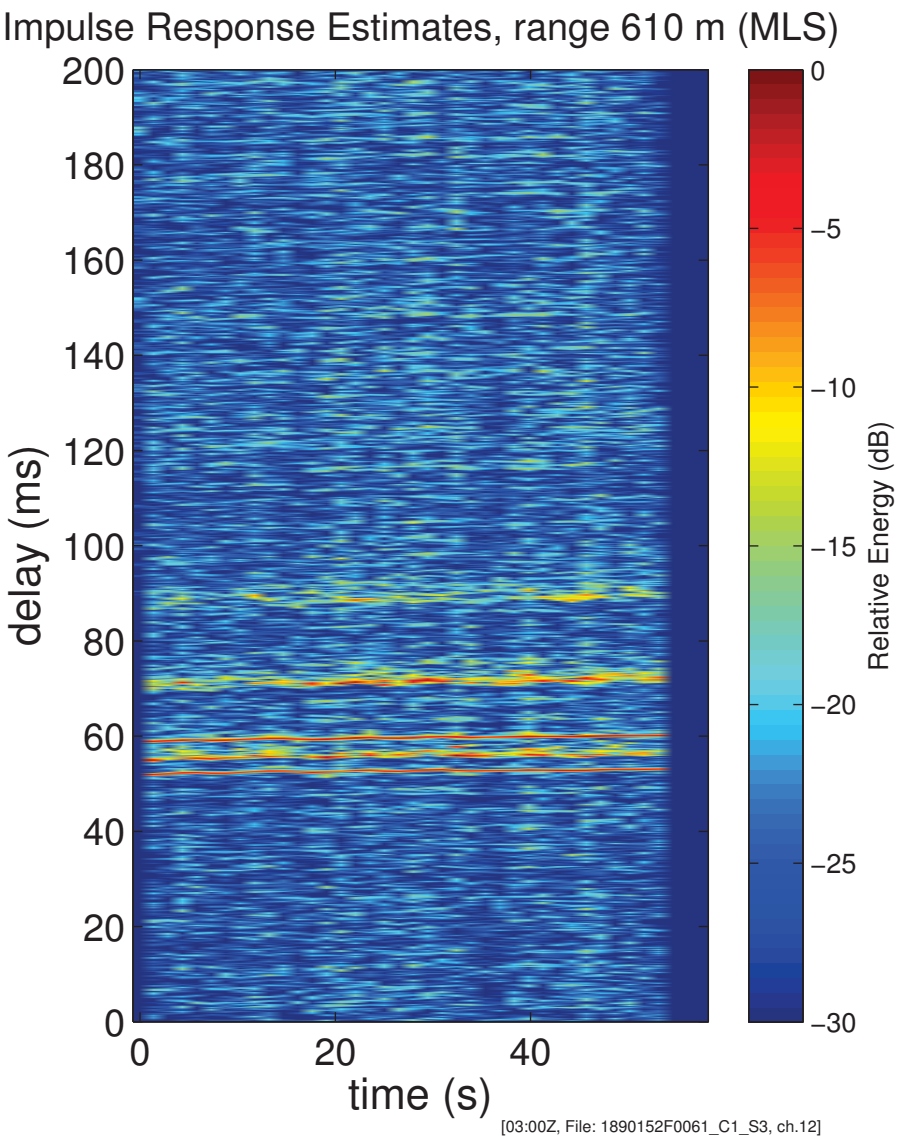

Figure 2.20. For the MLS signals, the coherent energy estimate was selected in the same way as for the LFM signals: the maximum energy within a rectangle manually selected on the time-delay plot (rectangle not shown on time-delay plot above). The regions for the incoherent energy estimate and the noise energy estimate are shown in Figure 2.19. The modest MLS processing gain is evident in the time-delay plot, though in most cases the MLS processing gain is not the limiting factor. The MLS signals have a repetition period of 1.4742 s, so the time resolution on the time-delay plot is much coarser than with the LFM signals with their 144 ms repetition rate.

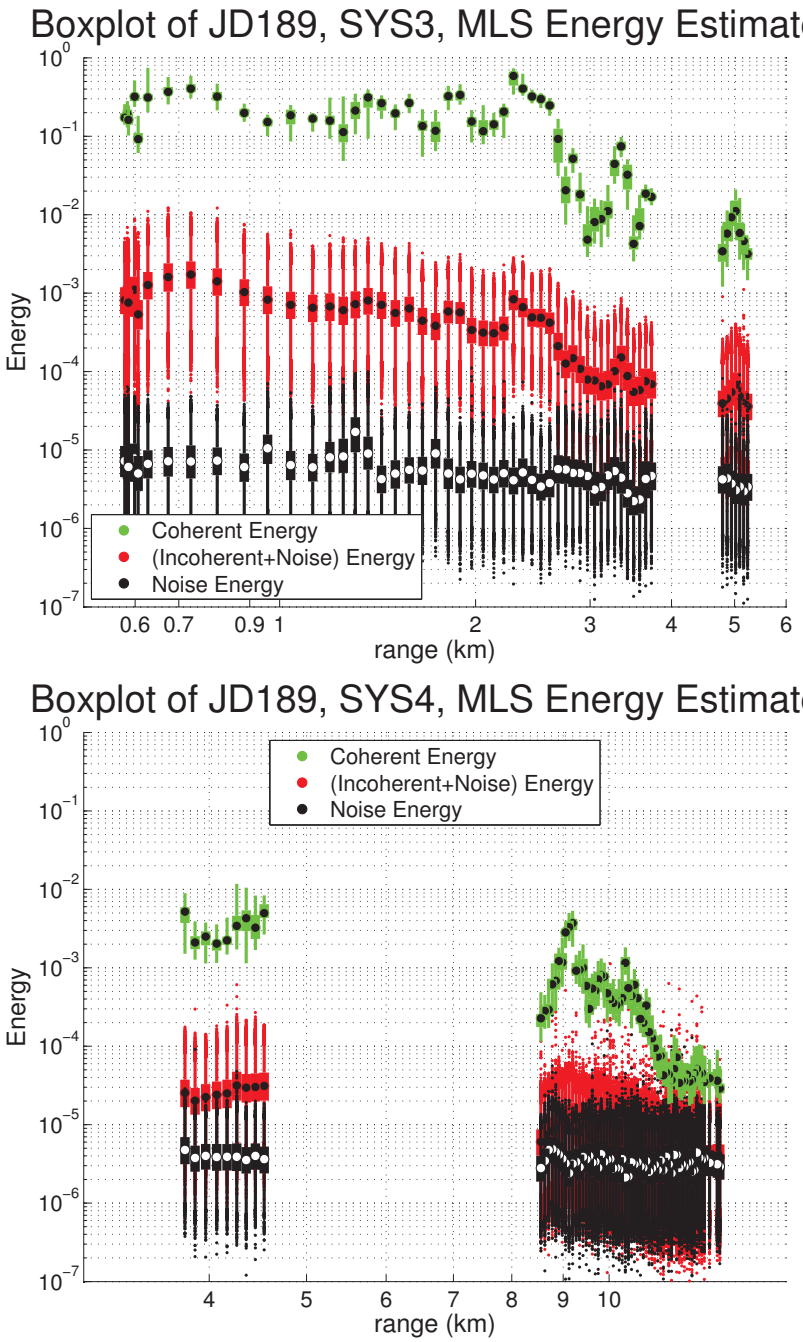

Figure 2.21. Boxplots showing the statistical distribution of the JD189 SYS3 energy estimates, from MLS signals. The coherent energy estimates are only weakly range-dependent.

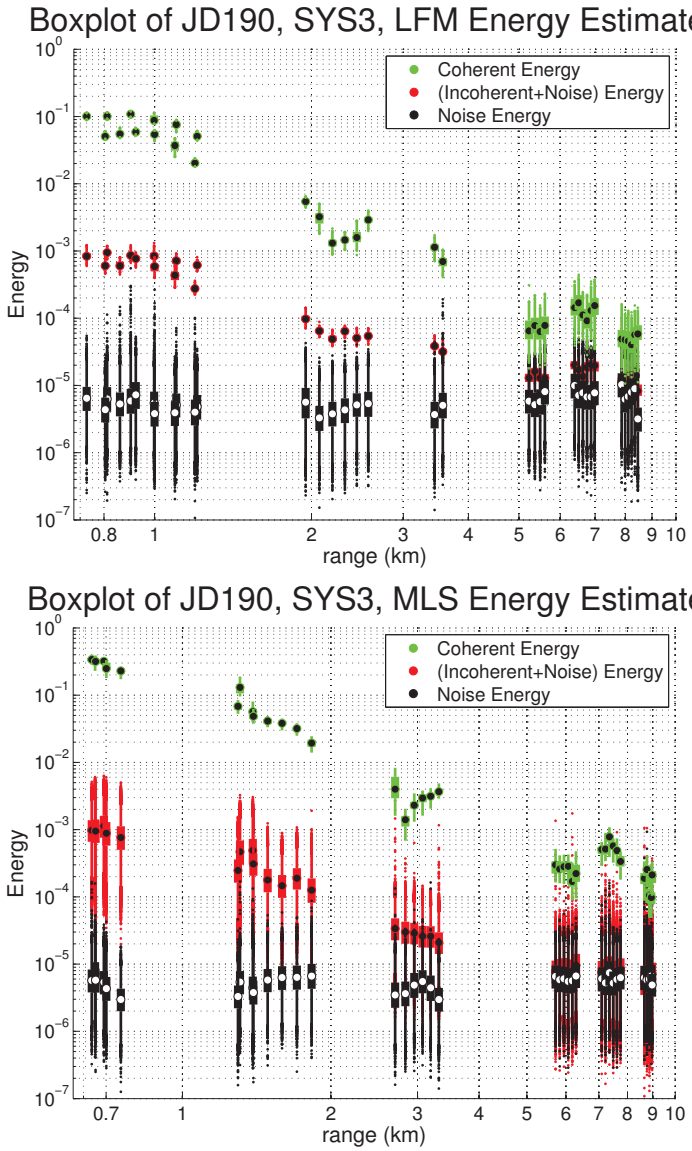

Figure 2.22. Boxplots showing the statistical distribution of the JD190, SYS3 energy estimates, from both LFM and MLS signals. The transmitter passed within about 600 m of SYS3, shown with the two sets of (range,energy) measurements below about 1.5 km with the LFM signals, and around 1.5 km with the MLS signals. For these particular repeated ranges, the repeatability of the coherent energy estimate is within several dB. The difference in the statistical dispersions of the LFM and MLS incoherent energy estimates is due to the number of samples averaged in each, and is discussed further in the text. The energy increases with range in a couple of places, most notably at around 2.5 km-3.5 km, again indicating more complex acoustic propagation than a simple spreading model.

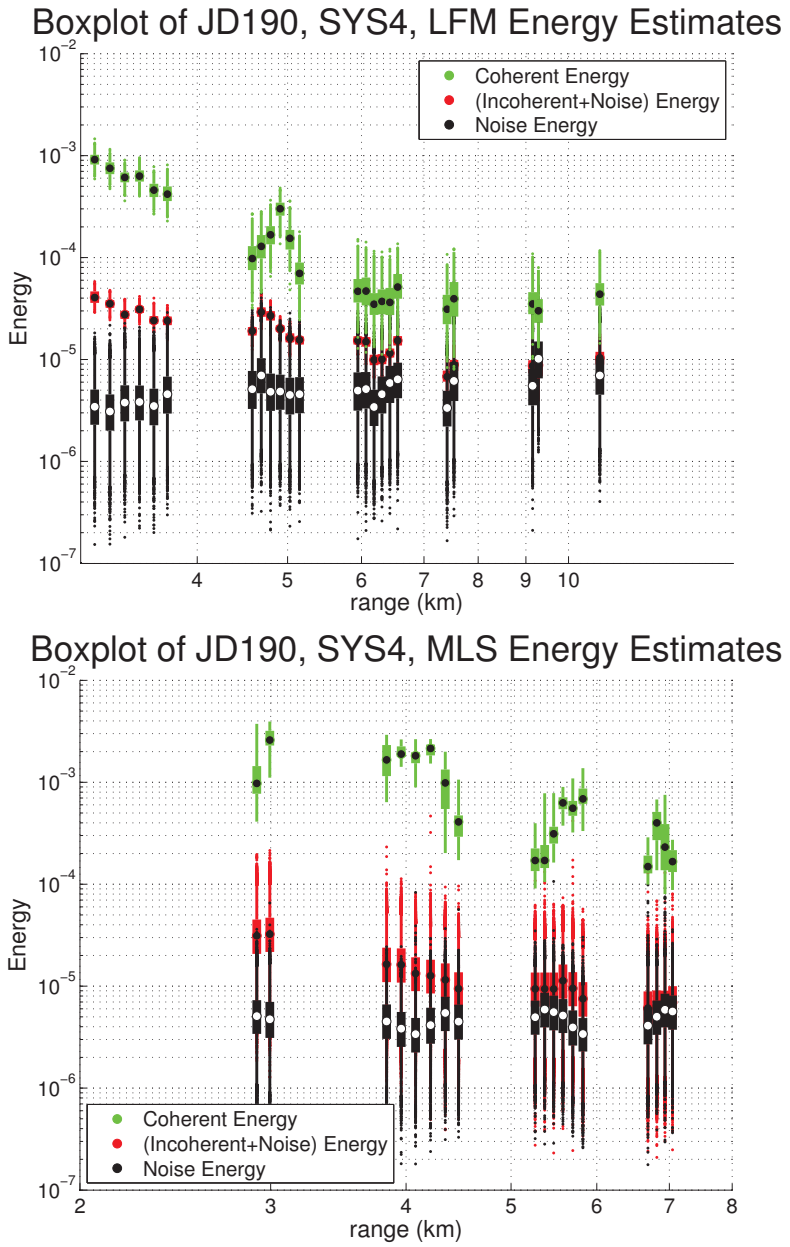

Figure 2.23. Boxplots showing the statistical distribution of the JD190,SYS4 energy estimates, from both LFM and MLS signals. In multiple places, the energy estimates increase with increasing range, for example around 5km with both the MLS and LFM signals, again indicating more complex acoustic propagation than a simple spreading model. Note the difference in incoherent energy statistical dispersion between LFM and MLS, due to the averaging of the LFM method.

2.6.4.2 Estimation of Spreading Exponents

Spreading exponents are an average measure, most useful for system design, including design and analysis of network protocols. At any specific period in time or region in space, the physics of the acoustic propagation may not cleanly follow a simple spreading-loss or energy-loss model. For example, the discussion of statistical characterization in the previous section identified several regions of the low-level datasets where the propagation clearly does not reduce to a simple model described by an energy-loss exponent. In those cases, estimating a value for the spreading exponent would not be physically meaningful. As the energy-versus-range dataset includes more samples, however, becoming a longer-term temporal and broader-scale spatial average, the environmental fluctuations should start to average out, and an estimate of a spreading loss exponent, or more generally the energy-loss exponent, can be attempted.

The six low-level datasets are JD189 SYS3 MLS and SYS4 MLS, and JD190, SYS3 MLS and LFM, and JD190, SYS4 MLS and LFM. From the statistical characterization of the low-level datasets, it appears that the environmental conditions were significantly different between JD189 and JD190, and that the acoustic propagation during JD189 in particular was not following a simple spreading exponent model. Of the two source tows, we focus first on the JD190 dataset, which appears to be closer to following a simple energy-loss exponent model. For completeness, we present plots of all five of the combined datasets, namely JD189 combined (SYS3 and SYS4) in Figure 2.24, with residuals characterized in Appendix D, Figure D.1; JD190,SYS3 (LFM and MLS) in Figure 2.25, with residuals in Figure D.2; JD190,SYS4 (LFM and MLS) in Figure 2.26, with residuals in Figure D.3; JD190 combined (SYS3 and SYS4) in Figure 2.27, with residuals in Figure D.4; and all data in Figure 2.28, with residuals in Figure D.5. We also tabulate all of the exponent estimates, including those for all six of the individual low-level datasets, in Table 2.1.

In the plots of energy-versus-range data and the fitted lines, the incoherent and coherent energy estimates have been corrected first for noise, and then for absorption loss. The fits are on log-log plots of energy versus range, and the estimates of the spreading exponents, k, are the slopes of the fitted lines, with the model $\log_{10}(E) = -k \log_{10}(r) + b$. There are two fits shown for each of the types of energy, one using unweighted linear least-squares estimation (LLSE) and the other using

Dataset	k_{coh} (unw)	R^2 (c)	k_{inc} (unw)	R^2 (i)	k_{noise} (unw)	R^2 (n)	N
All	2.6 ± 0.3	0.71	2.1 ± 0.2	0.86	0.2 ± 0.1	0.19	237
JD190, all	3.0 ± 0.3	0.87	2.3 ± 0.2	0.93	-0.1 ± 0.1	0.06	114
JD189, all	2.7 ± 0.3	0.82	2.1 ± 0.2	0.91	0.3 ± 0.1	0.62	123
JD190, SYS3	2.8 ± 0.3	0.90	2.3 ± 0.2	0.95	-0.1 ± 0.1	0.14	73
JD190, SYS4	2.9 ± 1.2	0.51	2.2 ± 1.0	0.65	-0.4 ± 0.3	0.29	41
JD190, SYS3 LFM	3.0 ± 0.3	0.96	2.2 ± 0.3	0.93	-0.1 ± 0.2	0.18	36
JD190, SYS3 MLS	2.7 ± 0.3	0.95	2.3 ± 0.2	0.97	-0.1 ± 0.1	0.11	37
JD190, SYS4 LFM	2.6 ± 1.2	0.76	2.3 ± 1.4	0.68	-0.5 ± 0.4	0.42	23
JD190, SYS4 MLS	2.4 ± 1.5	0.57	2.4 ± 0.6	0.90	-0.1 ± 0.5	0.05	18
JD189, SYS3 MLS	1.5 ± 0.6	0.50	1.4 ± 0.3	0.77	0.4 ± 0.2	0.48	55
JD189, SYS4 MLS	3.0 ± 1.0	0.50	2.1 ± 0.5	0.66	0.2 ± 0.2	0.17	68
Dataset	k_{coh} (w)	R^2 (c)	k_{inc} (w)	R^2 (i)	k_{noise} (w)	R^2 (n)	N
All	2.1 ± 0.3	0.67	2.1 ± 0.2	0.67	0.2 ± 0.1	0.19	237
JD190, all	2.2 ± 0.3	0.86	2.2 ± 0.2	0.92	-0.1 ± 0.1	0.06	114
JD189, all	2.5 ± 0.4	0.79	1.3 ± 0.3	0.51	0.3 ± 0.1	0.62	123
JD190, SYS3	2.6 ± 0.3	0.89	2.3 ± 0.3	0.95	-0.1 ± 0.1	0.14	73
JD190, SYS4	2.3 ± 1.3	0.43	1.6 ± 0.5	0.37	-0.4 ± 0.3	0.29	41
JD190, SYS3 LFM	3.0 ± 0.4	0.96	2.3 ± 0.3	0.93	-0.2 ± 0.1	0.18	36
JD190, SYS3 MLS	2.6 ± 0.2	0.95	2.0 ± 0.4	0.91	-0.1 ± 0.1	0.11	37
JD190, SYS4 LFM	3.1 ± 1.0	0.73	1.6 ± 0.4	0.57	-0.5 ± 0.4	0.42	23
JD190, SYS4 MLS	3.1 ± 1.4	0.46	2.5 ± 0.5	0.89	-0.1 ± 0.4	0.05	18
JD189, SYS3 MLS	0.9 ± 0.7	0.29	1.2 ± 0.4	0.73	0.4 ± 0.1	0.48	55
JD189, SYS4 MLS	2.7 ± 1.8	0.48	1.5 ± 0.5	0.44	0.2 ± 0.1	0.17	68

Table 2.1. Estimated exponents for all datasets, for unweighted (unw) and weighted (w) LLSE fits to the coherent (c), incoherent (i), and noise (n) energy-loss exponents. For the margins of error, 99% confidence intervals are used. The R^2 value and number of points N for the fits is also shown. The upper portion of the table gives data for the unweighted fits, and the lower portion of the table gives data for the weighted fits.

weighted LLSE. The markers on the plots indicate which of the low-level datasets a particular measurement came from. The errorbars are the standard deviations of the energy estimates, which appear asymmetric about the mean when plotted on a log-log plot.

2.6.4.2.1 Weights For weighted LLSE, the weights are typically the inverses of the (sample) variance for the values being fit, in which case the estimator is the best linear unbiased estimator of the parameters. Since we are fitting the slope of a log-log plot, rather than a linear-scale plot, we use $1/\mathrm{var}(\log_{10}(\mathrm{energy}))$ as the weights. Using the inverse of the variances of the energies themselves as the weights would effectively discard all of the short-range measurements, where the variances in energy are large simply because the energy is large, but where the relative size of the residuals is small. The weights are then normalized so that the largest weight is unity, so that weighted and unweighted residuals can be compared more easily.

2.6.4.2.2 Residuals For the weighted LLSE fit, the residual plots display unweighted rather than weighted residuals. The reasoning is that weighted LLSE will produce a more robust estimate of the parameters in the case of non-equal variances, especially if the outliers have high variances, but weighting the reported residuals would make the fit appear better than it is. As would be expected, the distributions of weighted residuals (not shown), where each raw residual is scaled by its weight, are much more tightly peaked than the unweighted residuals are. Similarly, in the Table 1, the R^2 values, measuring the fraction of total data variation explained by the fit, are calculated from the unweighted residuals for both the weighted and unweighted fits [133]. Therefore R^2 for the weighted fits will always be smaller than R^2 for the unweighted fits. Using the weighted residuals to calculate R^2 would result in all of the weighted fits having R^2 values of essentially 1.0.

The noise should have no dependence upon range. Therefore fitting noise over as a function of range should give an ideal R^2 value of 0, rather than the usual 1, since the fit should explain none of the variance of the data.

2.6.4.2.3 Margins of Error The margins of error are calculated using 99% confidence intervals from a t-distribution with $(N-2)$ degrees of freedom (two model parameters are fit, the slope and

the intercept). For unweighted fits, there is an explicit formula for the standard error of the slope [24]:

$$\text{standard error of slope} = \frac{s}{\sqrt{\sum (x - m_x)^2}}.$$

In this formula, the unbiased estimator of the sample variance for the slope, s^2, is

$$s^2 = \frac{\sum (\text{residuals})^2}{N - 2},$$

and m_x is the mean of the horizontal-axis values (where the horizontal axis is $\log_{10}$(range) in this case).

For the weighted fits, the standard errors for the estimate of the slope were estimated by bootstrapping [26] the data: in each of $B = 200$ trials, there were N randomly-selected tuples of (range,energy,weight) selected with replacement from the original dataset, where N is the size of the original dataset. There was a weighted LLS estimate of the slope k made with each randomized trial. The sample standard deviation of the B randomized trials is then taken as the estimate of the standard error of the statistic in question, namely the standard error of the estimate of the slope. As a check of the bootstrapping method, its calculated margins of error for the case of unweighted LLSE matched the formula.

The confidence intervals were selected to be 99% rather than the typical 95% to increase the sizes of the reported margins of error; there are clearly large uncertainties in the fits.

2.6.4.2.4 Noise Exponent The noise energy exponent is a useful metric for assessing the quality of the data and the fit. The noise energy should have no range dependence; its estimated spreading exponent should be close to zero. The noise energy may have some variation in time, however, and since range and time are related in the source tow experiments, variations in the noise level in time that do not average out over the finite duration of the source tow could appear as a variation in range and result in a non-zero noise spreading exponent. In general, however, the noise spreading exponent estimate should be close to zero. For example, we increased the sharpness of the low-pass filter's frequency cutoff after observing non-zero noise spreading exponents due to contamination from signals in the mid-frequency band.

2.6.4.2.5 Discussion There are many issues with these fits. There are robust estimation techniques [73] that might handle outliers in the data better than LLS estimates do. The problems with the fits, however, do not necessarily have to do with rejecting spurious outliers, but instead appear to be more fundamental issues, and so at this point we do not need a more robust estimation method.

For example, there are the previously mentioned issues with JD189, both SYS3 and SYS4, where for much of the track, the energy does not decrease with range. An energy-loss exponent of zero is not physically meaningful, and likely the received energy at the closest ranges was suppressed due to propagation effects. These effects are real, however, and are not due to noisy measurements: The energy estimates in JD189 do not have especially high variances, and the noise exponent for JD189,SYS4 is fairly flat, $k_{\text{noise}} = 0.2 \pm 0.1$, and looks fine. The noise exponent for JD189,SYS3 has a stronger slope, $k_{\text{noise}} = 0.4 \pm 0.1$, but even a flat noise exponent would not make the JD189,SYS3 dataset usable on its own to estimate spreading exponents. There do not appear to be significant processing problems for JD189; it just appears to reflect more complex propagation effects than simple spreading loss. Furthermore, the propagation effects are clearly time-varying, because the source tows of JD189 and JD190 followed nearly identical tracks, one day apart in time, and the energy-versus-range plots are very different.

In JD190, SYS4 (MLS and LFM), however, the noise energy has a relatively strong range dependence, $k_{\text{noise}} = -0.5 \pm 0.4$, suggesting that signal energy may be contaminating the noise estimates, or possibly there is a time-varying noise level near that receiver. JD190, SYS4 is the receiver which had long-range signal detection problems, mentioned previously when discussing MLS processing gain. There are only a few LFM signals which were detected beyond 7 km range, and no MLS signals detected beyond that range. The handful of low-SNR measurements from long range may be skewing the estimates. When the noise correction is done on the incoherent energy estimate, if the corrected incoherent energy becomes negative, we could either drop that data point or set it to a tiny positive value. We have chosen to reset negative corrected energies to tiny positive values, with the reasoning that if the lowest values were dropped completely, the energy estimates

at long ranges (low SNRs) would be skewed even higher, since only the highest-energy points would be retained.

In the combined dataset of JD190, SYS4 LFM and MLS, there is also a clear pattern of the MLS signals having systematically higher coherent estimates than the LFM signals. JD190, SYS3 also appears to have a slight systematic effect of the MLS coherent energy estimates are higher than the LFM coherent energy estimates, but the effect is much less pronounced, even though the processing steps are identical to JD190,SYS4. The pattern appears to be reversed with the JD190,SYS4 incoherent energy estimates, where the LFM incoherent energies appear to have a systematic effect of being higher than the MLS energies. JD190,SYS3 may have LFM incoherent energies systematically very slightly higher than MLS incoherent energies, but again the effect is much weaker than with JD190,SYS4, even though the processing steps are the same. The noise energy exponent in JD190 SYS3 appears to be fine, $k_{\text{noise}} = -0.1 \pm 0.1$.

Potential future work with the JD190 datasets would include re-checking the noise energy on SYS4, to see if there is contamination from another transmitter or another band, or if the region selected to estimate the noise energy inadvertently includes some of the signal. In addition, there may be a normalization mismatch in combining the MLS and LFM coherent energy estimates, although it is unclear why the effect would be more pronounced on JD190,SYS4 than on JD190,SYS3. The long-range MLS and LFM signals on JD190,SYS4 could perhaps be reprocessed, or perhaps dropped if their SNR is too low to make them reliable. Finally, there is the previously mentioned difference in variance between the two different methods used to calculate the MLS and LFM incoherent energy, which will weight the LFM incoherent energy estimates much more strongly than the MLS estimates when using weighted LLSE. On this last point, however, there do not appear to be any processing problems with the JD190, SYS3 incoherent energy fits, and the weighted and unweighted incoherent exponent estimates are very similar for that receiver.

Of the six low-level datasets, the two JD189 datasets appear to have complex propagation effects that do not fit the simple spreading exponent model. JD189 does have two regions where an energy-loss exponent would appear to hold, but neither makes physical sense as a spreading loss. The first region, from 600 m to 2.5 km, has no measured energy loss. Physically, there must be

spreading loss from 600 m to 2.5 km, but perhaps the propagation was such that at the shortest ranges, the received energy level was suppressed. The second region, from 2.5 km to 11 km, would have an energy-loss exponent of approximately 5.0. In Section 2.6.5, we present results showing that energy-loss exponents of order 5 can occur from bottom scattering losses when propagating in the bottom duct, as further explained in that section.

The two JD190,SYS4 datasets definitely have low SNR at long ranges, may have processing issues, and either have a time-varying noise level or have their noise estimates contaminated by signal energy.

The remaining two datasets, JD190,SYS3 give weighted LLSE estimates of $k_{\text{coh}} = 2.6 \pm 0.3$ ($R^2 = 0.89$) for the coherent exponent, $k_{\text{inc}} = 2.3 \pm 0.3$ ($R^2 = 0.95$) for the incoherent exponent, and a fairly flat noise exponent, $k_{\text{noise}} = -0.1 \pm 0.1$. With a waterdepth of 100 m and a signal bandwidth of 4 kHz, the hypothesized incoherent transition range will be of order 100 m, and the hypothesized coherent transition range will be of order 13 km, using the results from Section 2.3.3. The energy-versus-range data from JD190,SYS3 spans about 600 m to about 9 km. No transition ranges were observed, and the hypothesized transition ranges were outside the region spanned by the data. The estimates were not robust enough to allow bandwidth reduction below the 4 kHz bandwidth. Therefore, neither the existence nor the depth- and bandwidth-dependence of the hypothesized transition ranges could be validated experimentally.

Ideally, all of the datasets with no processing problems should be combined into the spreading exponent estimates, since the spreading exponent should be an average measure over time, depth, and range. With so few datasets, however, we are not combining JD189 with JD190,SYS3, because JD189 clearly has more complex propagation physics for which a spreading exponent is not meaningful.

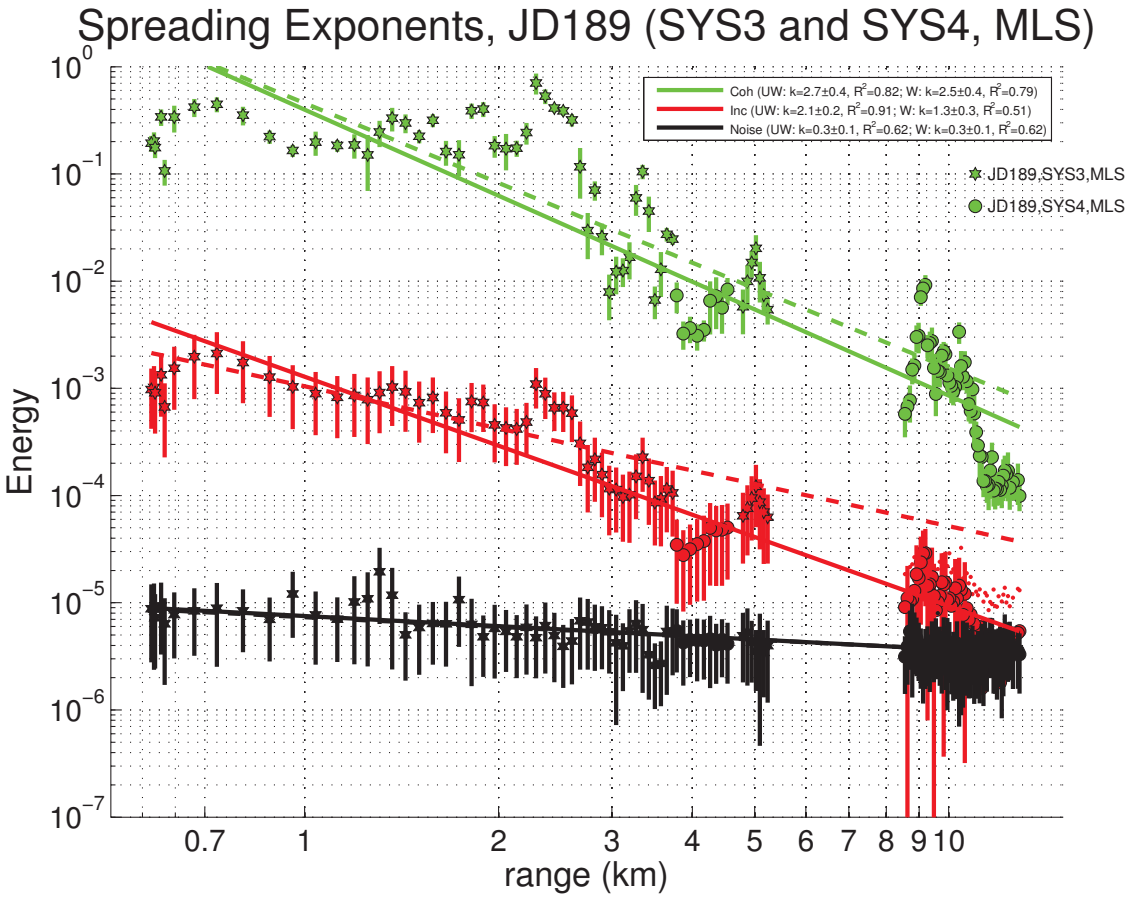

Figure 2.24. Energy-versus-range data (corrected for noise, then absorption) for JD189. Energy barely drops with range from 600 m to 2.5 km, implying a spreading exponent of zero in that region, which is not physically meaningful, followed by a energy-loss exponent of 5.0 from 2.5 km to 11 km. The errorbars are the standard deviations of the energy estimates, with the MLS incoherent and noise estimates averaged in blocks of the matched filter's characteristic "smoothing time" described in the text, to reduce their variances. Unweighted LLSE fits are plotted with solid lines, and weighted fits with dashed lines. Confidence intervals are 99% to maximize reported margins of error. Residuals are plotted in Appendix D, Figure D.1.

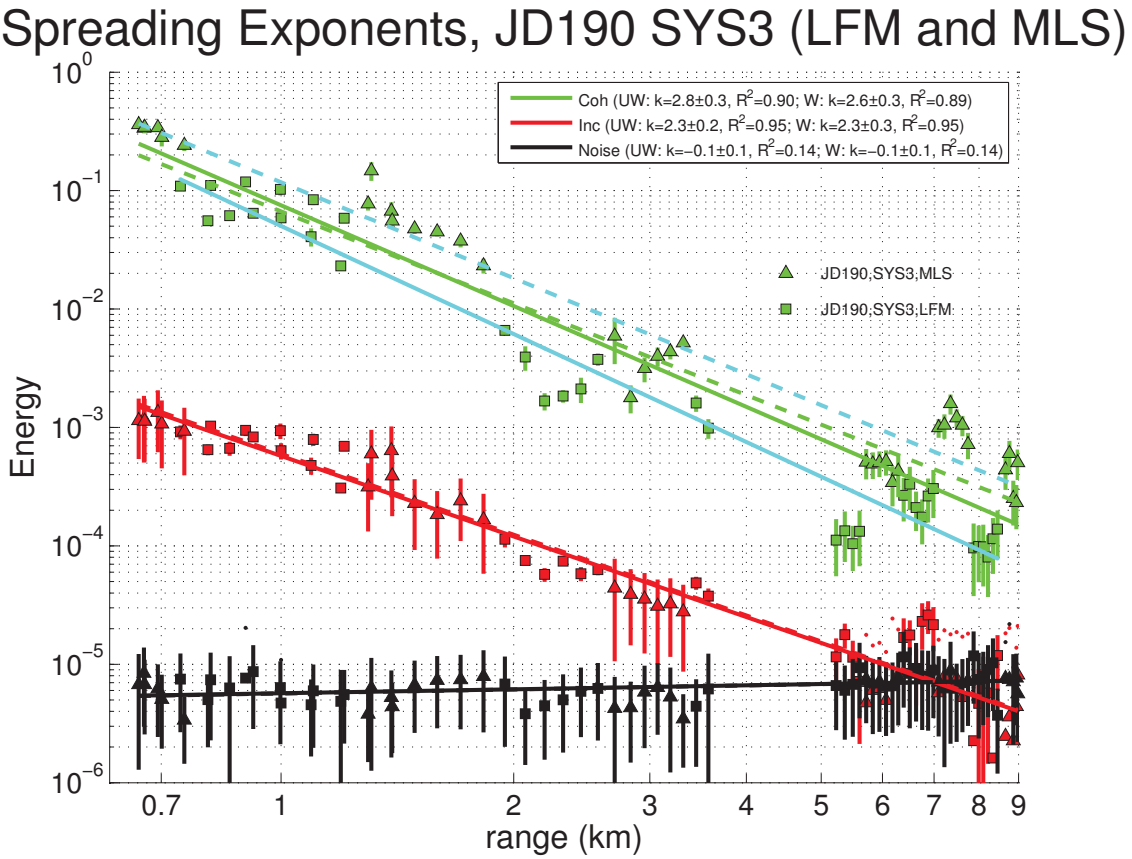

Figure 2.25. Energy-versus-range data (corrected for noise, then absorption) for JD190,SYS3. There appears to be a systematic effect where the coherent energy estimates are larger for the MLS signals than they are for LFM signals, but the effect is not as pronounced here as it is with JD190,SYS4. The variances of the incoherent energy estimates for LFM are significantly smaller than they are for MLS, as discussed in the text. The unweighted coherent-energy fit for MLS signals is plotted as a dashed cyan line, $k_c = 2.7 \pm 0.3$, and for LFM signals as a solid cyan line, $k_c = 3.0 \pm 0.3$, both within the margin of error of the overall fit. The errorbars are standard deviations, with the MLS incoherent and noise estimates averaged in blocks of the matched filter's characteristic "smoothing time" described in the text, to reduce their variances. Unweighted LLSE fits are plotted with solid lines, and weighted fits with dashed lines. Confidence intervals are 99% to maximize reported margins of error. Residuals are plotted in Appendix D, Figure D.2.

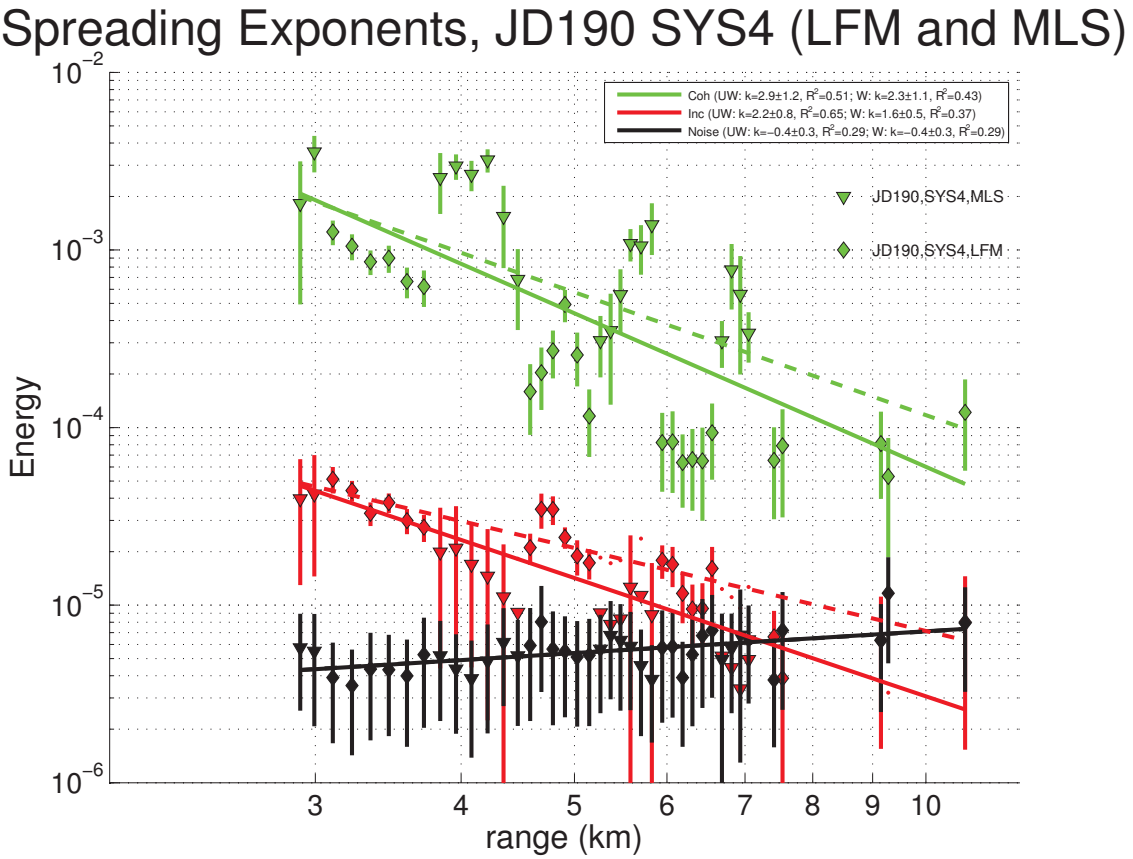

Figure 2.26. Energy-versus-range data (corrected for noise, then absorption) for JD190,SYS4. The noise exponent is not near zero, suggesting possible contamination. There appears to be a strong systematic effect where the coherent energy estimates are larger for the MLS signals than they are for LFM signals, much more pronounced here than with JD190,SYS3. The opposite effect appears to occur with the incoherent energies, with energies lower for MLS than LFM, which is not visible with JD190,SYS3. The variances of the incoherent energy estimates for LFM are significantly smaller than they are for MLS, as discussed in the text. The errorbars are standard deviations, with the MLS incoherent and noise estimates averaged in blocks of the matched filter's characteristic "smoothing time" described in the text, to reduce their variances. Unweighted LLSE fits are plotted with solid lines, and weighted fits with dashed lines. Confidence intervals are 99% to maximize reported margins of error. Residuals are plotted in Appendix D, Figure D.3.

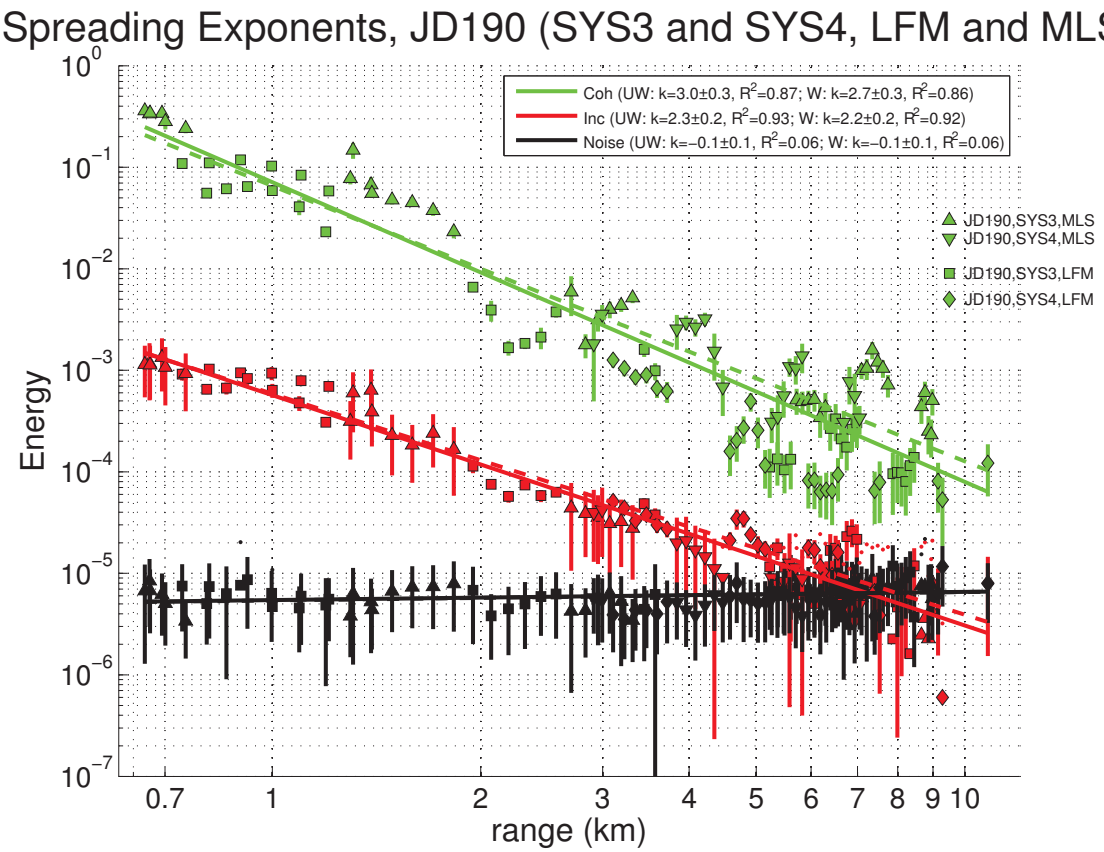

Figure 2.27. Energy-versus-range data (corrected for noise, then absorption) for JD190. The bad fits for JD190,SYS4 are somewhat obscured because JD190,SYS4 is mostly at larger ranges with higher variances. The variances of the incoherent energy estimates for LFM are significantly smaller than they are for MLS, as discussed in the text. The errorbars are standard deviations, with the MLS incoherent and noise estimates block-averaged in blocks of the matched filter "smoothing time" described in the text, to reduce their variances. Unweighted LLSE fits are plotted with solid lines, and weighted fits with dashed lines. Confidence intervals are 99% to maximize reported margins of error. Residuals are plotted in Appendix D, Figure D.4.

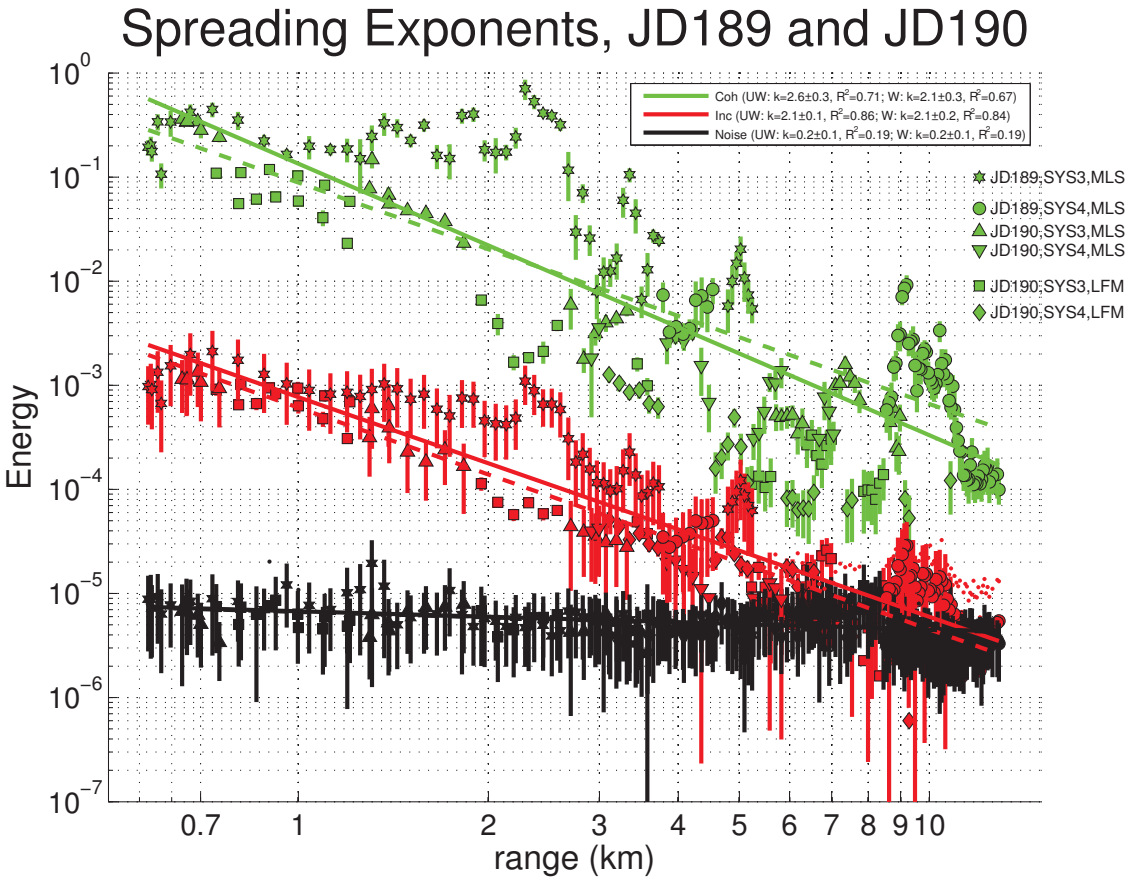

Figure 2.28. Energy-versus-range data (corrected for noise, then absorption) for both JD189 and JD190, all data. JD189,SYS3 is readily apparent, with its large excursions from a propagation model with a simple energy-loss exponent. The variances of the incoherent energy estimates for LFM are significantly smaller than they are for MLS, as discussed in the text. The incoherent data is tighter around the fitted lines than the coherent data is. The errorbars are standard deviations, with the MLS incoherent and noise estimates averaged in blocks of the matched filter's characteristic "smoothing time" described in the text, to reduce their variances. Unweighted LLSE fits are plotted with solid lines, and weighted fits with dashed lines. Confidence intervals are 99% to maximize reported margins of error. Residuals are plotted in Appendix D, Figure D.5.

2.6.5 KAM11 Modeling and Physical Explanations for Results

In this section, we model propagation the KAM11 environment to explain the qualitative features of the experimental results presented in the previous section. In particular, we address the difference between the JD189 and JD190 propagation and energy-loss exponent measurements, and suggest physical mechanisms explaining the results. Our model incorporates the KAM11 soundspeed profiles, surface and bottom scattering and reflection losses, and shows the qualitative propagation changes we can expect from internal waves.

2.6.5.1 KAM11 Soundspeed Profiles and Internal Waves

The most fundamental environmental component influencing acoustic propagation is the soundspeed profile. An example KAM11 soundspeed profile is shown in Figure 2.29, from JD187, two days before the JD189 source tow. Additional soundspeed profiles are shown in Figure 2.15, showing spatial and temporal variation.

The KAM11 soundspeed profile has several features to note. The upper portion of the watercolumn, from the surface down to about 50 m depth, has an approximately uniform soundspeed, and is called the *mixed layer*. Surface waves, usually driven by the wind, mix the water in the upper portion of the water column, homogenizing the temperature and creating an approximately uniform soundspeed profile. Below the surface mixed layer is a region of colder water where the soundspeed decreases due to decreasing temperature. Acoustic rays refract towards a soundspeed minimum, and in shallow water a soundspeed minimum at the bottom is sometimes called a *bottom duct*. A soundspeed profile such as the one shown in Figure 2.29 is called *downward-refracting*, and leads to increased bottom interactions as well as potential surface *shadow zones*, where rays from transmitters in the bottom duct do not propagate into the mixed layer. An additional feature to note, shown in the raytraces of Figure 2.30, is that in this downward-refracting environment, the direct path between the source and receiver is lost at a range of about 3-4 km, introducing additional scattering losses at all larger ranges.

The interface between the mixed layer and the bottom duct also is important for acoustic propagation in the KAM11 environment. The surface mixed layer consists of warmer, less dense

water, whereas the bottom duct consists of colder, denser water. Just as surface gravity waves propagate at the interface between two fluids of different densities — air and water — *internal waves* [49] propagate at the density interface between the mixed layer and the bottom duct. For internal waves, the difference in densities is relatively small, and so the gravitational restoring forces are much less than they are for surface gravity waves. The amplitudes, wavelengths, and periods of internal waves are therefore much larger than they are for surface gravity waves, on the order of ten or more meters for the amplitudes, hundreds of meters for the wavelengths, and tens of minutes for the periods of typical internal waves.

Internal waves can shift the depth of the interface between the mixed layer and bottom duct up or down, dramatically changing the propagation characteristics over relatively short temporal and spatial scales. Since the KAM11 transmitter and receiver depths (nominally 50 m and 45 m, respectively), are very close to the interface depth, even relatively small changes in the interface depth due to an internal wave can have strong effects on the received energy.

For example, the top two plots in Figure 2.30 show raytraces in the soundspeed profile of Figure 2.29, one with a transmitter at 50 m depth, and the other with a transmitter at 53 m depth, just above and just below the interface depth. Similarly, these plots could be thought of as an internal wave perturbing the interface depth such that the transmitter is just above or just below the interface depth. With the transmitter just above the interface depth at the bottom of the surface mixed layer (the plot at 50 m depth), the rays propagate throughout the watercolumn out to about 8-9 km in range, gradually losing energy to the boundary scattering losses. On the other hand, with the transmitter just below the interface depth at the top of the bottom duct (the plot at 53 m depth), there is ducted propagation near the bottom, and a surface shadow zone.

With the KAM11 transmitter and receiver very close to the interface depth, internal waves can have a very strong effect on the received energy level.

2.6.5.2 Modeled KAM11 Reflection Coefficients

The average surface reflection coefficient is modeled following Medwin and Clay [75]. The KAM11 Trip Report [57] gives RMS surface wave heights of about 70 cm to 100 cm on JD189

and JD190. The acoustic wavelength at 5.5 kHz is about 27 cm, leading to the average surface reflection coefficient plotted in Figure 2.31 as a function of grazing angle. The average surface reflection/scattering coefficient is strongly angle-dependent, and goes to zero for grazing angles above about 5°, due to the *acoustic roughness* of the surface. These modeled average surface reflection coefficients are heavily averaged and idealized. In reality, the surface scattering losses are highly variable.

The windspeed at KAM11 on JD189 and JD190 was variable, ranging from 3 m/s to about 15 m/s [57]. The prevailing wind and wave direction was from the northeast, which is essentially directly exposed to the North Pacific swell without being in the lee of any landmass. Therefore even in local low-wind conditions, there would be distantly generated swell roughening the surface.

The bottom reflection coefficients are calculated again following Medwin and Clay [75], using seafloor parameters from Vera et al. [129]. Vera et al. used geo-acoustic inversion methods to estimate the volcanic seafloor at the KAM11 site as having a soundspeed of 2200 m/s and density of 2.1 g/cm^3.

In addition, the seafloor directly under the source tow trackline is very steep, the edge of a Hawaiian volcano. Estimating the slope from the bathymetry charts in the KAM11 trip report [57], right under the trackline, the depth goes from 100 m to 200 m in about 600 m-700 m horizontally, sloping down to the northwest. Bottom reflections will therefore have some of their energy scattered out of plane, reducing the forward-scattered reflection coefficient. We model this additional loss with a crudely modeled roughness scattering loss of an additional 50% loss, independent of grazing angle.

The overall modeled bottom reflection/scattering coefficient is plotted in Figure 2.31 as a function of grazing angle.

2.6.5.3 Modeled KAM11 Energy versus Range

Figures 2.32 and 2.33 show modeled coherent and incoherent received energy in the KAM11 environment, using Bellhop raytracing.

In order to determine the independent effects of the non-uniform soundspeed profile and the lossy reflection coefficients, sets of raytracing runs were done with (1) uniform soundspeed profile and modeled KAM11 reflection coefficients, (2) KAM11 soundspeed profile and lossless reflection coefficients, and (3) KAM11 soundspeed profile and modeled KAM11 reflection coefficients.

With the uniform soundspeed profile and modeled KAM11 reflection coefficients, run (1) showed little qualitative change from the idealized raytracing runs presented in Section 2.4. The non-uniform soundspeed profile is therefore shown to be the most critical component of modeling the KAM11 environment.

To determine the role of the reflection coefficients, energy-versus-range plots with the results of runs (2) and (3) are shown in Figure 2.32. The results of run (2), with idealized lossless reflection coefficients, is the upper plot in Figure 2.32, and the estimates of the energy-loss exponents beyond ranges of about 500 m are $k_{\text{coh}} = 1.4 \pm 0.3$ and $k_{\text{inc}} = 0.6 \pm 0.1$, with 95% confidence intervals. These exponent values are smaller than, and inconsistent with, the measurements presented in Table 2.1. The results of run (3) the lower plot in Figure 2.32, and the estimates of the energy-loss exponents beyond ranges of about 500 m are $k_{\text{coh}} = 3.2 \pm 0.5$ and $k_{\text{inc}} = 2.4 \pm 0.2$, again with 95% confidence intervals.

Therefore *both* the non-uniform soundspeed profile *as well as* the lossy reflection coefficients are required to produce modeled results that are similar to the observed KAM11 field data.

Figure 2.33 plots the energy-versus-range for transmitter and receiver in the surface mixed layer (upper plot) and the bottom duct (lower plot). In lower plot, with the transmitter and receiver in the bottom duct, the estimates of the energy-loss exponents beyond ranges of about 1 km are $k_{\text{coh}} = 5.9 \pm 0.4$ and $k_{\text{inc}} = 5.8 \pm 0.4$, with 95% confidence intervals. These large energy-loss exponents are of similar magnitude to those beyond about 2.5 km range in the JD189 source tow. These results suggest that for the JD189 source tow, the interface depth was above the source and receiver, effectively putting them in the downward-refracting bottom duct, experiencing large scattering losses from repeated interactions with the bottom. In contrast, the upper plot shows a transmitter and receiver in the surface mixed layer, and is qualitatively similar to the JD190 source tow, with similar exponent estimates of $k_{\text{coh}} = 3.1 \pm 0.3$ and $k_{\text{inc}} = 2.7 \pm 0.2$, with 95% confidence

intervals. These results suggest that for the JD190 source tow, the interface depth was below the source and receiver, effectively putting them in the surface mixed layer.

2.6.5.4 KAM11 Modeling Conclusions

In this section, we presented results modeling the KAM11 environment. We showed that both the soundspeed profile and the reflection/scattering losses are important in modeling the environment appropriately. Furthermore, we showed that the interface depth between the surface mixed layer and the bottom duct is critically important, and can vary spatially and temporally. With the KAM11 transmitter and receiver both near the interface depth, the propagation is especially sensitive to perturbations in interface depth, which can be driven by internal waves.

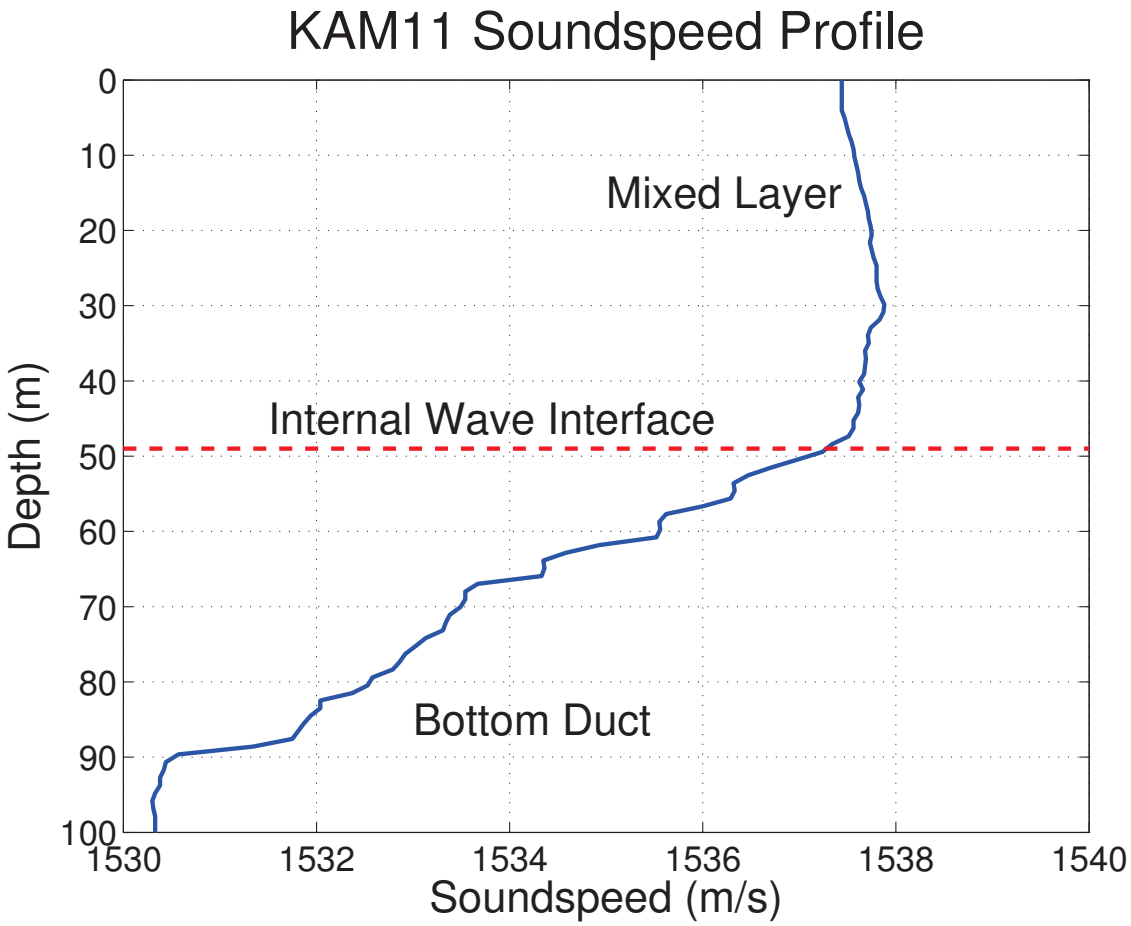

Figure 2.29. KAM11 soundspeed profile (JD187, 07:23Z, Cast 11). The components of the soundspeed profile are a surface mixed layer down to almost 50 m depth, above a colder bottom duct with a soundspeed minimum near the bottom. Sound waves refract towards a soundspeed minimum, so this is a downward-refracting environment. Sound propagating in the bottom duct will have many bottom interactions, with corresponding scattering losses. As described in the text, internal waves can propagate along the interface between fluids of different densities, changing the depth of the interface between the mixed layer and bottom duct. Raytraces for sources at different depths in this soundspeed profile are shown in Figure 2.30.

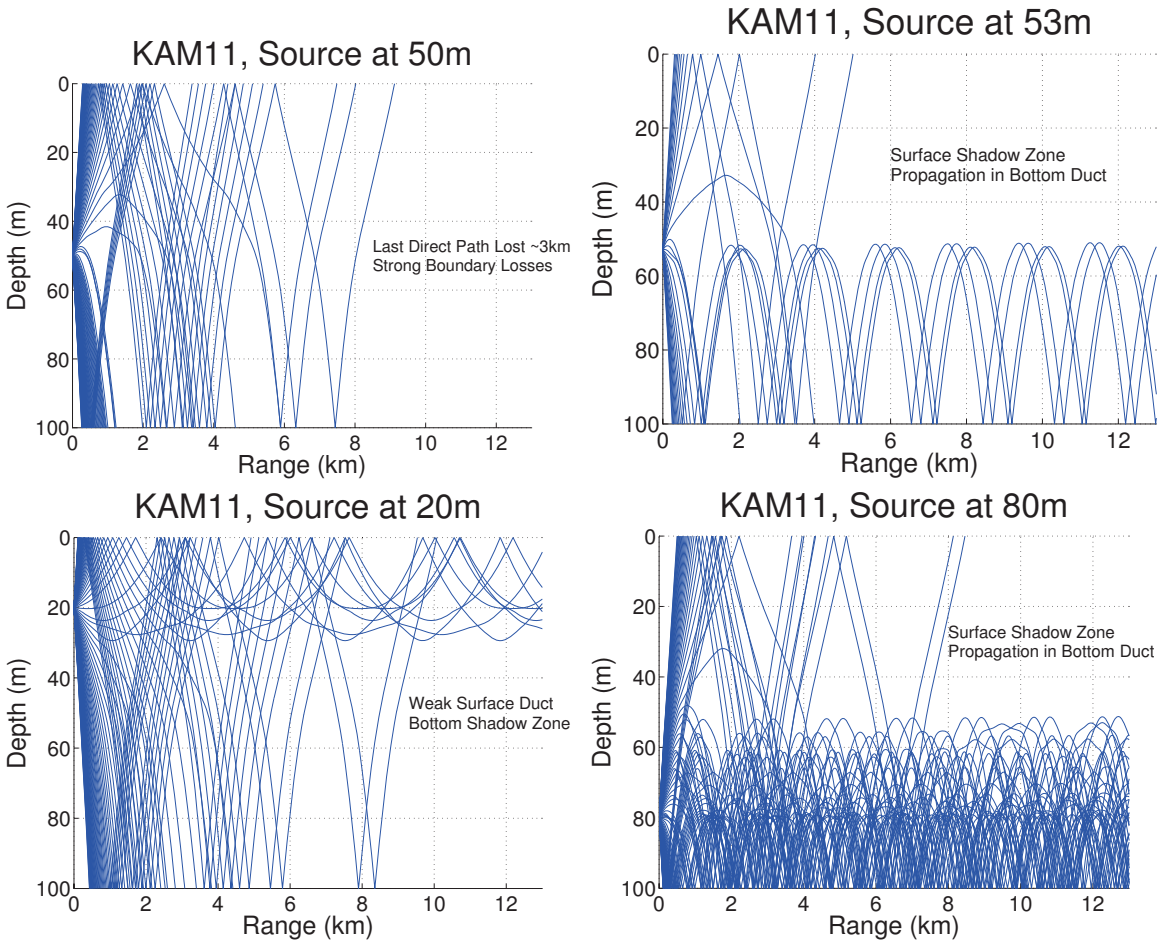

Figure 2.30. Raytraces for sources at different depths in the soundspeed profile shown in Figure 2.29. The upper two plots show the sensitivity to the interface depth: With a slight change in source depth, or similarly, interface depth, the propagation is dramatically different. The lower two plots show sources in the surface mixed layer (20 m depth) and in the bottom duct (80 m depth). In the bottom duct, there are many interactions with the bottom, leading to increased scattering loss. In many of the plots, there are *shadow zones*, or regions where the rays do not propagate due to the soundspeed profile.

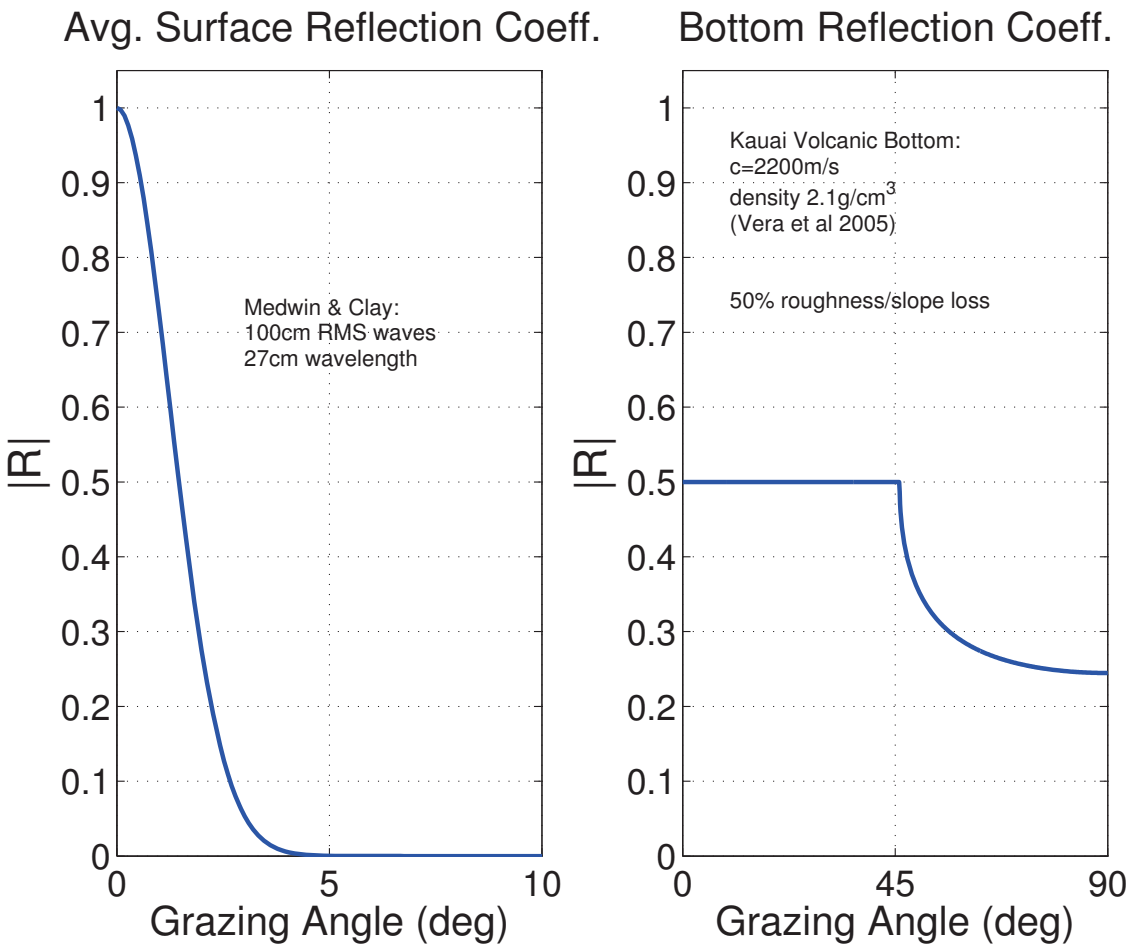

Figure 2.31. Bellhop environment's reflection coefficients to investigate the effects of non-perfect reflection, as a function of grazing angle (the complement to angle of incidence). The sea surface reflection coefficients are for an RMS wave height of 100 cm, typical from the KAM11 Trip Report [57], calculated for an acoustic wavelength of 27 cm following Medwin and Clay [75]. The bottom reflection coefficients are using seafloor parameters from Vera et al. [129], following Medwin and Clay [75]. The seafloor reflection coefficient is further reduced by an angle-independent 50% to roughly model the very steep seafloor as discussed in the text, reducing the forward-scattered energy.

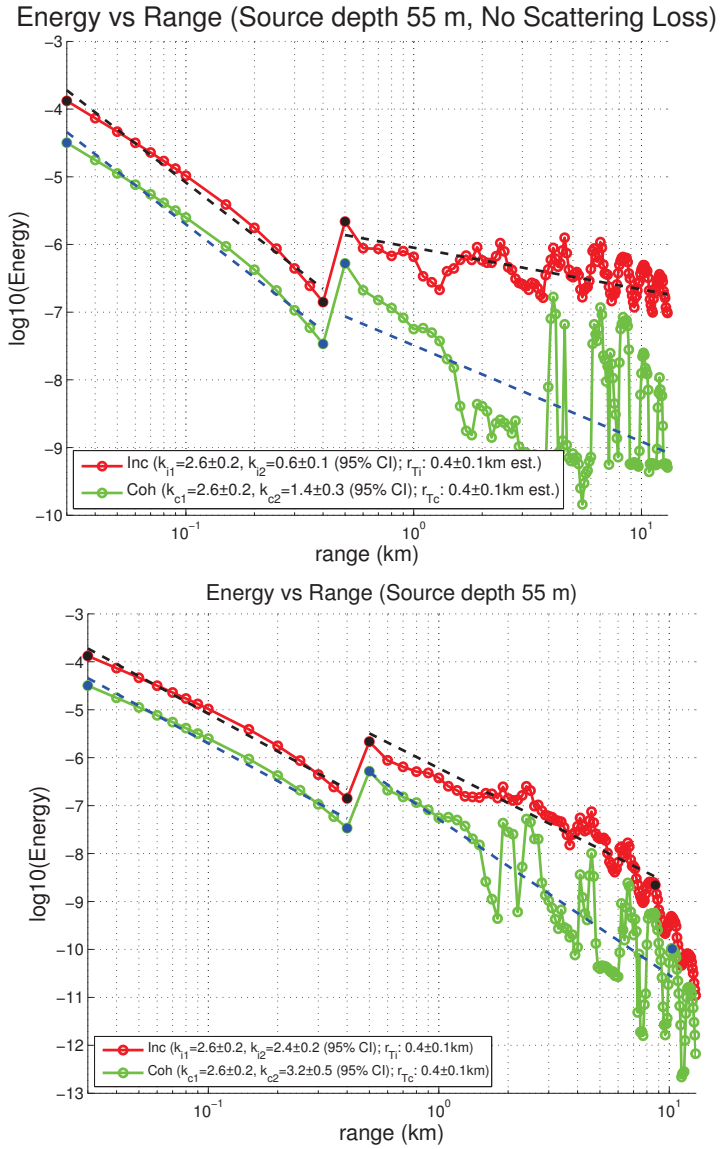

Figure 2.32. Received energy-versus-range plots for raytraced modeling of the KAM11 environment. Both plots use the KAM11 soundspeed profile shown in Figure 2.29. The upper plot has lossless boundaries, while the lower plot models KAM11 boundary losses shown in Figure 2.31. The energy-loss exponent estimates for the lossless boundaries are inconsistent with measured values. Therefore, *both* the soundspeed profile *as well as* the boundary losses are required to model the KAM11 environment appropriately.

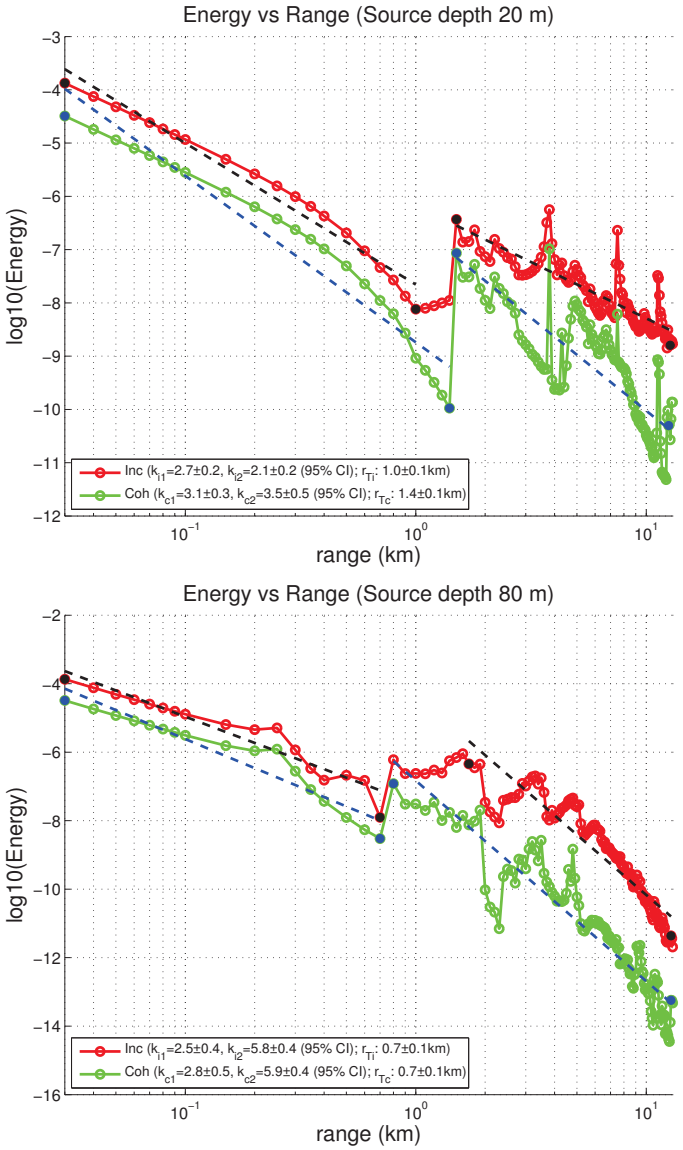

Figure 2.33. Received energy-versus-range plots for raytraced modeling of the KAM11 environment. Both plots use the KAM11 soundspeed profile shown in Figure 2.29. The upper plot has the source at 20 m depth, in the surface mixed layer, and is qualitatively similar to the JD190 source tow. The lower plot has the source at 80 m depth, in the bottom duct, and is qualitatively similar to the JD189 source tow. These plots suggest that the interface depth between the surface mixed layer and the bottom duct was above the source and receiver for JD189 (placing them in the bottom duct), and below the source and receiver for JD190 (placing them at the bottom of the mixed layer).

2.6.6 Conclusions from Field Experiment

We analyzed data from two source tows from the KAM11 experiment, to estimate coherent and incoherent energy-loss exponents in shallow water of 100m depth. The environmental conditions were highly variable. We identified some periods in time, namely JD189, where a simple energy-loss exponent model did not hold. For JD190,SYS3, an energy-loss exponent model did appear to hold. Our best estimate of the overall energy-loss exponents from the JD190,SYS3 dataset is a coherent loss exponent of 2.6 ± 0.3 and an incoherent loss exponent of 2.3 ± 0.3 (99% confidence intervals, to try to increase the reported margins of error). The overall energy-loss exponent includes both spreading loss as well as boundary scattering losses. Scattering losses are likely to be a significant component of the additional energy loss beyond what we would expect from spreading alone. We have corrected for absorption loss using Thorp's expression.

In terms of modeling shallow-water underwater acoustic networks, the results suggest caution when using simple spreading-loss models. A simple exponent-based model may not be valid at a particular time or location. Furthermore, even if it is valid, the overall energy-loss exponent may be significantly larger than the "practical spreading" model of $k = 1.5$ which is often used. A larger energy-loss exponent will reduce the distance at which an interferer can disrupt packet detection, reducing somewhat the problem of long-range interference.

We partially validated the mixed-exponent spreading model. There were differences in the measured coherent detection and incoherent interference energy-loss exponents. The detection exponents were usually larger than the interference exponents, implying that long-range unsuppressed interference would be a problem for a UAN deployed in the KAM11 environment, even considering the relatively large values of the energy-loss exponents.

Mixed-exponent transition ranges as described in Section 2.3.3 were not observed. The experiment was at a single depth (100m), and the estimates were not robust enough to allow bandwidth reduction below 4 kHz bandwidth. The hypothesized transition ranges would therefore be order 100 m for the incoherent transition range, and order 13 km for the coherent transition range. We had energy-versus-range data from approximately 600 m to 12 km. Unfortunately, therefore, the

depth- and bandwidth-dependence (or even the existence) of the hypothesized transition ranges could not be validated.

The acoustic propagation was very different between JD189 and JD190. Modeling analysis suggests that the difference may be due to a change in the depth of the interface layer between the surface mixed layer and the bottom duct. One possible mechanism for changing the depth of the interface layer might be internal waves, and while that is unconfirmed for this particular case, it is known that the KAM11 site has very high internal wave activity. The soundspeed profiles were downward-refracting and non-uniform, introducing additional range dependence and likely increasing bottom scattering losses.

The KAM11 experiment site was chosen in large part for its dynamic environmental conditions, including internal waves [49]. The resulting variability of the results also highlights the shortcomings of spreading exponents. While there may exist a stable long-term temporal and spatial average of the spreading exponents, the propagation conditions near a given network node at a specific time and place may well be fluctuating away from, or simply be different than, the long-term temporal average and broad-scale spatial average. Furthermore, a source-tow experiment inherently combines space and time in the measurements: there are no pure temporal averages or pure spatial averages. With environmental conditions changing in both space and time, results from a source tow experiment can be complex.

With adequate averaging over time, not necessarily achievable in a source-tow experiment, the variations in received energy with time due to internal waves should average out of the energy-loss exponent estimates. Similarly, with adequate spatial averaging in both range and depth, the variations in received energy at different depths and ranges due to non-uniform soundspeed profiles will likely average out of the exponent estimates. The scattering losses from the boundaries, however, will not average out of the exponent estimates. Many classical oceanographic results are from the deep ocean, which is simpler than shallow water. The "practical spreading" of $k = 1.5$ result [18], which is commonly used in modeling underwater networks [112], but which has minimal grounding [18], is sometimes uses as a "rule of thumb" from deep-water propagation. In deep-water propagation, there is a soundspeed minimum at about 1 km depth, where many propagating

rays are fully internally refracted, without scattering from the surface and bottom [75]. There are scattering losses on fully internally refracted rays, but the losses are much less than losses from interacting with the surface and bottom.

Spreading exponents are inherently averages in time and space. They are not detailed propagation models, but they are important for system design [18], including system design for network protocols. In particular, the effect of spreading loss on distant interferers is critical to networks, but it has not been a focus of point-to-point underwater acoustic communications research. Understanding energy-loss exponents and mechanisms is particularly important for designing medium-access network protocols.

Since scattering losses play a significant role in the amount of energy received by a node in a shallow-water network, we suggest that the spreading loss term in modeling performance of shallow-water underwater acoustic networks be updated to include scattering losses.

2.7 RTS/CTS Effectiveness for a Network in the KAM11 Environment

The ultimate goal of measuring the energy-loss exponents is to improve understanding and modeling of underwater acoustic networks. Using the measured exponents from Section 2.6, we can use results from Chapter 3 to estimate the effectiveness of the RTS/CTS collision-avoidance protocol for a network deployed in the KAM11 environment.

For the JD190 source tow, SYS3 measurements, the results followed a simple energy-loss exponent model. We measured coherent and incoherent energy-loss exponents of $k_{coh} = 2.8$ and $k_{inc} = 2.3$. The exponents are different, and so the mixed-exponent model applies. No transition ranges were observed, so we apply the mixed-exponent model with no transition ranges, but with different exponents for coherent detection and incoherent interference. For JD190,SYS3, the maximum range was only about 9 km, and here we are assuming that there were no transition ranges beyond what we could observe, which may be a questionable assumption, but is all we can do with the experimental data that we have. Since the KAM11 environment is highly variable, these measurements apply only to that specific time and location.

In the two KAM11 source tows, our maximum detection range was about 12 km, and our matched-filter processing gain was about 20 dB. With a coherent energy-loss exponent of $k_{coh} = 2.8$, Thorp absorption loss at a center frequency of 5.5 kHz, and ambient noise parameterized by 3 m/s wind and a "shipping factor" of 0.5 [18, 117], for a maximum detection range of about 12 km, we would need a matched-filter detection threshold of about 2 dB, or a signal-to-noise ratio of about -18 dB before the matched filter's processing gain. These values are reasonable, even if they are not necessarily completely accurate.

In the left-hand plot, Figure 2.34 shows the RTS/CTS effectiveness, defined in detail in Chapter 3. This measure of RTS/CTS effectiveness assumes a heavily loaded, uniformly-distributed, and relatively dense network, without transmit power control. The mixed-exponent model assumes modems which use a matched-filter detector as a low-power wakeup detector. The RTS/CTS effectiveness begins to drop for links with node separations of about 8.5 km or more. The mixed-exponent model, plotted in blue, generally has lower RTS/CTS effectiveness than the "practical spreading" model, plotted in red, even though the measured energy loss exponents for JD190,SYS3 were much larger than the practical spreading value of $k = 1.5$.

In the right-hand plot, Figure 2.34 also shows the interference regions: in the green region are nodes which are too distant to detect the RTS/CTS collision-avoidance packets, but which are also too distant to disrupt detection. In the yellow region are nodes which can detect the RTS/CTS collision-avoidance packets, and hence will not disrupt detection. In the red region are nodes which are too distant to detection the RTS/CTS collision-avoidance packets, but which are close enough to disrupt packet detection for receivers on links with the specified node separation, plotted on the horizontal axis.

Figure 2.35 plots the interference regions for a transmitter and receiver separated by 11 km in the KAM11 JD190,SYS3 environment. The unsuppressed interferers which can disrupt detection are in the red region. The potential interferers which will be suppressed are in the green region. The RTS/CTS effectiveness measure is the fraction of all potential interferers that can disrupt detection that will be suppress by the RTS/CTS collision-avoidance packets.

2.7.1 Generalized Interference Range from Detection Criterion

In general, the results from the KAM11 experiment and KAM11 modeling do not necessarily support simple energy-loss exponent models. For cases where a simple exponent model does not hold, we cannot directly use the results from Chapter 3 as we did in Figures 2.34 and 2.35. Instead, we need to return to the detection criterion, namely that the signal-to-interference-and-noise ratio (SINR) is above a detection threshold, T, i.e., SINR$\geq T$.

The upper plots of Figures 2.36-2.38 essentially plot the two sides of the detection criterion inequality. These figures correspond to the energy-versus-range plots in Figures 2.32 and 2.33, in turn corresponding to the raytraces in Figure 2.30. The green curves are the scaled detection energy, scaled up by the matched-filter processing gain and down by the detection threshold. The red curves are the interference plus noise energy. If the green curve is above the red curve for a particular range r, then for a transmitter and interferer both at range r from the receiver, detection will occur, otherwise interference will disrupt the detection. As in Chapter 3, however, we are interested in determining the *interference range*, the maximum range R_i at which an interferer will disrupt detection for a source and receiver with node separation d. Therefore, for each node separation d, we want to determine the maximum range R_i for which the red interference-energy curve is above the green detection-energy curve at range d.

For example, in the upper plot of Figure 2.36, at a range of $d \approx 1.75$ km, the red interference energy becomes larger than the green detection energy. The maximum range R_i for which the interference energy is larger than the detection energy at $d \approx 1.75$ km is $R_i \approx 5$ km. Therefore, on the lower plot of Figure 2.36, at a node separation of $d \approx 1.75$ km there are interfering nodes plotted at interference ranges out to about $R_i \approx 5$ km. Since these interfering nodes are closer than the maximum transmission range, they are suppressable by the RTS/CTS collision-avoidance protocol, and so they are plotted in green. Interfering nodes which are more distant than the maximum transmission range cannot be suppressed by the RTS/CTS protocol, and they are plotted in red. For example, at a node separation of $d \approx 7$ km, there are unsuppressed interferers out to more than 15 km. For Figure 2.36 The noise floor is visible at about 85 dB re:1μPa@1m at ranges above about 12 km.

The plots of interference ranges are scatterplots rather than continuous curves, since the curves for the detection energy and the interference energy are not smooth, and cross each other repeatedly. Since the energy loss is different for each of the environments plotted in Figures 2.36-2.38, the maximum transmission range is different in each case, ranging from about 9 km for the bottom duct case in Figure 2.38 to about 27 km for the surface mixed layer case in Figure 2.37.

In each of the three cases, shown in Figures 2.36-2.38, there are node separations less than the maximum transmission range for which there are unsuppressable interferers.

These results use the raytraced KAM11 modeling results rather than experimental measurements from field data because in the field data we were not able to make any energy measurements at ranges larger than the maximum transmission/detection range. This is because our measurement method required detecting the channel characterization signals in order to estimate their coherent and incoherent energy. Therefore we were not be able to measure interference energy from field data at ranges larger than the maximum transmission range. Unfortunately, these missing larger ranges are exactly the ranges at which interferers would be unsuppressable and would reduce the RTS/CTS effectiveness.

2.7.2 General Implications for Networks Deployed in KAM11 Environment

With our experimental measurements of energy-loss exponents, as well as propagation modeling in the KAM11 environment, we can discuss implications for underwater acoustic networks which would be potentially deployed in this environment.

The primary observation from the KAM11 site is its extreme variability. Propagation conditions can change dramatically on relatively short timescales, and with relatively small changes in node location relative to the interface depth. Networks deployed in similar environments will require robust protocols which do not rely on specific channel conditions.

In general in underwater acoustic networks, vertical links are typically more robust than horizontal links. In an extreme environment such as the KAM11 site, vertical links may become more critical than they usually are, because at times they may be the only reliable links. Again as a general rule, the routing algorithms should avoid routing on links that are close to the maxi-

mum transmission range because of the reduced RTS/CTS effectiveness; this is in contrast to the suggestion of routing over long links in radio networks [2].

For horizontal links, there are tradeoffs in both the surface mixed layer as well as the bottom duct. The bottom duct is a relatively strong propagation duct, with the downside that the frequent bottom scattering losses due to the downward refraction will limit the maximum range of a link, likely to order 3-7 km. The direct path is lost after about 3 km, and all other paths experience strong scattering losses.

The surface mixed layer may be relatively benign in low wind conditions and sea states, potentially with long links of greater than 10 km in some cases, especially if there is a weak surface duct such as the case in the soundspeed profile shown in Figure 2.29. With increasing sea states, surface scattering loss will become larger. With wind conditions increasing beyond about 8 m/s, breaking waves will lead to increased bubble production [21], leading to very strong losses in the upper mixed layer [28, 91]. In windy conditions with strong losses due to bubble clouds, network links in the bottom duct will likely become preferable to links near the surface, even despite the relatively large bottom scattering losses.

The relatively large propagation delay of the underwater acoustic channel makes it more difficult than in radio channels to get current channel state information at the transmitter. On the other hand, minimal channel state information, such as SNR at the receiver, will probably be adequate. Furthermore, there is some level of predictability in many underwater acoustic channels [124], which may mean that channel state information does not always need to be explicitly transmitted.

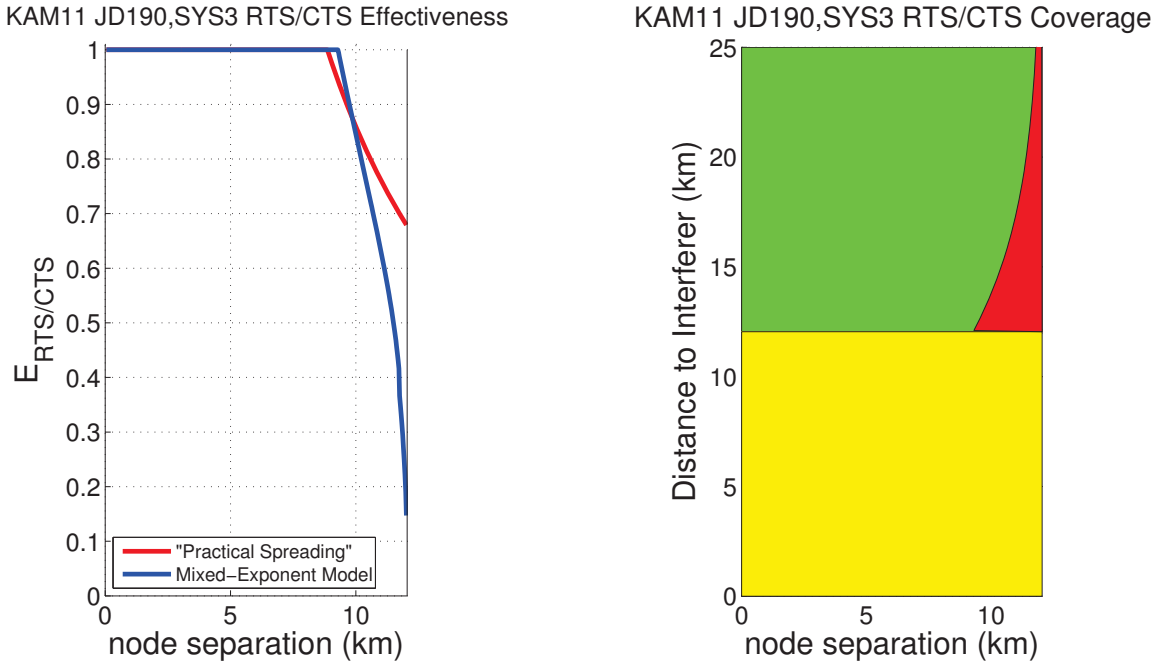

Figure 2.34. The left-hand plot shows RTS/CTS effectiveness, defined in detail in Chapter 3. The blue line shows the RTS/CTS effectiveness for the mixed-exponent model using the measured energy-loss exponents from the KAM11 JD190,SYS3 source tow results. The red line shows the RTS/CTS effectiveness for the "practical spreading" model. Even though the energy-loss exponents for JD190,SYS3 are large compared with the practical spreading model, the mixed-exponent model predicts significantly lower RTS/CTS effectiveness, and the experimental measurements show different exponenents for detection and interference, supporting the mixed-exponent model. The right-hand plot shows the interference regions: nodes in the green region are too far away to disrupt detection, nodes in the yellow region will be suppressed by the RTS/CTS collision-avoidance protocol, but nodes in the red region are too far away to detect the RTS/CTS packets, but close enough to disrupt detection for receivers on links with the specified node separation, plotted on the horizontal axis.

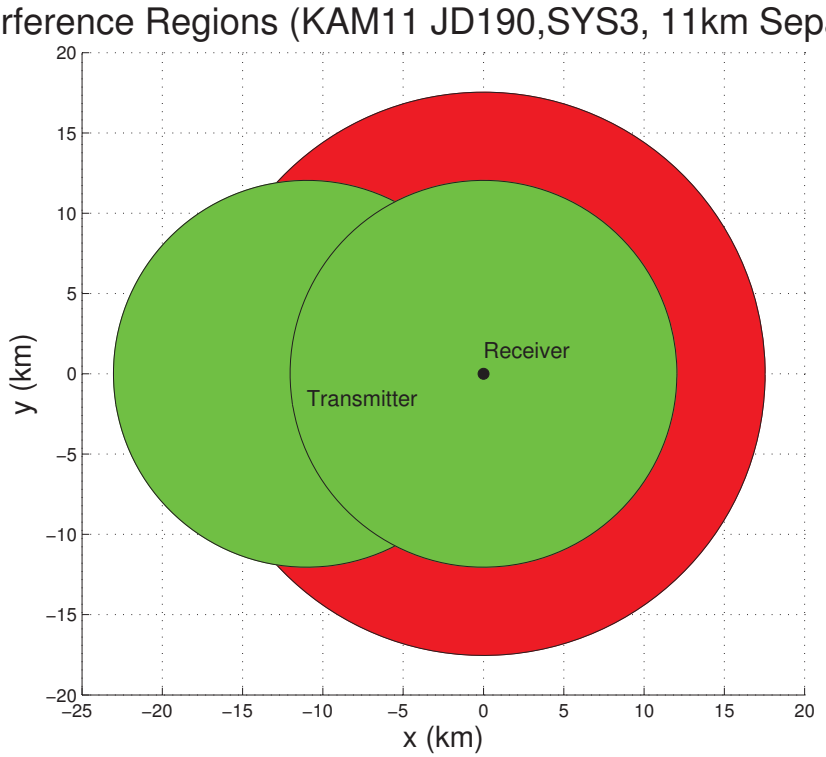

Figure 2.35. Interference regions for a transmitter and receiver separated by 11 km in the KAM11 JD190,SYS3 environment. The unsuppressed interferers which can disrupt detection are in the red region. The potential interferers which will be suppressed are in the green region.

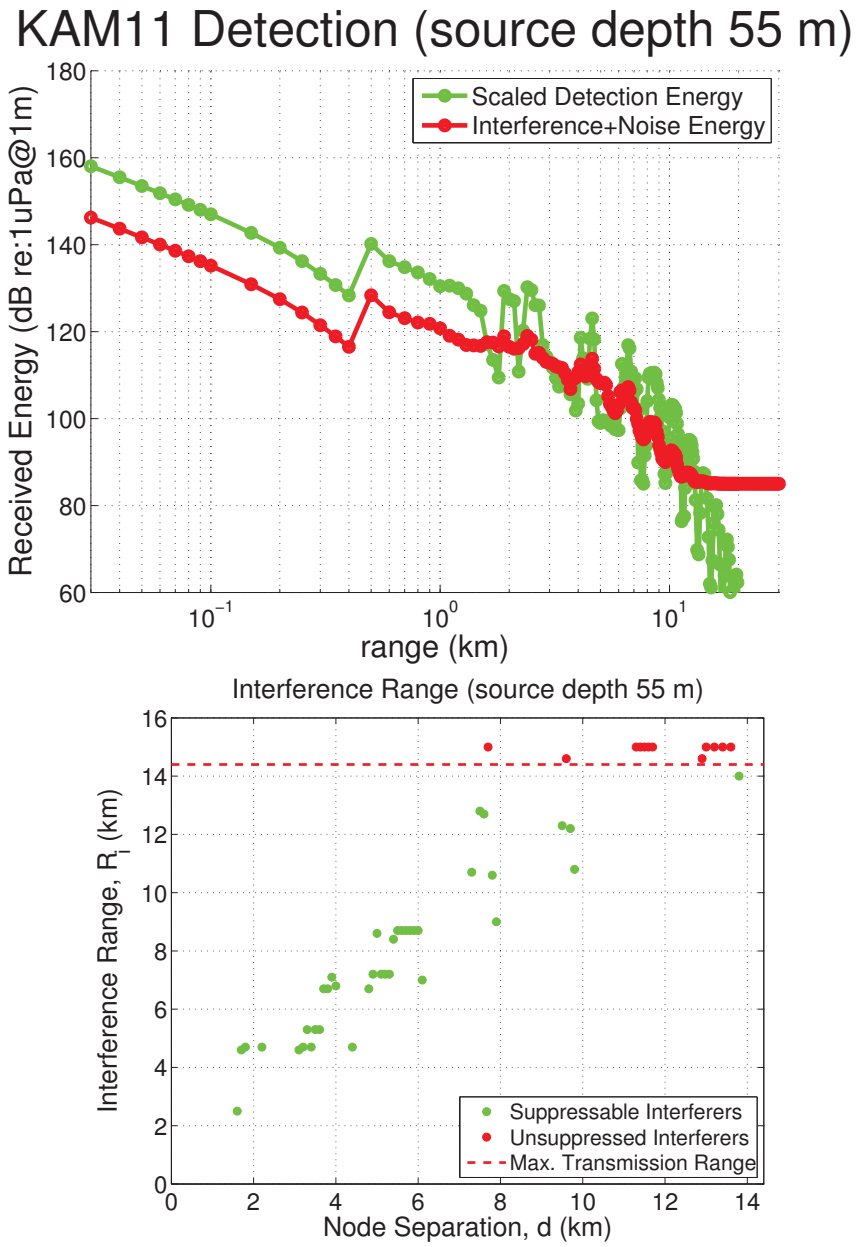

Figure 2.36. In the upper plot, the two sides of the detection criterion are plotted for a source and receiver at 55 m depth in a modeled KAM11 environment. When the green detection energy curve is above the red interference energy curve, detection occurs, otherwise detection is disrupted. The lower plot shows the maximum interference range, R_i, for which detection is disrupted at node separation d.

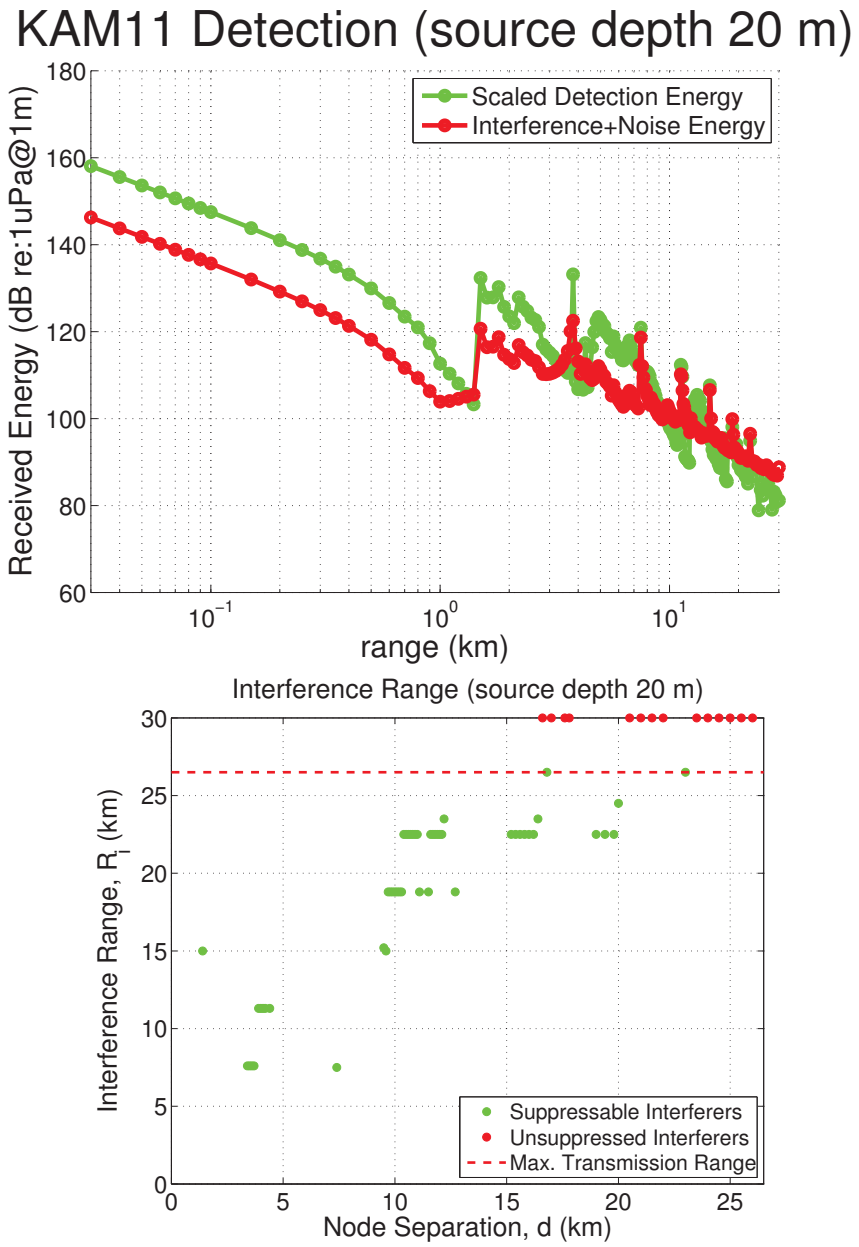

Figure 2.37. In the upper plot, the two sides of the detection criterion are plotted for a source and receiver at 20 m depth, in the surface mixed layer, in a modeled KAM11 environment. When the green detection energy curve is above the red interference energy curve, detection occurs, otherwise detection is disrupted. The lower plot shows the maximum interference range, R_i, for which detection is disrupted at node separation d.

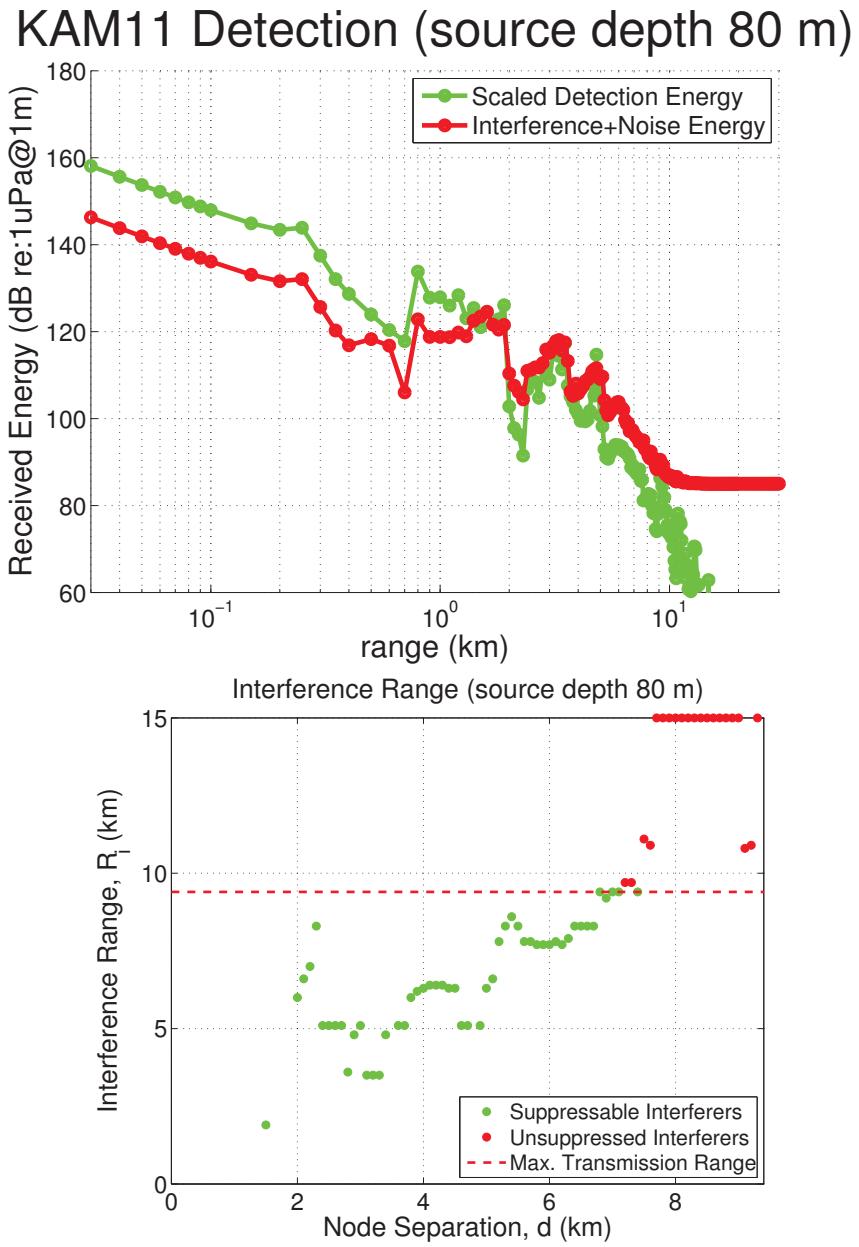

Figure 2.38. In the upper plot, the two sides of the detection criterion are plotted for a source and receiver at 80 m depth, in the bottom duct, in a modeled KAM11 environment. When the green detection energy curve is above the red interference energy curve, detection occurs, otherwise detection is disrupted. The lower plot shows the maximum interference range, R_i, for which detection is disrupted at node separation d.

2.8 Future Work and Directions

There are several directions for future work. One direction is to change the detector method so that the energy from all multipath paths is combined, rather than just energy from the non-resolvable arrivals; one potential approach is discussed in Section 2.8.1. Another direction is in terms of continued basic research on a long-term yet economically feasible experiment to further characterize and estimate energy-loss exponents; an experiment is proposed in Section 2.8.2. Finally, a long-term future direction is described in Section 2.8.3 in which a high-complexity detector would be implemented in a low-energy (but expensive) method using a custom silicon detector chip.

2.8.1 Autocorrelation Detector

The WHOI Micromodem [36] uses a low-complexity matched-filter detector in order to achieve low power consumption during the potentially long periods between packet detection. Another benefit of a matched-filter detector is that it only requires a single receive element to be powered, rather than powering a multi-element receive array. As discussed in Section 2.3, a matched-filter detector only detects on the energy of multipath paths whose arrivals are unresolved in time from the first arrival.

There are, however, other potential detection approaches for energy-constrained modems. One potential approach would be an *autocorrelation detector*. The complexity of an autocorrelation detector would be comparable to the complexity of a matched-filter (correlator) detector. The transmitter would send a signal, then wait for a lag τ, then re-send the same signal. The receiver would run an autocorrelator looking for a peak at lag τ. As long as the lag is relatively short, the channel will not have changed. The received signal will be convolved with the channel response, and will combine energy from *all* the multipath arrivals.

Although this is not yet investigated, and is reserved for future work, there may be negative tradeoffs associated with an autocorrelation detector. In particular, the receiver-operator characteristic (ROC) curve, describing conditional probability of detection and false alarm, may not be as good for an autocorrelation detector as it is for a matched-filter detector, although this is not confirmed at this point.

2.8.2 Proposed Experiment

Measuring spreading exponents requires significant averaging over time and space. To measure the spreading loss itself, isolated from the boundary scattering losses, would also involve estimating scattering losses from boundaries, or performing propagation losses without boundaries, for example in deep water.

Experiment cost scales with the amount of hardware required and the number of ship days utilized. Many current experimental approaches to measuring spreading exponents would be cost-prohibitive. For example, the KAM11 experimental setup of a few fixed receivers and a ship-towed source could be extended into a longer-duration experiment, accumulating ship costs throughout the entire experiment. Much more expensive would be to deploy many fixed receivers and one or more fixed transmitters, which would be very expensive in terms of deployment, recovery, and hardware costs typically this approach is only used where cost is not a significant concern, and where the hardware infrastructure will be used for years, such as military submarine test ranges, such as AUTEC, and production monitoring of sub-sea oil reservoirs [56].

An alternate experimental approach would minimize ship costs and hardware costs, while maximizing the number of repeated energy measurements for averaging into estimates of energy loss exponents. The experimental approach would be to deploy two autonomous vehicles with long deployment durations to run on the order of a hundred trials per month, each one gathering energy-versus-range data comparable to each of the KAM11 source tows. A surface vehicle with access to solar power would serve as the transmitter, while an underwater vehicle would be the receiver, profiling range and depth for received acoustic energy as well as soundspeed profile measurements.

To minimize noise at the receiver, generally acoustic receivers would be placed on stationary moorings, rather than on moving platforms. For extremely noisy moving platforms, such as ships, this approach is critical. Even propeller-driven autonomous vehicles can be relatively loud, in part due to flow noise. Gliders, however, achieve their low energy consumption by having no propeller — at the turns, a motor drives a buoyancy controller to change dive pitch, but aside from that, there are no continuously-driven motors generating noise. Furthermore, in terms of flow noise, a glider's

typical slow speed of about 20 cm/s through the water is actually lower than the typical flow speeds due to tidal currents past moored receivers.

A critical question for this proposed experiment, which is mostly unanswered from the data from the two KAM11 source tows analyzed, is how much variability in energy-versus-range is there, and how many transects would need to be run for a good characterization of the spreading exponents? The variability would clearly be site-specific, but some estimates could be made of energy variability at single ranges from the fixed-transmitter-to-fixed-receiver data from KAM11 and its similar predecessor experiments, RACE and SPACE. We can make a preliminary estimate of the variability of exponent estimates with the total number of measurements by using a bootstrapping approach on the KAM11 results. Figure 2.39 shows the bootstrapped margins of error in exponent estimates as a function of number of (range,energy) measurements in the dataset. The margin of error (derived from the standard error) appears to have the expected dependence upon $1/\sqrt{N}$, but until we have an approach on how (or even whether) to correct the energy loss exponent estimates for scattering losses, this preliminary estimate of number of measurements required is premature.

An enabling component of this approach is the availability of autonomous vehicles with long deployment durations. Gliders are a class of autonomous underwater vehicles with long deployment durations because they control their motion by infrequently adjusting their buoyancy and "gliding" to the next turning depth, rather than by continuously driving a propeller. Standard battery-powered gliders have deployment durations on the order of a month, even in relatively shallow water where turning is frequent [131]. Wave Gliders are a brand of autonomous surface vehicle with essentially unlimited deployment duration, using solar panels for electric power and converting wave motion into propulsion energy [71]. The ship costs would be limited to deployment and recovery of the vehicles, and would not accumulate throughout the experiment.

A constraint of gliders is that their battery energy is extremely limited. A glider could run a duty-cycled receiver, but not a transmitter, which requires much more energy. A constraint of Wave Gliders is that they operate on the surface, in contrast to gliders which could operate over the full water depth. A Wave Glider could potentially tow a receiver element on a cable [8], perhaps even down to 50 m depth, but the receiver depth would not be easily controllable and it could not profile

over depth. A Wave Glider would have the electrical power to run a transmitter, but acoustic transmitters are physically larger and heavier than receivers, especially at lower frequencies, and so the transmitter depth would be likely be limited to the length of the Wave Glider umbilical tether, or about 7 m depth, which is typically in the surface mixed layer of the soundspeed profile. A deeper transmitter would be preferable, but probably not required, since signals transmitted from the higher soundspeed of the surface mixed layer would propagate into the lower soundspeeds in the colder water, but signals propagated from the colder, lower soundspeed region could be totally internally refracted and not penetrate the warmer, higher-soundspeed surface mixed layer. Alternately, a single fixed duty-cycled transmitter with a large battery housing could be used — the amount of experimental hardware and ship time would still be relatively small. Wave Gliders have continuous GPS fixes for navigation, whereas gliders dead-reckon their navigation between infrequent surfacings for GPS fixes. Nevertheless, the accuracy of the range estimates required for the spreading exponent measurement is probably still within the tolerances of dead-reckoned glider navigation, which might be several hundred meters with a GPS fix every 4-6 hours, and which can probably be improved with post-processing.

The natural division of roles in this experimental setup would be to have the Wave Glider (or alternately, a fixed mooring) as the transmitter and an underwater glider as the receiver. The low speed of the glider limits the flow noise on the receiver, so it can be a fairly quiet acoustic receiver platform even at low acoustic frequencies [9]. The glider can profile in both range and depth, including measuring soundspeed profiles for post-experiment propagation modeling. The Wave Glider can collect sea-state and wave period measurements from accelerometers, to help estimate and model surface scattering losses in post-processing.

A low acoustic frequency such as 2 kHz would also have less absorption loss and scattering loss when reflecting from rough surfaces, focusing the measurements on spreading loss rather than other loss mechanisms. With a center frequency of about 2 kHz, typical transducers would limit the bandwidth to about 1 kHz or less, roughly 1/4 to 1/3 of the KAM11 bandwidth, reducing the number of impulse response estimates per minute of recorded data, as well as reducing the hypothesized coherent transition range. (Longer transition ranges could still be investigated by

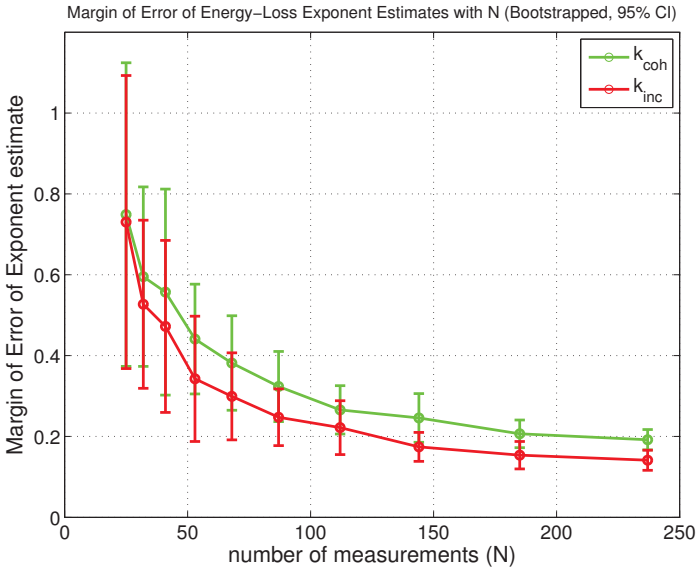

Figure 2.39. A preliminary estimate of how the margins of error (for a 95% confidence interval) for the energy-loss exponent decrease with the number of (range,energy) measurements. The estimates are derived from randomly selecting subsets of the full JD189 and JD190 of size N, and in turn bootstrapping those subsets to estimate the standard error of the exponent estimates. The errorbars are the standard deviations of the bootstrapped size of the estimated margin of error. To measure actual spreading exponents rather than energy-loss exponents, the effects of scattering loss would likely have to be accounted for, which would almost certainly increase the number of measurements required for a given margin of error.

driving the vehicles to deeper water.) When the Wave Glider and underwater glider were close to each other, the various multipath arrivals in the impulse responses could potentially be identified with individual ray paths, based on ray-tracing models using soundspeed profiles collected by the underwater glider. Identifying multipath arrivals with the type of path (e.g. surface, bottom, surface-bottom, etc) might allow estimates of surface and bottom reflection coefficients. To help improve estimates of scattering losses, shorter ranges might be over-sampled, where ray paths could potentially be identified. To help with initial estimates and modeling of bottom reflection coefficients and scattering losses, the approximate seafloor characteristics would be determined from a literature search for previous geological surveys and previous geoacoustic inversions for the seafloor acoustic parameters [93], if any exist for the desired experiment site.

Typical underwater glider speeds are slow, about 20 cm/s, while Wave Glider speeds are higher, about 1 m/s. The movements of the underwater glider and Wave Glider could potentially be coordinated autonomously [50] to complete transects more quickly than a glider could with a fixed transmitter. With the Wave Glider's relatively high speed, a 20 km experiment in range could be conducted about every six hours, or about four times a day for the month that the underwater glider's batteries would last. Transmitting and receiving on an average duty cycle of one minute out of every five minutes (which could be log-spaced in range) would give energy estimates at about 60-80 ranges per 20 km transect. The experiment site could move with time to provide additional spatial averaging, or to experiment with different depths.

2.8.3 Technology Advances in Energy-Efficient Detection

This work has focused on a low-complexity, low-power matched-filter detector on a single receive channel, detecting on energy from a single multipath arrival, implemented on a sequential processor. When waiting for an incoming packet, an energy-constrained modem needs to minimize power consumption (hence computational complexity), and a matched-filter detector is an effective and common way to achieve that.

With a custom-fabricated equalizer/detector chip which has an internal parallelized architecture, or potentially an equivalent design implemented on a low-power FPGA, at some point the high-complexity approach of equalizing the channel and detecting on energy from multiple combined multipath arrivals will become feasible in terms of its power consumption, as well as its implementation and fabrication costs. If the detector can combine energy from multiple arrivals, there will be no significant difference between the coherent and incoherent spreading exponents, and long-range interference will become much less of a problem. Furthermore, the combined equalizer/detector approach would by its nature require multiple receive channels, and the next question is what their array configuration would be. In shallow-water point-to-point communications, vertical receive arrays are generally used since the multipath arrivals have different vertical angles of arrival. With shallow-water networks, different nodes will have different azimuthal angles of arrival, but likely a similar spread in their vertical angles of arrival, and so horizontal arrays will be useful [34]. If the

receive array for the combined equalizer/detector chip were to include a horizontal aperture as well as a vertical aperture, packet detection in the presence of interferers would be much less difficult in most cases. Multiple access protocols for underwater networks are challenging in large part because of the high propagation delays [3]. Azimuthal beamforming could help to reduce the likelihood of collisions, by limiting collisions to packets received at similar times with similar angles of arrival (modulo the array's angular ambiguity) [10].

2.9 Conclusions

Interference is fundamental to wireless networks, and spreading loss is a major determining factor in the level of interference experienced by nodes in a network. Nevertheless, there has been little research into the role of spreading in the performance underwater acoustic networks. Furthermore, many underwater acoustic networks are modeled using the "practical spreading" model with a spreading exponent of $k = 1.5$ [112], which has little grounding in theory or experiment [18].

In this chapter, we have questioned and tested the validity of the spreading model that has been assumed to be valid by many researchers in underwater acoustic networks.

In addition, we have proposed and tested the validity of a new spreading model, the *mixed-exponent spreading model*.

This chapter made several contributions:

- *We proposed and derived the theory for the mixed-exponent spreading model*, from first principles in acoustic propagation as well as the detection signal processing of the Micromodem [36], a commonly-used underwater acoustic modem.

- *We validated the mixed-exponent spreading model* using numerical acoustic propagation packages. We used two different packages for validation, a raytracing package as well as a direct solution of the wave equation.

- *We directly measured energy-loss exponents from data from a field experiment.* This validated that there are indeed differences in the measured detection energy exponent and the interference energy exponent for a real environment, one of the predictions of the mixed-exponent

model. As a network-level implication, long-range unsuppressed interference with the mixed-exponent model is significantly worse than it is with single-exponent spreading model; this is discussed in much more detail in Chapter 3. The depth- and bandwidth-dependences of the transition regions in the mixed-exponent model could not be determined from the field data, and were therefore neither validated nor invalidated.

- The energy-loss exponent estimates from field data were all larger than the $k = 1.5$ suggested by the "practical spreading" model. *For this particular shallow-water environment, the "practical spreading" model is invalidated. Caution should be used when using modeling underwater acoustic networks with the "practical spreading" model, particularly in shallow water.*

- *We modeled the propagation in the highly-variable field experiment environment, and explained the qualitative features observed in the estimates of energy-loss exponents from the field data.*

- *We estimated the interference range and effectiveness of the RTS/CTS collision-avoidance protocol using field data measurements and modeling,* for a potential network deployed at the field experiment site.

CHAPTER 3

LOW SPREADING LOSS IN UNDERWATER ACOUSTIC NETWORKS REDUCES RTS/CTS EFFECTIVENESS

Effectiveness of collision-avoidance MAC protocols is not a measure of throughput. Rather, collision-avoidance effectiveness measures the protocol's ability to prevent collisions, and in this analysis is independent of propagation delay.

The relatively low spreading loss in underwater acoustic channels allows increased interference from distant interferers, which reduces the effectiveness of collision-avoidance MAC protocols. These collisions in turn reduce spatial reuse and network goodput, and increase power consumption. A competing channel effect, however, is the frequency-dependent absorption. The absorption can strongly suppress distant interferers, improving the effectiveness of collision-avoidance protocols. A third channel effect is frequency-dependent ambient noise, which reduces effectiveness for links consisting of widely separated nodes. RTS/CTS effectiveness generally decreases with decreasing acoustic frequency.

We present analytic, numerical, and simulated results detailing how each of the major characteristics of the physical channel and physical layer affects the RTS/CTS effectiveness. We analyze the limiting case of dense *ad hoc* networks with high offered loads, since this case is where the effects of low spreading losses will most strongly affect RTS/CTS effectiveness. While in practice most actual deployments of underwater acoustic networks will not be dense networks with high offered loads, the analysis in this chapter offers theoretical insight into the physical causes for the limits on RTS/CTS effectiveness in UANs, beyond propagation delay.

---

[1] An earlier and shorter version of this chapter has been published in the proceedings of the ACM 6$^{\text{th}}$ International Workshop on Underwater Networks (WUWNet), 2011, as: J. Partan, J. Kurose, B.N. Levine, and J. Preisig. Low Spreading Loss in Underwater Acoustic Networks Reduces RTS/CTS Effectiveness. [83]

We find that RTS/CTS effectiveness can drop to between 50%–90% for source and receiver separated by more than about two-thirds of the maximum packet range. The effectiveness depends heavily on the acoustic frequency.

In this chapter, we study the MAC-layer implications of the alternative mixed-exponent spreading model developed in Chapter 2. That model hypothesizes different spreading exponents for detection of packets and processing of interfering packets. In the WHOI Micromodem-1, a common underwater acoustic modem for UANs, packets are detected with a coherent matched-filter detector, detecting on the energy in the largest of the multipath arrivals. In contrast, interference combines energy from all of the multipath arrivals, suggesting the hypothesized spreading model. The hypothesized model allows analysis and intution to be used in understanding spatial reuse in RTS/CTS MAC protocols, without requiring numerical acoustic propagation models to be run for every situation.

3.1 Introduction

Underwater wireless sensor networks for oceanographic applications rely on underwater acoustic communication at the physical layer. Underwater acoustic communication channels have a number of physical differences from terrestrial radio communication channels, including speed of propagation, spreading loss model, as well as frequency-dependent absorption and ambient noise. Previous work on RTS/CTS-based MAC protocols in the domain of underwater acoustic networks (UANs) has mostly focused on propagation delay issues. While RTS/CTS-based protocols are usually relatively inefficient due to large propagation delays [3, 56], they are nevertheless being proposed for underwater acoustic networks, in part due to their practical simplicity [53, 76, 86, 106, 112].

In this chapter, we analyze the effects of spreading losses, frequency-dependent absorption, and frequency-dependent ambient noise on collision-avoidance protocols derived from MACA [62] and MACAW [11], i.e., using RTS/CTS/DATA handshakes. Specifically, we use analytic results, numerical results, and simulations to evaluate the effectiveness of RTS/CTS-based collision avoidance in UANs. The collision-avoidance protocol's effectiveness is related to the spatial reuse available within the network; if distant nodes must have their transmissions suppressed to avoid collisions,

then less spatial reuse is possible. Previous work on UAN spatial reuse has dealt with TDMA and FDMA cellular architectures [116], rather than RTS/CTS-based ad hoc networks.

We build on previous work by Xu et al. [135], which argues that for 802.11-based radio networks, packets can cause collisions at ranges significantly larger than the range at which they can be detected. In this case, the RTS/CTS handshake cannot prevent all collisions, which reduces spatial reuse, network efficiency, and energy efficiency. The range at which interferers can cause collisions depends upon the distance between transmitter and receiver, the packet detection threshold, and the physical channel characteristics.

In UANs, physical waveguide effects in the communications channel reduce spreading losses significantly relative to radio channels. The small spreading loss allows interference from distant nodes. A competing physical effect is from absorption, which can suppress distant interferers strongly, improving spatial reuse. A third effect is that of ambient noise, which reduces the effectiveness of RTS/CTS collision avoidance for widely spaced nodes. Aside from spreading, these effects are frequency-dependent, and analyzing spatial reuse in UANs is a complex problem.

Our contributions in this chapter include the following:

- We extend Xu et al.'s basic model to a simple channel model for UANs that considers spreading losses only. One of their approximations is invalid in UANs, which we correct and generalize appropriately for both UANs and RF networks. With this simple spreading-only channel model, neglecting absorption and ambient noise, the results initially suggest that RTS/CTS effectiveness is significantly lower in UANs than in radio networks, with RTS/CTS handshakes beginning to lose effectiveness for node separations of only 22% of the maximum range, versus about 56% for radio networks, for typical parameters.

- Using a more realistic channel model, incorporating absorption and ambient noise, we derive analytic expressions to explain how various physical-layer communication parameters affect RTS/CTS effectiveness. These parameters include detection threshold, node separation, transmit power, and center frequency (determining absorption coefficients and ambient noise power). We find that the strong effects from absorption improve spatial reuse for most

intermediate node separations to approximately the level of collision-avoidance performance in radio networks.

- We analyze how the mixed-exponent spreading model studied in Chapter 2 affects RTS/CTS effectiveness. With this model, RTS/CTS effectiveness would drop significantly compared with the widely used $k \approx 1.5$ "practical spreading" model, especially at lower frequencies. For example, at 3 kHz center frequency, on average the RTS/CTS handshake would suppress under 10% of potential interferers for all but the smallest node separations.

- We validate the numerical results from our analytical model with simulations incorporating the channel model, physical layer, and link-layer MAC protocols.

We conclude with a discussion of several possible methods for improving spatial reuse in UANs using RTS/CTS-based MAC protocols.

3.2 Background

Our contributions extend a basic model of RF MAC-layer behavior by Xu et al. [135] (and Ye et al. [136]). Their study of RTS/CTS-based MAC protocols found that interference from nodes that are out of data communication range can cause collisions; that is, the interference range of transmissions is typically larger than the data range. In this section, we re-state their model and results, and in the next section, we extend the model to account for the physical properties of underwater acoustic communication channels.

Xu et al.'s analysis begins with the simple statement that collision avoidance requires the successful detection of RTS/CTS packets. There is a *vulnerable period* at packet detection, and if detection is disrupted by interfering packets, the RTS/CTS handshake cannot complete, and no data will be transferred. The condition for packet detection is

$$T \leq \text{SINR}, \tag{3.1}$$

where T is the receiver's detection threshold, and SINR is the signal-to-interference-and-noise ratio at the receiver. Following the notation introduced by Xu et al., let d be the distance between transmitter and receiver. Let r be the distance from receiver to the closest interferer. The simple model analyzed by Xu et al. does not include ambient noise and signal absorption, reducing SINR to SIR, the signal-to-interference ratio. In that case, Eq. 3.1 becomes

$$T \leq \text{SIR} = \frac{Pd^{-k}}{Pr^{-k}} = \left(\frac{r}{d}\right)^{k} \tag{3.2}$$

where P is the transmit power for all nodes. Choosing equality in Eq. 3.2 gives the minimum allowable distance r to the interferer such that detection of the collision-avoidance handshake packets between source and receiver is successful. Let this minimum allowable distance be denoted by R_i. Define the *interference range ratio*, γ, as

$$\gamma = R_i/d. \tag{3.3}$$

The interference range ratio, γ, is the fundamental quantity of interest in this chapter: it determines the effectiveness of the collision-avoidance protocol. In general, RTS/CTS effectiveness is higher when γ is lower.

The simple channel model here, with spreading only, and no absorption or ambient noise, gives a constant value for the interference range ratio, $\gamma_o = T^{1/k}$. Xu et al. use a detection threshold of $T = 10$ dB and a simple single spreading exponent model with $k = 4$, from the two-ray ground-reflection model [94]. The interference range ratio is therefore $\gamma_o = 1.8$. Even at this relatively small value of γ_o, Xu et al. and Ye et al. conclude that interference in RF networks can greatly reduce collision-avoidance protocol effectiveness, as detailed below.

For UANs, using the "practical spreading" model with $k = 1.5$ and again $T = 10$ dB, we have $\gamma_o = 4.6$. This results suggests that long-range interference, and reduced RTS/CTS effectiveness, will be a more significant problem in UANs than in radio-based networks.

We examine the interference range ratio γ in greater detail in the remainder of the chapter, extending it to a frequency-dependent form for more realistic UAN channel models.

3.2.1 Definition of RTS/CTS Effectiveness

The RTS/CTS effectiveness can be derived directly from the interference range ratio, γ.

Let R_{tx} be the maximum transmission range of all packets such that detection is successful. If $R_i \leq R_{\text{tx}}$, then the CTS packet will reach all potential interferers, and suppress their transmissions. If, however, $R_i > R_{\text{tx}}$, then some interferers will not be suppressed, leading to packet collisions.

The maximum separation, d, of any two communicating nodes is when $d = R_{\text{tx}}$, and so if $\gamma > 1$, then R_i can be greater than R_{tx} for some nodes in the network. In this case, the collision-avoidance protocol is not fully effective. As R_i (or γ) increases, the number of potential interferers increases dramatically, roughly as R_i^2 for a 2-dimensional network deployment with uniform node distribution. (It is possible for UANs to be 3-dimensional [89], but most applications are in fact 2-dimensional deployments.) While it is well-known that wireless network nodes do not have a circular (or spherical) coverage region [65], and that UANs can often have low node density and low offered loads [85] this approximation allows the physical analysis in this chapter, offering theoretical insight into the protocol performance.

Xu et al. define the RTS/CTS effectiveness, $E_{\text{RTS/CTS}}$, as the fraction of the interference region that is covered by the collision-avoidance RTS/CTS handshake packets. In a 2-dimensional network deployment, assuming uniform node distribution and transmission times, this is a ratio of areas:

$$E_{\text{RTS/CTS}} = \frac{A_{(i \cap \text{RTS/CTS})}}{A_i}, \tag{3.4}$$

where A_i is the area in which there could be a potential interferer, $A_{\text{RTS/CTS}}$ is the area covered by the RTS/CTS collision avoidance protocol, and $A_{(i \cap \text{RTS/CTS})}$ is the intersection of these regions. The effectiveness measure is implicitly an average over time, and assumes a high offered load in the network.

3.3 Extension of Xu et al. to UANs: Spreading Loss Only

To extend the model to underwater acoustic channels, the first step is to apply the simple "practical spreading" model [18, 112, 117], with a spreading exponent of $k \approx 1.5$ to account for the waveguide effects and low spreading losses in the underwater acoustic channel.

An additional step is required before simply changing the spreading exponent, in Xu et al.'s work, since their results make the assumption that Scenario IIb shown in Figure 3.1c does not occur. Scenario IIb can often occur in underwater acoustic channels, however. In Appendix E to this chapter, we generalize Xu et al.'s results to cover Scenarios I, IIa, and IIb.

3.3.1 RTS/CTS Effectiveness

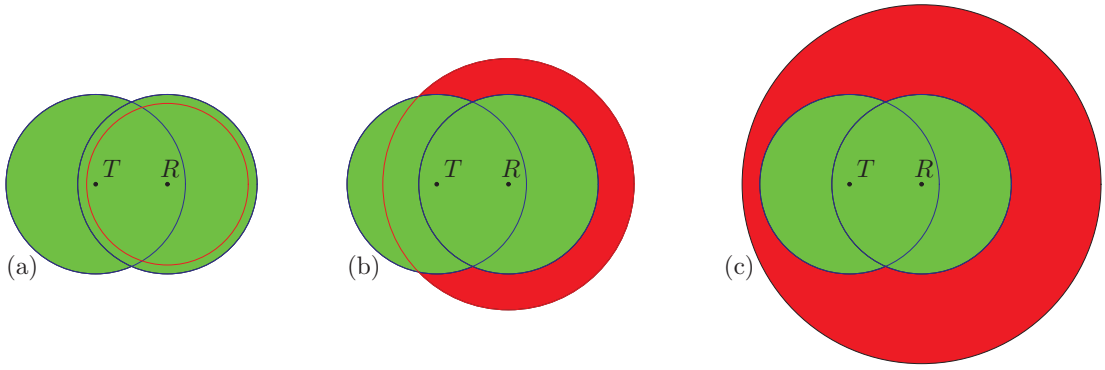

Figure 3.1. Three scenarios: (I) Interference range R_i is less than transmission range R_{tx}, and all potential interferers suppressed by the RTS/CTS handshake; (IIa) Some of the potential interferers are not suppressed by the RTS/CTS handshake (red); (IIb) Many potential interferers not suppressed (red). Scenario IIb is not considered in previous radio-based work.

Figure 3.1 illustrates the three possible scenarios when comparing the distances of the source, receiver, and interferer:

I: $0 < R_i < R_{\text{tx}}$: the spatial range of CTS packets covers all potential interferers.

IIa: $R_{\text{tx}} < R_i < R_{\text{tx}} + d$: the range of CTS packets covers most of the area from which third parties can interfere; Xu et al.'s approximation applies.

IIb: $R_{\text{tx}} + d < R_i$: The range of CTS packets covers a small fraction of the area from which third parties can interfere. Generally does not occur in RF networks, and Xu et al.'s approximation does not apply.

Note that in RF networks with $k = 4$ and a detection threshold of $T < 12$ dB, Scenario IIb does not occur, and so it is not analyzed in previous work. Xu et al. and Ye et al. use an approximation for $A_{(i \cap \text{RTS/CTS})}$ based on an idealized circular geometry for wireless range that only is valid for Scenario IIa. When Scenario IIb does occur, as it will for most underwater networks, that approximation will lead to a discontinuity in $E_{\text{RTS/CTS}}$.

In Appendix E, we derive a new calculation of $A_{(i \cap \text{RTS/CTS})}$, exact for the idealized case of circular transmission ranges, that is valid for all three scenarios. For the simplified channel model (*i.e.* without considering absorption or ambient noise), we use the results from the appendix to plot $E_{\text{RTS/CTS}}$ for RF and underwater acoustic networks in Figure 3.2. We set the detection threshold $T = 10$ dB, and use spreading exponents of $k = 4$ and $k = 1.5$, respectively. In Figure 3.2, the dashed line shows the values obtained by Xu et al.'s approximation, and the solid lines are the result of our calculation. In underwater acoustic networks, the approximation in Xu et al.'s results would lead to incomplete results and a discontinuity for the RTS/CTS effectiveness.

Figure 3.2 replicates Xu et al.'s results, and extends them to a simple underwater acoustic channel model, with spreading losses only. In an RF network, when the source/receiver pair are in Scenario I (i.e., when d/R_{tx} is less than about 56% for $T = 10$ dB) then the RTS/CTS collision avoidance protocol is fully effective — all potential interferers are suppressed. For larger source-to-receiver separations, the RTS/CTS protocol becomes increasingly ineffective. For RF networks with detection threshold $T < 12$ dB, the network will always be in Scenarios I or IIa, as Figure 3.3a illustrates graphically.

For UANs, however, with a typical spreading loss of $k = 1.5$ and using a detection threshold of $T = 10$ dB, the results for the simple spreading-only model considered in this section would suggest that the RTS/CTS collision avoidance protocol starts losing effectiveness when d/R_{tx} is larger than about 22%. The collision-free region would therefore cover less than 5% of the area within the maximum transmission range.

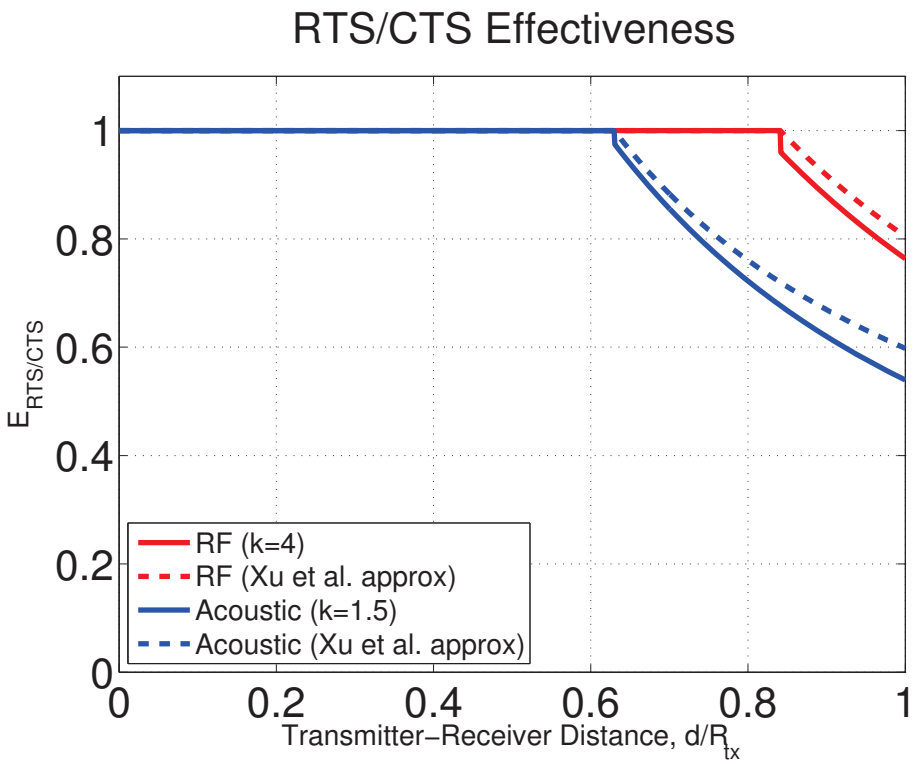

Figure 3.2. RTS/CTS effectiveness in underwater networks is hurt significantly by long-range interference. The dashed lines use the approximation in [135] and [136], and the solid lines use the equations derived in Appendix E. The plot assumes $T = 10$ dB and no absorption or ambient noise.

3.3.2 Effects of Detection Threshold on γ_o

For their analysis of radio-based networks, Xu et al. assume a detection threshold of $T = 10$ dB, and they do not analyze the effects of varying the detection threshold on spatial reuse.

In UANs, a 10 dB detection threshold would lead to a large interference range ratio γ_o and hence low spatial reuse, according to the simple spreading-only model used in this section. Figure 3.3b shows that γ_o increases sharply with an increasing detection threshold T. For RTS/CTS MAC protocols to have high effectiveness, it is therefore *important to minimize the packet detection threshold.*

The WHOI Micromodem-1 [36] implements two modulations, frequency-hopped frequency-shift keying (FH-FSK) and quadrature phase shift keying (QPSK or more generally, PSK).

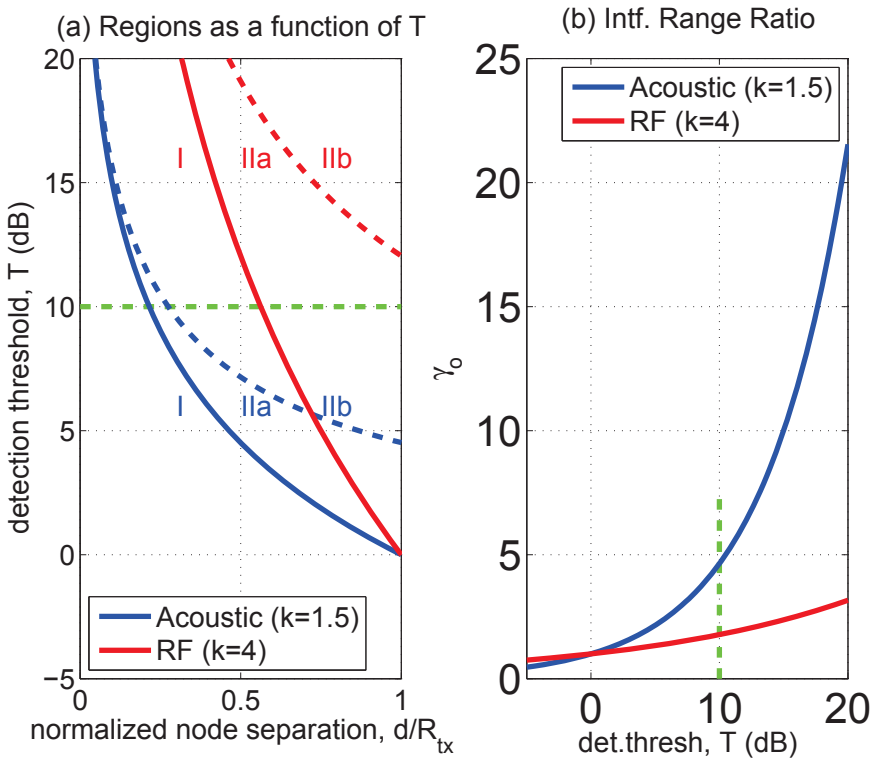

Figure 3.3. (a) Regions for Scenarios I, IIa, and IIb as a function of detection threshold (T on vertical axis). See Figure 3.1 for scenario definitions. Solid lines separate Scenarios I and IIa, while dashed lines separate Scenarios IIa and IIb. For the underwater acoustic networks, the lines separating the scenarios are blue, and for radio networks, the lines are red. (b) Interference range ratio γ_o as a function of detection threshold T. In both (a) and (b), the green dashed line indicates $T = 10$ dB. These plots are valid only for no ambient noise and no absorption; see Figure 3.6 for the case with ambient noise and absorption.

Incoherent detection methods, such as detecting the start of the packet by detecting a coded pattern of of FH-FSK tones, generally have low detection thresholds, which can be 3 dB or less [92]. As shown in Figure 3.3, with a low detection ratio, the interference range ratio γ will be small, allowing significant spatial reuse.

For PSK-modulated data packets, the standard detection and synchronization signal used by the Micromodem-1 (a linear frequency-modulated sweep) has had its software-configurable processing gain increased to drop the detection threshold from its original value of about 7 dB down to its present default value of approximately 0 dB, to allow communication to be detection-limited when

using lower-rate error-correcting codes. As a side benefit, with about a 0 dB detection threshold, spatial reuse will not be appreciably reduced.

There are, however, other underwater acoustic modems focusing on low-power detection states which in some cases are planning to use analog in-band energy detectors [134]. An analog in-band energy detector will likely require a detection threshold of 10 dB or higher, increasing the interference range ratio γ and reducing spatial reuse.

The results presented in the remainder of this chapter use a detection threshold of 10 dB, for comparison more directly with Xu et al.'s results, to highlight the importance of low detection thresholds in underwater acoustic modems, and to show the effects of spreading losses and spreading loss models more clearly than with a lower detection threshold.

3.4 Incorporating Spreading, Absorption, and Ambient Noise into Model

In the previous section, we extended the analysis from Xu et al. a closed-form solution for γ_0 using a simple channel model with spreading only. In this section, we introduce a more realistic underwater acoustic channel model, incorporating frequency-dependent absorption losses and frequency-dependent ambient noise. For this case, we are only able to solve for $\gamma(f, d)$ with a numerical solution, though we can find approximate analytic solutions using physical reasoning in several limiting cases.

Absorption losses are a significant effect, and must be included in the channel model, especially at higher frequencies. Ambient noise from ships, wind-driven waves, rain, shrimp, etc. is a fundamental part of the natural acoustic environment and cannot be neglected. Following Stojanovic [117], we use Thorp's expression[1] for the frequency-dependent acoustic energy absorption coefficient, $\alpha(f)$, which is generally expressed in dB per unit distance. To model ambient noise power, $\sigma_N(f)$, we use the empirical power spectral density (PSD) from Coates [18, 112, 117], parameterized by wind speed and an empirical shipping factor between 0 and 1. In the analysis in this chapter, we use a

[1] Marsh and Schulkin [12] offer an alternative to Thorp's expression that can be more accurate for frequencies above about 3 kHz, with somewhat lower absorption, but Thorp's expression is easier to use, since it depends only upon frequency. Alternative models for absorption coefficients depend upon temperature, depth, and other parameters.

wind speed of 3 m/s and a shipping factor of 0.5. We integrate this PSD across a bandwidth of 1/3 of the center frequency, which is typical of acoustic transducers used in UANs.

For our spreading model, at first we again use the "practical spreading" model, with a spreading exponent of $k = 1.5$. In Section 3.5, we analyze the MAC-layer implications of the alternate mixed-exponent spreading model studied in Chapter 2, which has lower spreading losses for interfering packets and higher spreading losses for packet detection.

The analysis in this chapter does not use transmit power control, since we are using the WHOI Micromodem-1 as our underwater acoustic modem model. We use a fixed transmit power of 185 dB re:1μPa@1m, a typical value for underwater acoustic modems.

3.4.1 Calculating $\gamma(f, d)$

By including absorption and ambient noise, γ is no longer a constant. In this extended model, $\gamma(f, d)$ is a function of frequency f and source-receiver separation d. We start with the condition for detection $T \leq \text{SINR}$ (Eq. 3.1). This expression achieves equality for the minimum allowable SINR for detection, which occurs at the minimum allowable interferer range, R_i:

$$T = \text{SINR} = \frac{P_s \; S_o(d, k) \; A(f, d)}{P_i \; S_o(R_i, k) \; A(f, R_i) + \sigma_N(f)}. \tag{3.5}$$

In this expression, the transmit powers for source and interferer are P_s and P_i, respectively. In all plots in this section, we set $P_s = P_i$, since we are not considering transmit power control. The spreading loss factor is $S_o(r, k) = (r/r_o)^{-k}$, where r_o is a reference distance, typically taken as $r_o = 1$ m. The absorption factor is $A(f, r) = 10^{-\alpha(f)r/10}$, where the absorption coefficient $\alpha(f)$ is in dB/km, and the range r is converted to kilometers. The ambient noise power at the receiver is $\sigma_N(f)$, the power in the PSD integrated across the transducer bandwidth.

SINR is a critical metric for this chapter, but using it also has a number of practical complications, explored for radio receivers by Son et al. [111]. In practice, interference power from multiple interferers does not necessarily add linearly. There can also be hardware variation among receivers, and adding interferers can increase the effective detection threshold of the detection algorithm [111]. For the purposes of this chapter, we consider a single interferer at range R_i and idealized receivers.

Since $R_i = \gamma\, d$, then from Eq. 3.5, we have

$$\gamma^{-k}\,(A(f,d))^{(\gamma-1)} = \frac{P_s}{P_i T} - \frac{\sigma_N(f)}{P_i\, S(d,k)\, A(f,d)} \tag{3.6}$$

In general, there is no closed-form solution of Eq. 3.6 for $\gamma(f,d)$. We solve this equation numerically, and we discuss the results below.

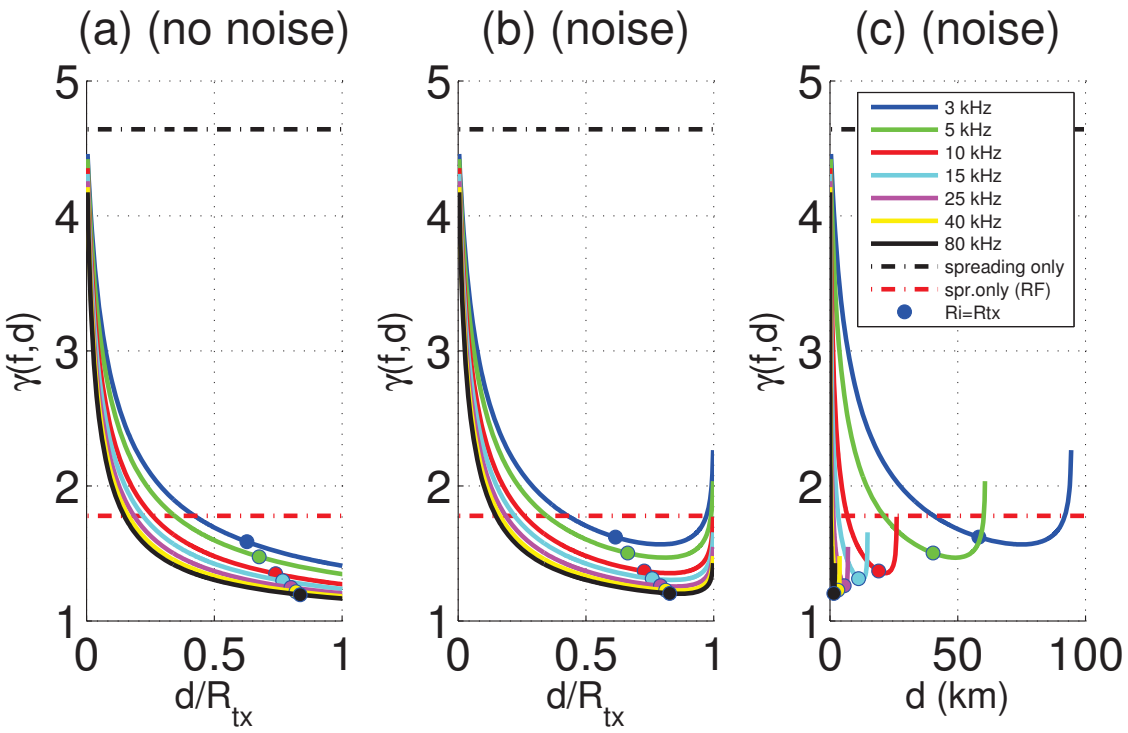

Figure 3.4. Numerical solutions for $\gamma(f,d)$ for the spreading model $k = 1.5$, with absorption, for several frequencies. (a) is without ambient noise; (b) includes ambient noise. The dashed lines show comparisons with the case of spreading losses only, where γ_o is constant; the black dashed line is for underwater acoustic networks, and the red dashed line is for radio networks. The circles show the node separation, d, where the minimum allowable interferer range equals the maximum packet transmission range. For larger node separations, the RTS/CTS effectiveness starts to drop.

3.4.2 Effects of Ambient Noise and Absorption

Absorption and ambient noise add strong frequency-dependent effects to the interference range ratio, $\gamma(f,d) = R_i/d$. Figure 3.4 shows $\gamma(f,d)$ for typical acoustic communication frequencies ranging from 3 kHz to 80 kHz for a spreading exponent of $k = 1.5$. Figure 3.4a shows $\gamma(f,d)$ *without* ambient noise, while Figure 3.4b shows $\gamma(f,d)$ *with* ambient noise, to help distinguish the effects of each component of the channel model. We examine the results in three parts: small, intermediate, and large node separations.

For small node separations, spreading losses dominate. In that case, absorption and ambient noise can be neglected, and γ approaches γ_o. This effect can be seen in both Figures 3.4a and 3.4b.

For intermediate node separations, the interferer's absorption losses dominate the interferer's spreading losses. Therefore, the interferer's absorption losses largely determine the shape of the $\gamma(f,d)$ curves in Figure 3.4. If we neglect ambient noise (letting $\sigma_N(f) = 0$), and focus on the intermediate separation distances, we can ignore the interferer's spreading term γ^{-k} in Eq. 3.6. In that case, $\gamma(f,d)$ for intermediate node separations can be approximated as

$$\gamma(f,d) \approx 1 + \left(\frac{10\log_{10}(T)}{\alpha(f)}\right)\frac{1}{d}. \tag{3.7}$$

Spreading losses are polynomial in range, whereas absorption losses are exponential in range (*i.e.*, for range r, spreading losses scale as r^{-k}, and absorption losses scale as $10^{-\alpha(f)r/10}$). For all but the smallest node separations, therefore, this intermediate case applies, and $\gamma(f,d)$ scales as $1/d$ in this region.

When node separations are large and approach the maximum transmission range, ambient noise starts to increase $\gamma(f,d)$ significantly. This effect can be seen by comparing Figures 3.4a and 3.4b.

The maximum transmission range is when no interferers are present, so the signal-to-noise ratio equals the detection threshold, i.e., $T = \text{SNR}$. In that case, R_{tx} is the numerical solution of Eq. 3.5, with $P_i = 0$:

$$\left(\frac{R_{\text{tx}}}{r_o}\right)^{-k} A(f, R_{\text{tx}}) = \frac{T\,\sigma_N(f)}{P_s}. \tag{3.8}$$

As the node separation approaches the maximum transmission range, even a small amount of interference will prevent detection. Therefore, the minimum allowable distance from the receiver to an interferer for successful detection will approach infinity. So, when ambient noise is included in the model, $\gamma(f, d)$ will approach infinity as the node separation approaches the maximum transmission range.

One way to avoid the susceptibility of widely separated nodes to ambient noise is to set the UAN's routing tables so that packets are not routed on links whose node separation approaches the maximum transmission range. This is a caveat to the general idea that one should route over long hops in a wireless network [2].

The competing effects of absorption and ambient noise lead to the minimum in $\gamma(f, d)$ apparent in Figure 3.4b.

3.4.3 RTS/CTS Effectiveness with Absorption and Ambient Noise

The RTS/CTS MAC protocol can avoid all collisions only if all potential interferers can detect the RTS or CTS successfully. Since interference occurs at the receiver, it is especially important that a potential interferer can detect the CTS packet. Section 3.2 introduces the RTS/CTS effectiveness metric, $E_{\mathrm{RTS/CTS}}$. We can derive expressions for $E_{\mathrm{RTS/CTS}}$ and the regimes of node separations over which each expression applies (see Figure 3.3a and Appendix E for the details). Given a node separation d, we can calculate the interference range, $R_i = \gamma(f, d)\, d$, where $\gamma(f, d)$ is the numerical solution of Eq. 3.6, plotted in Figure 3.4. From Eq. 3.8, we can calculate the maximum transmission range, R_{tx}.

In the expressions for $E_{\mathrm{RTS/CTS}}$, the terms $A_i = \pi R_i^2 = \pi \gamma^2 d^2$, and both $A_{\mathrm{RTS/CTS}}$ as well as $A_{(i \cap \mathrm{RTS/CTS})}$, are derived analytically in Appendix E to this chapter. We can then calculate $E_{\mathrm{RTS/CTS}}$ for a given frequency f as a function of node separation d, up to the maximum node separation, R_{tx}. This function is plotted in Figure 3.5.

Since the absorption reduces $\gamma(f, d)$ compared with the spreading-only case, $E_{\mathrm{RTS/CTS}}$ is improved compared with the spreading-only case, as shown in Figure 3.5. When ambient noise is

included, $E_{\text{RTS/CTS}}$ drops for node separations which approach the maximum transmission range, shown in Figure 3.5b. Effectiveness is lower for lower acoustic frequencies.

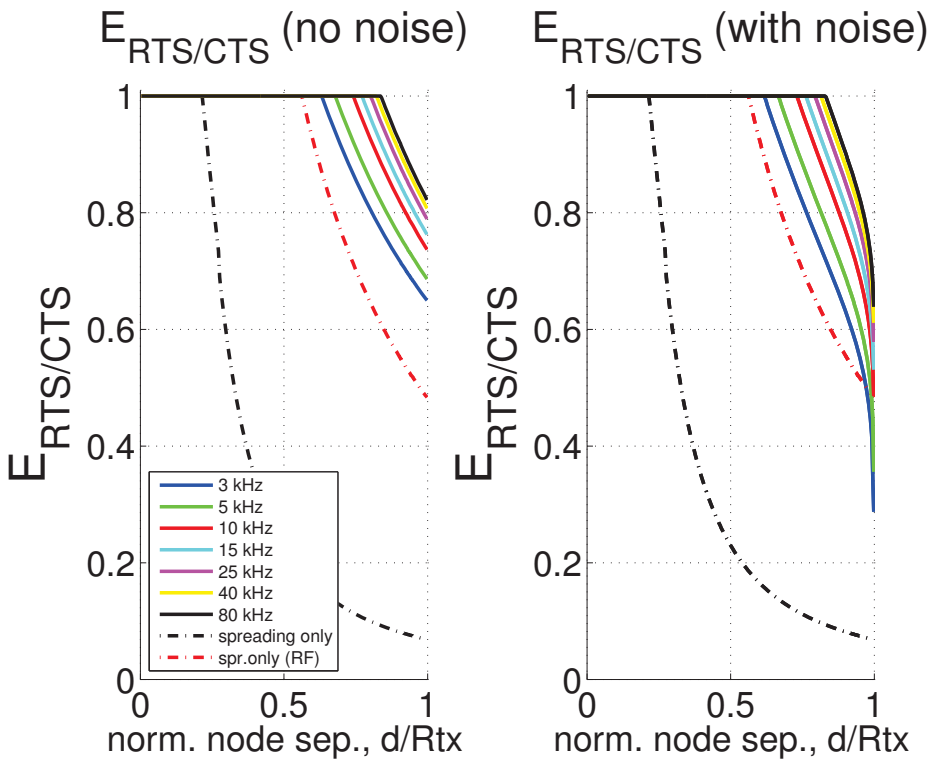

Figure 3.5. $E_{\text{RTS/CTS}}$, calculated with $\gamma(f,d)$ from Figure 3.4 for several frequencies, with spreading and absorption losses. (a) is without ambient noise, while (b) includes ambient noise. The dashed lines show the cases with spreading losses only, in black for UANs ($k = 1.5$) and in red for radio networks ($k = 4$). The plot legends are the same for both (a) and (b).

3.4.4 Effects of Detection Threshold on $\gamma(f,d)$

In Section 3.3.2 and Figure 3.3b, we show the effects of detection threshold T on γ_o in the simple spreading-only channel model. With absorption and ambient noise, the results are similar: $\gamma(f,d)$ increases rapidly with increasing detection threshold. Figure 3.6 plots $\gamma(f,d)$ as a function of detection threshold for several frequencies, and for both the "practical spreading" model with $k = 1.5$ as well as the alternate mixed-exponent spreading model introduced in Section 3.5.

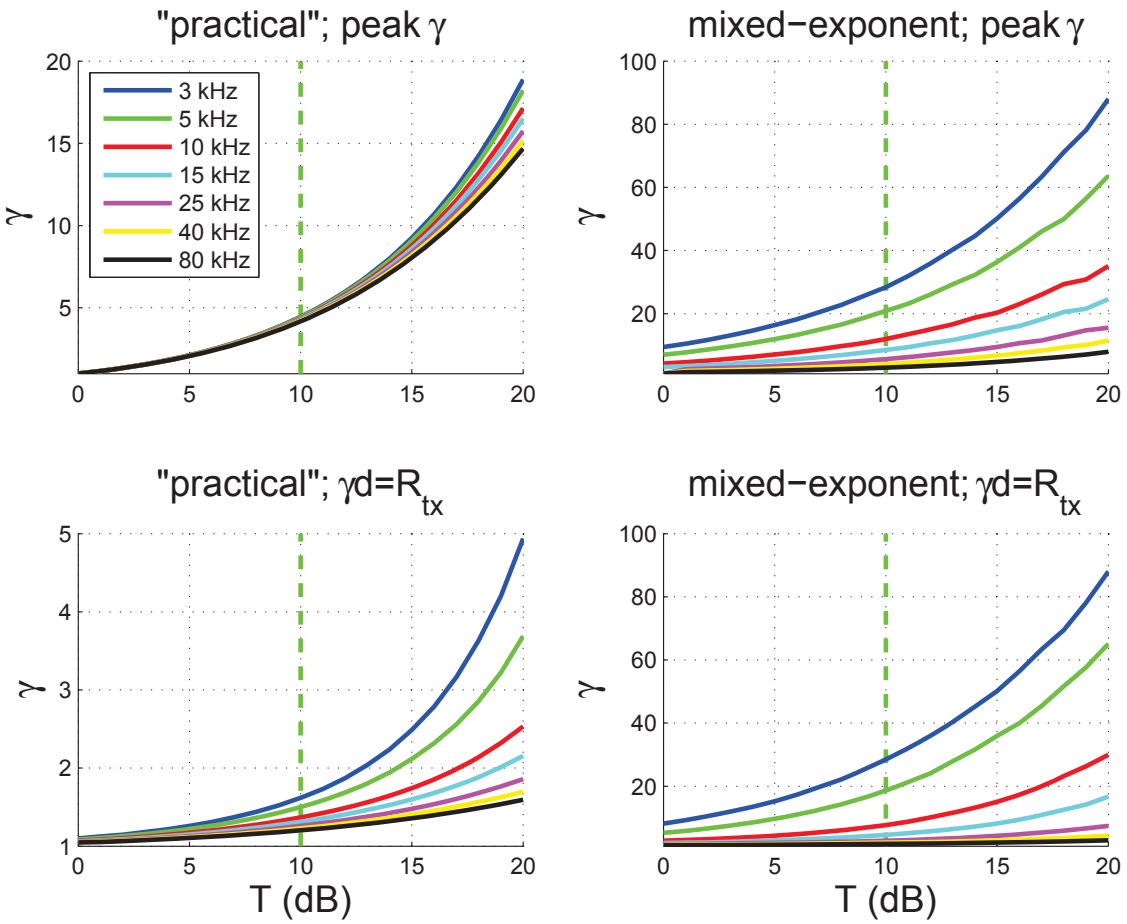

Figure 3.6. $\gamma(f, d)$ as a function of detection threshold T for several frequencies, with absorption and ambient noise, for both the "practical" $k = 1.5$ spreading model and mixed-exponent spreading model (see Section 3.5). The plots labeled "peak γ" show the highest values of γ in Figures 3.4 and 3.8, as a function of detection threshold, even if RTS/CTS is not necessarily reduced. The plots labeled "$\gamma d = R_{\text{tx}}$" show the highest value of γ which reduces RTS/CTS effectiveness, (*i.e.* where the minimum allowable range to an interferer, $R_i = \gamma d$, begins to exceed the maximum packet transmission range R_{tx}), again as a function of detection threshold. The green dashed vertical lines mark the case $T = 10$ dB. Note different vertical scales of the plots.

3.4.5 Visualization of Unsuppressed Interferers

The effectiveness of the RTS/CTS collision-avoidance protocol depends upon suppressing potential interferers. Figure 3.7 allows visualization of the unsuppressed interferers, which are the cause of reduced RTS/CTS effectiveness. The figure plots the "operating regime" of UANs, namely

the maximum link range (maximum detection range) as a function of communications band center frequency: links below the maximum link range curves, shown as solid lines, are realizable and useful in UANs. In contrast, nodes in the region above the maximum link range curves cannot detect the RTS/CTS handshake packets, and therefore are unsuppressed potential interferers.

The dashed curves in Figure 3.7 show the range at which spreading loss equals absorption loss; below the dashed curves, spreading loss is the larger component of pathloss, and above the curves, absorption loss is the larger component. Spreading loss is polynomial in increasing range, and absorption loss is exponential in increasing range. Therefore, as range to an interferer increases into the region where absorption loss dominates, interfering packets become strongly attenuated and will no longer disrupt detection of desired packets at the intended receiver.

The region of Figure 3.7 between the maximum packet detection range and the range at which spreading loss equals absorption loss is where unsuppressed interfering nodes exist. These unsuppressed interferers are too far away to detect the RTS/CTS collision-avoidance packets, but are close enough to disrupt detection of desired packets at the intended receiver.

At lower frequencies, and especially with the mixed-exponent spreading model discussed in Section 3.5, there can be a significant number of potential unsuppressed interferers, leading to increased interference range ratio $\gamma(f, d)$ and hence decreased RTS/CTS effectiveness. The details of the spreading model are therefore signficant in determining spatial reuse in a UAN.

Providing more details for Figure 3.7, the detection range is determined in turn by the detection threshold (0 dB and 10 dB are plotted), the spreading model (both the "practical spreading" model and the mixed-exponent model introduced in Section 3.5 are plotted), the absorption model (Thorp's expression [117]), a typical transmit power level (185 dB re:1μPa@1m), and the ambient noise (Coates's parameterized Wenz curves [18], using a wind speed of 3 m/s and an empirical "shipping factor" of 0.5) along with the transducer bandwidth (using a typical quality factor of $Q = 3$).

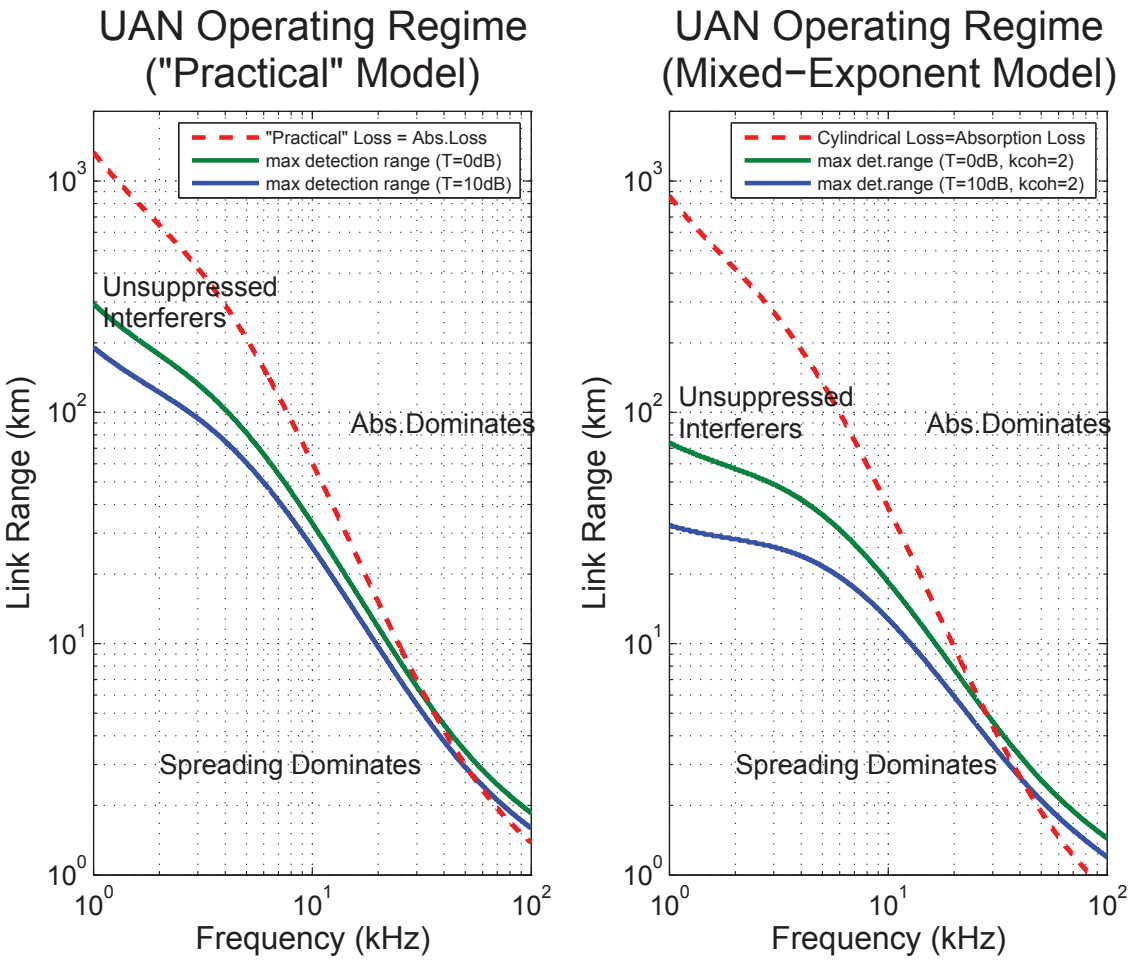

Figure 3.7. Operating regime for underwater acoustic networks, for the "practical" spreading model (left), and the mixed-exponent spreading model described in Section 3.5. The blue solid line shows the maximum link range for a given acoustic frequency with a packet detection threshold of 10 dB, Thorp's absorption loss, Coates's parameterized ambient noise model (with wind speed of 3 m/s, empirical shipping factor of 0.5, and transducer quality factor of $Q = 3$), and a transmitter power level of 185 dB re:1μPa@1m. The green solid line shows the maximum link range for a detection threshold of 0 dB. The red dashed line shows the range at which the spreading loss equals the absorption loss; below the line, spreading losses are more significant, and above the line, absorption losses dominate. The unsuppressed interferers are located at ranges larger than the maximum detection range, but before absorption losses reduce the interference energy to a negligible level. At lower frequencies, there are significant unsuppressed interferers, especially in the mixed-exponent spreading model. The absorption loss provides the ultimate limit on the maximum link range, but for links within the UAN operating regime, spreading losses are larger than absorption losses in general, so the details of the spreading model are significant to network performance.

3.5 Mixed-Exponent Spreading Model

The so-called "practical spreading" approximation of $k \approx 1.5$ is a widely used spreading model for point-to-point underwater communication links [18,112,117]. The details of the spreading model are generally not significant in point-to-point acoustic communications research, but *the spreading model is significant for understanding interference in a network*.

In Chapter 2, we have presented an alternative spreading model called the *mixed-exponent spreading model*, detailed in Section 2.3. The mixed-exponent spreading model applies to acoustic modems which use a low-power wakeup detector based on a matched-filter detector. For example, the WHOI Micromodem-1 [36], which is a common underwater acoustic modem for UANs, uses this method. The mixed-exponent model includes different spreading exponents for packet detection and for interference, reflecting the Micromodem-1's signal processing for packet detection.

In the previous chapter, we showed from both experimental and numerical results that there can be different exponents for packet detection and interference. We also validated the waterdepth- and bandwidth-dependence of the mixed-exponent model for uniform soundspeed profiles with numerical modeling. In this chapter, we present results showing that, with the mixed-exponent spreading model, the RTS/CTS effectiveness can be very low, especially for UANs transmitting on lower frequencies.

The $k \approx 1.5$ "practical spreading" model is not solidly grounded, but has been considered adequate for underwater acoustic communications because other physical channel effects are much more significant, though this is not necessarily true at the network layer. On the other hand, numerical acoustic propagation models [79] are fairly well-accepted, but do not aid intuition and analysis for understanding the physical channel's effects upon spatial reuse in RTS/CTS-based MAC protocols.

Energy from a point source transmitter in an idealized channel of very deep, uniformly mixed water will experience spherical spreading, such that $k \approx 2$. In most situations, however, multipath effects from either shallow water reflections or a deep-water refractive sound channel will lead to waveguide effects reducing the effective spreading exponent. In the idealized case of shallow water with a perfectly reflecting lossless surface and bottom, the *incoherent* sum of the energy from a

point source will experience cylindrical spreading, such that $k \approx 1$, at large ranges relative to the water depth. The practical spreading model with $k \approx 1.5$ is simply an average of cylindrical and spherical spreading, as a first-pass approximation for system design [18].

3.5.1 Signal Spreading During Packet Detection

To minimize energy use, during packet detection, the WHOI Micromodem-1 runs a low-complexity, low-power-consumption matched-filter detector to detect a known wakeup signal. Upon detection of the wakeup signal, the primary communcations receiver is enabled.

As described in Section 2.3, the packet detection detects on the energy from just a *single* peak in the impulse response, corresponding to one multipath arrival or perhaps several non-resolved multipath arrivals. When the Micromodem-1 detects the start of a data packet, the detection signal's effective spreading loss is hypothesized to be the spreading loss experienced by a single peak in the impulse response, and accordingly $k_p \approx 2$; the subscript p is for packet detection.

Beyond a certain range, however, separate multipath arrivals become unresolvable, and they coherently combine in the received signal. As described in Section 2.3, beyond this transition range, the coherent detection energy exponent transitions from a spherical-spreading regime ($k_p \approx 2$) to a regime with $k_p \approx 1.5$. This transition range increases linearly with bandwidth and quadratically with waterdepth, and is discussed in the previous chapter.

Detection generally is the limiting factor for most packets, since the error-correction coding can be designed appropriately so that essentially all detected packets can be decoded successfully.

3.5.2 Interference Spreading During Packet Detection

As described in Section 2.3, with a matched-filter detector as in the Micromodem-1, interference is received via all multipath arrivals and combines as noise, degrading the SINR and limiting the detection of desired signals. The energy from these arrivals is combined incoherently to determine the interference level.

There still is, however, a transition range for the interference spreading exponent k_i. At small ranges relative to the waterdepth, w_d, the interference has not yet interacted with the boundaries and so spreads spherically. As the range increases, the acoustic paths start to reflect from the

boundaries and the spreading exponent decreases away from spherical spreading and towards cylindrical spreading. The transition range for interference is therefore on the order of the waterdepth. (Similarly, in deep water, the transition range for the interference would be the vertical extent of the refractive sound channel for a given interferer.)

3.5.3 Mixed-Exponent Spreading Model Equations

The mixed-exponent spreading model is detailed in Section 2.3, and summarized in Section 2.3.3.

The form of the mixed-exponent spreading model is

$$S_m(r, r_T, k_2, k_1) = \begin{cases} \left(\frac{r}{r_o}\right)^{-k_2} & r < r_T \\ \left(\frac{r_T}{r_o}\right)^{-k_2} \left(\frac{r}{r_T}\right)^{-k_1} & r \geq r_T \end{cases} \tag{3.9}$$

where r is the range from transmitter to receiver (ignoring slant range for the time being), r_o is a reference distance (typically 1 m), r_T is the transition range from spherical spreading. The spreading exponent before the transition range is roughly spherical, $k_2 \approx 2$. After the transition range, the interference spreading exponent is roughly cylindrical, $k_1 \approx 1$, while the detection spreading exponent beyond the transition range is roughly $k_1 \approx 1.5$.

For packet detection, we hypothesize that the transition range, developed in the previous chapter, increases linearly with bandwidth and quadratically with waterdepth, *i.e.* $r_{Tp} \sim \frac{w_d^2 B}{2c}$.

For interference, we hypothesize that the transition range from spherical to cylindrical spreading occurs at a range of the order of the waterdepth, *i.e.* $r_{Ti} \sim w_d$.

In general, we expect that the transition range for interference will be smaller than the transition range for packet detection, *i.e.* $r_{Ti} \sim w_d < r_{Tp} \sim \frac{w_d^2 B}{2c}$. In this case, there is a region where the spreading loss for interfering packets is less than the spreading loss for detection, which means that the RTS/CTS effectiveness will be reduced, perhaps significantly.

In situations where $B < \frac{2c}{w_d}$, however, the ordering of the transition ranges would be reversed, and the spreading loss for interference would be larger than the spreading loss for packet detection, improving spatial reuse. Such situations could include OFDM with narrow sub-bands in shallow water, or, less relevant for UANs, extremely narrowband sources such as RAFOS sources in deep

water. In the remainder of this chapter, we assume the first ordering of transition ranges, as is true for the case of a more broadband detection signal, as is currently used in the WHOI Micromodem-1.

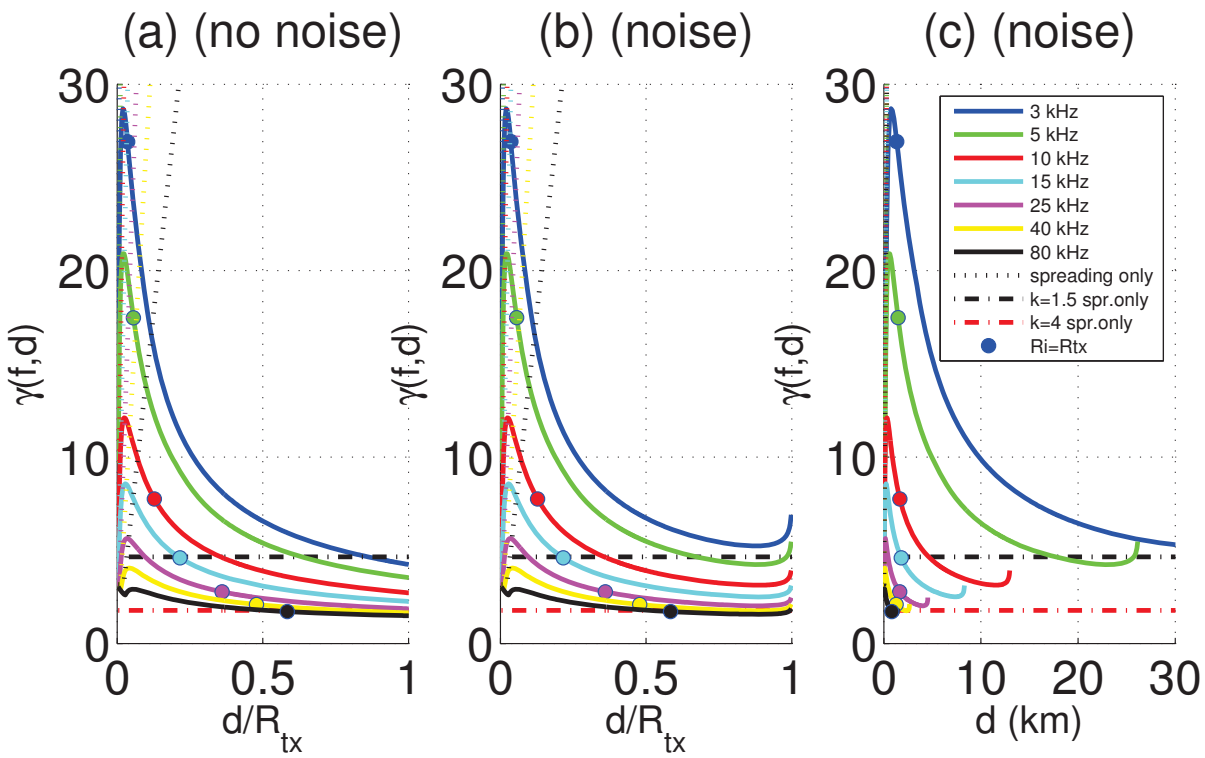

Figure 3.8. Numerical solutions for $\gamma(f,d)$ for the mixed-exponent spreading model with $k_2 = 2$, $k_{1i} = 1$, $k_{1p} = 1.5$ with absorption, for several frequencies. (a) is without ambient noise; (b) includes ambient noise. The dashed lines show comparisons with the case of spreading loss only, where γ_o is constant, the black dashed line is for underwater acoustic networks, and the red dashed line is for radio networks. The circles show the node separation, d, where the minimum allowable interferer range equals the maximum packet transmission range. For larger node separations, the RTS/CTS effectiveness starts to drop. The steep dotted lines at small node separations show the spreading-only case, a valid approximation only for small node separations; see Eq. 3.12.

3.5.4 Implications for $\gamma(f,d)$ and $E_{\text{RTS/CTS}}$

To use the interference spreading model from Eq. 3.9, we adjust Eq. 3.5 slightly:

$$T = \text{SINR} = \frac{P_s \; S_m(d, r_{Tp}, k_{2p}, k_{1p}) \; A(f,d)}{P_i \; S_m(R_i, r_{Ti}, k_{2i}, k_{1i}) \; A(f,R_i) + \sigma_N(f)}, \tag{3.10}$$

Where the subscript p refers to packet detection (transition range r_{Tp}, roughly spherical spreading exponent k_{2p}, and spreading exponent $k_{1p} \approx 1.5$ beyond the transition range), and the subscript i refers to interference (r_{Ti}, $k_{2i} \approx 2$, $k_{1i} \approx 1$). As before, the node separation on the desired link is d, and the interferer is separated from the desired receiver by $R_i = \gamma(f,d)d$.

We can then numerically solve for $\gamma(f,d)$ as before. The transition ranges for both packet detection as well as interference include the waterdepth. For the results in Figures 3.8 and 3.9, we use a shallow-water environment with water depth $w_d = 100$ m, since shallow water is often the situation of most interest for littoral military operations as well as coastal environmental monitoring, two potential applications of UANs. The bandwidth, B, used in calculating the coherent transition range, r_{Tp}, is f/Q, where f is the channel's center frequency, and Q is the transducer quality factor, taken to be $Q = 3$, which is a typical value.

The notable differences between Figures 3.4 and 3.8 are that there now is a maximum $\gamma(f,d)$ value for small node separations, and that maximum can be much larger than the $\gamma(f,d)$ values for the single-exponent "practical spreading" model with $k = 1.5$. For large node separations, Figures 3.4 and 3.8 are qualitatively similar, though in Figure 3.8, $\gamma(f,d)$ remains quite large even for large node separations; for example, for center frequencies of 5 kHz and below, the minimum value of $\gamma(f,d)$ is actually larger than the value of $\gamma_o = 4.6$ calculated from a simple spreading-only channel model, applying Xu et al.'s results directly to UANs.

We can provide an intuitive physical explanation for the maximum in $\gamma(f,d)$, deriving its location and amplitude in terms of physical parameters of the communications channel.

For small node separations, we can ignore ambient noise, and we are in the before the detection transition range, i.e. spherical spreading for the detection energy. Then with the alternate spreading model, Eq. 3.6 from the previous section becomes

$$\gamma^{-k_{1i}} \left(A(f,d)\right)^{\gamma-1} = \frac{P_s}{P_i T} \frac{d^{(k_{1i}-k_{2p})}}{r_{Ti}^{(k_{1i}-k_{2i})}} \left(r_o^{(k_{2p}-k_{2i})}\right) \tag{3.11}$$

For very small node separations, we can also ignore absorption losses, so $A(f,d) = 1$ and drops out of the expression. In the case of very small node separations, with $k_2 = 2$ and $k_{1i} = 1$, and

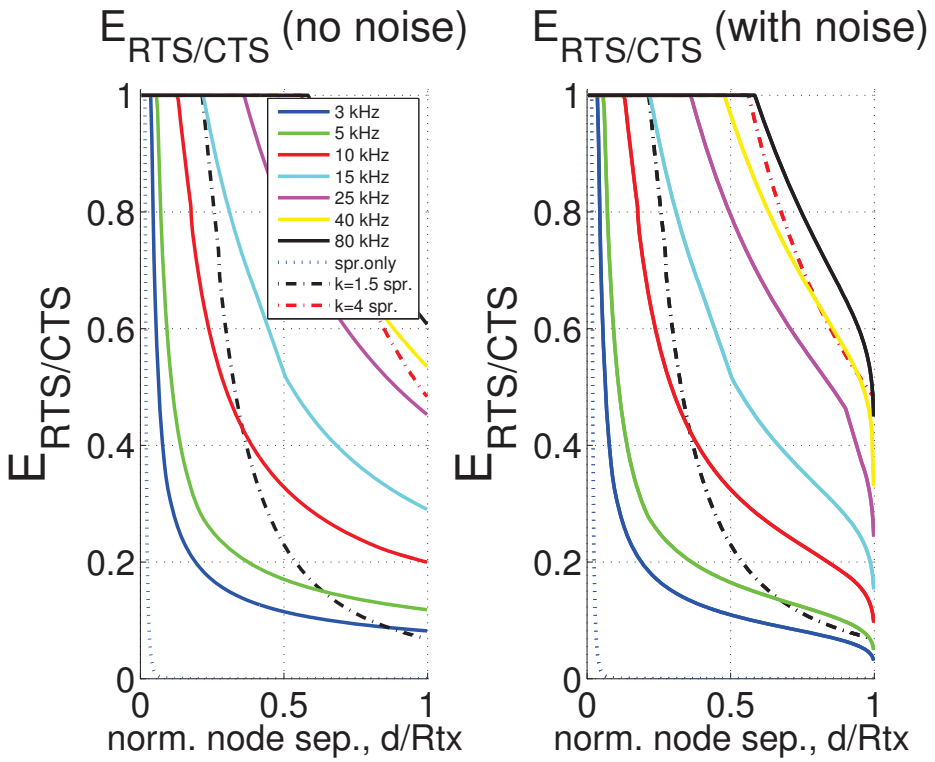

Figure 3.9. $E_{\mathrm{RTS/CTS}}$, calculated with $\gamma(f,d)$ from Figure 3.8, with absorption losses and the mixed-exponent spreading model. (a) is without ambient noise, while (b) includes ambient noise. The dashed and dotted lines show the cases of spreading losses only: the $k = 1.5$ UAN case in black dash-dots, the $k = 4$ RF case in red dash-dots, and the mixed-exponent UAN model with $k_2 = 2$, $k_{1i} = 1$, $k_{1p} = 1.5$ in dots.

with $r_{Ti} = w_d$, we have

$$\gamma \approx \left(\frac{P_i T}{P_s} \frac{d}{w_d} \right). \tag{3.12}$$

Therefore, for very small node separations, and with $k_2 = 2$ and $k_{1i} = 1$, $\gamma(f,d)$ increases approximately linearly with node separation, up to a maximum. This spreading-only approximation for $\gamma(f,d)$, valid only for small node separations, is plotted in dotted lines in Figure 3.8. The maximum occurs when spreading losses balance with absorption losses for the interferer. When the absorption losses dominate, then $\gamma(f,d)$ drops sharply, as explained in Section 3.4.

To find the maximum, $\gamma_{\max} = \gamma(f, d_{\max})$, we differentiate Eq. 3.11 with respect to d, and set the derivative of γ equal to zero. From Figure 3.8 we can see that $\gamma_{\max}$ is relatively large (so for

this analytical derivation we approximate $\gamma_{\max} \gg 1$), and the maximum occurs for small $d_{\max}$ (and so $A(f, d_{\max}) \approx 1$). Again setting $k_2 = 2$, $k_{1i} = 1$, and $r_{Ti} = w_d$, these approximations give

$$d_{\max} \approx \beta \left(\frac{P_s}{TP_i} \frac{w_d}{\alpha(f)} \right)^{1/2}, \tag{3.13}$$

where $\beta = (10 \log_{10}(\exp(1)))^{1/2}$. Plugging this value for $d_{\max}$ back into Eq. 3.12 gives an overestimate for $\gamma_{\max}$, since $\gamma(f, d)$ is convex in the neighborhood of its maximum:

$$\gamma_{\max} \approx \beta \left(\frac{TP_i}{P_s} \frac{1}{w_d \, \alpha(f)} \right)^{1/2}. \tag{3.14}$$

This result gives an intuition for which physical parameters control the amplitude and location of the maximum in $\gamma(f, d)$. Specifically, the maximum value of $\gamma(f, d)$ increases with increasing detection threshold, and decreases with increasing waterdepth and frequency.

With the mixed-exponent spreading model, $\gamma(f, d)$ obtains much higher values than it does with the "practical spreading" model. As a result, we see significantly lower RTS/CTS effectiveness, as shown in Figure 3.9b. For low frequencies, the MAC effectiveness is particularly low. The plot shows center frequencies as low as 3 kHz. These are realistic frequencies for actual UANs; for instance, the PLUSNet deployment [51] includes a long-range channel with a center frequency of about 3 kHz.

The maximum values of $\gamma_{\max}$ do not always reduce RTS/CTS effectiveness, because $E_{\mathrm{RTS/CTS}}$ is only reduced when there are unsuppressed interferers, *i.e.* $\gamma d = R_i > R_{\mathrm{tx}}$. The circles in Figure 3.8 show the node separation d where $\gamma d = R_{\mathrm{tx}}$; for smaller node separations, even though $\gamma(f, d)$ may be large, the RTS/CTS effectiveness is not reduced.

One implication of Figure 3.9b is that for multiband UANs [51, 106], different bands might use different MAC protocols. For certain deployments, RTS/CTS effectiveness might be considered acceptable on a high-frequency band, which would have small node separations, reducing the propagation delays. But it might be unacceptable for the low-frequency bands, with long node separations and the double penalty of low $E_{\mathrm{RTS/CTS}}$ due to spreading effects, and low throughput due to propagation delays.

3.6 Simulations

To validate our numerical results, we extended the Castalia/ OMNET++ simulator (version 3.1, `http://castalia.npc.nicta.com.au`) to include the underwater acoustic physical channel model described above, with spreading, absorption, and ambient noise. Absorption is simulated according to Thorp's expression, and we parameterize noise by the same values as in Section 3.4, using the empirical PSD in Coates [18, 117]. The modifications we made to adapt Castalia-v3.1's wireless channel model to the underwater acoustic channel are in Appendix F.

The main goal of the simulations was to calculate $\gamma(f, d)$, and therefore the key measurement is the interference range, R_i. By definition, any interferer within the interference range will prevent packet detection, preventing the RTS/CTS handshake from completing.

To measure the minimum allowable interference range, we ran simulations with three nodes. Node 1 and node 2 were a source and receiver pair. They attempted to complete data transfer handshakes with RTS/CTS/DATA/ACK control packets, with node 2 receiving the DATA packet. The third node was placed co-linearly with the first two nodes, with the receiver node in the center. Node 3 transmitted an interfering data packet with a duration equal to the length of the simulation. Node 3 started at a very large separation where it did not affect packet detection at Node 2, and gradually moved closer until its interference prevented packet detection at Node 2.

The parameters for a simulation run included the following. (1) The frequency f of the transmitted data and interference packets. We varied f from 3 kHz to 100 kHz, closely matching the analytical plots. (2) The spreading model. Using Equation 3.9, in one group of runs, we set $k = 1.5$; in the second, we set $k_2 = 2.0$ and $k_1 = 1.0$. Note that using a coherent packet detection spreading exponent of $k_{1p} = 1.0$ rather than $k_{1p} = 1.5$ does not visibly change the plots in Figures 3.8 and 3.9, and is not expected to change the results shown in Figure 3.10 either.

(3) The separation distance d of the source and receiver pair (labeled *node separation* on the x-axis) (4) The distance r between the interfering node and receiver. (5) Communication channel parameters such as detection threshold and fixed transmit power, as in Section 3.4.

For each frequency f and source-receiver separation d, we ran simulations where Node 3 gradually reduced its interferer-receiver separation r. The last value of interferer range r for which the

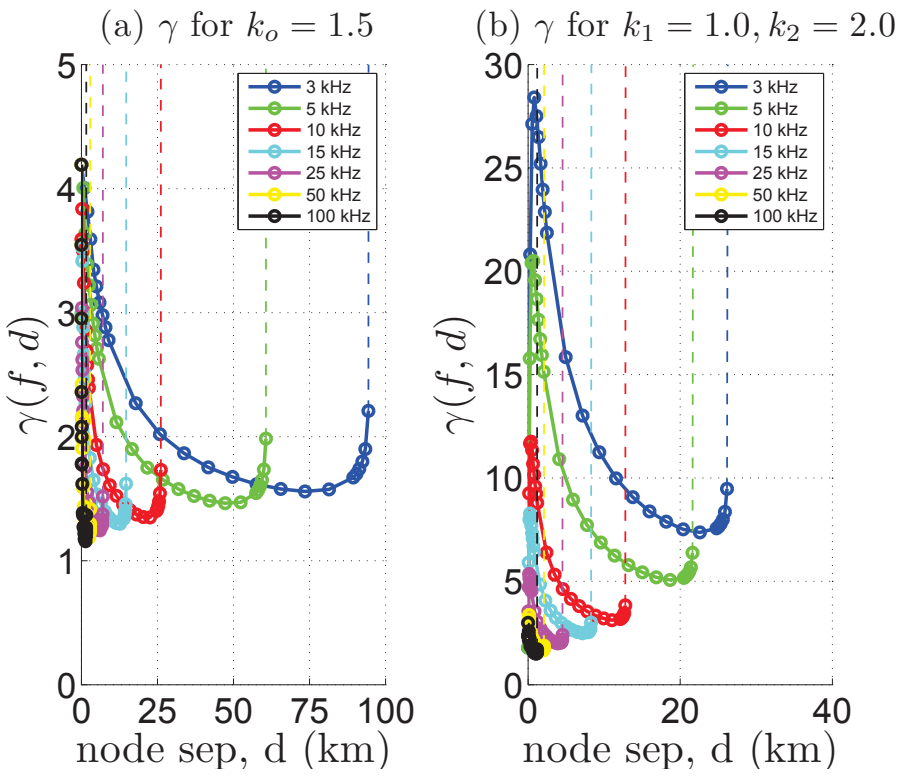

Figure 3.10. Simulation results for $\gamma(f, d)$. Note different horizontal and vertical axis scales for the two plots. Compare against Figs. 3.4b and 3.8b, respectively, which cross validate the simulation and numerical results. Note that these simulations use a coherent detection exponent beyond the transition range of $k_{1p} = 1.0$ rather than $k_{1p} = 1.5$. This does not significantly change the results, as described in the text.

RTS/CTS/DATA/ACK transaction between Nodes 1 and 2 succeeded gives an estimate of γ, *i.e.* $\hat{\gamma} = r(\text{last success})/d$.

The results in Figure 3.10a should be compared against Figure 3.4b. Figure 3.10b should be compared against Figure 3.8b. Both simulation results agree well with the numerical results.

3.7 Improving Spatial Reuse

The best and most generally-applicable long-term approach to improving spatial reuse is to implement transmitter power control. Transmit power control would improve spatial reuse, reduce

energy consumption, and reduce the probability of detection for covert communication. Linear power amplifiers are not as power-efficient as clipped non-linear power amplifiers, which are the standard power amplifiers for many energy-constrained UANs, including those based upon the WHOI Micromodem-1 [36]. Pulse-width modulation (PWM) amplifiers allow power-efficient transmit power control, however, and will likely solve many of these problems for UANs built using future underwater acoustic modems. In the meantime, however, UANs built from many existing acoustic modems, including the Micromodem-1, cannot rely on transmit power control to improve spatial reuse.

Aside from transmit power control, the main approaches to improving spatial reuse primarily center on increasing the range of the RTS/CTS handshake. While extending the range of the RTS suppresses other nodes needlessly (the "exposed terminal" problem), a CTS control packet with range equal to the interference range would suppress only potential interferers, since interference occurs at the receiver.

Successful detection is usually the limiting factor in determining the maximum successful transmission range of a packet when the error-correcting coding is designed appropriately. To increase the maximum transmission range of a packet with a fixed detection threshold T, we need to increase the SINR at the receiver for the start-of-packet synchronization signal. This is usually done by increasing the transmitter power or by increasing the time duration of the synchronization signal. Alternately, the frequency band of the packet might be shifted, generally to a band with less absorption (lower frequencies), though in some situations shifting to a higher-frequency band would help, since there is generally less ambient noise at higher frequencies. At higher center frequencies of about 40kHz, typical transducer bandwidths (with quality factor $Q \approx 3$) are wide enough to potentially allow a shorter-range channel (for data and RTS) and a longer-range channel (for CTS) with a single transducer, which might be a future possibility. Similarly, new single-crystal transducers can be very broadband ($Q \lesssim 2$), and could support multiple channels (*e.g.* control and data) with different effective ranges.

In extending the range of the CTS signal, the minimum information that needs to be transmitted to potential interferers is the single bit that a reception is about to occur within their interference

range. The interferers do not necessarily need to decode any other information from the CTS header. This might lend itself to a very practical implementation for existing acoustic modems: right before transmitting a CTS packet, transmit a signal with high processing gain (and hence longer range). Any node detecting the CTS signal would enter a quiet backoff state, just as if it had received the CTS packet itself. This would not require any changes to the existing hardware, and would not require hardware which supports either transmit power control or frequency agility.

Finally, the mixed-exponent spreading model has significantly worse performance than the "practical spreading" model in terms of γ and spatial reuse. The primary reason is that with the mixed-exponent spreading model, packet detection uses energy from only one multipath arrival in the matched-filter detector. An alternate detector could be an autocorrelation detector: the transmitting node would send the same signal twice, separated by a lag known by the receiver. The receiver would detect when the autocorrelation at the known lag exceeded the detection threshold. This approach would have time resolution comparable to the matched-filter detector, but would also use energy from all multipath arrivals, so that there would not be a difference in effective spreading loss exponents between packet detection and interference processing.

3.8 Conclusions

Underwater acoustic networks are significantly different environments than RF networks. Our results demonstrate that RTS/CTS effectiveness in UANs is subject to frequency-dependent physical channel effects and long-range interference, and not simply acoustic propagation delays.

We significantly extended radio-based results from Xu et al., and we analyze the interference range ratio γ and its effect on RTS/CTS effectiveness.

We present a closed-form solution for γ_0 in a simple channel model, and a numerical solution for $\gamma(f, d)$ in an extended channel model. Our results show, for the "practical spreading" model, that both acoustic networks and RF networks have similar performance predictions, despite dramatically different channel models. In both cases, RTS/CTS effectiveness can drop to between 50%–90% for source and receiver separated by more than about two-thirds of the maximum packet range, depending on the frequency in the underwater acoustic case.

We also study the MAC-layer effects of using an alternative physically based spreading model that distinguishes between spreading losses in packet detection and in processing interfering packets from distant nodes, using the Micromodem-1 as a model underwater acoustic modem. The mixed-exponent spreading model allows intuition and understanding of spatial reuse and long-range interference in UANs, without relying on non-generalizable results from acoustic propagation packages.

Under the mixed-exponent spreading model, we predict that RTS/CTS effectiveness drops significantly, relative to RTS/CTS effectivess using the "practical spreading" model. For example, for the 3 kHz deployment of PLUSNet, RTS/CTS effectiveness would quickly drop to 10% after source and receiver were separated by only 20% of signal range.

We implemented our models in a network simulator, and validated that the simulation results matched our numerical results quantitatively. Finally, we suggest several possible methods of improving spatial reuse; the most effective of which would be at the physical layer. The Micromodem-1 design is frozen, but the Micromodem-2, whose design decisions are detailed in the next chapter, could implement many of the possible solutions to improving spatial reuse in UANs.

CHAPTER 4

THE MICROMODEM-2: A SCALABLE SYSTEM FOR ACOUSTIC COMMUNICATIONS AND NETWORKING

A successor to the WHOI Micromodem-1 underwater acoustic modem has recently been developed. The Micromodem-2 has the same compact form-factor as the Micromodem-1 and will support all of the existing applications for the Micromodem-1, as well as interoperate with the Micromodem-1. Existing acoustic communications protocols using phase-shift keying (PSK) as well as frequency-hopping frequency-shift keying (FH-FSK) are supported, as are navigation features including narrow-band and broadband long-baseline (LBL) navigation.

The Micromodem-2 is significantly more capable than the Micromodem-1 in computational ability and memory, bandwidth, non-volatile data storage, user expansion interfaces, and real-time clock precision. The expanded capabilities will allow new communications algorithms, modulation, error correction methods, navigation features, and networking capabilities to be implemented. The improvements in processing capability and acoustic interfaces on the Micromodem-2 allow it to operate at acoustic frequencies from approximately 1kHz to 100kHz. The significant increases in available non-volatile storage enable the Micromodem-2 to capture data in-situ for diagnostic and research purposes.

The Micromodem-2's firmware architecture is similar to the Micromodem-1's firmware architecture, using a real-time operating system based on modular signal processing blocks. It has been improved to increase modularity and facilitate future portability, and it offers significant improvements in timing for use with navigation and networking applications.

---

[1]This chapter is published in very similar form as: E.Gallimore, J.Partan, I.Vaughn, S.Singh, J.Shusta, and L.Freitag. The WHOI Micromodem-2: A Scalable System for Acoustic Communications and Networking. In *Proc. IEEE Oceans*, Sept. 2010 [48]

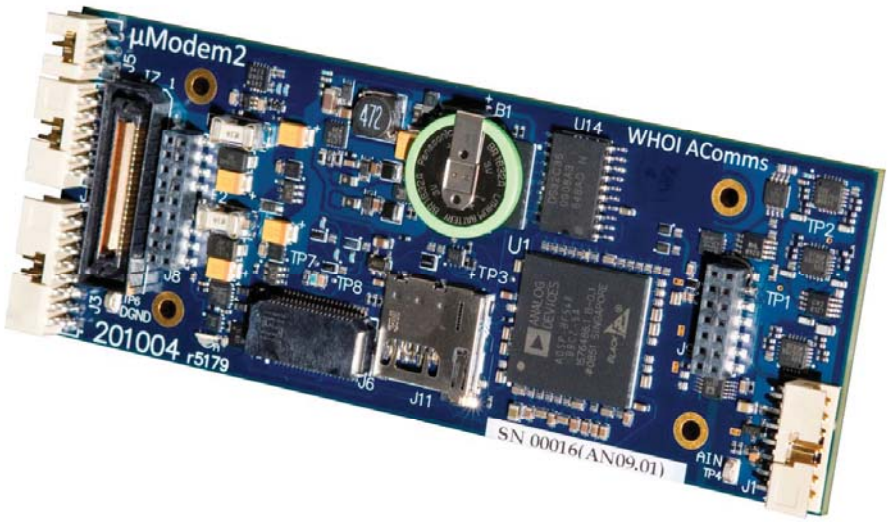

Figure 4.1. The 4.5" x 1.75" Micromodem-2 preserves the physical form factor of the Micromodem-1 while providing improved expansion connectors and I/O capabilities.

4.1 Introduction

The WHOI Micromodem [36] was originally designed as a compact, low-power modem with modest capabilities, intended for use on small underwater vehicles and to be integrated into oceanographic sensors for point to point or network applications [45, 51]. As it was developed, many capabilities were added, including navigation and high-rate phase-coherent transmission and reception.

Navigation features included in the original development phase included compatibility with REMUS broadband transponders to allow a vehicle to operate in a REMUS navigation network, and narrow-band transponder compatibility that supports many commercially-available deep and shallow-water transponders [38]. These features made it easier to add both acoustic communications and navigation to small vehicles by integrating these functions into one subsystem and transducer.

In the early 2000s, the communications capability of the modem evolved from support of the frequency-hopping frequency-shift keying (FH-FSK) open standard developed at WHOI for inter-

operability among multiple modems to high rate phase-coherent signaling. The FH-FSK standard is slow, only 80 bps, but reliable and simple. Originally the modem could only transmit PSK signals, requiring a more capable system, the WHOI Utility Acoustic Modem, for reception. However, in collaboration with NUWC-Newport, a very small floating-point co-processor was designed and software was ported to perform the adaptive equalization required for use of these signals in shallow water. The resulting system provides data rates from 80 to 5000 bps (burst rate), and supports not only shallow-water communications, but deep-water, direct path links as well [109]. An additional improvement was addition of a multi-channel (4 or 8) analog input card that improves performance in multi-path environments. The adaptive decision feedback equalizer can optimize over multiple channels, greatly improving data rate in many situations.

Development of new applications on the Micromodem-1 has been constrained by several factors, in particular its limited memory, fixed analog front end, and simple expansion buses. With the Micromodem-2 design (Figure 4.1), these constraints have been addressed, and we are now positioned to develop new capabilities for underwater networking, add expanded communication rates, and support acoustic communications research.

The design goals, described in Section 4.3, are derived from the extensive deployment experiences with the Micromodem-1 [36], while also taking advantage of technology advances. The Micromodem-2 preserves backwards compatibility with the Micromodem-1, in terms of its acoustic communication packet types, NMEA command set, and physical form factor, while providing a scalable path for future applications.

4.2 Previous Work

The first fully-embedded underwater acoustic modem from WHOI was the Utility Acoustic Modem (UAM) [60], designed in 1996. While quite capable, the UAM had a constant 3W power consumption due to its floating-point DSP, and it had a relatively large form factor.

The Micromodem-1 adopted a fixed-point DSP, reducing the power consumption by about 95%, and shrinking the form factor significantly, as detailed in Table 4.1. The original Micromodem-1 design is over 11 years old, and, in that time, only minor hardware updates have been incorporated

Specifications of the Utility Acoustic Modem, Micromodem-1, and Micromodem-2			
	Utility Acoustic Modem	Micromodem-1	Micromodem-2
First designed	1996	1999	2009
Dimensions	3.5" x 8"	1.75" x 4.5"	1.75" x 4.5"
Input Voltage[1]		5V-16V	5V-24V ($\pm$ 5%)
DSP Performance (nominal maximum)	30 MFLOPS (TI 'C44)	160 MMACS (TI 'C5416)	1066 MMACS (ADI BF548)
FPGA	N/A	N/A	13k LUTs, flash-based
Boot Time		$>$ 1100ms	$<$ 100ms
Power			
Hibernate	N/A	220μW @ 5V 640μW @ 12V	165μW @ 5V 455μW @ 12V
Low-Power Detect	N/A	$<$ 100mW ([45], deprecated)	80mW (preliminary est.)
Active	3W	158mW	300mW (using current software)
Receive PSK	3W	158mW + coproc	300mW + coproc (using current software)
Transmit[2] (185 dB re:1μPa@1m)	30W nominal	8W-48W	8W-48W
Volatile Memory			
Data RAM	2 MB	128 kB	8MB (total, shared with Program RAM)
Program RAM	1 MB	2 MB	8MB (total, shared with Program RAM)
Non-Volatile Memory			
Flash	1 MB NOR	16 MB NAND	64 MB NOR
Configuration	N/A	96B, backed by RTC battery	8kB FRAM
Removable	N/A	N/A	32 GB microSD

Table 4.1. Specifications and Performance of the Utility Acoustic Modem, Micromodem-1, and Micromodem-2

into the system. However, the Micromodem software has continuously evolved, and for several years, some development has been impeded by hardware limitations.

Based on this experience with the Micromodem-1, the Micromodem-2 has been designed with the expectation that it will need to be actively supported and used as a development platform for at least ten years. Table 4.1 compares the specifications of the three systems.

With the Micromodem-1, insufficient processing power and RAM required the use of an add-on coprocessor card to receive PSK-modulated signals [36]. The coprocessor is based on a TI TMS320C6713B floating-point DSP, and consumes roughly 2W when equalizing and decoding PSK signals. It is turned off when not in use.

4.3 Micromodem-2 Design Goals

The Micromodem-2 was designed to support networking and communications research by addressing the constraints of the Micromodem-1, while maintaining backward compatibility. An important requirement is scalability to allow the same system to be used in both power-constrained situations (e.g. multi-year ocean-bottom or glider deployments) and computation-constrained situations (e.g. short deployments for acoustic communications research or deployments on AUVs). A further need identified early in the re-design process was higher sampling and baseband processing rates, to support newer wideband transducers and higher frequencies.

Central to the plan to use the Micromodem-2 for the next decade is design flexibility and modularity. Advancements in components over the next several years will provide opportunities to increase capabilities as well as reduce power consumption, and the hardware and software have been selected and constructed such that these incremental hardware upgrades will be possible. Additionally, the hardware currently has significant headroom in terms of processing power, RAM, and storage, which will allow for extensive future development.

A common difficulty encountered when testing Micromodem-1 systems was a lack of data that could be used forensically to determine the causes of good or poor communication. Statistics had to be recorded by the host system controlling the Micromodem, and therefore were often incomplete. To remedy this, the Micromodem-2 includes significant non-volatile storage that can be used to

record channel statistics or make passband recordings for later analysis. These data can then be used to analyze the performance of the modem and characterize the propagation channel.

The following subsections provide background on design decisions including processor choice, power supplies, memory and storage, acoustic input and output stages, and user interfaces.

4.3.1 Computational Capability

While the Micromodem-1 used a Texas Instruments TMS320VC5416 with a nominal maximum of 160 MMACS (million multiply-accumulates per second), the Micromodem- 2 is equipped with an Analog Devices Blackfin ADSP-BF548 that provides over 1000 MMACS. Both processors are 16-bit fixed-point digital signal processors (DSPs), although the Blackfin incorporates more general-purpose microprocessor functionality and a larger peripheral set than the 'c5416. On both Micromodems, the DSP's clock frequency is dynamically scaled based on the processing load.

When selecting the processor for the Micromodem-2, only low-power (and therefore fixed-point) devices that were readily available at design time were considered. Our view is that, over the past decade, the market for fixed-point digital signal processors (DSPs) has shifted away from traditional low-power DSPs with modest memory spaces toward higher power DSPs with features closer to general-purpose processors. This apparent shift can be seen by observing which DSP product lines have seen continued development, and which have stalled. We suspect that the shift has probably been driven by smart phones, which require complex operating systems yet can be recharged nightly. The TI 'c5x line of traditional DSPs (of which the Micromodem-1's 'c5416 is a member) appears to have had its development stalled for quite a few years (although TI's dual-core OMAP processors combining a 'c5x DSP and an ARM microprocessor are still being actively developed for the smartphone market). In contrast to the TI 'c5x product line, the Blackfin DSP product line appears to have a solid roadmap for the future. Thus, although processors were available that may have provided an easier software transition from the Micromodem-1, we chose to switch processor families and use a Blackfin due to its capabilities and a future upgrade path.

After the design decisions for the Micromodem-2 were made, TI came out with the 'c674x series, which combines a fixed-point DSP with low static power dissipation as well as two-cycle floating-

point operations. The 'c674x DSPs could address two issues with the Blackfin. The first issue is that the present Blackfins have fairly high static power dissipation (though their roadmap indicates an improved fabrication process with lower static power dissipation in the future). The second issue is that a fixed-point DSP is limited to algorithms which are more stable numerically, in particular limiting the adaptive equalizer to using LMS (least-mean squares) algorithms rather than various RLS (recursive least squares) algorithms. Probably as a result of its fabrication process, the TI 'c674x series has both lower static power dissipation but also lower maximum clock rates than the ADI BF548, so there is a fixed-point performance advantage to using the ADI BF548.

An important use of the increased computational capability will be the implementation of the adaptive decision feedback equalizer and error-correction software on the Micromodem-2, removing the need for the current floating-point coprocessor card. This will save a significant amount of power and reduce the cost of a complete system. However, in the interim, the Micromodem-2 is compatible with the coprocessor card. In the event that an application needs to scale to higher processing power, the Micromodem-2 has a high-speed expansion connector which will allow multiple Micromodem-2's (or other processors, such as a WHOI Optical Modem [29]) to be connected and used concurrently.

4.3.2 Power Consumption

A trade-off associated with the improved computational ability of the Micromodem-2 DSP is an increase in the typical power consumption during packet decode relative to the Micromodem-1 (300mW vs 158mW, plus in both cases 2W for the coprocessor when equalizing and decoding PSK packets). To offset this increase in receive power, we improved the low-power states of the Micromodem-2. The Micromodem-2 operates in three modes, designated "active", "low-power detect", and "hibernate".

The *active mode* is used in standard applications where energy use is not a concern, and it runs multiple acoustic detectors and provides a full-featured user interface. In this mode, the Micromodem-2 draws about 300mW (measured at 25C and 5V input voltage; this increases slightly with input voltage and temperature). In this mode as well as all others, the modem disables power

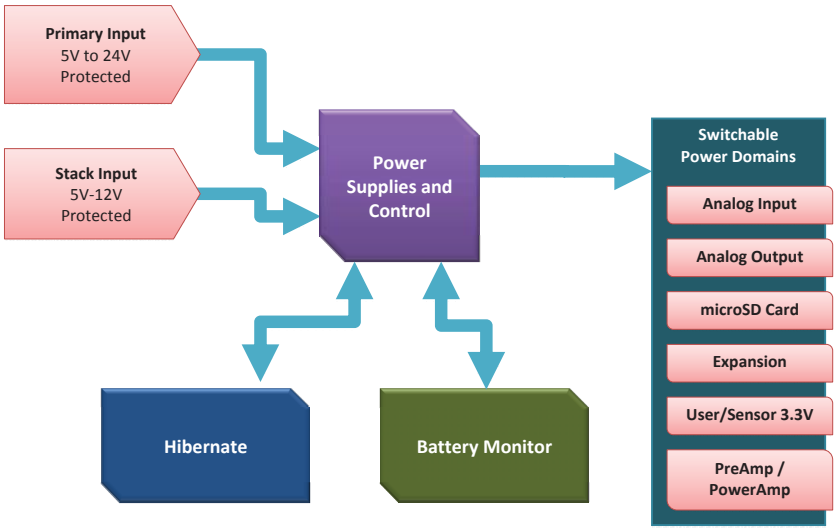

Figure 4.2. Micromodem-2 Power Control System

to subsystems that are not in use, such as the microSD card and the analog output circuitry as illustrated in Figure 4.2.

Hibernate mode is primarily useful on long deployments or other applications where energy is very limited and the modem can operate with a low duty cycle. In this mode, the primary power supply on the modem is turned off, along with all the downstream components. Thus, while in hibernate, the modem cannot detect incoming packets or respond to user input. However, the modem can transition from hibernate to active mode based on a number of events such as a real-time clock alarm, a user signal on specific I/O pins, or a signal from another board using the modem's expansion bus. With the Micromodem-2, we decreased the hibernate power to 165μW versus 220μW for the Micromodem-1, with a 5V battery voltage. The hibernate state uses a linear voltage regulator, so power consumption will scale roughly linearly with battery voltage. For example, with a 12V battery voltage, the hibernate power consumption is 455μW and 640μW, for the Micromodem-2 and -1, respectively.

The *low-power detect mode* is a new feature of the Micromodem-2 that will run a matched-filter detector using a flash-based FPGA, while leaving the DSP powered off. The importance of a low-power detector has been emphasized in many papers [54, 134]. We are currently developing and testing several different detection algorithms based on matched filter FM sweep detection, as well as BPSK sequence detection [47]. Based on initial experimentation using the Micromodem-2, we estimate that a low-power detector state running a matched filter for an FM sweep will use 75mW-80mW. When a packet is detected, or user serial input is received, the Micromodem-2's improved boot time (0.1s vs. 1.1s) allows it to wake rapidly from the low-power detect state and respond. An alternative approach is analog tone detection, which uses significantly less power, though it is less robust than FM sweep detection. In addition, an FM sweep provides high-resolution timing synchronization.

Future revisions will incorporate hardware and software improvements to reduce power in the low-power detect and active modes.

4.3.3 Memory

Easy implementation of new features is a key aspect of research and development systems such as the Micromodem, and restrictions on data memory made this difficult or in extreme cases (such as a PSK equalizer) impossible.

The wider memory address bus of the Blackfin DSP supports more data RAM, 8MB as opposed to 128 KB. Data RAM may be increased to 128MB in the future, when higher density RAM becomes available. To maintain low-power capability yet provide large amounts of RAM, micropower asynchronous static RAM is used. This memory has a standby power of a few microWatts, at a cost of slower access speeds relative to high-power synchronous dynamic RAM.

The Micromodem-2 also adds significant non-volatile memory storage. The boot device is a 64MB parallel NOR flash, rather than a serial EEPROM, as was used on the Micromodem-1. This reduces the boot time and allows additional non-volatile user storage. The configuration parameters (such as node ID and communication parameters) are now stored in 8kB of FRAM rather than RAM backed by the real-time clock (RTC) battery. This means that the configuration parameters cannot

be lost in the event of RTC battery failure, and no power is required to maintain the configuration parameters.

Perhaps most significantly, a slot for removable microSD cards with up to tens of GB of storage was added. This allows temporary storage of network packets, such as in a "data mule" application [25], logging communication performance such as bit error rates, transmitting research waveforms, and recording raw signals for purposes such as channel characterization or communications research.

4.3.4 Acoustic Input and Output

There are a wide range of modem acoustic frequencies, depending upon the application. Frequencies down to 900Hz [78] and up to 100kHz or more are of interest. To support this, the Micromodem-2 has a highly configurable fully-differential analog input, allowing frequency-agile operation by selecting among four bands, which are defined by high-pass noise rejection and low-pass anti-aliasing filters. It also has programmable gain and a 16-bit analog-to-digital converter (ADC) that can sample at up to 1MHz. The Micromodem-1 had fixed high- and low-pass filters, and a low-power 12-bit ADC which was not well suited to sampling above 80kHz. With our improvements in the analog front end, the Micromodem-2 is better suited to supporting multi-band network deployments [35, 51, 106].

To provide flexibility and capability beyond the single analog input on the modem board, both the Micromodem-1 and the Micromodem-2 can interface to existing multi-channel analog input boards. Future multi-channel analog input boards with improved capabilities will take advantage of the high speed SPI or SpaceWire interfaces provided by the Micromodem-2.

Transmit power on the standard Micromodem-1 power amplifier is fixed, using a class D output stage for efficiency. For short-range networking experiments, a low-power linear power amplifier (at 25kHz, about 150dB re:1Pa@1m, about 1W electrical power) was developed for experiments in transmit power control and spatial reuse in a network [83]. New interfaces available on the Micromodem-2 will allow use of a digital pulse-width-modulated (PWM) power amplifier driven directly by the modem's DSP.

4.3.5 Various Improvements: Input Voltage Range, UARTs, Timing, and Temperature

Based on direct experience and user feedback a number of new features not present on the Micromodem-1 have been added. See Table 4.2 for a summary of some of these features.

We have added a wider input power range to support power buses up to 24V, with reverse-voltage and over-voltage protection. The primary power input from the cable-terminated edge connector is combined with an alternate power input on a stacking expansion connector using an pseudo-ideal diode OR circuit, which can be used to provide redundant power to the modem.

The Micromodem-2 incorporates improved I/O capabilities and is designed to reduce overall complexity, particularly in systems that required a separate microcomputer to interface simple sensors to the modem. Almost all I/O is routed through the modem's FPGA, which allows software configuration of almost all I/O on the board.

In contrast to the Micromodem-1's two RS232 serial ports, the Micromodem-2 has four asynchronous serial ports, including two standard serial ports with RS232 signaling levels, one serial port using 3.3V logic levels for low-power integration, and one which can be switched by software between RS232 and RS485/RS422 signaling. A logic-level (3.3V) serial port is also available via the high-density stacking interface connector on the modem.

The modem provides a total of 14 reconfigurable digital I/O pins to users, all of which operate at 3.3V and are 5V tolerant. In addition to the aforementioned asynchronous serial ports (RS232/422/485), the modem offers I2C and SPI synchronous serial buses. For analog signals from user sensors, the modem includes an auxiliary low-speed analog to digital converter that is capable of up to 240 samples per second. The modem can also measure its own input voltage. The status of all of these inputs can be provided to users acoustically or locally via the control interface. Finally, a switchable 3.3V power output from the modem can provide up to 100mA to external circuitry.

The Micromodem-2 includes a real-time clock with a precision of 2ppm (versus 20ppm for typical crystals) to provide better support for networks with synchronized sleeping and longer sleep times [45, 123], as well as improved navigation support [27, 35, 108], and tighter bounds on TDMA network timeslots [53, 76].

Features of Micromodem-1 and Micromodem-2		
	Micromodem-1	Micromodem-2
Async. Serial Ports	2 RS232	4 total (two RS232, one 3.3V logic level, one switchable between RS232 and RS485/RS422)
Transmit timing	Transmit on Pulse-Per-Second (PPS) signal	Transmit on n^{th} PPS, hardware line toggle, and precision timer
System interfaces	one general-purpose input, one general-purpose output	14 reconfigurable I/O pins, I2C, auxiliary analog input, battery voltage monitor
Expansion interface	8-bit parallel data bus at up to 8MHz, half-duplex; SPI	SpaceWire-based bus capable of 100Mbps; SPI
Real-time Clock	accurate to 20ppm; battery life $<$ 10 years at 25°C	accurate to 2ppm battery life $>$ 15 years at 25°C
Operating temperature	0°C to +70°C	−40°C to +70°C or −40°C to +85°C (build options)

Table 4.2. Comparison of features of the Micromodem-1 and Micromodem-2

In some long-term deployments, the modem is configured to spend most time in the hibernate state and wake periodically to detect scheduled transmissions of acoustic data. The improved real-time clock accuracy results in further power savings in these applications, as shorter "active" periods are necessary to account for worst-case clock drift between the transmitter and receiver.

As with the Micromodem-1, the modem also supports an external pulse-per-second (PPS) input, though now it can also provide a PPS output if desired. The Micromodem-2 now has a dedicated external transmit trigger input as well as handshake signals for sharing a transducer with another acoustic system.

All Micromodem-2 components are specified from −40°C to +85°C to support Arctic deployments, though, to reduce cost, some versions include the commercial temperature range FPGA. Although the commercial-grade FPGA is only guaranteed from 0°C to +70°C, the manufacturer states that it should work properly to −40°C. In any case, we individually test and qualify units from −40°C to +70°C if required for specific deployments.

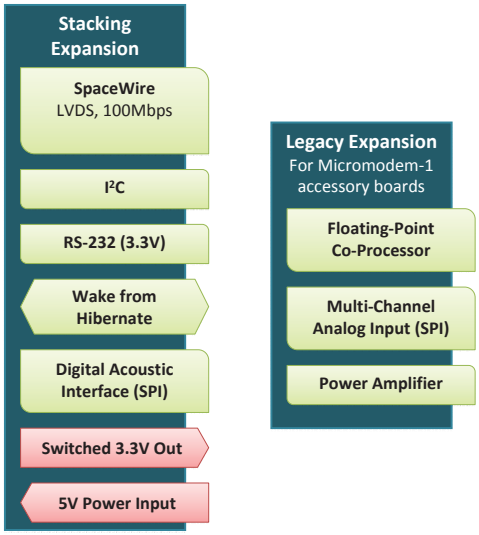

Figure 4.3. Micromodem-2 Expansion Interfaces

4.4 Expansion Interfaces

The original Micromodem-1 uses an expansion header with an 8-bit wide parallel interface to the floating-point coprocessor board. In addition, the receive hydrophone array is sampled by a multichannel analog input board that is connected to the main Micromodem-1 board with another expansion header, using a four-wire SPI synchronous serial interface. Additional connections are used to provide control signals to power amplifiers. These legacy connectors are included on the Micromodem-2 to provide backward compatibility (Figure 4.3).

The Micromodem-2 provides a pair of high-density, high-speed stacking connectors to interface with other devices (Figure 4.3). While intended for future development, the connectors may be employed by users to eliminate wiring harnesses when connecting the modem to other systems. These connectors can provide power to the modem, regulated 3.3V power from the Micromodem-2 to other devices, asynchronous logic-level serial communication, wake-from-hibernate functionality, SPI and I2C synchronous serial buses, digital I/O, and a high-speed SpaceWire interface.

4.4.1 SpaceWire

The Micromodem-2 incorporates an interface based on SpaceWire (ECSS-E-ST-50-12C) for high-speed off-board communication. SpaceWire is a flexible yet simple-to-implement protocol originally developed by the European Space Agency for use in connecting subsystems aboard spacecraft [82]. It uses low-voltage differential signaling (LVDS) to connect devices with bi-directional, full-duplex, point-to-point links, and a simple protocol allows data packets to be routed among devices without large processing overhead. Open-source implementations of this protocol are available, for example on opencores.org. The Micromodem-2 complies with the electrical specifications of the standard, but it uses the high-speed stacking connector to pass the signals rather than the prescribed DB-9 connector. As implemented on the modem, it is capable of full-duplex wire speeds of 100Mbps. Intended uses include communication with coprocessors (including other stacked Micromodem-2 boards used as coprocessors), multi-channel analog input and output devices, vehicle computers, Ethernet or CAN bridges, sensors, and Gumstix-based single-board Linux control computers. SpaceWire (and the associated LVDS signaling) is robust enough to operate over distances of several meters, so it may also be used to transfer high-speed audio data to or from remote hydrophones or amplifiers.

4.5 Software Architecture

The software architecture for the Micromodem-2 builds upon the real-time operating system (RTOS) developed for real-time signal processing on the Micromodem-1, previously described in [36]. The RTOS is a small and portable executive which enforces real-time read-locks and write-locks on streaming data buffers passing through processing modules, connected together as drawn in a typical signal-processing block diagram to build the modem and network applications. At the application level, backward compatibility with the Micromodem-1 is maintained. However, new features are being added, including transmit queues, a streamlined user interface and built-in support for some wireless network functions.

4.5.1 Transmit and Data Queues

Queues for transmit signals and payload data records are now possible due to the additional memory that is available. These will allow users (or the network stack) to enqueue signals, such as communication packets or navigation signals, with four different transmit timing methods. The queue for data records allows sensor samples to be collected before transmission and can be used as a temporary storage location for network data packets, for example in a "data-muling" application.

The transmit queue with the highest priority is a timer-driven queue used for enforcing turn-around times on transmissions such as "ping" packets and long-baseline (LBL) navigation signals, where a two-way travel time needs to be measured precisely using a specified turn-around time. An additional use of the timer-driven transmit queue could be for transmitting packets within appropriate network timeslots [53, 76]. The second-highest priority transmit queue is for signals which are to be transmitted on an external trigger provided by the user, often used for synchronous one-way navigation [27, 35, 108]. Third is a queue for transmitting signals at every nth pulse-per-second (PPS), from either an internally-generated or externally-generated PPS, as required by, for example, periodic navigation signals. Finally, the default transmit signal queue is for signals with no detailed timing requirements, such as standard communication packets. Each of the transmit queues allows enqueueing signals at the tail, at the head (next to be transmitted), or by sorted priority.

4.5.2 User Interface

The standard user interface to the Micromodem-2 is an NMEA-style asynchronous serial interface (RS232, RS485, or logic-level UART), as is typical of many oceanographic instruments. Complete backwards compatibility for the Micromodem-1 NMEA commands is preserved. NMEA-style ASCII interfaces can be somewhat awkward to interact with, however, and they are inefficient at transferring binary data. While the modem is flexible enough to act as an instrument's primary controller, we are investigating various designs for a binary protocol intended to interact with typical host processors. Although more difficult for a human to read during debugging, a binary mode would simplify interfacing the modem to the current class of very low-power microcontrollers (e.g.,

TI's MSP-430s) that are becoming increasingly popular for low-powered instrument control. In the process of changing the interface, it will be generalized to all of the modem's interfaces, including the acoustic link itself.

4.5.3 Applications and Integrated Networking Support

For user payload data, many Micromodem-1 users have been using the Compact Control Language [122]. A recent extensible encoding language payload data has also been developed, the Dynamic Compact Control Language [103]. The Micromodem-2 continues to support these methods of transferring user data.

Networking support [107] will be integrated directly onto the Micromodem-2. The goal is to develop and support a networking toolbox, which will allow users to build simple underwater networks quickly for specific applications.

4.6 Conclusions

The Micromodem-2 provides significant improvements in processing capability, storage, and bandwidth. These improvements overcome previous limitations present in the Micromodem-1, and will allow development of new capabilities with support for expanded communication rates, underwater network deployments, and research in acoustic communications and underwater acoustic networks.

CHAPTER 5
CONCLUSIONS

This thesis has presented several related pieces of work on underwater acoustic networks (UANs).

Packet detection in interference in UANs, and its critical role in the effectiveness of collision-avoidance medium-access control (MAC) protocols, is a primary focus of this thesis. Spreading loss measures the decrease in received energy as a function of range, and determines the level of long-range interference.

In Chapter 2, we presented a new spreading model, the mixed-exponent spreading model, for UAN nodes using a matched-filter detector as a low-power wakeup detector. Under this model, there are distinct spreading-loss exponents for packet detection and interference, due to the matched-filter detector's signal processing. We validated this spreading model numerically, and with direct measurements of the spreading exponents from shallow-water experimental data. The "practical spreading" model, which is widely used to model UANs, but which is poorly grounded in experiment and theory, is inconsistent with our experimental measurements. Our results suggest caution for its continued use to model performance of UANs.

Building on our spreading analysis, in Chapter 3, we analyzed the effectiveness of collision-avoidance MAC protocols in UANs, namely what fraction of collisions are avoided when using the protocol, independent of propagation delay. The low spreading loss in UANs, in particular with the mixed-exponent spreading model, can lead to low collision-avoidance effectiveness compared with radio networks.

In addition, in Chapter 1, we argued that many UANs will be relatively mobile and sparse relative to terrestrial sensor networks, reducing the importance of network energy consumption and throughput of medium-access control protocols as metrics. This survey challenges some of the

assumptions made in past UAN research, with a goal of aiding researchers entering the area of UANs from terrestrial sensor networks.

Finally, in Chapter 4, we documented the design decisions for a new underwater acoustic modem, as a contribution to researchers entering the field from terrestrial sensor networks.

The following sections of this concluding chapter provides an additional summary of the contributions of each chapter mentioned above.

Practical Issues in Underwater Acoustic Networks

The contributions of Chapter 1 are:

- *We bring practical experience from deployments as well as literature from the ocean engineering literature into the sensor network community.* Previous UAN surveys were drawing largely from terrestrial sensor networking literature, and did not adequately emphasize the importance of mobility in UANs, nor the sparseness of many UANs.

- *We identify and diagram UAN operating regimes* versus geographic area and node population. We identify the network challenges in regimes ranging from dense, small networks to sparse, geographically large networks. There is no single regime for UANs, but in general they are likely to be *sparser and more mobile* than terrestrial sensor networks with similar applications.

- *In mobile networks, the energy efficiency of the network is not necessarily a constraint*, since the network energy consumption is usually dominated by vehicle propulsion energy. This is in contrast to the assumptions of many sensor networks, as well as the assumptions of previous UAN surveys.

- *In sparse networks, channel access is not necessarily a constraint.* Many papers in UANs focus on energy-efficient medium access control protocols, which are not necessarily important for in sparse regions of mobile UANs.

- *We highlighted the issue of channel access for periodic acoustic navigation signals, which for physical reasons share the communications band in mobile UANs, unlike in terrestrial radio-based networks.*

- We also raised the issue of *long-term fairness in disconnected mobile UANs*, where mobile nodes returning briefly to a connected region of the network need increased access to the channel relative to nodes remaining in the connected region.

Speading Models: Understanding Interference in UANs

The contributions of Chapter 2 include:

- *We derive an alternate spreading model, which call the mixed-exponent model*, using physical reasoning. The mixed-exponent model applies to energy-constrained acoustic modems that use matched-filter detectors as a low-power wakeup detector. A distinction is drawn between the spreading exponents for the matched-filter detector's response to the wakeup signal versus distant interference. The model retains most of the simplicity of the "practical spreading" model, aiding in intuitive physical understanding of network performance.

- *We validate the mixed-exponent model* in uniform soundspeed profiles using two distinct numerical acoustic propagation packages, on based on raytracing and one based on solving the forward-propagating wave equation.

- *We analyze data from the Kauai Acomms MURI 2011 (KAM11) shallow-water field experiment, directly measuring energy-loss exponents.* With scattering losses from the boundaries, we are measuring energy-loss exponents rather than spreading-loss exponents. For modeling shallow-water underwater acoustic networks, we recommend generalizing the spreading loss model to an energy-loss model that includes scattering losses. We identify periods in time where simple exponent models appear to hold, and other periods where they do not.

- *We provide physical explanations for propagation differences explaining the differences between periods when simple spreading-loss exponent models appear to hold, and when they do not.*

- *The "practical spreading" model is inconsistent with the measured energy-loss exponent values* for this particular experiment. The measured energy-loss exponents, k, were significantly larger than 2, compared with $k = 1.5$ for the practical spreading model. Caution should be used if "practical spreading" is used to model network performance.

- *We partially validate the mixed-exponent model from the field experiment data analysis.* In most cases, even when simple exponent models do not hold, there is a difference between the exponents for packet detection and interference. Usually *the energy-loss exponent for packet detection is larger than that for interference, implying that long-range interference will be a problem for MAC protocols in UANs.* Due to experimental limitations, we were not able to validate or invalidate the waterdepth-dependence and bandwidth-dependence of the transition ranges in the mixed-exponent spreading model.

- Using results developed in Chapter 3, on the effects of spreading on the effectiveness of RTS/CTS MAC protocols, *we evaluate RTS/CTS effectiveness for a potential network deployed at the field experiment site*, using the energy-loss exponent measurements from the KAM11 field experiment.

- The extreme variability acoustic propagation at the KAM11 experiment site suggests that *robustness* of network protocols would be critical in such an environment, likely in a tradeoff with energy consumption.

Collision-Avoidance Effectiveness in UANs

The contributions of Chapter 3 include:

- *We identify collision-avoidance effectiveness as an additional area of performance loss for RTS/CTS MAC protocols in UANs, independent of propagation delay and throughput.*

- *We first extend previous radio-based work [135] in order to analyze RTS/CTS effectiveness for the "practical spreading" model for UANs.* With this simple spreading-only channel model,

neglecting absorption and ambient noise, the results initially suggest that RTS/CTS effectiveness is significantly lower in UANs than in radio networks, with RTS/CTS handshakes beginning to lose effectiveness for node separations of only 22% of the maximum range, versus about 56% for radio networks, for typical parameters.

- *We next derive analytic expressions explaining how various physical-layer communication parameters affect RTS/CTS effectiveness in UANs*, with a more realistic underwater acoustic channel model, incorporating absorption and ambient noise, and again using the "practical spreading" model with a spreading exponent of $k = 1.5$. These communication parameters include detection threshold, node separation, transmit power, and center frequency (determining absorption coefficients and ambient noise power). We find that the strong effects from absorption improve spatial reuse for most intermediate node separations to approximately the level of collision-avoidance performance in radio networks.

- *We analyze how the mixed-exponent spreading model studied in Chapter 2 affects RTS/CTS effectiveness.* With this model, RTS/CTS effectiveness drops significantly compared with the widely used "practical spreading" model, especially at lower frequencies. For example, at 3 kHz center frequency, on average the RTS/CTS handshake would suppress under 10% of potential interferers for all but the smallest node separations.

- *We validate the results from our analytical model with network simulations* incorporating the channel model and physical layer.

Micromodem-2: An Acoustic Modem Enabling Next-Generation UANs

The contributions of Chapter 4 include:

- *We document design decisions and tradeoffs* for the electronics hardware design of an underwater acoustic modem, to aid other researchers in their own designs.

- *Design decisions were drawn from extensive deployment experience,* as well as the practical considerations described in Chapter 1.

- *Frequency agility* is designed in from the start, allowing operation from below 1 kHz to over 100 kHz, and supporting new wideband transducers. Long-range, low-frequency, low-datarate links are supported, for example for 100 km links under the Arctic ice at 1 kHz and 10 bps [40]. In addition, short-range, high-frequency, higher-datarate links will be supported with carrier frequencies over 100 kHz, improving data rate, covertness, and spatial reuse as well as RTS/CTS effectiveness as described in Chapter 3.

- *Precision timing* is supported and tightly integrated, with precision and power consumption ranging from an onboard 2 ppm temperature-compensated crystal consuming 3 μW, up to chip-scale atomic clocks with drifts on the order of milliseconds per year consuming about 120 mW. As described in Chapter 1, precision timing is critical for vehicle navigation methods that use travel-time measurements. Critically for scientific surveys, vehicle navigation allows sensor measurements to be geo-referenced. On small underwater vehicles, a single acoustic transducer is generally shared between acoustic communication and navigation, so navigation functions must be integrated with the acoustic modem.

- *We describe interface requirements for robust integrations* in vehicles and subsea systems, again drawing from deployment experience. These include practical details on voltage ranges and power supply protection, input and output protection, and data interfaces.

APPENDIX A

SUPPLEMENTAL ENERGY-VERSUS-RANGE PLOTS FROM RAYTRACING VALIDATION

For completeness, this appendix presents Bellhop raytracing energy-versus-range results, beyond the results shown in the main text. Coherent and incoherent energy are plotted for a fixed bandwidth of 4 kHz and varying depths of 50 m, 75 m, 100 m, 150 m, and 200 m, as well as at a fixed depth of 100 m and varying bandwidths of 4 kHz to 31 Hz.

Incoherent transition range is unaffected by bandwidth, whereas coherent transition range scales linearly with bandwidth.

The coherent exponent estimates for depths of 200 m and 150 m beyond the transition range have only a few points in their fits. Those fits have exponent estimates lower than 1.5 and have larger margins of error compared with the other coherent exponent estimates. The plot for a depth of 50 m has its energies dropping slightly at the largest ranges, explained in the caption for Figure 2.6. The energy within the transition region is somewhat variable since the addition of individual arrivals still is a relatively large effect to the overall energy.

Each energy estimate at each range is the average of 1000 realizations of impulse responses with independent randomized phases, as described in Section 2.4.3.

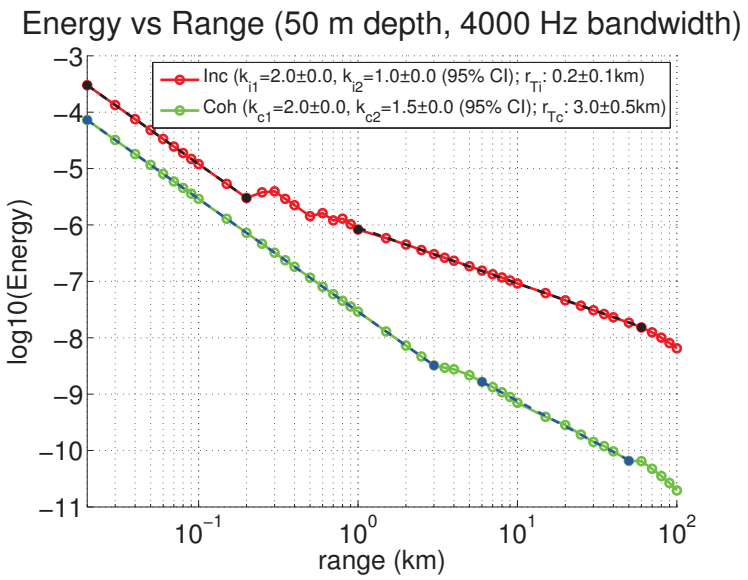

Figure A.1. Coherent and incoherent energy for a bandwidth of 4 kHz and a depths of 50 m.

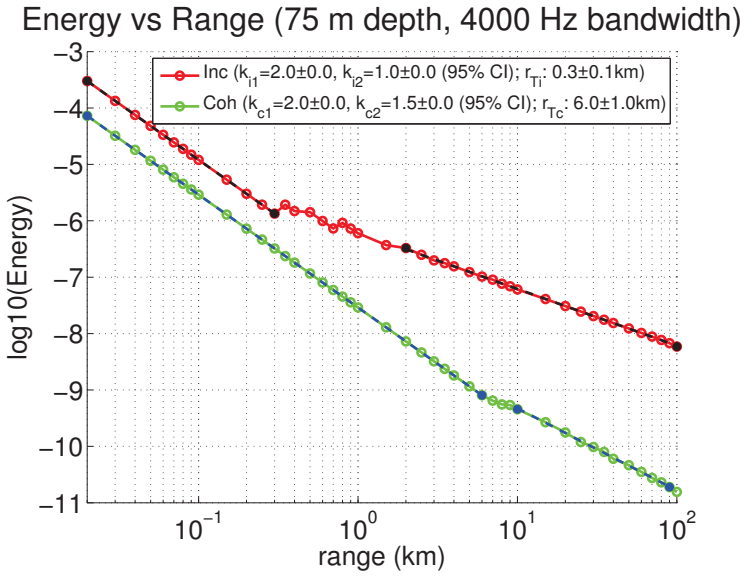

Figure A.2. Coherent and incoherent energy for a bandwidth of 4 kHz and a depths of 75 m.

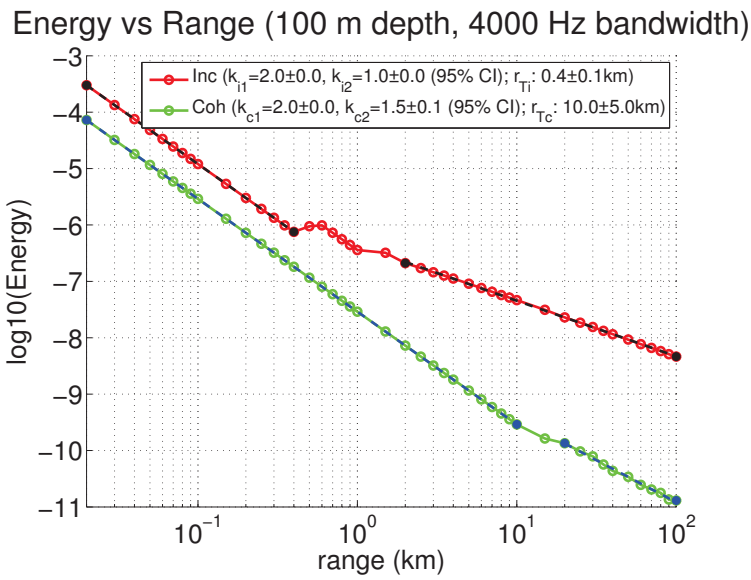

Figure A.3. Coherent and incoherent energy for a bandwidth of 4 kHz and a depths of 100 m.

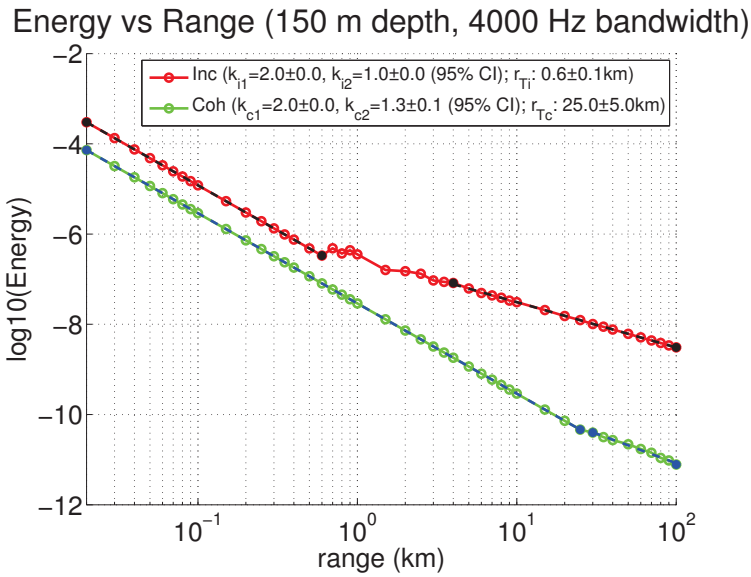

Figure A.4. Coherent and incoherent energy for a bandwidth of 4 kHz and a depths of 150 m.

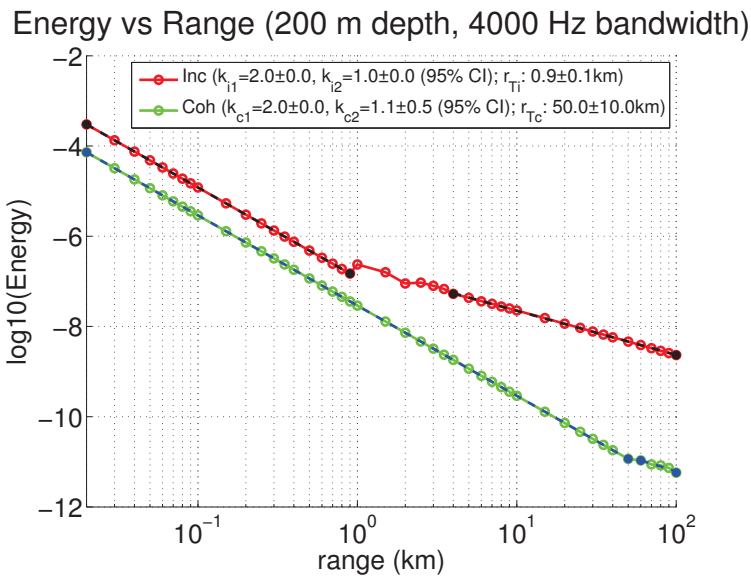

Figure A.5. Coherent and incoherent energy for a bandwidth of 4 kHz and a depths of 200 m.

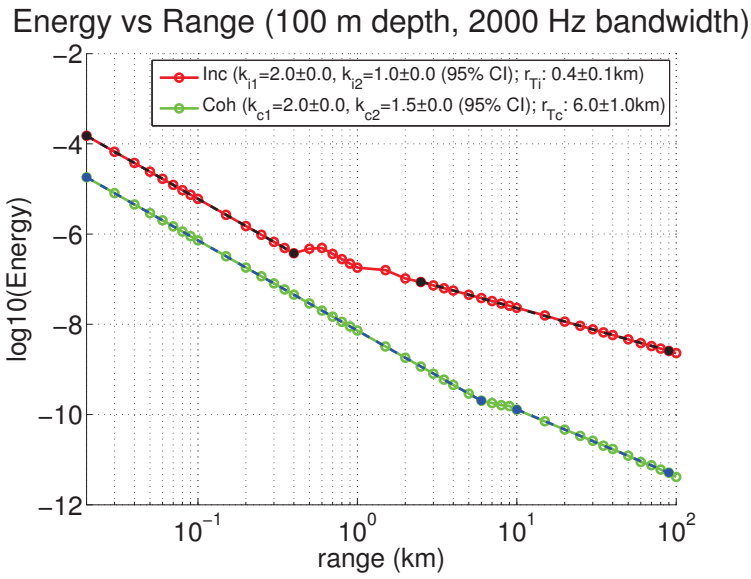

Figure A.6. Coherent and incoherent energy for a bandwidth of 2 kHz and a depths of 100 m.

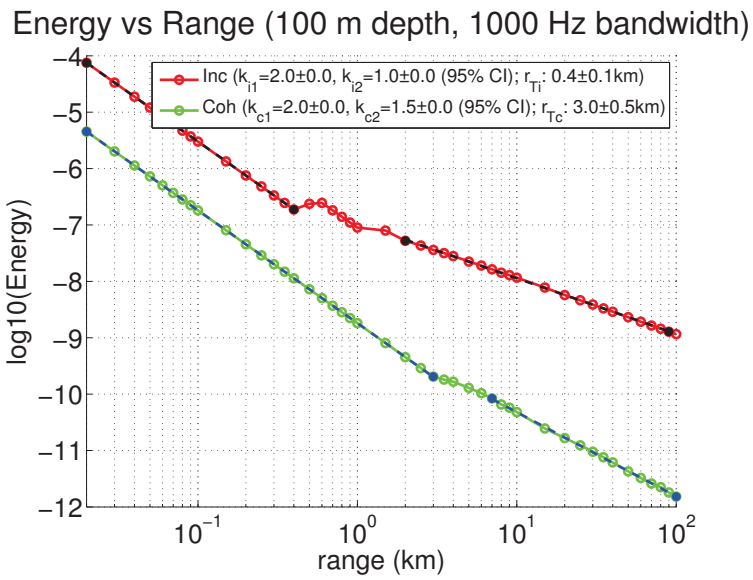

Figure A.7. Coherent and incoherent energy for a bandwidth of 1 kHz and a depths of 100 m.

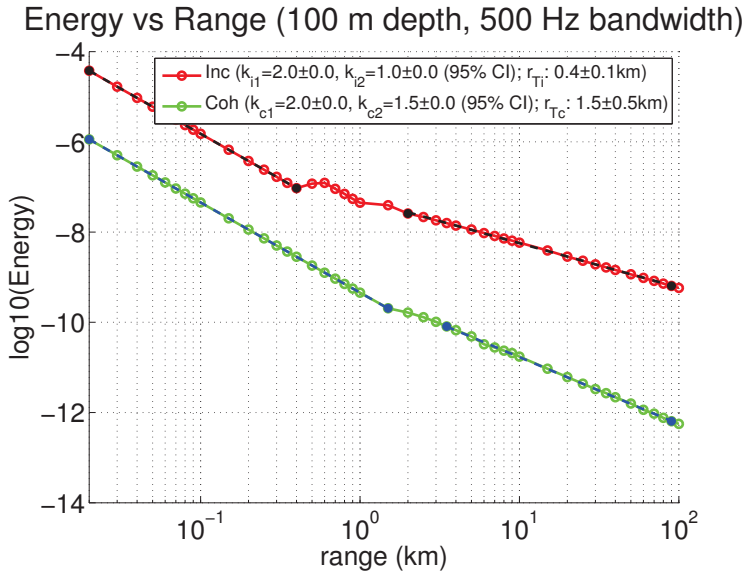

Figure A.8. Coherent and incoherent energy for a bandwidth of 500 Hz and a depths of 100 m.

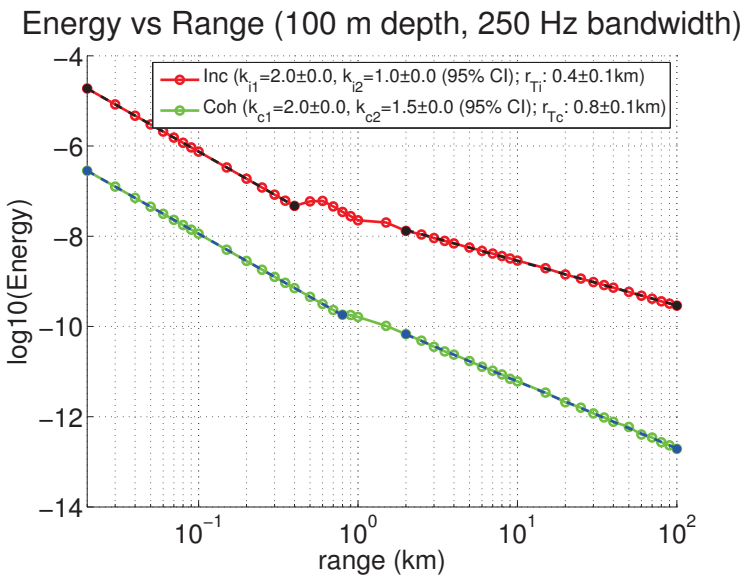

Figure A.9. Coherent and incoherent energy for a bandwidth of 250 Hz and a depths of 100 m.

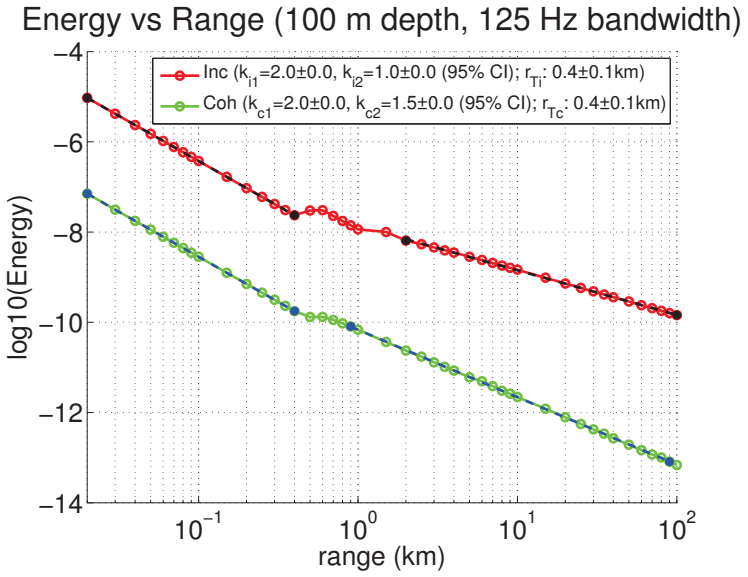

Figure A.10. Coherent and incoherent energy for a bandwidth of 125 Hz and a depths of 100 m.

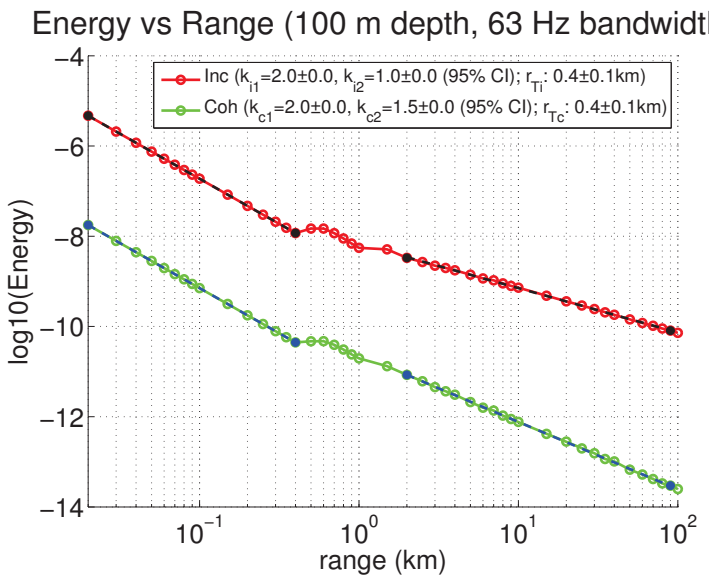

Figure A.11. Coherent and incoherent energy for a bandwidth of 63 Hz and a depths of 100 m.

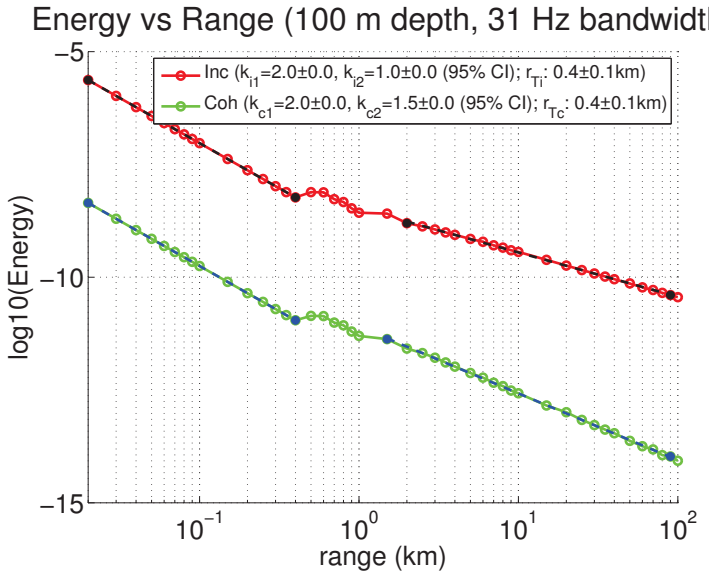

Figure A.12. Coherent and incoherent energy for a bandwidth of 31 Hz and a depths of 100 m.

APPENDIX B

RAM CODE

The RAM code we are using is Version 1.1, dated 30 April 1998 by M.D. Collins [19], but it has been modified by Jim Preisig and Tim Duda to output complex pressure amplitude rather than the magnitude of pressure. (Due to the linear output of complex pressure amplitudes, the filename is `lorambathfollowbottom.f`.)

The Fortran code listing is below:

```
      program ram

c     Modified by Tim Duda to take just a single bottom specification in the
c     beginning and carry it through in matrc subr.    March 2002
c
c     Make a new proflu sub to 'update profiles' for water but not bottom.
c     Taken from  profl sub.
c
c     Bottom  profiles are now indexed from the seabed at input time,
c     so z=zero on those profiles is equal to the seabed 'surface'.
c
c     Extra input parameter in a line by itself at the start, depth range
c     of bottom parameters update as bathy varys with range.
c
c     Has Jim Preisig's Linear Output format at toutput time, from lofepe.
```

```
c
c     ********************************************************************
c     ***** Range-dependent Acoustic Model, Version 1.1, 30-Apr-98 *****
c     ********************************************************************
c
c     This code was developed by Michael D. Collins at the Naval
c     Research Laboratory in Washington, DC. It solves range-dependent
c     ocean acoustics problems with the split-step Pade algorithm
c     [M. D. Collins, J. Acoust. Soc. Am. 93, 1736-1742 (1993)]. A
c     user's guide and updates of the code are available via anonymous
c     ftp from ram.nrl.navy.mil. Version 1.0 is designed for running on
c     a single processor. Version 1.0p (which requires double precision
c     for very large range steps) is designed for parallel processing.
c
c     Version 1.1 contains two improvements:
c
c     (1) An improved self starter. Stability is improved by using the
c     factor (1-X)**2 instead of (1+X)**2 to smooth the delta function.
c     The factor (1+X)**2 is nearly singular for some problems involving
c     deep water and/or weak attenuation. Numerical problems associated
c     with this singularity were detected by Eddie Scheer of Woods Hole
c     Oceanographic Institute.
c
c     (2) Elimination of underflow problems. A very small number is
c     added to the solution in subroutine solve to prevent underflow,
c     which can adversely affect run time on some computers. This
c     improvement was suggested by Ed McDonald of the SACLANT Undersea
c     Research Centre.
```

```
c
      complex ci,ksq,ksqb,u,v,r1,r2,r3,s1,s2,s3,pd1,pd2
      real k0,ksqw
      character (LEN=256) :: fileroot
c
c     mr=bathymetry points, mz=depth grid, mp=pade terms.
c     mbz=bottom grid
c
      parameter (mr=8000,mz=80000,mp=16,mbz=15000)
      dimension rb(mr),zb(mr),cw(mz),cb(mbz),rhob(mbz),
     >   attn(mbz),alpw(mz),
     >   alpb(mbz),f1(mz),f2(mz),f3(mz),ksq(mz),
     >   ksqw(mz),ksqb(mbz),u(mz),
     >   v(mz),tlg(mz),r1(mz,mp),r2(mz,mp),r3(mz,mp),s1(mz,mp),
     >   s2(mz,mp),s3(mz,mp),pd1(mp),pd2(mp)
c


      call get_command_argument( 1, fileroot)


      open(unit=1,status='old',    file=trim( fileroot ) // '.in')
      open(unit=2,status='unknown',file=trim( fileroot ) // '.pch')
      open(unit=3,status='unknown',file=trim( fileroot ) // '.tll')
      open(unit=4,status='unknown',file=trim( fileroot ) // '.tlg')
      open(unit=5,status='unknown',file=trim( fileroot ) // '.afg')
      open(unit=6,status='unknown',file=trim( fileroot ) // '.af1')
c
c     MAIN PROGRAM LOOP ----------------------------------MAIN
c
```

```
      call setup(mr,mz,nz,mp,np,ns,mdr,ndr,ndz,iz,nzplt,lz,ib,ir,dir,dr,
     >   dz,pi,eta,eps,omega,rmax,c0,k0,ci,r,rp,rs,rb,zb,cw,cb,rhob,
     >   attn,alpw,alpb,ksq,ksqw,ksqb,f1,f2,f3,u,v,r1,r2,r3,s1,s2,s3,
     >   pd1,pd2,tlg,zmaxbot,nzbot,mbz)
c
c     March the acoustic field out in range.
c
    1 call updat(mr,mz,nz,mp,np,iz,ib,dr,dz,eta,omega,rmax,c0,k0,ci,r,
     >   rp,rs,rb,zb,cw,cb,rhob,attn,alpw,alpb,ksq,ksqw,ksqb,f1,f2,f3,
     >   r1,r2,r3,s1,s2,s3,pd1,pd2,nzbot,mbz)
c
      call solve(mz,nz,mp,np,iz,u,v,r1,r2,r3,s1,s2,s3)
      r=r+dr
c     if(mod(r,1000.0).eq.0)write(*,*)r

      call outpt(mz,mdr,ndr,ndz,iz,nzplt,lz,ir,dir,eps,r,f3,u,tlg)
      if(r.lt.rmax)go to 1
c
      close(1)
      close(2)
      close(3)
      close(4)
c
      close(5)
      close(6)
c
      stop
      end
```

```
c
c     ------------------------------------------------------------
c     Initialize the parameters, acoustic field, and matrices.
c
c      ---------------------------------------------- SETUP
c
      subroutine setup(mr,mz,nz,mp,np,ns,mdr,ndr,ndz,iz,nzplt,lz,ib,ir,
     >   dir,dr,dz,pi,eta,eps,omega,rmax,c0,k0,ci,r,rp,rs,rb,zb,cw,cb,
     >   rhob,attn,alpw,alpb,ksq,ksqw,ksqb,f1,f2,f3,u,v,r1,r2,r3,s1,s2,
     >   s3,pd1,pd2,tlg,zmaxbot,nzbot,mbz)
c
      complex ci,u(mz),v(mz),ksq(mz),ksqb(mbz),r1(mz,mp),r2(mz,mp),
     >   r3(mz,mp),s1(mz,mp),s2(mz,mp),s3(mz,mp),pd1(mp),pd2(mp)
      real k0,rb(mr),zb(mr),cw(mz),cb(mbz),rhob(mbz),attn(mbz),alpw(mz),
     >   alpb(mbz),f1(mz),f2(mz),f3(mz),ksqw(mz),tlg(mz)
c
      read(1,*)
      read(1,*)freq,zs,zr
      read(1,*)rmax,dr,ndr
      read(1,*)zmax,dz,ndz,zmplt
      read(1,*)c0,np,ns,rs
      read(1,*)zmaxbot
c        --------- Tim D. march 2001 zmaxbot is  z max of bottom model
c
      write(3,*)(rmax/dr)
c
      i=1
    1 read(1,*)rb(i),zb(i)
```

```
      if(rb(i).lt.0.0)go to 2
      i=i+1
      go to 1
    2 rb(i)=2.0*rmax
      zb(i)=zb(i-1)
c
      pi=4.0*atan(1.0)
      ci=cmplx(0.0,1.0)
      eta=1.0/(40.0*pi*alog10(exp(1.0)))
      eps=1.0e-20
      ib=1
      mdr=0
      r=dr
      omega=2.0*pi*freq
      ri=1.0+zr/dz
      ir=ifix(ri)
      dir=ri-float(ir)
      k0=omega/c0
      nz=zmax/dz-0.5
      nzbot=zmaxbot/dz-0.5
      nzplt=zmplt/dz-0.5
      z=zb(1)
      iz=1.0+z/dz
      iz=max(2,iz)
      iz=min(nz,iz)
      if(rs.lt.dr)rs=2.0*rmax
c
      if(nz+2.gt.mz)then
```

```
      write(*,*)'   Need to increase parameter mz to ',nz+2
      stop
      end if
      if(np.gt.mp)then
      write(*,*)'   Need to increase parameter mp to ',np
      stop
      end if
      if(i.gt.mr)then
      write(*,*)'   Need to increase parameter mr to ',i
      stop
      end if
c
      do 3 j=1,mp
      r3(1,j)=0.0
      r1(nz+2,j)=0.0
    3 continue
      do 4 i=1,nz+2
      u(i)=0.0
      v(i)=0.0
    4 continue
      lz=0
      do 5 i=ndz,nzplt,ndz
      lz=lz+1
    5 continue
      write(4,*)lz
      write(5,*)lz,dz,ndz,ndr,dr
c
c     The initial profiles and starting field.
```

```
c
      call profl(mz,nz,ci,dz,eta,omega,rmax,c0,k0,rp,cw,cb,rhob,attn,
     >   alpw,alpb,ksqw,ksqb,nzbot,mbz)
      call selfs(mz,nz,mp,np,ns,iz,zs,dr,dz,pi,c0,k0,rhob,alpw,alpb,ksq,
     >   ksqw,ksqb,f1,f2,f3,u,v,r1,r2,r3,s1,s2,s3,pd1,pd2,mbz,nzbot)
      call outpt(mz,mdr,ndr,ndz,iz,nzplt,lz,ir,dir,eps,r,f3,u,tlg)
c
c     The propagation matrices.
c
      call epade(mp,np,ns,1,k0,c0,dr,pd1,pd2)
      call matrc(mz,nz,mp,np,iz,iz,dz,k0,rhob,alpw,alpb,ksq,ksqw,ksqb,
     >   f1,f2,f3,r1,r2,r3,s1,s2,s3,pd1,pd2,nzbot,mbz)
c
      return
      end
c
c         ----------------------------------------
c
c     Initialize all parameter profiles ---------- PROFL
c
      subroutine profl(mz,nz,ci,dz,eta,omega,rmax,c0,k0,rp,cw,cb,rhob,
     >   attn,alpw,alpb,ksqw,ksqb,nzbot,mbz)
      complex ci,ksqb(mbz)
      real k0,cw(mz),cb(mbz),rhob(mbz),attn(mbz),alpw(mz),
     >  alpb(mbz),ksqw(mz)
c
      call zread(mz,nz,dz,cw)
```

```
      call zread(mbz,nz,dz,cb)
      call zread(mbz,nz,dz,rhob)
      call zread(mbz,nz,dz,attn)
      rp=2.0*rmax
      read(1,*,end=1)rp
c     write(*,*)'read the input through next range value'
c
    1 do 2 i=1,nz+2
      ksqw(i)=(omega/cw(i))**2-k0**2
c         ksqb(i)=((omega/cb(i))*(1.0+ci*eta*attn(i)))**2-k0**2
      alpw(i)=sqrt(cw(i)/c0)
c         alpb(i)=sqrt(rhob(i)*cb(i)/c0)
    2 continue

   30 do 20 i=1,nzbot+2
        ksqb(i)=((omega/cb(i))*(1.0+ci*eta*attn(i)))**2-k0**2
        alpb(i)=sqrt(rhob(i)*cb(i)/c0)
c       write(*,*)'botdep ksqb alpb  ',i*dz,ksqb(i),alpb(i)
   20 continue
c
      return
      end
c
c     Update water profiles while propagating ----------- PROFLU
c
      subroutine proflu(mz,nz,ci,dz,eta,omega,rmax,c0,k0,rp,cw,
     >   alpw,ksqw)
      complex ci
```

```
      real k0,cw(mz),alpw(mz),ksqw(mz)
c
      call zread(mz,nz,dz,cw)
      rp=2.0*rmax
      read(1,*,end=1)rp
c
    1 do 2 i=1,nz+2
      ksqw(i)=(omega/cw(i))**2-k0**2
      alpw(i)=sqrt(cw(i)/c0)
    2 continue
c
      return
      end
c
c     Individual profile reader and interpolator ---------- ZREAD
c
      subroutine zread(mz,nz,dz,prof)
      real prof(mz)
c
      do 1 i=1,nz+2
      prof(i)=-1.0
    1 continue
      read(1,*)zi,profi
      prof(1)=profi
      i=1.5+zi/dz
      prof(i)=profi
      iold=i
    2 read(1,*)zi,profi
```

```
      if(zi.lt.0.0)go to 3
      i=1.5+zi/dz
      if(i.eq.iold)i=i+1
      prof(i)=profi
      iold=i
      go to 2
    3 prof(nz+2)=prof(i)
      i=1
      j=1
    4 i=i+1
      if(prof(i).lt.0.0)go to 4
      if(i-j.eq.1)go to 6
      do 5 k=j+1,i-1
      prof(k)=prof(j)+float(k-j)*(prof(i)-prof(j))/float(i-j)
    5 continue
    6 j=i
      if(j.lt.nz+2)go to 4
c
      return
      end
c
c     The tridiagonal matrices. ----------------------- MATRC
c
      subroutine matrc(mz,nz,mp,np,iz,jz,dz,k0,rhob,alpw,alpb,ksq,ksqw,
     >   ksqb,f1,f2,f3,r1,r2,r3,s1,s2,s3,pd1,pd2,nzbot,mbz)
      complex d1,d2,d3,rfact,ksq(mz),ksqb(mbz),r1(mz,mp),r2(mz,mp),
     >   r3(mz,mp),s1(mz,mp),s2(mz,mp),s3(mz,mp),pd1(mp),pd2(mp)
      real k0,rhob(mbz),f1(mz),f2(mz),f3(mz),alpw(mz),alpb(mbz),ksqw(mz)
```

```
c
      a1=k0**2/6.0
      a2=2.0*k0**2/3.0
      a3=k0**2/6.0
      cfact=0.5/dz**2
      dfact=1.0/12.0
c
c     New matrices when iz.eq.jz.  NEW INPUT POINTS
c
      if(iz.eq.jz)then
      i1=2
      i2=nz+1
      do 1 i=1,iz
       f1(i)=1.0/alpw(i)
       f2(i)=1.0
       f3(i)=alpw(i)
       ksq(i)=ksqw(i)
    1 continue
      ico=0
c     do 2 i=iz+1,nz+2  commented out
c                     CHANGE THE BOTTOM STUFF HERE.
      do 2 i=iz+1,iz+1+nzbot
       ico=ico+1
       f1(i)=rhob(ico)/alpb(ico)
       f2(i)=1.0/rhob(ico)
       f3(i)=alpb(ico)
       ksq(i)=ksqb(ico)
    2 continue
```

```
      end if
c
c     Updated matrices when iz.ne.jz.  (Bottom depth changed)
c
      if(iz.gt.jz)then
      i1=jz
      i2=iz+1
c        change this to update galerkin with new bottom
      i2=nz+1
      do 3 i=jz+1,iz
        f1(i)=1.0/alpw(i)
        f 2(i)=1.0
        f3(i)=alpw(i)
        ksq(i)=ksqw(i)
c       write(*,*)'chgd water pt i= ', i
    3 continue
      ico=0;
      do 32 i=iz+1,iz+1+nzbot
       ico=ico+1
       f1(i)=rhob(ico)/alpb(ico)
       f2(i)=1.0/rhob(ico)
       f3(i)=alpb(ico)
       ksq(i)=ksqb(ico)
   32  continue
c      write(*,*)' chgd bot to ind i= ',i
c      write(*,*)'  ksq(i-200)= ',ksq(i-200)
c      write(*,*)'   changed bottom through depth i*dz= ',i*dz
      end if
```

```
c
c                     CHANGE THE BOTTOM STUFF HERE.
      if(iz.lt.jz)then
      i1=iz
c     i2=jz+1
      i2=nz+1
      ico=0
      do 42 i=iz+1,iz+1+nzbot
       ico=ico+1
       f1(i)=rhob(ico)/alpb(ico)
       f2(i)=1.0/rhob(ico)
       f3(i)=alpb(ico)
       ksq(i)=ksqb(ico)
   42  continue
c      write(*,*)'   changed bottom through depth i*dz= ',i*dz
      end if
c
      do 6 i=i1,i2
c
c     Discretization by Galerkin's method.
c
      c1=cfact*f1(i)*(f2(i-1)+f2(i))*f3(i-1)
      c2=-cfact*f1(i)*(f2(i-1)+2.0*f2(i)+f2(i+1))*f3(i)
      c3=cfact*f1(i)*(f2(i)+f2(i+1))*f3(i+1)
      d1=c1+dfact*(ksq(i-1)+ksq(i))
      d2=c2+dfact*(ksq(i-1)+6.0*ksq(i)+ksq(i+1))
      d3=c3+dfact*(ksq(i)+ksq(i+1))
c
```

```
      do 5 j=1,np
      r1(i,j)=a1+pd2(j)*d1
      r2(i,j)=a2+pd2(j)*d2
      r3(i,j)=a3+pd2(j)*d3
      s1(i,j)=a1+pd1(j)*d1
      s2(i,j)=a2+pd1(j)*d2
      s3(i,j)=a3+pd1(j)*d3
    5 continue
    6 continue
c
c     The matrix decomposition.
c
      do 9 j=1,np
      do 7 i=i1,iz
      rfact=1.0/(r2(i,j)-r1(i,j)*r3(i-1,j))
      r1(i,j)=r1(i,j)*rfact
      r3(i,j)=r3(i,j)*rfact
      s1(i,j)=s1(i,j)*rfact
      s2(i,j)=s2(i,j)*rfact
      s3(i,j)=s3(i,j)*rfact
    7 continue
c
      do 8 i=i2,iz+2,-1
      rfact=1.0/(r2(i,j)-r3(i,j)*r1(i+1,j))
      r1(i,j)=r1(i,j)*rfact
      r3(i,j)=r3(i,j)*rfact
      s1(i,j)=s1(i,j)*rfact
      s2(i,j)=s2(i,j)*rfact
```

```
      s3(i,j)=s3(i,j)*rfact
    8 continue
c
      r2(iz+1,j)=r2(iz+1,j)-r1(iz+1,j)*r3(iz,j)
      r2(iz+1,j)=r2(iz+1,j)-r3(iz+1,j)*r1(iz+2,j)
      r2(iz+1,j)=1.0/r2(iz+1,j)
c
    9 continue
c
      return
      end
c
c     The tridiagonal solver.   ----------------------- SOLVE
c
      subroutine solve(mz,nz,mp,np,iz,u,v,r1,r2,r3,s1,s2,s3)
      complex u(mz),v(mz),r1(mz,mp),r2(mz,mp),r3(mz,mp),s1(mz,mp),
     >   s2(mz,mp),s3(mz,mp)
      eps=1.0e-30
c
      do 6 j=1,np
c
c     The right side.
c
      do 1 i=2,nz+1
      v(i)=s1(i,j)*u(i-1)+s2(i,j)*u(i)+s3(i,j)*u(i+1)+eps
    1 continue
c
c     The elimination steps.
```

```
c
      do 2 i=3,iz
      v(i)=v(i)-r1(i,j)*v(i-1)+eps
    2 continue
      do 3 i=nz,iz+2,-1
      v(i)=v(i)-r3(i,j)*v(i+1)+eps
    3 continue
c
      u(iz+1)=(v(iz+1)-r1(iz+1,j)*v(iz)-r3(iz+1,j)*v(iz+2))*
     >   r2(iz+1,j)+eps
c
c     The back substitution steps.
c
      do 4 i=iz,2,-1
      u(i)=v(i)-r3(i,j)*u(i+1)+eps
    4 continue
      do 5 i=iz+2,nz+1
      u(i)=v(i)-r1(i,j)*u(i-1)+eps
    5 continue
    6 continue
c
      return
      end
c
c     Matrix updates.     ------------------------ UPDAT
c
      subroutine updat(mr,mz,nz,mp,np,iz,ib,dr,dz,eta,omega,rmax,c0,k0,
     >   ci,r,rp,rs,rb,zb,cw,cb,rhob,attn,alpw,alpb,ksq,ksqw,ksqb,f1,f2,
```

```
     >   f3,r1,r2,r3,s1,s2,s3,pd1,pd2,nzbot,mbz)
      complex ci,ksq(mz),ksqb(mbz),r1(mz,mp),r2(mz,mp),r3(mz,mp),
     >   s1(mz,mp),s2(mz,mp),s3(mz,mp),pd1(mp),pd2(mp)
      real k0,rb(mr),zb(mr),attn(mbz),cb(mbz),rhob(mbz),cw(mz),ksqw(mz),
     >   f1(mz),f2(mz),f3(mz),alpw(mz),alpb(mbz)
c
c     Varying bathymetry.
c
      if(r.ge.rb(ib+1))ib=ib+1
      jz=iz
      z=zb(ib)+(r+0.5*dr-rb(ib))*(zb(ib+1)-zb(ib))/(rb(ib+1)-rb(ib))
      iz=1.0+z/dz
      iz=max(2,iz)
      iz=min(nz,iz)
      if(iz.ne.jz)then
c       write(*,*)'var bath at range r = ',r,z,iz,jz,' ( r z iz jz)'
        call matrc(mz,nz,mp,np,iz,jz,dz,k0,rhob,alpw,alpb,ksq,
     >   ksqw,ksqb,f1,f2,f3,r1,r2,r3,s1,s2,s3,pd1,pd2,nzbot,mbz)
      end if
c
c     Varying profiles.
c
      if(r.ge.rp)then
      call profl(mz,nz,ci,dz,eta,omega,rmax,c0,k0,rp,cw,cb,rhob,
     >   attn,alpw,alpb,ksqw,ksqb,nzbot,mbz)
c     call proflu(mz,nz,ci,dz,eta,omega,rmax,c0,k0,rp,cw,
c    >   alpw,ksqw)
      call matrc(mz,nz,mp,np,iz,iz,dz,k0,rhob,alpw,alpb,ksq,ksqw,ksqb,
```

```
     >   f1,f2,f3,r1,r2,r3,s1,s2,s3,pd1,pd2,nzbot,mbz)
      end if
c
c     Turn off the stability constraints.
c
      if(r.ge.rs)then
      ns=0
      rs=2.0*rmax
      call epade(mp,np,ns,1,k0,c0,dr,pd1,pd2)
      call matrc(mz,nz,mp,np,iz,iz,dz,k0,rhob,alpw,alpb,ksq,ksqw,ksqb,
     >   f1,f2,f3,r1,r2,r3,s1,s2,s3,pd1,pd2,nzbot,mbz)
      end if
c
      return
      end
c
c     The self-starter.            ------------------ SELFS
c
      subroutine selfs(mz,nz,mp,np,ns,iz,zs,dr,dz,pi,c0,k0,rhob,alpw,
     > alpb,ksq,ksqw,ksqb,f1,f2,f3,u,v,r1,r2,r3,s1,s2,s3,pd1,pd2,mbz,
     > nzbot)
      complex u(mz),v(mz),ksq(mz),ksqb(mbz),r1(mz,mp),r2(mz,mp),
     >   r3(mz,mp),s1(mz,mp),s2(mz,mp),s3(mz,mp),pd1(mp),pd2(mp)
      real k0,rhob(mbz),alpw(mz),alpb(mbz),f1(mz),f2(mz),f3(mz),
     >  ksqw(mz)
c
c     Conditions for the delta function.
c
```

```
      si=1.0+zs/dz
      is=ifix(si)
      dis=si-float(is)
      u(is)=(1.0-dis)*sqrt(2.0*pi/k0)/(dz*alpw(is))
      u(is+1)=dis*sqrt(2.0*pi/k0)/(dz*alpw(is))
c
c     Divide the delta function by (1-X)**2 to get a smooth rhs.
c
      pd1(1)=0.0
      pd2(1)=-1.0
      call matrc(mz,nz,mp,1,iz,iz,dz,k0,rhob,alpw,alpb,ksq,ksqw,ksqb,
     >   f1,f2,f3,r1,r2,r3,s1,s2,s3,pd1,pd2,nzbot,mbz)
      call solve(mz,nz,mp,1,iz,u,v,r1,r2,r3,s1,s2,s3)
      call solve(mz,nz,mp,1,iz,u,v,r1,r2,r3,s1,s2,s3)
c
c     Apply the operator (1-X)**2*(1+X)**(-1/4)*exp(ci*k0*r*sqrt(1+X)).
c
      call epade(mp,np,ns,2,k0,c0,dr,pd1,pd2)
      call matrc(mz,nz,mp,np,iz,iz,dz,k0,rhob,alpw,alpb,ksq,ksqw,ksqb,
     >   f1,f2,f3,r1,r2,r3,s1,s2,s3,pd1,pd2,nzbot,mbz)
      call solve(mz,nz,mp,np,iz,u,v,r1,r2,r3,s1,s2,s3)
c
      return
      end
c
c     Output field.       ----------------------- OUTPT
c
      subroutine outpt(mz,mdr,ndr,ndz,iz,nzplt,lz,ir,dir,eps,r,f3,u,tlg)
```

```
      complex ur,u(mz),ci,af(mz)
      real f3(mz),tlg(mz)
c
      eye=cmplx(0.0,1.0)
c
      ur=(1.0-dir)*f3(ir)*u(ir)+dir*f3(ir+1)*u(ir+1)
      tl=-20.0*alog10(cabs(ur)+eps)+10.0*alog10(r+eps)
      write(3,*)r,tl
c     write(*,*)r,tl
c
      mdr=mdr+1
      if(mdr.eq.ndr)then
      mdr=0
c
      j=0
      iflag=1
c        OUTPUT:  first point is at surface, and always
c      gets skipped unless ndz=1;
      do 1 i=ndz,nzplt,ndz
      ur=u(i)*f3(i)
      j=j+1
      tlg(j)=-20.0*alog10(cabs(ur)+eps)+10.0*alog10(r+eps)
      af(j)=ur*( exp(eye*ko*r)/sqrt(r+eps) )
c
c     Mark the ocean bottom.
c
      if((i.gt.iz).and.(iflag.eq.1))then
      tlg(j)=0.0
```

```
      iflag=0
      end if
c
    1 continue
      write(4,*)(tlg(j),j=1,lz)
C     write(5,*)(af(j),j=1,lz)
      write(5,701)( real(af(j)), j=1,lz)
      write(5,701)( aimag(af(j)), j=1,lz)
701   format(f14.11)
      end if
c
      return
      end
c
c     The coefficients of the rational approximation.   ---- EPADE
c
      subroutine epade(mp,np,ns,ip,k0,c0,dr,pd1,pd2)
c
      implicit real*8 (a-h,o-z)
      complex*16 ci,z1,z2,g,dg,dh1,dh2,dh3,a,b
      complex*8 pd1(mp),pd2(mp)
      real*8 nu
      real*4 k0,c0,dr
      parameter (m=40)
      dimension bin(m,m),a(m,m),b(m),dg(m),dh1(m),dh2(m),dh3(m),fact(m)
      pi=4.0d0*datan(1.0d0)
      ci=dcmplx(0.0d0,1.0d0)
      sig=k0*dr
```

```
      n=2*np
c
      write(2,*)' '
      if(ip.eq.1)then
      write(2,*)'  Split-step Pade approximation.'
      write(2,*)' '
      write(2,*)'  x               cp            err            amp'
      nu=0.0d0
      alp=0.0d0
      else
      write(2,*)'  Self-starter approximation.'
      write(2,*)' '
      write(2,*)'  x               cp            err            amp'
      nu=1.0d0
      alp=-0.25d0
      end if
      write(2,*)' '
c
c     The factorials.
c
      fact(1)=1.0d0
      do 1 i=2,n
      fact(i)=dfloat(i)*fact(i-1)
    1 continue
c
c     The binomial coefficients.
c
      do 2 i=1,n+1
```

```
      bin(i,1)=1.0d0
      bin(i,i)=1.0d0
    2 continue
      do 4 i=3,n+1
      do 3 j=2,i-1
      bin(i,j)=bin(i-1,j-1)+bin(i-1,j)
    3 continue
    4 continue
c
      do 6 i=1,n
      do 5 j=1,n
      a(i,j)=0.0d0
    5 continue
    6 continue
c
c     The accuracy constraints.
c
      call deriv(m,n,sig,alp,dg,dh1,dh2,dh3,bin,nu)
c
      do 7 i=1,n
      b(i)=dg(i+1)
    7 continue
      do 9 i=1,n
      if(2*i-1.le.n)a(i,2*i-1)=fact(i)
      do 8 j=1,i
      if(2*j.le.n)a(i,2*j)=-bin(i+1,j+1)*fact(j)*dg(i-j+1)
    8 continue
    9 continue
```

```
c
c     The stability constraints.
c
      if(ns.ge.1)then
      z1=-3.0d0
      b(n)=-1.0d0
      do 10 j=1,np
      a(n,2*j-1)=z1**j
      a(n,2*j)=0.0d0
   10 continue
      end if
c
      if(ns.ge.2)then
      z1=-1.5d0
      b(n-1)=-1.0d0
      do 11 j=1,np
      a(n-1,2*j-1)=z1**j
      a(n-1,2*j)=0.0d0
   11 continue
      end if
c
      call gauss(m,n,a,b)
c
      dh1(1)=1.0d0
      do 12 j=1,np
      dh1(j+1)=b(2*j-1)
   12 continue
      call zroots(dh1,np,dh2)
```

```
      do 13 j=1,np
      pd1(j)=-1.0d0/dh2(j)
   13 continue
c
      dh1(1)=1.0d0
      do 14 j=1,np
      dh1(j+1)=b(2*j)
   14 continue
      call zroots(dh1,np,dh2)
      do 15 j=1,np
      pd2(j)=-1.0d0/dh2(j)
   15 continue
c
c     Check accuracy and stability.
c
      x=-2.0d0
      delx=0.02d0
      do 17 i=1,151
      z1=1.0d0
      z2=1.0d0
      do 16 j=1,np
      z1=z1*(1.0d0+pd1(j)*x)
      z2=z2*(1.0d0+pd2(j)*x)
   16 continue
      z1=z1/z2
      z2=0.0d0
      cp=0.0d0
      if(x.gt.-0.99d0)then
```

```
      z2=g(ci,sig,x,alp,nu)
      cp=c0/dsqrt(1.0d0+x)
      end if
      write(2,*)sngl(x),sngl(cp),sngl(cdabs(z2-z1)),sngl(cdabs(z1))
      x=x+delx
   17 continue
c
      return
      end
c
c     The operator function.   ---------------- FUNCTION G
c
      function g(ci,sig,x,alp,nu)
      complex*16 ci,g
      real*8 alp,sig,x,nu
      g=(1.0d0-nu*x)**2*cdexp(alp*dlog(1.0d0+x)+
     >   ci*sig*(-1.0d0+dsqrt(1.0d0+x)))
      return
      end
c
c     The derivatives of the operator function at x=0.  -- DERIV
c
      subroutine deriv(m,n,sig,alp,dg,dh1,dh2,dh3,bin,nu)
      implicit real*8 (a-h,o-z)
      complex*16 ci,dg(m),dh1(m),dh2(m),dh3(m)
      real*8 bin(m,m),nu
      ci=dcmplx(0.0d0,1.0d0)
c
```

```
      dh1(1)=0.5d0*ci*sig
      exp1=-0.5d0
      dh2(1)=alp
      exp2=-1.0d0
      dh3(1)=-2.0d0*nu
      exp3=-1.0d0
      do 1 i=2,n
      dh1(i)=dh1(i-1)*exp1
      exp1=exp1-1.0d0
      dh2(i)=dh2(i-1)*exp2
      exp2=exp2-1.0d0
      dh3(i)=-nu*dh3(i-1)*exp3
      exp3=exp3-1.0d0
    1 continue
c
      dg(1)=1.0d0
      dg(2)=dh1(1)+dh2(1)+dh3(1)
      do 3 i=2,n
      dg(i+1)=dh1(i)+dh2(i)+dh3(i)
      do 2 j=1,i-1
      dg(i+1)=dg(i+1)+bin(i,j)*(dh1(j)+dh2(j)+dh3(j))*dg(i-j+1)
    2 continue
    3 continue
c
      return
      end
c
c     Gaussian elimination. -------------------------- GAUSS
```

```
c
      subroutine gauss(m,n,a,b)
      implicit real*8 (a-h,o-z)
      complex*16 a(m,m),b(m)
c
c     Downward elimination.
c
      do 4 i=1,n
      if(i.lt.n)call pivot(m,n,i,a,b)
      a(i,i)=1.0d0/a(i,i)
      b(i)=b(i)*a(i,i)
      if(i.lt.n)then
      do 1 j=i+1,n
      a(i,j)=a(i,j)*a(i,i)
    1 continue
      do 3 k=i+1,n
      b(k)=b(k)-a(k,i)*b(i)
      do 2 j=i+1,n
      a(k,j)=a(k,j)-a(k,i)*a(i,j)
    2 continue
    3 continue
      end if
    4 continue
c
c     Back substitution.
c
      do 6 i=n-1,1,-1
      do 5 j=i+1,n
```

```
      b(i)=b(i)-a(i,j)*b(j)
    5 continue
    6 continue
c
      return
      end
c
c     Rows are interchanged for stability.
c
      subroutine pivot(m,n,i,a,b)
      implicit real*8 (a-h,o-z)
      complex*16 temp,a(m,m),b(m)
c
      i0=i
      amp0=cdabs(a(i,i))
      do 1 j=i+1,n
      amp=cdabs(a(j,i))
      if(amp.gt.amp0)then
      i0=j
      amp0=amp
      end if
    1 continue
      if(i0.eq.i)return
c
      temp=b(i)
      b(i)=b(i0)
      b(i0)=temp
      do 2 j=i,n
```

```
      temp=a(i,j)
      a(i,j)=a(i0,j)
      a(i0,j)=temp
    2 continue
c
      return
      end
c
c     Subroutine zroots modified from Numerical Recipes.--- ZROOTS
c
      subroutine zroots(a,m,roots)
      implicit real*8 (a-h,o-z)
      parameter (maxm=101)
      complex*16 x,b,c,ad(maxm),a(m+1),roots(m)
      eps=1.0d-14
c
      do 1 j=1,m+1
      ad(j)=a(j)
    1 continue
c
      do 3 j=m,1,-1
      x=dcmplx(0.0d0,0.0d0)
      call laguer(ad,j,x,its)
      xre=2.0d0*dabs(dreal(x))*eps**2
      xim=dabs(dimag(x))
      if(xim.le.xre)x=dcmplx(dreal(x),0.d0)
      roots(j)=x
      b=ad(j+1)
```

```
      do 2 jj=j,1,-1
      c=ad(jj)
      ad(jj)=b
      b=x*b+c
    2 continue
    3 continue
c
      do 4 j=1,m
      call laguer(a,m,roots(j),its)
    4 continue
c
      do 7 j=2,m
      x=roots(j)
      do 5 i=j-1,1,-1
      if(dreal(roots(i)).le.dreal(x))go to 6
      roots(i+1)=roots(i)
    5 continue
      i=0
    6 roots(i+1)=x
    7 continue
c
      return
      end
c
c     Subroutine laguer modified from Numerical Recipes. --------- LAGUER
c
      subroutine laguer(a,m,x,its)
      implicit real*8 (a-h,o-z)
```

```
      parameter (mr=8,mt=10,maxit=mt*mr)
      real*8 frac(mr)
      complex*16 dx,x,x1,b,d,f,g,h,sq,gp,gm,g2,a(m+1)
      save frac
      data frac /0.5d0,0.25d0,0.75d0,0.13d0,0.38d0,0.62d0,0.88d0,1.0d0/
      epss=2.0d-15
c
      do 2 iter=1,maxit
      its=iter
      b=a(m+1)
      err=abs(b)
      d=dcmplx(0.0d0,0.0d0)
      f=dcmplx(0.0d0,0.0d0)
      abx=cdabs(x)
      do 1 j=m,1,-1
      f=x*f+d
      d=x*d+b
      b=x*b+a(j)
      err=abs(b)+abx*err
    1 continue
c
      err=epss*err
      if(cdabs(b).le.err) then
      return
      else
      g=d/b
      g2=g*g
      h=g2-2.0d0*f/b
```

```
      sq=cdsqrt(dfloat(m-1)*(dfloat(m)*h-g2))
      gp=g+sq
      gm=g-sq
      abp=cdabs(gp)
      abm=cdabs(gm)
      if(abp.lt.abm)gp=gm
      if(dmax1(abp,abm).gt.0.0d0)then
      dx=dfloat(m)/gp
      else
      dx=cdexp(dcmplx(dlog(1.0d0+abx),dfloat(iter)))
      endif
      endif
      x1=x-dx
      if(x.eq.x1)return
      if(mod(iter,mt).ne.0)then
      x=x1
      else
      x=x-dx*frac(iter/mt)
      endif
    2 continue
c
c     pause '   too many iterations in laguer'
c
      return
      end
```

APPENDIX C

SUPPLEMENTAL ENERGY-VERSUS-RANGE PLOTS FROM WAVE-EQUATION MODELING

For completeness, this appendix presents RAM wave-equation energy-versus-range results, beyond the results shown in the main text. Coherent and incoherent energy are plotted for a fixed bandwidth of 4 kHz and varying depths of 50 m, 75 m, 100 m, 150 m, and 200 m, as well as at a fixed depth of 100 m and varying bandwidths of 4 kHz to 500 Hz.

Incoherent transition range is unaffected by bandwidth, whereas coherent transition range scales linearly with bandwidth.

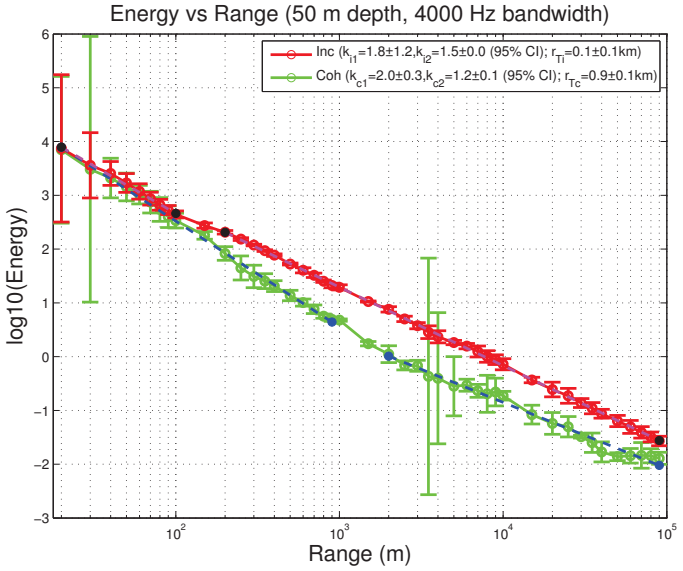

Figure C.1. Coherent and incoherent energy for a bandwidth of 4 kHz and a depths of 50 m.

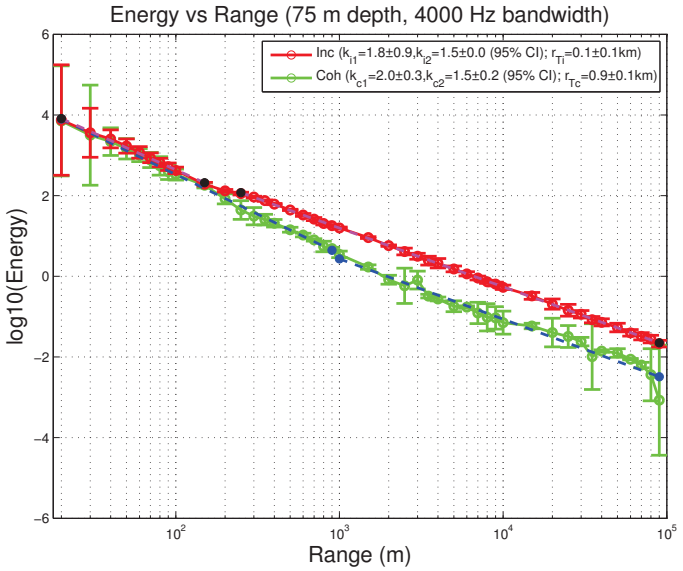

Figure C.2. Coherent and incoherent energy for a bandwidth of 4 kHz and a depths of 75 m.

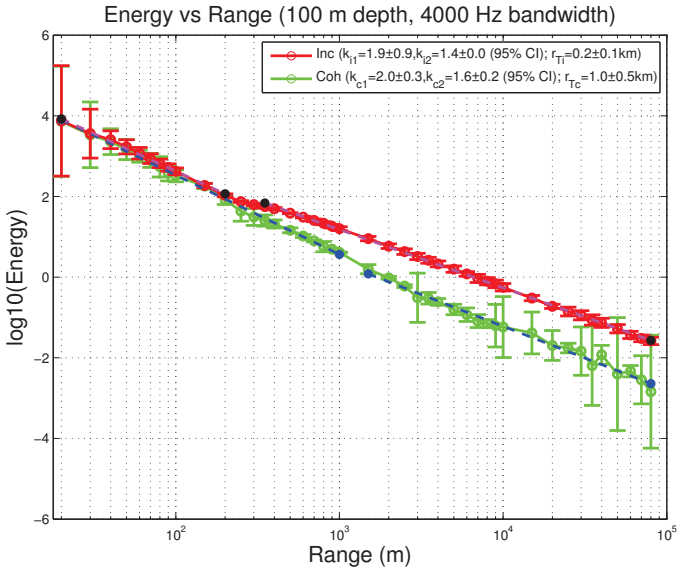

Figure C.3. Coherent and incoherent energy for a bandwidth of 4 kHz and a depths of 100 m.

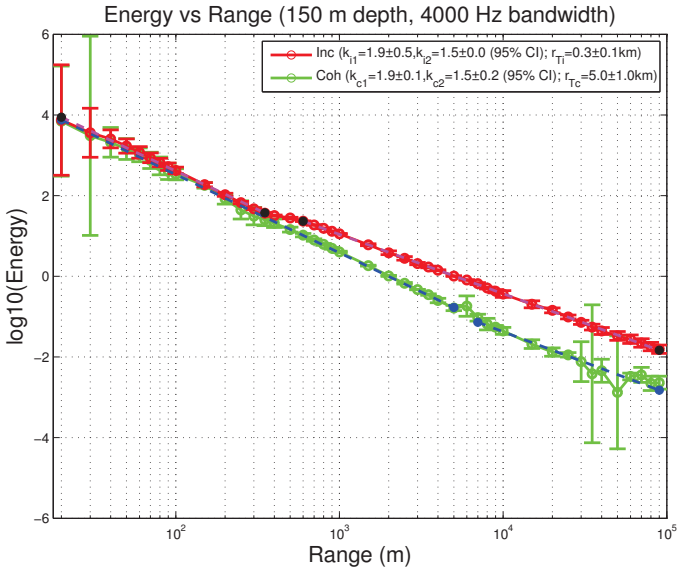

Figure C.4. Coherent and incoherent energy for a bandwidth of 4 kHz and a depths of 150 m.

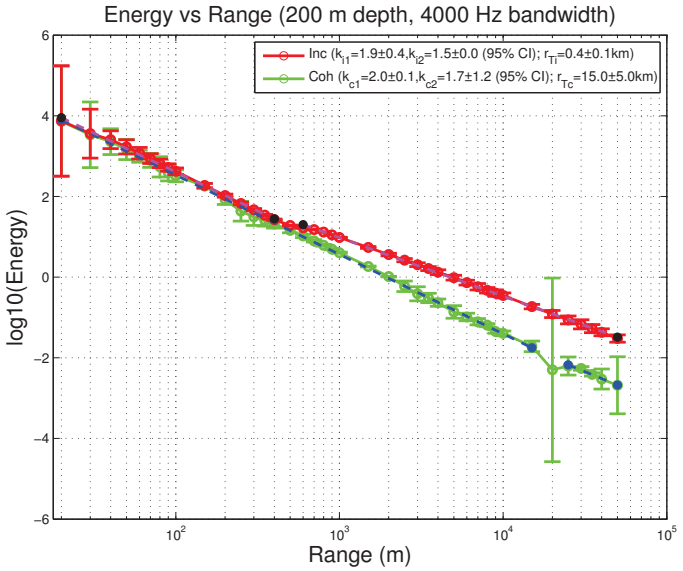

Figure C.5. Coherent and incoherent energy for a bandwidth of 4 kHz and a depths of 200 m.

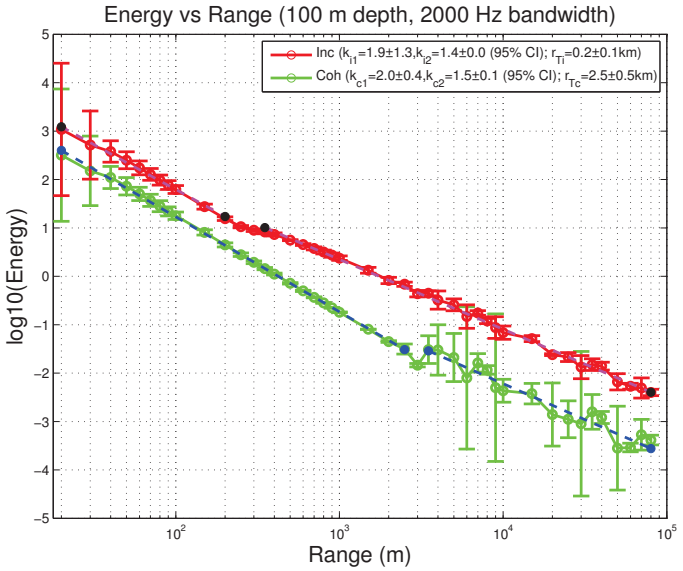

Figure C.6. Coherent and incoherent energy for a bandwidth of 2 kHz and a depths of 100 m.

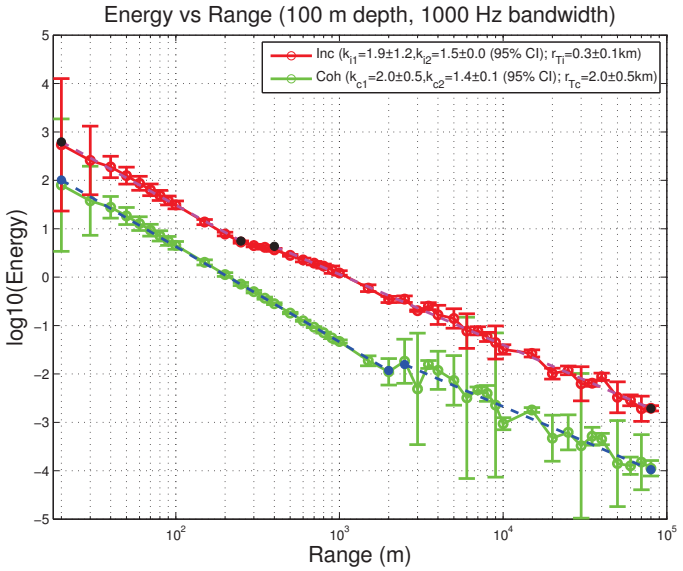

Figure C.7. Coherent and incoherent energy for a bandwidth of 1 kHz and a depths of 100 m.

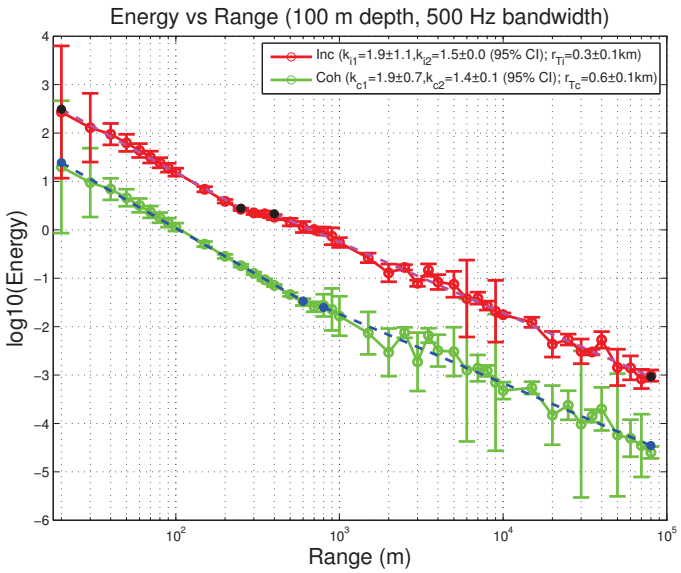

Figure C.8. Coherent and incoherent energy for a bandwidth of 500 Hz and a depths of 100 m.

APPENDIX D

CHARACTERIZATION OF RESIDUALS FOR ENERGY-VERSUS-RANGE EXPONENT FITS FROM KAM11 FIELD EXPERIMENT

In this appendix, we characterize the residuals from the linear least-squares estimates (LLSEs) of the energy-loss exponents in Section 2.6.4. For quality-of-fit assessment, we assess the normality of the residual distribution as well as the linearity and variance of the residuals as a function of fitted value [104].

The normality of the residual distribution is assessed visually with histograms as well as a quantile-quantile plot versus a normal distribution. The histograms give a direct visual assessment of the distribution function. The quantile-quantile plots graph the empirical cumulative distribution function of the residuals on the vertical axis, versus the sorted residual values on the horizontal axis. The residuals are plotted with "+" symbols. A normal distribution with the same 25^{th} and 75^{th} percentiles is overlaid in dashed lines on the plot for comparison. If the residuals have approximately normal distributions, they will lie over the dashed lines. In general, deviations of the residual distributions are most visible at the tails of the distributions. LLSE fits and confidence intervals are moderately robust to non-normal errors (hence residuals), so long as there are not large outliers [104].

Two additional assessments of the quality of fit are visualized by plotting binned residual values as a function of fitted value. We used five bins spread equally across the range of fitted values, and plotted boxplots with a box shown for each of the five bins. The boxplots show the median residual value and the central fifty percentiles of residual values for each of the bins across fitted values. Good quality fits will have approximately equal residual variances across fitted values, as well as residual means and medians which are approximately zero, indicating that the fitted data

is in fact consistent with a linear model. Though there are some issues with the fits assessed here, they are generally of acceptable quality for our estimates, in particular for JD190,SYS3.

Each of the figures on the following pages, Figures D.1-D.5, shows six sets of plots. There is one set of plots for each of the unweighted and weighted fits for the coherent (green), incoherent (red), and noise (black) energies. Each set of characterization plots consists of is a histogram of the residuals, a quantile-quantile plot of the residuals versus a normal distribution, and a boxplot of residuals versus fitted value.

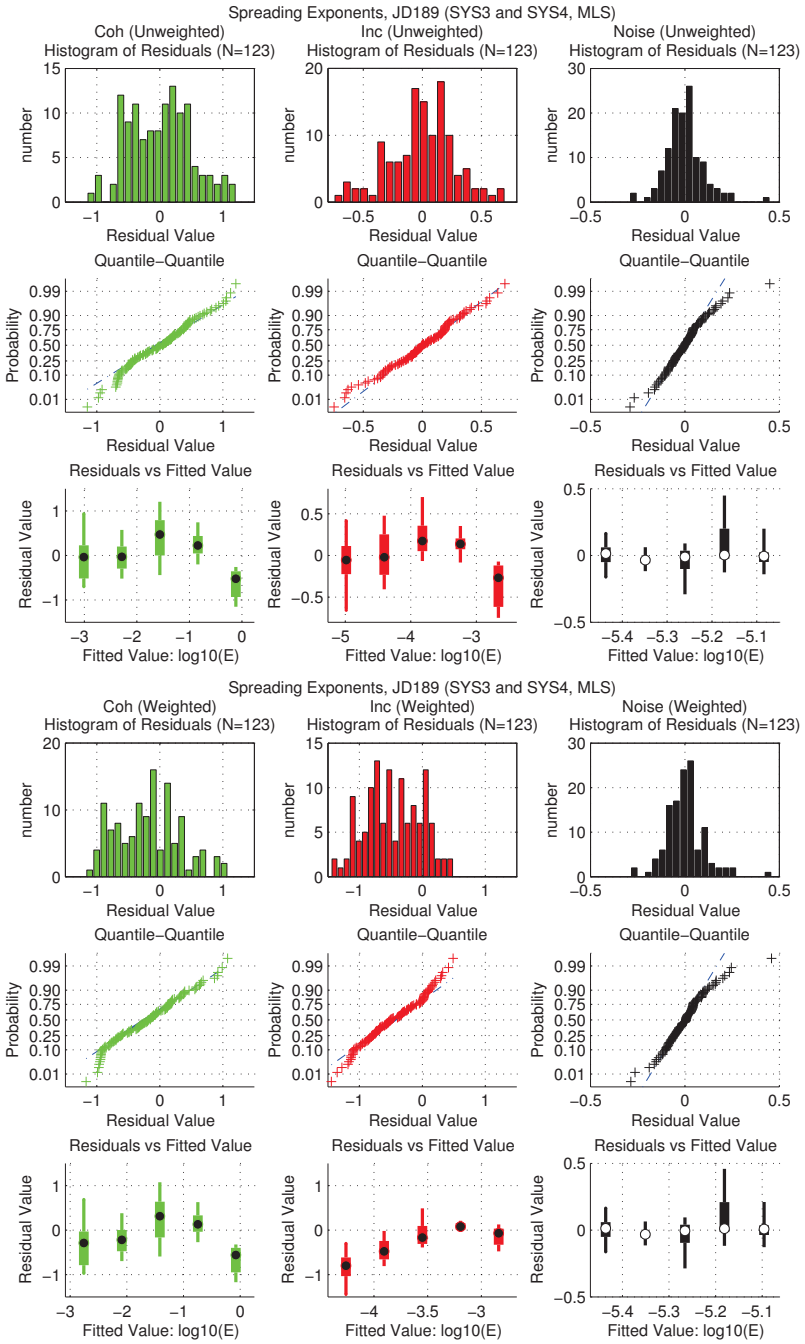

Figure D.1. JD189 fit residuals for fits shown in Figure 2.24. Unweighted LLSE fits at top, and weighted LLSE fits at bottom (showing unweighted residuals).

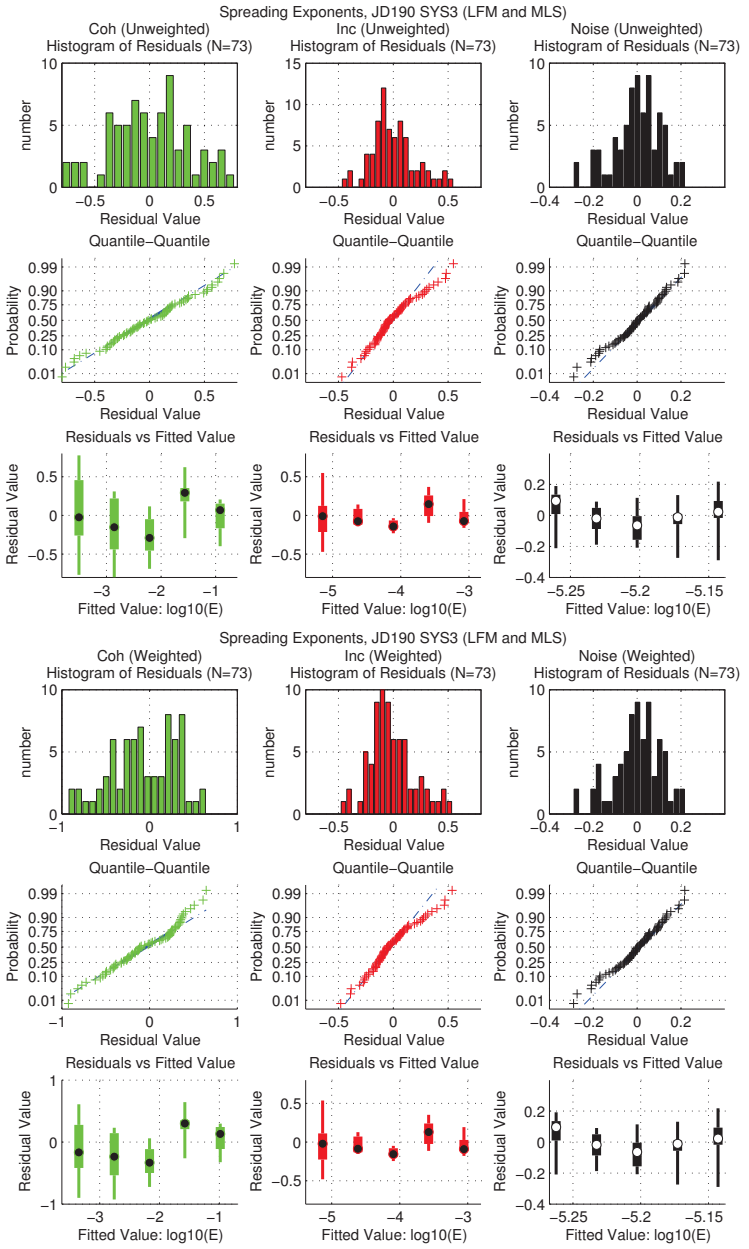

Figure D.2. JD190,SYS3 fit residuals for fits shown in Figure 2.25. Unweighted LLSE fits at top, and weighted LLSE fits at bottom (showing unweighted residuals). The residual distribution for the weighted fit is bimodal due to the differences in coherent energy estimates for LFM and MLS signals.

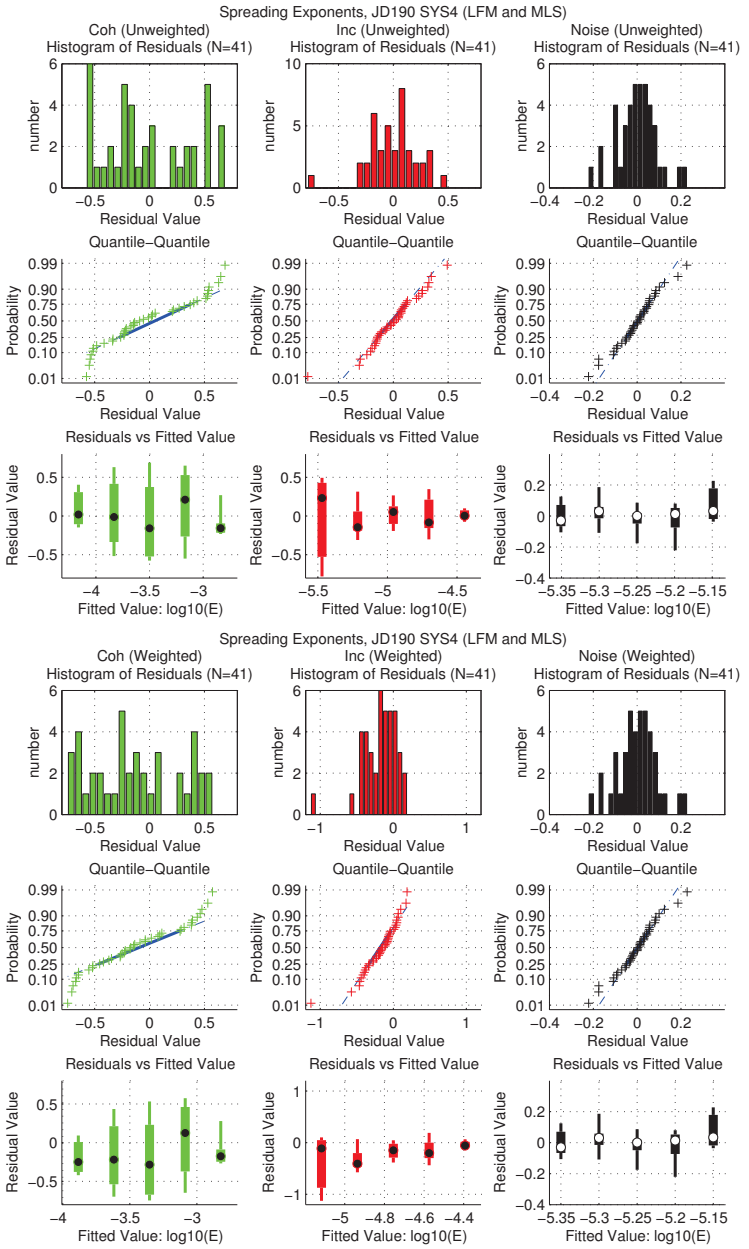

Figure D.3. JD190,SYS4 fit residuals for fits shown in Figure 2.26. Unweighted LLSE fits at top, and weighted LLSE fits at bottom (showing unweighted residuals). The coherent residual distribution is bimodal (or worse) due to the significant differences between coherent energy estimates for LFM and MLS.

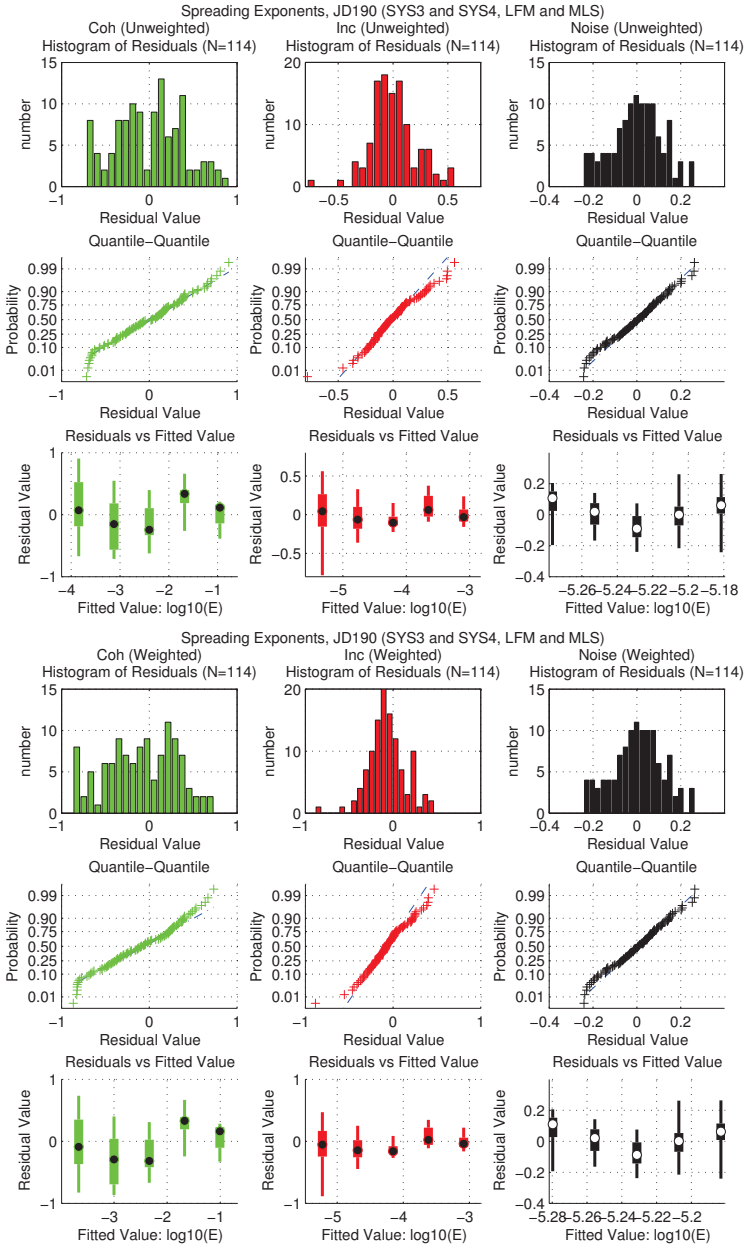

Figure D.4. JD190 fit residuals for fits shown in Figure 2.27. Unweighted LLSE fits at top, and weighted LLSE fits at bottom (showing unweighted residuals). The incoherent and noise residuals look fine, as do the R^2 value of the fits (the noise fit as a function of range should explain none of the variance, so it should have $R^2 = 0$, ideally). The bad fits of JD190,SYS4 are mostly obscured.

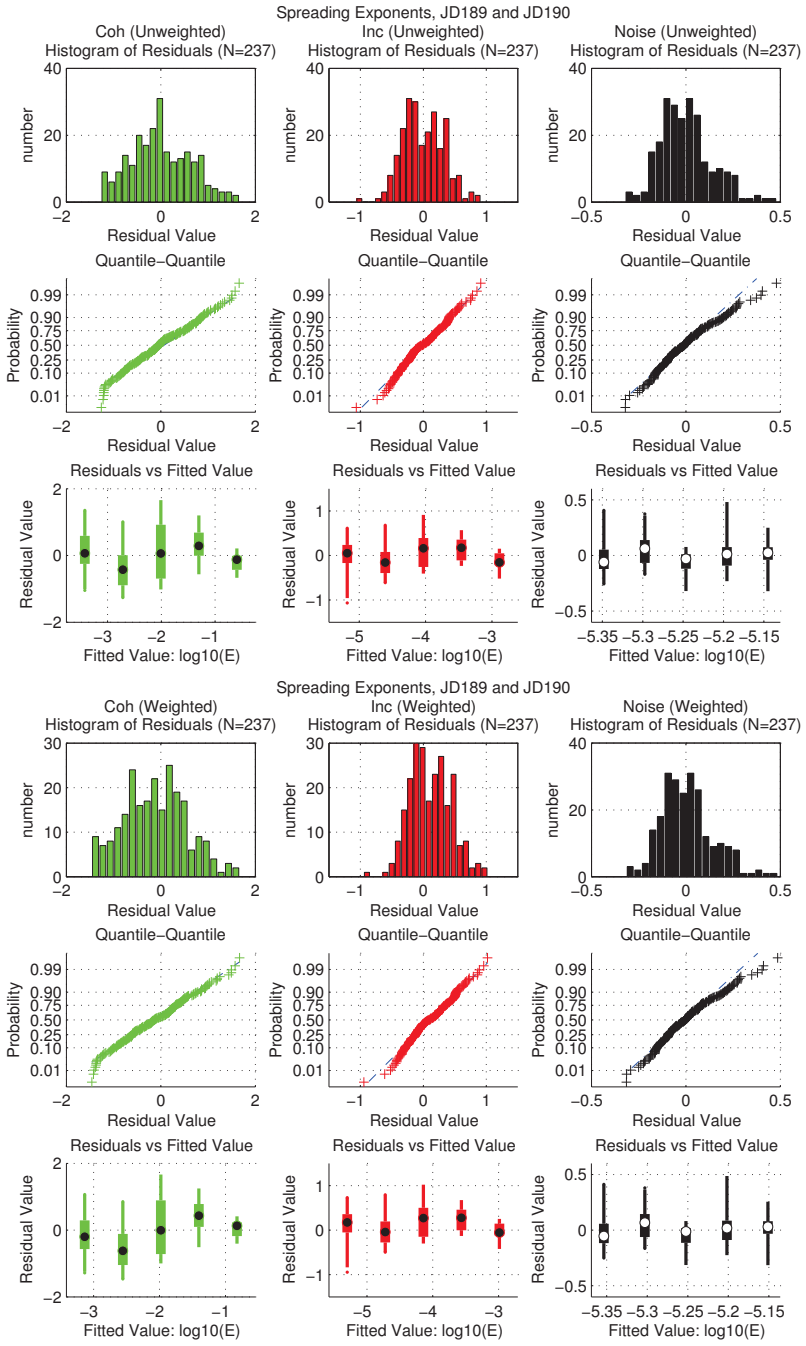

Figure D.5. JD189 and JD190 (all data) fit residuals for fits shown in Figure 2.28. Unweighted LLSE fits at top, and weighted LLSE fits at bottom (showing unweighted residuals).

APPENDIX E

CALCULATION OF INTERFERENCE SCENARIO IIA EFFECTIVENESS

Xu et al. make an approximation in calculating the area of potential interferers in Scenario IIa in Figure 3.1b. Since Scenario IIb does not occur for radio networks with spreading exponent $k = 4$ and detection threshold $T < 12$ dB, there is no problem in Xu et al.'s paper. Extending their results to UANs, however, leads to a discontinuity in the RTS/CTS effectiveness $E_{\text{RTS/CTS}}$ between Scenario IIa and Scenario IIb, both of which commonly occur in UANs.

To avoid discontinuities in $E_{\text{RTS/CTS}}$ between Scenario IIa and Scenario IIb, we need to calculate the area of potential interferers in Scenario IIa exactly. In Scenario IIa, the RTS/CTS effectiveness is

$$E_{\text{RTS/CTS}} = \frac{A_{(i \cap \text{RTS/CTS})}}{A_i}, \tag{E.1}$$

introduced in Section 3.2 of this chapter. The area of the interference region is $A_i = \pi R_i^2$. There are several approaches to calculating $A_{(i \cap \text{RTS/CTS})}$.

Xu et al. [135] and Ye et al. [136] calculate the area of the interference region that is not covered by the RTS/CTS handshake; i.e., the red region in Scenario IIa of Figure 3.1b. They approximate this region as an angular segment of an annulus. For UANs, Scenario IIb will be common, and that approach leads to a discontinuity in $E_{\text{RTS/CTS}}$ at the transition from Scenario IIa to Scenario IIb.

We calculate instead the area of the RTS/CTS handshake that is outside of the interference region; i.e., the green crescent moon at the left side of Scenario IIa in Figure 3.1. This shape is also illustrated in Figure E.1, and it is where $R_{\text{tx}} < R_i < R_{\text{tx}} + d$. For the idealized geometry in our example, we can calculate $A_{(i \cap \text{RTS/CTS})}$ exactly.

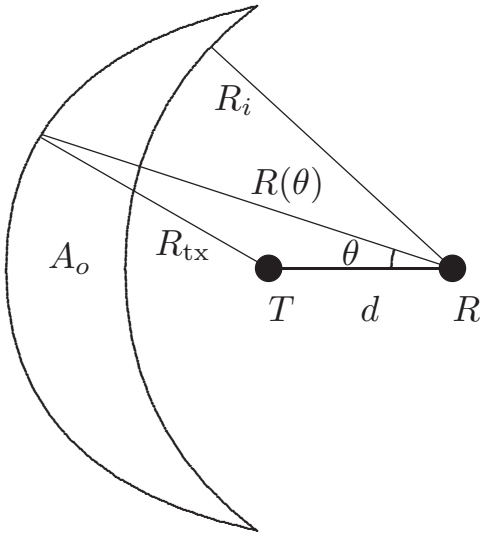

Figure E.1. Area A_o, shown in relation to transmitter T and receiver R. See also Figure 3.1b.

First, we calculate the area covered by the RTS/CTS handshake, $A_{\text{RTS/CTS}}$. In Scenario IIa, $R_i < R_{tx} + d$. The area of the region reached by either the RTS packet or the CTS packet is

$$A_{\text{RTS/CTS}} = 2\left\{\pi R_{\text{tx}}^2 - A_{\text{chord}}\right\}. \tag{E.2}$$

Note that the area of a chordal segment of a circle of radius R_{tx} is

$$A_{\text{chord}} = R_{\text{tx}}^2 \tan^{-1}\left[\sqrt{\left(\frac{R_{\text{tx}}}{a}\right)^2 - 1}\right] - a\sqrt{R_{\text{tx}}^2 - a^2}, \tag{E.3}$$

where a is the apothem of the chord (see `http://mathworld.wolfram.com/Chord.html`). The transmitter and receiver are separated by a distance d, and so the sagitta s of the chord is $s = d/2$. Therefore, by definition and substitution,

$$a = R_{\text{tx}} - s = R_{\text{tx}} - d/2.$$

Now, we calculate $A_{(i \cap \text{RTS/CTS})}$. Let A_o be the area of the RTS/CTS region that is not in the interference region. Therefore, the RTS/CTS effectiveness in Scenario IIa is

$$E_{\text{RTS/CTS}} = \frac{A_{(i \cap \text{RTS/CTS})}}{A_i} = \frac{A_{\text{RTS/CTS}} - A_o}{A_i} \tag{E.4}$$

What remains is to derive the area A_o, shown in Figure E.1

$$A_o = 2 \int_{\theta=0}^{\theta_o} \int_{r=R_i}^{R(\theta)} r \; dr \; d\theta \tag{E.5}$$

where, θ_o is the angle where $R(\theta) = R_i$. By the law of cosines,

$$\theta_o = \cos^{-1} \frac{d^2 + R_i^2 - R_{\text{tx}}^2}{2dR_i} \tag{E.6}$$

Again using the law of cosines, and solving for $R(\theta)$ with the quadratic formula,

$$R(\theta) = d\cos\theta \pm \sqrt{R_{\text{tx}}^2 - d^2 \sin^2\theta}. \tag{E.7}$$

At $\theta = 0$, we can see that we need to take the plus in the $\pm$ for the case of interest. Evaluating the integral for A_o gives

$$\begin{aligned} A_o &= \left(R_{\text{tx}}^2 - R_i^2\right)\theta_o + \frac{d^2}{2}\sin 2\theta_o \\ &\pm 2d^2 \left[\frac{u}{2}\sqrt{\left(\frac{R_{\text{tx}}}{d}\right)^2 - u^2} + \frac{R_{\text{tx}}^2}{2d^2}\sin^{-1}\left(\frac{ud}{R_{\text{tx}}}\right) \right]_{u=0}^{\sin\theta_o} \end{aligned} \tag{E.8}$$

Again, the plus is taken in the $\pm$. Now we have solved for all quantities required to express the RTS/CTS effectiveness for Scenario IIa, following Equation E.4.

APPENDIX F

CASTALIA CODE

We are using Castalia version 3.1. This appendix includes our modifications to the wireless channel physical layer code, as a diff against the Castalia-v3.1 distribution. The Castalia simulator can be downloaded from `http://castalia.research.nicta.com.au`.

```
Index: src/wirelessChannel/WirelessChannel.cc
===================================================================
--- src/wirelessChannel/WirelessChannel.cc (revision 1)
+++ src/wirelessChannel/WirelessChannel.cc (revision 101)
@@ -11,6 +11,7 @@
  ****************************************************************************/

 #include "WirelessChannel.h"
+#include <assert.h>

 Define_Module(WirelessChannel);

@@ -19,10 +20,43 @@
  return 2;
 }

+
+
```

```
+
+/*****************************************************
+ * Calculate the distance, beyond which we cannot
+ * have connectivity between two nodes. This calculation is
+ * based on the maximum TXPower the signalDeliveryThreshold
+ * the pathLossExponent, the PLd0. For the random
+ * shadowing part we use 3*sigma to account for 99.7%
+ * of the cases. We use this value to considerably
+ * speed up the filling of the pathLoss array,
+ * especially for the mobile case.
+ *****************************************************/
+double WirelessChannel::distanceThreshold_m(void)
+{
+ double distanceThreshold_m;
+
+ if (underwater_acoustic_not_radio) {
+ // just set the distance threshold to max node separation for the time being
+ double dx_m = xFieldSize - 0.0;
+ double dy_m = yFieldSize - 0.0;
+ double dz_m = zFieldSize - 0.0;
+ distanceThreshold_m = sqrt(dx_m*dx_m + dy_m*dy_m + dz_m*dz_m);
+ } else {
+ distanceThreshold_m = d0 *
+ pow(10.0,(maxTxPower - signalDeliveryThreshold - PLd0 + 3 * sigma) /
+ (10.0 * pathLossExponent));
+ }
+ return distanceThreshold_m;
+}
```

```
+
+
 void WirelessChannel::initialize(int stage)
 {
  if (stage == 0) {
  readIniFileParameters();
+ set_noiseFloor();
  return;
  }

@@ -176,7 +210,7 @@
  int elementSize = sizeof(PathLossElement) + 3 * sizeof(PathLossElement *);
  int totalElements = 0; //keep track of pathLoss size for reporting purposes

-float x1, x2, y1, y2, z1, z2, dist;
+ float x1, x2, y1, y2, z1, z2, dist; // all in meters
  float PLd; // path loss at distance dist, in dB

  /*********************************************************
@@ -189,9 +223,7 @@
   * speed up the filling of the pathLoss array,
   * especially for the mobile case.
   *********************************************************/
-float distanceThreshold = d0 *
-pow(10.0,(maxTxPower - signalDeliveryThreshold - PLd0 + 3 * sigma) /
-(10.0 * pathLossExponent));
+ double distanceThreshold = distanceThreshold_m();
```

```
  for (int i = 0; i < numOfSpaceCells; i++) {
  if (onlyStaticNodes) {
@@ -230,7 +262,7 @@
  if (dist > distanceThreshold)
  continue;

-PLd = PLd0 + 10.0 * pathLossExponent * log10(dist / d0) + normal(0, sigma);
+ PLd = pathloss_dB(dist, false);

  float bidirectionalPathLossJitter = normal(0, bidirectionalSigma) / 2;

@@ -289,6 +321,10 @@
  ************************************************************************/
 void WirelessChannel::handleMessage(cMessage * msg)
 {
+ double x0_m, y0_m, z0_m, x1_m, y1_m, z1_m, r_m, delay_s;
+ double x2_m, y2_m, z2_m, intf_r_m;
+ double rx_power_coh_dBm, rx_power_inc_dBm, pathloss_coh_dB, pathloss_inc_dB;
+
  switch (msg->getKind()) {

  case WC_NODE_MOVEMENT:{
@@ -364,58 +400,92 @@

  /* Find the cell that the transmitting node resides */
  int cellTx = nodeLocation[srcAddr].cell;
+ x0_m = nodeLocation[srcAddr].x;
+ y0_m = nodeLocation[srcAddr].y;
```

```
+ z0_m = nodeLocation[srcAddr].z;


  /* Iterate through the list of cells that are affected
   * by cellTx and check if there are nodes there.
   * Update the nodesAffectedByTransmitter array
   */
-list < PathLossElement * >::iterator it1;
-for (it1 = pathLoss[cellTx].begin(); it1 != pathLoss[cellTx].end(); it1++) {
-/* If no nodes exist in this cell, move on. */
-if (cellOccupation[(*it1)->cellID].empty())
+
+ for (int dest=0; dest<numOfNodes; dest++) {
+ trace() << "signal from node[" << srcAddr << "] starting on node[" \
                        << dest << "]";
+
+ if (dest == srcAddr) {
+ trace() << "signal from node[" << srcAddr << "] skipping node[" \
                             << dest << "]";
  continue;
+ }
+ x1_m = nodeLocation[dest].x;
+ y1_m = nodeLocation[dest].y;
+ z1_m = nodeLocation[dest].z;
+ r_m = range_m(x0_m, y0_m, z0_m, x1_m, y1_m, z1_m);
+ pathloss_coh_dB = pathloss_dB(r_m, true);
+ pathloss_inc_dB = pathloss_dB(r_m, false);
+ rx_power_coh_dBm=signalMsg->getPower_coh_dBm() - pathloss_coh_dB;
+ rx_power_inc_dBm=signalMsg->getPower_inc_dBm() - pathloss_inc_dB;
```

```
-/* Otherwise there are some nodes in that cell.
- * Calculate the signal received by these nodes
- * It is exactly the same for all of them.
- * The signal may be variable in time.
- */
-float currentSignalReceived = signalMsg->getPower_dBm() - \
                                            (*it1)->avgPathLoss;
+ /*
  if (temporalModelDefined) {
-simtime_t timePassed_msec = (simTime() - \
                                         (*it1)->lastObservationTime) * 1000;
+ simtime_t timePassed_msec =
+ (simTime() - (*it1)->lastObservationTime) * 1000;
  simtime_t timeProcessed_msec =
-temporalModel->runTemporalModel(SIMTIME_DBL(timePassed_msec),
+ temporalModel->runTemporalModel(
+ SIMTIME_DBL(timePassed_msec),
  &((*it1)->lastObservedDiffFromAvgPathLoss));
-currentSignalReceived += (*it1)->lastObservedDiffFromAvgPathLoss;
+ rx_power_coh_dBm += (*it1)->lastObservedDiffFromAvgPathLoss;
+ rx_power_inc_dBm += (*it1)->lastObservedDiffFromAvgPathLoss;
  collectHistogram("Fade depth distribution",
-     (*it1)->lastObservedDiffFromAvgPathLoss);
-/* Update the observation time */
+      (*it1)->lastObservedDiffFromAvgPathLoss);
+ // Update the observation time
  (*it1)->lastObservationTime = simTime() -
```

```
-(timePassed_msec - timeProcessed_msec) / 1000;
+ (timePassed_msec - timeProcessed_msec) / 1000;
  }
+ */

-/* If the resulting current signal received is not strong enough,
- * to be delivered to the radio module, continue to the next cell.
+ /* If the resulting incoherent signal received is not strong enough
+  * to be delivered to the radio module, continue to the next node.
   */
-if (currentSignalReceived < signalDeliveryThreshold)
+ trace() << "signal from node[" << srcAddr << "] dropped, below \
                     threshold on node[" << dest << "]";
+ if (rx_power_inc_dBm < signalDeliveryThreshold) {
  continue;
+ }

-/* Else go through all the nodes of that cell.
- * Iterator it2 returns node IDs.
- */
-list < int >::iterator it2;
-for (it2 = cellOccupation[(*it1)->cellID].begin();
-it2 != cellOccupation[(*it1)->cellID].end(); it2++) {
-if (*it2 == srcAddr)
-continue;
-receptioncount++;
-WirelessChannelSignalBegin *signalMsgCopy = signalMsg->dup();
-signalMsgCopy->setPower_dBm(currentSignalReceived);
```

```
-send(signalMsgCopy, "toNode", *it2);
-nodesAffectedByTransmitter[srcAddr].push_front(*it2);
-} //for it2
-} //for it1
+ receptioncount++;
+ WirelessChannelSignalBegin *signalMsgCopy = signalMsg->dup();
+ signalMsgCopy->setPower_coh_dBm(rx_power_coh_dBm);
+ signalMsgCopy->setPower_inc_dBm(rx_power_inc_dBm);
+ signalMsgCopy->setNoiseFloor(noiseFloor);
+ signalMsgCopy->setRange_m(r_m);

+ if (numOfNodes==2) {
+ intf_r_m = -1.0;
+ } else {
+ x1_m = nodeLocation[1].x;
+ y1_m = nodeLocation[1].y;
+ z1_m = nodeLocation[1].z;
+ x2_m = nodeLocation[2].x;
+ y2_m = nodeLocation[2].y;
+ z2_m = nodeLocation[2].z;
+ intf_r_m = range_m(x1_m, y1_m, z1_m, x2_m, y2_m, z2_m);
+ }
+ signalMsgCopy->setIntf_range_m(intf_r_m);
+
+ signalMsgCopy->setInclude_noise(include_noise);
+ signalMsgCopy->setUse_mixed_exponents(use_mixed_exponents);
+ signalMsgCopy->setKo(ko);
+ signalMsgCopy->setK_inc(k_inc);
```

```
+ signalMsgCopy->setK_coh(k_coh);
+
+ delay_s = propagation_delay_s(r_m);
+ sendDelayed(signalMsgCopy, delay_s, "toNode", dest);
+
+ trace() << "Prop.delay from node[" << srcAddr << "] to node["
+ << dest << "] is " << delay_s << " seconds ("
+ << r_m << " meters); pathloss: coh:" << pathloss_coh_dB << \
                     "dB, inc:" << pathloss_inc_dB << "dB";
+ nodesAffectedByTransmitter[srcAddr].push_front(dest);
+ } //for dest
+
  if (receptioncount > 0)
  trace() << "signal from node[" << srcAddr << "] reached " <<
  receptioncount << " other nodes";
@@ -426,6 +496,9 @@
  WirelessChannelSignalEnd *signalMsg =
      check_and_cast <WirelessChannelSignalEnd*>(msg);
  int srcAddr = signalMsg->getNodeID();
+ x0_m = nodeLocation[srcAddr].x;
+ y0_m = nodeLocation[srcAddr].y;
+ z0_m = nodeLocation[srcAddr].z;

  /* Go through the list of nodes that were affected
   *  by this transmission. *it1 holds the node ID
@@ -434,7 +507,13 @@
  for (it1 = nodesAffectedByTransmitter[srcAddr].begin();
  it1 != nodesAffectedByTransmitter[srcAddr].end(); it1++) {
```

```
  WirelessChannelSignalEnd *signalMsgCopy = signalMsg->dup();
-send(signalMsgCopy, "toNode", *it1);
+ x1_m = nodeLocation[*it1].x;
+ y1_m = nodeLocation[*it1].y;
+ z1_m = nodeLocation[*it1].z;
+ r_m = range_m(x0_m, y0_m, z0_m, x1_m, y1_m, z1_m);
+ delay_s = propagation_delay_s(r_m);
+ sendDelayed(signalMsgCopy, delay_s, "toNode", *it1);
+ trace() << "Prop.delay from node[" << srcAddr << "] to node[" \
                        << *it1 << "] is " << delay_s << " seconds (" << \
r_m << " meters)";
  } //for it1

  /* Now that we are done processing the msg we delete the whole list
@@ -492,7 +571,24 @@
  getParentModule()->par("debugInfoFileName").stringValue());

  onlyStaticNodes = par("onlyStaticNodes");
-pathLossExponent = par("pathLossExponent");
+
+ underwater_acoustic_not_radio = par("underwater_acoustic_not_radio");
+ c_ms = par("c_ms");
+ fc_kHz = par("fc_kHz");
+ BW_kHz = par("BW_kHz");
+ waterdepth_m = par("waterdepth_m");
+ use_mixed_exponents = par("use_mixed_exponents");
+ ko    = par("ko");
+ k_coh = par("k_coh");
```

```
+ k_inc = par("k_inc");
+ include_noise = par("include_noise");
+ shipping_factor = par("shipping_factor");
+ wind_ms = par("wind_ms");
+ include_atten = par("include_atten");
+ use_thorp_not_marshschulkin = par("use_thorp_not_marshschulkin");
+ temperature_C = par("temperature_C");
+ salinity_psu = par("salinity_psu");
+
  sigma = par("sigma");
  bidirectionalSigma = par("bidirectionalSigma");
  PLd0 = par("PLd0");
@@ -595,3 +691,225 @@
  return 1;
  return 0;
 }
+
+
+/* Include code from mac_simulator/chan_physics.c
+ *
+ * Underwater acoustic channel model: channel physics.
+ *
+ * Jim Partan, Apr 2008.
+ *
+ * $Author: partan $
+ * $Date: 2010-06-20 15:23:57 -0400 (Sun, 20 Jun 2010) $
+ * $Revision: 619 $
+ * $Id: chan_physics.c 619 2010-06-20 19:23:57Z partan $
```

```
+ *
+ */
+
+/* $Id: chan_physics.c 619 2010-06-20 19:23:57Z partan $ */
+
+
+double WirelessChannel::range_m(double x0_m, double y0_m, double z0_m,
+     double x1_m, double y1_m, double z1_m)
+{
+  double dx_m, dy_m, dz_m;
+
+  dx_m = x0_m - x1_m;
+  dy_m = y0_m - y1_m;
+  dz_m = z0_m - z1_m;
+  return sqrt(  dx_m*dx_m + dy_m*dy_m + dz_m*dz_m );
+}
+
+
+double WirelessChannel::propagation_delay_s(double r_m)
+{
+ return (r_m/c_ms);
+}
+
+
+double PHYSICS_atten_marshschulkin_dBkm(double f_kHz, double T_C,\
        double S_psu, double z_m)
+{
+  double f2;
```

```
+  double A, B, fT_exp, fT, alpha_dBkm, S_ppt;
+  double P_atm, rho_kgm3, g_ms2, P_kgm2, P_kgcm2;
+  assert(f_kHz > 0.0);
+
+  S_ppt = S_psu; // Parts Per Thousand and Practical Salinity Units\
                     are almost the same...
+
+  f2 = f_kHz*f_kHz;
+
+  /* Marsh and Schulkin's expression for attenuation, in dB/km */
+  A = 2.34e-6;
+  B = 3.38e-6;
+  fT_exp = 6.0 - 1520.0/(T_C + 273.0);
+  fT = 21.9*pow(10, fT_exp);
+
+  P_atm = 101.5e3;                     /* atmospheric pressure, Pa */
+  rho_kgm3 = 1.0e3*(1.0+S_ppt/1.0e3);  /* density of seawater, kg/m3 */
+  g_ms2 = 9.8;                         /* gravitational acceleration, m/s2 */
+  P_kgm2 = rho_kgm3*g_ms2*z_m + P_atm; /* pressure at depth z_m */
+  P_kgcm2 = P_kgm2/(1.0e4);            /* pressure in kg/cm2 */
+
+  alpha_dBkm = 8.68e3 *
+ (((S_ppt*A*fT*f2)/(fT*fT + f2)) + ((B*f2)/(fT)))*(1-P_kgcm2*6.54e-4);
+
+  return alpha_dBkm;
+
+}
+
```

```
+
+double PHYSICS_atten_thorp_dBkm(double f_kHz)
+{
+  double f2;
+  assert(f_kHz > 0.0);
+
+  f2 = f_kHz*f_kHz;
+
+  /* Thorp's expression for attenuation, in dB/km */
+  return (0.11*(f2/(1.0+f2)) + 44.0*(f2/(4100.0+f2)) + (0.000275)*f2 + 0.003);
+}
+
+
+// Checked against Matlab script for {3,10,20}kHz, Thorp and \
             Marsh-Schulkin (T=5C, S=30psu, z=50m)
+double WirelessChannel::atten_dBkm(double f_kHz)
+{
+ double alpha_dBkm;
+
+ if (include_atten) {
+ if (use_thorp_not_marshschulkin) {
+ alpha_dBkm = PHYSICS_atten_thorp_dBkm(f_kHz);
+ trace() << "Wireless Channel attenuation (Thorp) is: " \
             << alpha_dBkm << " dB/km, for f=" << f_kHz << "kHz";
+ } else {
+ alpha_dBkm = PHYSICS_atten_marshschulkin_dBkm(f_kHz, temperature_C, \
                          salinity_psu, waterdepth_m/2.0);
+ trace() << "Wireless Channel attenuation (Marsh-Schulkin) is: " << \
```

```
                    alpha_dBkm << " dB/km, for f=" << f_kHz << "kHz, T=" << \
temperature_C << "C, salinity " << salinity_psu << \
"PSU, depth=" << waterdepth_m/2.0 << "m";
+ }
+ } else {
+ alpha_dBkm = 0.0;
+ trace() << "Wireless Channel attenuation (none) is: " \
                << alpha_dBkm << " dB/km";
+ }
+ return alpha_dBkm;
+}
+
+
+
+double PHYSICS_spreading_loss_dB(double r_m, double waterdepth_m,
+      double k1, double k2)
+{
+  double spreading_dB, log10_arg1, log10_arg2;
+
+  /* Spreading loss: k2 to waterdepth, k1 beyond waterdepth */
+  if (r_m <= waterdepth_m + 1.0) {
+        log10_arg1 = r_m;
+ assert(log10_arg1 > 0.0);
+ spreading_dB = k2*10.0*log10(r_m);
+  } else {
+        log10_arg1 = waterdepth_m;
+ log10_arg2 = (r_m/waterdepth_m);
+ assert(log10_arg1 > 0.0);
```

```
+ assert(log10_arg2 > 0.0);
+ spreading_dB =   k2*10.0*log10(waterdepth_m)
+                + k1*10.0*log10(r_m/waterdepth_m);
+  }
+  return spreading_dB;
+}
+
+
+// Checked mixed-exponent model for k_coh=1.8, k_inc=1.2, waterdepth=100m, \
    ranges r_m=141.421m, 58.2215m, 83.1998m
+// Checked single-exponent model for ko=1.5, waterdepth=100m, ranges \
    r_m=141.421m, 58.2215m, 83.1998m
+double WirelessChannel::spreading_loss_dB(double r_m, \
                          bool coherent_not_incoherent)
+{
+ double spreading_dB;
+
+ if (use_mixed_exponents) {
+ if (coherent_not_incoherent) {
+ spreading_dB = PHYSICS_spreading_loss_dB(r_m, waterdepth_m, k_coh, k_coh);
+   trace() << "Wireless Channel spreading loss (coherent) for " << \
              r_m << "m is: " << spreading_dB << " dB, for k_coh=" \
  << k_coh << ", waterdepth=" << waterdepth_m << "m";
+ } else {
+ spreading_dB = PHYSICS_spreading_loss_dB(r_m, waterdepth_m, k_inc, k_coh);
+   trace() << "Wireless Channel spreading loss (incoherent) for " << \
              r_m << "m is: " << spreading_dB << " dB, for k_coh=" \
  << k_coh << ", k_inc=" << k_inc << ", waterdepth=" << \
```

```
  waterdepth_m << "m";
+ }
+ } else {
+ spreading_dB = PHYSICS_spreading_loss_dB(r_m, waterdepth_m, ko, ko);
+   trace() << "Wireless Channel spreading loss (single exponent) for " << \
                r_m << "m is: " << spreading_dB << " dB, for ko=" << ko << \
", waterdepth=" << waterdepth_m << "m";
+ }
+ return spreading_dB;
+}
+
+
+double WirelessChannel::pathloss_dB(double r_m, bool coherent_not_incoherent)
+{
+ if (underwater_acoustic_not_radio) {
+ double r_km = r_m/1000.0;
+ return (r_km*atten_dBkm(fc_kHz) + spreading_loss_dB(r_m, \
                                  coherent_not_incoherent));
+ } else {
+ double PLd_dB;
+
+ PLd_dB = PLd0 + 10.0*pathLossExponent*log10(r_m / d0)+normal(0, sigma);
+ return PLd_dB;
+ }
+}
+
+
+double WirelessChannel::noise_psd_dBre1uPa1m_Hz(double f_kHz)
```

```
+{
+  double Nt_dBre1uPa1m_Hz;    /* turbulence  */
+  double Ns_dBre1uPa1m_Hz;    /* shipping    */
+  double Nw_dBre1uPa1m_Hz;    /* wind        */
+  double Nth_dBre1uPa1m_Hz;   /* thermal     */
+  double log10_arg, noise_dBre1uPa1m_Hz;
+
+  assert(wind_ms >= 0.0);
+  assert(f_kHz   >  0.0);
+  assert((shipping_factor >= 0.0) && (shipping_factor <= 1.0));
+
+  /* expressions from Milica's capacity paper, in turn from Coates */
+  Nt_dBre1uPa1m_Hz  = 17.0 - 30.0*log10(f_kHz);
+  Ns_dBre1uPa1m_Hz  = 40.0 + 20.0*(shipping_factor-0.5) + \
                       26.0*log10(f_kHz) - 60.0*log10(f_kHz+0.03);
+  Nw_dBre1uPa1m_Hz  = 50.0 + 7.5*sqrt(wind_ms) + 20.0*log10(f_kHz) - \
                       40.0*log10(f_kHz+0.4);
+  Nth_dBre1uPa1m_Hz = -15.0 + 20.0*log10(f_kHz);
+
+  log10_arg = (
+        pow(10.0,(Nt_dBre1uPa1m_Hz/10.0)) +
+        pow(10.0,(Ns_dBre1uPa1m_Hz/10.0)) +
+        pow(10.0,(Nw_dBre1uPa1m_Hz/10.0)) +
+        pow(10.0,(Nth_dBre1uPa1m_Hz/10.0)) );
+
+  assert(log10_arg > 0.0);
+  noise_dBre1uPa1m_Hz = 10.0*log10(log10_arg);
+
```

```
+  return noise_dBre1uPa1m_Hz;
+}
+
+
+double WirelessChannel::noise_RMS_dBre1uPa1m(void)
+{
+  double f_kHz, df_kHz, f_lo_kHz, f_hi_kHz, noise_dBre1uPa1m_Hz, \
          noise_RMS_uPa1m, noise_RMS_dBre1uPa1m;
+
+  f_lo_kHz = fc_kHz - BW_kHz/2.0;
+  f_hi_kHz = fc_kHz + BW_kHz/2.0;
+  df_kHz = 0.001;
+
+  noise_RMS_uPa1m = 0.0;
+  for (f_kHz=f_lo_kHz; f_kHz<f_hi_kHz; f_kHz += df_kHz) {
+        noise_dBre1uPa1m_Hz = noise_psd_dBre1uPa1m_Hz(f_kHz);
+ noise_RMS_uPa1m += (df_kHz*1000.0)*pow(10.0, (noise_dBre1uPa1m_Hz/10.0));
+  }
+
+  assert(noise_RMS_uPa1m > 0.0);
+  noise_RMS_dBre1uPa1m = 10.0*log10(noise_RMS_uPa1m);
+
+  return noise_RMS_dBre1uPa1m;
+}
+
+
+void WirelessChannel::set_noiseFloor(void)
+{
```

```
+ if (underwater_acoustic_not_radio && include_noise) {
+ noiseFloor = noise_RMS_dBre1uPa1m();
+ trace() << "Wireless Channel ambient noise floor is: " << noiseFloor << \
                   " dB re: 1uPa@1m, for fc=" << fc_kHz << "kHz, BW=" \
   << BW_kHz << "kHz, shipping factor " << shipping_factor \
   << ", wind " << wind_ms << "m/s.";
+ } else {
+ noiseFloor = 0.0;
+ trace() << "Wireless Channel ambient noise floor is: " \
                << noiseFloor << " dBm";
+ }
+}
+
Index: src/wirelessChannel/WirelessChannel.h
===================================================================
--- src/wirelessChannel/WirelessChannel.h (revision 1)
+++ src/wirelessChannel/WirelessChannel.h (revision 101)
@@ -55,7 +55,25 @@
  double zCellSize;

  // variables corresponding to Wireless Channel module parameters
-double pathLossExponent; // the path loss exponent
+
+ bool   underwater_acoustic_not_radio;
+ double c_ms;
+ double fc_kHz;
+ double BW_kHz;
+ double waterdepth_m;
```

```
+ bool   use_mixed_exponents;
+ double ko;
+ double k_coh;
+ double k_inc;
+ bool   include_noise;
+ double shipping_factor;
+ double wind_ms;
+ bool   include_atten;
+ bool   use_thorp_not_marshschulkin;
+ double temperature_C;
+ double salinity_psu;
+
+ double pathLossExponent;
  double noiseFloor; // in dBm
  double PLd0; // Power loss at a reference distance d0 (in dBm)
  double d0; // reference distance (in meters)
@@ -106,6 +124,16 @@
  void updatePathLossElement(int, int, float);
  float calculateProb(float, int);

+ double distanceThreshold_m(void);
+ double range_m(double x0_m, double y0_m, double z0_m, double x1_m, \
            double y1_m, double z1_m);
+ double propagation_delay_s(double r_m);
+ double atten_dBkm(double f_kHz);
+ double spreading_loss_dB(double r_m, bool coherent_not_incoherent);
+ double pathloss_dB(double r_m, bool coherent_not_incoherent);
+ double noise_psd_dBre1uPa1m_Hz(double f_kHz);
```

```
+ double noise_RMS_dBre1uPa1m(void);

+ void set_noiseFloor(void);
```

BIBLIOGRAPHY

[1] Açar, G., and Adams, A.E. ACMENet: an underwater acoustic sensor network for real-time environmental monitoring in coastal areas. *IEE Proc. Radar, Sonar, and Nav. 153*, 4 (Aug. 2006), 365–380.

[2] Aguayo, D., Bicket, J., Biswas, S., Judd, G., and Morris, R. Link-level measurements from an 802.11b mesh network. In *Proc. ACM SIGCOMM* (Aug 2004).

[3] Akyildiz, I., Pompili, D., and Melodia, T. Challenges for efficient communication in underwater acoustic sensor networks. *SIGBED Rev. 1*, 2 (July 2004), 3–8.

[4] Akyildiz, I.F., Pompili, D., and Melodia, T. Underwater acoustic sensor networks: research challenges. *Ad Hoc Networks (Elsevier) 3*, 3 (May 2005), 257–279.

[5] Ali, M., Saif, U., Dunkels, A., Voigt, T., Römer, K., Langendoen, K., Polastre, J., and Uzmi, Z.A. Medium access control issues in sensor networks. *SIGCOMM Comput. Commun. Rev. 36*, 2 (Apr. 2006), 33–36.

[6] Baierlein, R. *Newtonian Dynamics*. McGraw-Hill, 1983.

[7] Baldo, N., Miozzo, M., Guerra, F., Rossi, M., and Zorzi, M. Miracle: The Multi-Interface Cross-Layer Extension of ns2. *EURASIP J. Wireless Comm. and Networking* (2010).

[8] Baumgartner, M., Fratantoni, D., and Partan, J. Autonomous detection of baleen whales using Wave Gliders, 2013. Funded proposal, Woods Hole Oceanographic Institution Marine Mammal Center.

[9] Baumgartner, M.F., Fratantoni, D.M., Hurst, T.P., Brown, M.W., Cole, T.V.N., Parijs, S.M. Van, and Johnson, M. Real-time reporting of baleen whale passive acoustic detections from ocean gliders. *Journal of the Acoustical Society of America* (submitted).

[10] Bazan, O., and Jaseemuddin, M. A Survey on MAC Protocols for Wireless Adhoc Networks with Beamforming Antennas. *IEEE Communications Surveys and Tutorials* (2012).

[11] Bharghavan, V., Demers, A., Shenker, S., and Zhang, L. MACAW: a media access protocol for wireless LANs. In *Proc. ACM SIGCOMM* (Oct. 1994), pp. 212–225.

[12] Brekhovskikh, L., and Lysanov, Y. *Fundamentals of Ocean Acoustics*, 3rd ed. Springer-Verlag, 2003.

[13] Burgess, J., Gallagher, B., Jensen, D., and Levine, B.N. MaxProp: Routing for Vehicle-Based Disruption-Tolerant Networks. In *Proc. IEEE INFOCOM* (April 2006).

[14] Burns, B., Brock, O., and Levine, B.N. Mv routing and capacity building in disruption tolerant networks. In *IEEE Infocom* (2005).

[15] Burns, B., Brock, O., and Levine, B.N. Autonomous Enhancement of Disruption Tolerant Networks. In *Proc. IEEE International Conference on Robotics and Automation* (May 2006).

[16] Burns, B., Brock, O., and Levine, B.N. MORA Routing and Capacity Building in Disruption Tolerant Networks. *In submission* (2006). technical report number:.

[17] Catipovic, J.A. Performance limitations in underwater acoustic telemetry. *IEEE Journal of Oceanic Engineering 15*, 3 (Jul. 1990), 205–216.

[18] Coates, R.F.W. *Underwater Acoustic Systems*. Halsted Press, 1989. See p.19 for "practical spreading" model; pp.91–93 for parameterized ambient noise power spectral density curves.

[19] Collins, M.D. A split-step Padé solution for the parabolic equation method. *Journal of the Acoustical Society of America* (April 1993).

[20] Cui, J.H., Kong, J., Gerla, M., and Zhou, S. Challenges: Building Scalable Mobile Underwater Wireless Sensor Networks for Aquatic Applications. *IEEE Network, Special Issue on Wireless Sensor Networking 20*, 3 (May/June 2006), 12–18.

[21] Dahl, P.H. High-frequency forward scattering from the sea surface: the characteristic scales of time and angle spreading. *IEEE J. Oceanic Engineering 26*, 1 (2001), 141–151.

[22] Davis, J.A., Fagg, A.H., and Levine, B.N. Wearable computers as packet transport mechanisms in highly-partitioned ad-hoc networks. In *IEEE ISWC '01: Proc. of the 5th IEEE Intl. Symposium on Wearable Computers* (2001).

[23] Doukkali, H., and Nuaymi, L. Analysis of MAC protocols for Underwater Acoustic Data Networks. In *Proc. MTS/IEEE Oceans Europe 2005* (2005).

[24] Dowdy, S., and Wearden, S. *Statistics for Research*. Wiley, 1983.

[25] Dunbabin, M., Corke, P., Vasilescu, I., and Rus, D. Data muling over underwater wireless sensor networks using an autonomous underwater vehicle. In *Proc. 2006 IEEE Intl. Conf. on Robotics and Automation (ICRA)* (May 2006), pp. 2091–2098.

[26] Efron, B. Bootstrap Methods: Another Look at the Jacknife. *Ann. Statist. 7*, 1 (1979).

[27] Eustice, R., Singh, H., and Whitcomb, L. Synchronous-Clock One-Way-Travel-Time Acoustic Navigation for Underwater Vehicles. *Journal of Field Robotics* (2010).

[28] Farmer, D.M., Deane, G.B., and Vagle, S. The influence of bubble clouds on acoustic propagation in the surf zone. *IEEE Journal of Oceanic Engineering 26*, 1 (Jan. 2001), 113–124.

[29] Farr, N., Bowen, A., Ware, J., Pontbriand, C., and Tivey, M. An Integrated Underwater Optical/Acoustic Communications System. In *Proc. IEEE OCEANS* (2010).

[30] Farr, N., Chave, A., Freitag, L., Preisig, J., White, S., Yoerger, D., and Titterton, P. Optical Modem Technology for Seafloor Observatories. In *Proc. IEEE OCEANS Conference* (Sept. 2005).

[31] Foo, K., Atkins, P., Collins, T., Morley, C., and Davies, J. A routing and channel-access approach for an ad hoc underwater acoustic network. In *Proc. MTS/IEEE Oceans 2004* (Nov. 2004), vol. 2, pp. 789–795.

[32] Frater, M.R., Ryan, M.J., and Dunbar, R.M. Electromagnetic Communications within Swarms of Autonomous Underwater Vehicles. In *Proc. ACM WUWNet 2006* (2006), pp. 64–70.

[33] Freitag, L., Ball, K., Partan, J., Gallimore, E., Singh, S., and Koski, P. Underwater Acoustic Network Testbed. In *Extended Abstract, Sixth ACM International Workshop on Underwater Networks (WUWNet)* (December 2011).

[34] Freitag, L., Grund, M., Catipovic, J., Nagle, D., Pazol, B., and Glynn, J. Acoustic Communications with Small UUVs Using a Hull-Mounted Conformal Array. In *Proc. IEEE OCEANS'01 Conference* (Nov. 2001), vol. 4, pp. 2270–2275.

[35] Freitag, L., Grund, M., Partan, J., Ball, K., Singh, S., and Koski, P. Multi-Band Acoustic Modem for the Communications and Navigation Aid AUV. In *Proc. IEEE OCEANS'05 Conference* (Sept. 2005).

[36] Freitag, L., Grund, M., Singh, S., Partan, J., Koski, P., and Ball, K. The WHOI Micro-Modem: An Acoustic Communications and Navigation System for Multiple Platforms. In *Proc. IEEE OCEANS* (Sept. 2005).

[37] Freitag, L., Grund, M., Singh, S., Smith, S., Christenson, R., Marquis, L., and Catipovic, J. A Bidirectional Coherent Acoustic Communication System for Underwater Vehicles. In *Proc. IEEE OCEANS'98 Conference* (Sept. 1998), vol. 1, pp. 482–486.

[38] Freitag, L., Grund, M., von Alt, C., Stokey, R., and Austin, T. A Shallow Water Acoustic Network for Mine Countermeasures Operations with Autonomous Underwater Vehicles. In *Underwater Defense Technology (UDT)* (2005).

[39] Freitag, L., Johnson, M., Grund, M., Singh, S., and Preisig, J. Integrated Acoustic Communication and Navigation for Multiple UUVs. In *Proc. IEEE OCEANS Conference* (Nov. 2001).

[40] Freitag, L., Koski, P., Morozov, A., Singh, S., and Partan, J. Acoustic Communications and Navigation under Arctic Ice. In *IEEE Oceans 2012* (2012).

[41] Freitag, L., Stojanovic, M., Grund, M., and Singh, S. Acoustic Communications for Regional Undersea Observatories. In *In Proc. Oceanology Intl* (2002).

[42] Freitag, L., Stojanovic, M., Kilfoyle, D., and Preisig, J. High-Rate Phase-Coherent Acoustic Communication: A Review of a Decade of Research and a Perspective on Future Challenges. In *Proc. European Conf. on Underwater Acoustics* (July 2004).

[43] Freitag, L., Stojanovic, M., Singh, S., and Johnson, M. Analysis of Channel Effects on Direct-Sequence and Frequency-Hopped Spread-Spectrum Acoustic Communications. *IEEE J. Oceanic Engineering 26*, 4 (Oct. 2001), 586–593.

[44] Frisk, G., 2010. Personal communication.

[45] Frye, D., Ware, J., Grund, M., Partan, J., Koski, P., Singh, S., Freitag, L., Collins, J., and Detrick, R. An Acoustically-Linked Deep-Ocean Observatory. In *Proceedings of Oceans 2005 - Europe* (June 2005), vol. 2, pp. 969–974.

[46] Fullmer, C.L., and Garcia-Luna-Aceves, J.J. Floor acquisition multiple access (FAMA) for packet-radio networks. In *SIGCOMM '95: Proc. Conf. Appl., tech., arch., and protocols for computer communication* (1995), pp. 262–273.

[47] Fumo, J.P., and Ornée, M.W. Implementation of an Advanced Ocean Transponder and Deckset Utilizing Complex Waveforms. In *Proc. IEEE OCEANS* (2001). In particular, Section V.A and Figure 4.

[48] Gallimore, E., Partan, J., Vaughn, I., Singh, S., Shusta, J., and Freitag, L. The WHOI Micromodem-2: A Scalable System for Acoustic Communications and Networking. In *Proc. IEEE OCEANS* (Sept. 2010).

[49] Garrett, C., and Munk, W. Internal Waves in the Ocean. *Ann. Rev. Fluid Mech.* (1979).

[50] German, C.R., Jakuba, M.V., Kinsey, J.C., Partan, J., Suman, S., Belani, A., and Yoerger, D.R. A long-term vision for long-range ship-free deep ocean operations: persistent presence through coordination of Autonomous Surface Vehicles and Autonomous Underwater Vehicles. In *Proc. IEEE AUV 2012* (2012).

[51] Grund, M., Freitag, L., Preisig, J., and Ball, K. The PLUSNet Underwater Communications System. In *Proc. IEEE OCEANS* (Sept 2006).

[52] Guerra, F., Casari, P., and Zorzi, M. World ocean simulation system (WOSS): a simulation tool for underwater networks with realistic propagation modeling. In *WUWNet* (2009).

[53] Guo, X., Frater, M.R., and Ryan, M.J. Design of a Propagation-delay-tolerant MAC Protocol for Underwater Acoustic Sensor Networks. *IEEE J. Oceanic Engineering 34*, 2 (Apr 2009), 170–180.

[54] Harris, A.F. III, Stojanovic, M., and Zorzi, M. Idle-Time Energy Savings through Wake-up Modes in Underwater Acoustic Networks. *Ad Hoc Networks 7*, 4 (2009), 770–777.

[55] Heidemann, J., Ye, W., Wills, J., Syed, A., and Li, Y. Research Challenges and Applications for Underwater Sensor Networking. In *Proc. IEEE Wireless Comm. and Networking Conf.* (Apr. 2006).

[56] Heidemann, J., Ye, W., Wills, J., Syed, A., and Li, Y. Research Challenges and Applications for Underwater Sensor Networking. In *Proc. IEEE WCNC* (2006).

[57] Hodgkiss, W.S., Song, H.C., Deane, G., Preisig, J., Badiey, M., and Song, A. The Kauai Acomms MURI 2011 (KAM11) Experiment Trip Report. Tech. rep., July 2011.

[58] Jaffe, J., and Schurgers, C. Sensor Networks of Freely Drifting Autonomous Underwater Explorers. In *Proc. ACM WUWNet 2006* (2006), pp. 93–96.

[59] Jensen, F.B., Kuperman, W.A., Porter, M.B., and Schmidt, H. *Computational Ocean Acoustics*. Springer-Verlag, 2000.

[60] Johnson, M., Preisig, J., Freitag, L., and Stojanovic, M. FSK and PSK Performance of the Utility Acoustic Modem. In *Proc. IEEE OCEANS* (Sept. 1999).

[61] Kanthan, R.R. The ICoN Integrated Communication and Navigation Protocol for Underwater Acoustic Networks. Master's thesis, MIT, Sept. 2005.

[62] Karn, P. MACA – A new channel access method for packet radio. In *ARRL/CRRL Amateur Radio 9th Computer Networking Conference* (1990).

[63] Kebkal, A., Kebkal, K., and Komar, M. Data-link protocol for underwater acoustic networks. In *Proc. MTS/IEEE Oceans Europe 2005* (2005), pp. 1174–1180.

[64] Kilfoyle, D.B., and Baggeroer, A.B. The state of the art in underwater acoustic telemetry. *IEEE Journal of Oceanic Engineering 25*, 1 (Jan. 2000), 4–27.

[65] Kotz, D., Newport, C., Gray, R., Liu, J., Yuan, Y., and Elliott, C. Experimental Evaluation of Wireless Simulation Assumptions. In *IEEE MSWiM* (Oct 2004), pp. 78–82.

[66] Lapierre, G., Chevallier, L., Gallaud, F., and Ayela, G. Design of a communication protocol for underwater acoustic modems and networks. In *Proc. MTS/IEEE Oceans 2001* (Nov. 2001), vol. 4, pp. 2220–2226.

[67] Leguay, J., Friedman, T., and Conan, V. Dtn routing in a mobility pattern space. In *ACM WDTN* (2005), pp. 276–283.

[68] Leonard, N.E., Paley, D., Lekien, F., Sepulchre, R., Fratantoni, D.M., and Davis, R. Collective Motion, Sensor Networks and Ocean Sampling. *Proc. IEEE 95*, 1 (2007), 48–74.

[69] Lindgren, A., Doria, A., and Schelén, O. Probabilistic routing in intermittently connected networks. *ACM SIGMOBILE Mob. Comput. Commun. Rev. 7*, 3 (2003), 19–20.

[70] Liu, T.T., and Towsley, D. Window and Tree Protocols for Satellite Channels. In *Proc. Infocom* (1983).

[71] Manley, J., and Willcox, S. The Wave Glider: A persistent platform for ocean science. In *Proc. IEEE Oceans* (2010).

[72] Marn, W., Rice, J., Fletcher, C., Creber, R., Babicz, R., and Rogers, K. The Evolution of Radio/Acoustic Communication Gateway Buoys. In *Proc. IEEE Oceans* (2005).

[73] Maronna, R.A., Martin, R.D., and Yohai, V.J. *Robust Statistics: Theory and Methods*. Wiley, 2006.

[74] McCanne, S., and Floyd, S. Network Simulator Version 2. `http://www.isi.edu/nsnam/ns`.

[75] Medwin, H., and Clay, C.S. *Fundamentals of Acoustic Oceanography*. Academic Press, 1998.

[76] Molins, M., and Stojanovic, M. Slotted FAMA: A MAC Protocol for Underwater Acoustic Networks. In *Proc. IEEE OCEANS Conf.* (Sept 2006).

[77] Morns, I.P., Hilton, O., Adams, A., and Sharif, B. Protocols for sub-sea communications networks. In *Proc. MTS/IEEE Oceans 2001* (2001).

[78] Morozov, A.K., and Webb, D.C. A Sound Projector for Acoustic Tomography and Global Ocean Monitoring. *IEEE J. Oceanic Engineering 28*, 2 (2003), 174–185.

[79] Ocean Acoustics Library. `http://oalib.hlsresearch.com`.

[80] Ouimet, S.P., Hahn, M.J., and Rice, J. Undersea Communication Network as a UUV Navigation Aid. In *Proc. IEEE OCEANS Conf.* (Sept. 2005).

[81] Park, M.K., and Rodoplu, V. UWAN-MAC: An Energy-Efficient MAC Protocol for Underwater Acoustic Wireless Sensor Networks. *IEEE J. Oceanic Engineering 32*, 3 (2007), 710–720.

[82] Parkes, S., and Rosello, J. SpaceWire ECSS-E50-12A. In *International SpaceWire Seminar* (2003).

[83] Partan, J., Kurose, J., Levine, B., and Preisig, J. Low Spreading Loss in Underwater Acoustic Networks Reduces RTS/CTS Effectiveness. In *ACM WUWNet 2011* (2011).

[84] Partan, J., Kurose, J., and Levine, B.N. A Survey of Practical Issues in Underwater Networks. In *ACM 1st Int'l Workshop on Underwater Networks (WUWNet)* (2006).

[85] Partan, J., Kurose, J., and Levine, B.N. A Survey of Practical Issues in Underwater Networks. *ACM SIGMOBILE MC2R 11*, 4 (2007).

[86] Peleato, B., and Stojanovic, M. A MAC protocol for ad hoc underwater acoustic sensor networks. In *WUWNet* (2006).

[87] Petrioli, C., and Petroccia, R. SUNSET: Simulation, Emulation, and Real-life Testing of Underwater Wireless Sensor Networks. In *Proc. IEEE UComms* (Sept. 2012).

[88] Peyravi, H. Medium access control protocols performance in satellite communications. *IEEE Communications Magazine 37*, 3 (Mar. 1999), 62–71.

[89] Pompili, D., Melodia, T., and Akyildiz, I. Routing algorithms for delay-insensitive and delay-sensitive applications in underwater sensor networks. In *Proc. MobiCom* (Sept 2006).

[90] Porter, M.B., and Liu, Y.-C. Finite Element Ray Tracing. In *Theoretical and Computational Acoustics - Volume 2*, D. Lee and M.H. Schultz, Eds. World Scientific Publishing Co., 1994.

[91] Preisig, J. Acoustic propagation considerations for underwater acoustic communications network development. *ACM SIGMOBILE MC2R 11*, 4 (2007), 2–10.

[92] Preisig, J.C., and Johnson, M.P. Signal detection for communications in the underwater acoustic environment. *IEEE J. Oceanic Engineering 26*, 4 (2001), 572–585.

[93] Rajan, S.D., Lynch, J.F., and Frisk, G.V. Perturbative inverse methods for obtaining bottom geoacoustic parameters in shallow water. *Journal of the Acoustical Society of America 82*, 3 (1987), 998–1017.

[94] Rappaport, T.S. *Wireless Communications: Principles and Practice*. Prentice Hall, 1996.

[95] Rice, J. Seaweb Acoustic Communication and Navigation Networks. In *Proc. Int. Conf. Underwater Acoustic Measurements: Technologies & Results* (July 2005).

[96] Rice, J., Creber, B., Fletcher, C., Baxley, P., Rogers, K., McDonald, K., Rees, D., Wolf, M., Merriam, S., Mehio, R., Proakis, J., Scussel, K., Porta, D., Baker, J., Hardiman, J., and Green, D. Evolution of Seaweb Underwater Acoustic Networking. In *Proc. IEEE Oceans 2000* (2000).

[97] R.Murali, and B.L.Hughes. Random Access with Large Propagation Delay. *IEEE/ACM Trans. Networking 5*, 6 (Dec. 1997), 924–935.

[98] Rom, R., and Sidi, M. *Multiple Access Protocols: Performance and Analysis*. Springer-Verlag, 1990.

[99] Salvá-Garau, F., and Stojanovic, M. Multi-Cluster Protocol for Ad Hoc Mobile Underwater Acoustic Networks. In *Proc. IEEE OCEANS'03 Conference* (Sept. 2003).

[100] Sarwate, D.V., and Pursley, M.B. Crosscorrelation properties of pseudorandom and related sequences. *Proc. IEEE 68*, 5 (May 1980), 593–619.

[101] Schill, F., Zimmer, U.R., and Trumpf, J. Visible Spectrum Optical Communication and Distance Sensing for Underwater Applications. In *Proc. Australasian Conf. Robotics and Automation* (2004).

[102] Schill, F., Zimmer, U.R., and Trumpf, J. Towards Optimal TDMA Scheduling for Robotic Swarm Communication. In *Proc. TAROS Intl. Conf.* (Sept. 2005).

[103] Schneider, T., and Schmidt, H. The Dynamic Compact Control Language: A Compact Marshalling Scheme for Acoustic Communications. In *Proc. IEEE OCEANS* (2010).

[104] Seltman, H. *Experimental Design and Analysis*. published online at `http://www.stat.cmu.edu/~hseltman/309/Book/Book.pdf`, June 2013. Chapter 9, "Simple Linear Regression".

[105] Serafina AUV. `http://serafina.anu.edu.au/`.

[106] Shahabudeen, S., Chitre, M., and Motani, M. A multi-channel MAC protocol for AUV networks. In *Proc. IEEE Oceans Europe* (June 2007).

[107] Shusta, J., Freitag, L., and Partan, J. A Modular Data Link Layer for Underwater Networks. In *Proc. IEEE OCEANS* (Sept. 2008).

[108] Singh, S., Grund, M., Bingham, B., Eustice, R., Singh, H., and Freitag, L. Underwater Acoustic Navigation with the WHOI Micro-Modem. In *Proc. IEEE OCEANS* (Sept. 2006).

[109] Singh, S., Webster, S.E., Freitag, L., Whitcomb, L.L., Ball, K., and Bailey, J. Acoustic communication performance of the WHOI Micro-Modem in sea trials of the Nereus vehicle to 11,000 m depth. In *Proc. IEEE OCEANS* (Oct. 2009).

[110] Smith, S., Park, J.C., and Neel, A. A Peer-to-Peer Communication Protocol for Underwater Acoustic Communication. In *Proc. IEEE Oceans 1997* (1997).

[111] Son, D., Krishnamachari, B., and Heidemann, J. Experimental study of concurrent transmission in wireless sensor networks. In *Proc. ACM SenSys* (2006).

[112] Sözer, E., Stojanovic, M., and Proakis, J. Underwater Acoustic Networks. *IEEE J.Oceanic Eng. 25*, 1 (2000), 72–83.

[113] Stojanovic, M. Recent Advances in High-Speed Underwater Acoustic Communications. *IEEE J. Oceanic Engineering 21*, 2 (Apr. 1996), 125–136.

[114] Stojanovic, M. Optimization of a Data Link Protocol for an Underwater Acoustic Channel. In *Proc. IEEE OCEANS'05 Conference* (June 2005).

[115] Stojanovic, M. Low Complexity OFDM Detector for Underwater Acoustic Channels. In *Proc. IEEE OCEANS* (Sept 2006).

[116] Stojanovic, M. Frequency reuse underwater: capacity of an acoustic cellular network. In *WUWNet* (2007).

[117] Stojanovic, M. On the Relationship Between Capacity and Distance in an Underwater Acoustic Communication Channel. *ACM SIGMOBILE MC2R 11*, 4 (Oct 2007), 34–43.

[118] Stojanovic, M., and Freitag, L. Multichannel Detection for Wideband Underwater Acoustic CDMA Communications. *IEEE Journal of Oceanic Engineering 31*, 3 (2006), 685–695.

[119] Stojanovic, M., Freitag, L., Leonard, J., and Newman, P. A Network Protocol for Multiple AUV Localization. In *Proc. IEEE OCEANS'02 Conf.* (Oct. 2002).

[120] Stojanovic, M., and Zvonar, Z. Multichannel Processing of Broad-Band Multiuser Communication Signals in Shallow Water Acoustic Channels. *IEEE Journal of Oceanic Engineering 21*, 2 (Apr. 1996), 156–166.

[121] Stokey, R., Allen, B., Austin, T., Goldsborough, R., Forrester, N., Purcell, M., and von Alt, C. Enabling Technologies for REMUS Docking: An Integral Component of an Autonomous Ocean-Sampling Network. *IEEE Journal of Oceanic Engineering 26*, 4 (Oct. 2001), 487–497.

[122] Stokey, R.P., Freitag, L.E., and Grund, M.D. A Compact Control Language for AUV Acoustic Communication. In *Proc. IEEE OCEANS Europe* (June 2005).

[123] Syed, A., and Heidemann, J. Time Synchronization for High Latency Acoustic Networks. In *Proc. IEEE Infocom* (April 2006).

[124] Tomasi, B., Preisig, J.C., and Zorzi, M. On the Predictability of Underwater Acoustic Communications Performance: the KAM11 Data Set as a Case Study. In *ACM WUWNet 2011* (2011).

[125] UNOLS day rates. `www.unols.org/meetings/2011/201110fic/201110ficap09.pdf`, Pages 8-9. Downloaded Aug 2013.

[126] Urick, R.J. *Principles of Underwater Sound*, 3rd ed. McGraw-Hill, 1983.

[127] van Trees, H.L. *Detection, Estimation, and Modulation Theory, Vol.3*. Wiley, 1968.

[128] Vasilescu, I., Kotay, K., Rus, D., Dunbabin, M., and Corke, P. Data collection, storage, and retrieval with an underwater sensor network. In *SenSys '05: Proc. 3rd International Conf. on Embedded networked sensor systems* (2005), pp. 154–165.

[129] Vera, M.D., Heaney, K.D., and Group, NPAL. The effect of bottom interaction on transmissions from the North Pacific Acoustic Laboratory Kauai source. *Journal of the Acoustical Society of America 117*, 3 (2005), 1624–1634. (NPAL Group consists of J.A. Colosi, B.D. Cornuelle, B.D. Dushaw, M.A. Dzieciuch, B.M. Howe, J.A. Mercer, W.H. Munk, R.C. Spindel, and P.F. Worcester).

[130] Webb, D. C., Simonetti, P. J., and Jones, C .P. SLOCUM: an underwater glider propelled by environmental energy. *IEEE Journal of Oceanic Engineering* (Oct. 2001).

[131] Webb Research. `http://www.webbresearch.com`.

[132] Widmer, J., and Boudec, J. Le. Network coding for efficient communication in extreme networks. In *ACM WDTN* (2005), pp. 284–291.

[133] Willett, J.B., and Singer, J.D. Another Cautionary Note about R^2: Its Use in Weighted Least-Squares Regression Analysis. *The American Statistician 42*, 3 (August 1988).

[134] Wills, J., Ye, W., and Heidemann, J. Low-Power Acoustic Modem for Dense Underwater Sensor Networks. In *Proc. First ACM Intl Workshop on UnderWater Networks (WUWNet)* (Sept. 2006).

[135] Xu, K., Gerla, M., and Bae, S. Effectiveness of RTS/CTS handshake in IEEE 802.11 based ad hoc networks. *Ad Hoc Networks* (2003).

[136] Ye, F., Yi, S., and Sikdar, B. Improving Spatial Reuse of IEEE 802.11 Based Ad hoc Networks. In *GLOBECOM* (2003).

[137] Ye, W., Heidemann, J., and Estrin, D. Medium access control with coordinated adaptive sleeping for wireless sensor networks. *IEEE/ACM Trans. Netw. 12*, 3 (2004), 493–506.

[138] Zhang, P., Sadler, C.M., Lyon, S.A., and Martonosi, M. Hardware design experiences in zebranet. In *SenSys '04: Proceedings of the 2nd international conference on Embedded networked sensor systems* (New York, NY, USA, 2004), ACM, pp. 227–238.

[139] Zhang, X., Neglia, G., Kurose, J., and Towsley, D. On the Benefits of Random Linear Coding for Unicast Applications in Disruption Tolerant Networks. In *IEEE Network Coding Workshop* (2006).

[140] Zhao, W., and Ammar, M. Message Ferrying: Proactive Routing In Highly Partitioned Wireless Ad hoc Networks. In *Proc. IEEE Wkshp on Future Trends in Distributed Computing Systems* (May 2003).

[141] Zhao, W., Ammar, M., and Zegura, E. A Message Ferrying Approach for Data Delivery in Sparse Mobile Ad hoc Networks. In *Proc. ACM Mobihoc* (May 2004).

[142] Zhao, W., Ammar, M., and Zegura, E. Controlling the mobility of multiple data transport ferries in a delay-tolerant network. In *IEEE INFOCOM* (2005).